

Using Polymers to Improve the Performance of Sulfur and Organic Cathodes

by

Xiguang Gao

A thesis

presented to the University of Waterloo

in fulfillment of the

thesis requirement for the degree of

Doctor of Philosophy

in

Chemical Engineering (Nanotechnology)

Waterloo, Ontario, Canada, 2022

© Xiguang Gao 2022

Examining Committee Membership

The following served on the Examining Committee for this thesis. The decision of the Examining Committee is by majority vote.

External Examiner

Dr. Zhibin Ye

(Professor, Department of Chemical and Materials Engineering, Concordia University)

Supervisor

Dr. Yuning Li

(Professor, Department of Chemical Engineering, University of Waterloo)

Internal Member

Dr. Michael Pope

(Associate Professor, Department of Chemical Engineering, University of Waterloo)

Internal Member

Dr. Xianshe Feng

(Professor, Department of Chemical Engineering, University of Waterloo)

Internal-external Member

Dr. Jean Duhamel

(Professor, Department of Chemistry, University of Waterloo)

Author's Declaration

This thesis consists of material all of which I authored or co-authored: see Statement of Contributions included in the thesis. This is a true copy of the thesis, including any required final revisions, as accepted by my examiners.

I understand that my thesis may be made electronically available to the public.

Statement of Contributions

This thesis consists of materials from two published papers and two draft papers in which I, Xiguang Gao, was the principal author or co-first-author. All authors reviewed and commented on the manuscripts.

The content in **Chapter 3** has been published in “Ionically cross-linked PEDOT:PSS as a multifunctional conductive binder for high-performance lithium–sulfur batteries”, Longlong Yan, Xiguang Gao, Joseph Palathinkal Thomas, Jenner Ngai, Haig Altounian, Kam Tong Leung, Yuezhong Meng and Yuning Li, *Sustainable Energy Fuels*, **2018**, 2, 1574, where Xiguang Gao was a co-first-author. Dr. Yuning Li conceived the idea. Longlong Yan and Xiguang Gao co-performed the experiments including crosslinking of PEDOT:PSS by $\text{Mg}(\text{NO}_3)_2$, polysulfide trapping by UV-Vis spectroscopy, battery fabrication and testing, and data analysis. Joseph Palathinkal Thomas and Jenner Ngai conducted the four-probe conductivity measurement, Haig Altounian participated in the synthesis of sulfur nanoparticle. Dr. Kam Tong Leung and Dr. Yuezhong Meng provided technical advice.

The content in **Chapter 4** has been published in “Boosting Li–S battery performance using an in-cell electropolymerized conductive polymer”, Xiguang Gao, Chenyang Guo, Zhong Ma, Guan Xi, Yuezhong Meng and Yuning Li, *Materials Advances*, **2021**, 2, 974, where Xiguang Gao was the first-author. Dr. Yuning Li conceived the idea, Xiguang Gao designed and conducted the experiments. Xiguang Gao and Dr. Yuning Li co-wrote the manuscript. Chenyang Guo, Dr. Zhong Ma, Dr. Guan Xi and Dr. Yuezhong Meng provided technical advice.

The content in **Chapter 5** has not been published and will be submitted for publication in the near future: “A stable 2,5-dihydroxy-1,4-benzoquinone (DHBQ) based organic cathode enabled by coordination polymer formation and binder optimization”, Xiguang Gao, Zhe Huang and Yuning Li, **2022** (in preparation), where Xiguang Gao was the first-author. Xiguang Gao and Dr. Yuning Li co-conceived the idea and co-designed the experiments. Xiguang Gao performed the experiments, and co-wrote the manuscript with Dr. Yuning Li. Zhe Huang participated in the XRD and FTIR characterizations.

The content in **Chapter 6** has not been published and will be submitted for publication in the near future: “Conjugated Diketopyrrolopyrrole (DPP) Polymer Based P-type and Bipolar-type

Organic Cathodes”, Xiguang Gao and Yuning Li, **2022** (in preparation), where Xiguang Gao was the first-author. Dr. Yuning Li and Xiguang Gao co-conceived the idea. Xiguang Gao performed the experiments. Xiguang Gao and Dr. Yuning Li co-wrote the manuscript.

Abstract

Pollution, climate change and the rapid consumption of fossil fuel resources are driving widespread development and adoption of clean and renewable energy sources, including hydro, wind and solar power, as well as non-fossil fuel powered products such as electric vehicles. Therefore, there is an urgent and growing demand for corresponding high-efficiency, high-density, and low-cost energy storage systems. Among them, Li, Na, K, Mg, Zn, and Al-ion batteries and other types of rechargeable batteries have the characteristics of high efficiency and reversibility, light weight, environmental friendliness, and low cost, and have been widely studied in academia and industries. While extensive research over the past decades has led to the highly successful commercialization of lithium-ion batteries in portable electronics and electric vehicles, there have been many efforts to develop next-generation batteries with higher energy density, longer cycle life, and lower cost, such as batteries based on sulfur and organic materials.

This thesis has explored the use of functional polymers to improve the specific capacity, discharge voltage, cycling stability, and rate performance of sulfur and organic cathodes. Through a combination of characterization techniques including thermal gravimetric analysis (TGA), X-ray diffraction (XRD), Fourier transform infrared spectroscopy (FTIR), ultraviolet-visible spectroscopy (UV-Vis), peel test, cyclic voltammetry (CV), chronoamperometry (CA), electrochemical impedance spectroscopy (EIS), and galvanostatic cycling, a deep understanding toward the development of strategies for tackling the dissolution issue of sulfur and organic cathodes, conductivity change of conductive polymers during the battery cycling process, capacity fading mechanism, electrochemical reaction kinetics, and charge storage mechanism have been gained. Our findings may inspire the development of novel cathode materials with higher energy density and lower cost for the next-generation electrical energy storage.

Firstly, a multi-functional poly(3,4-ethylenedioxythiophene):poly(styrenesulfonate) (PEDOT:PSS)-Mg²⁺ binder formed by cross-linking PEDOT:PSS with Mg²⁺ was developed for the sulfur cathode. This new binder has a robust 3-D network structure, and a strong binding ability toward lithium polysulfides due to the strong interaction between the oxygen atoms in PEDOT and lithium polysulfides. These functionalities can increase the charge transfer reactions, and cushion the drastic volume change during discharge/charge cycling. The Li-S battery with a cathode using this new binder exhibited an initial capacity of 1097 mA h g⁻¹ with a capacity

retention of 74% over 250 cycles at 0.5 C, which are significant improvements compared with the Li-S battery using a conventional PVDF binder. Moreover, the preparation of the cathode slurry for coating the cathode film uses water present in the PEDOT:PSS dispersion as the only dispersing solvent, which eliminates the use of toxic organic solvent such as N-methyl-2-pyrrolidone (NMP), making the fabrication of Li-S batteries more environmentally friendly.

Secondly, an innovative and facile in-cell electrochemical polymerization method has been developed to incorporate a conductive polymer PEDOT into the sulfur cathode. The PEDOT was formed on the surface and in the pores of the sulfur cathode film by the chronoamperometry method (4.1 V vs. Li^+/Li for 800s) in a coin cell. The in-cell synthesis method enables an intimate contact between PEDOT and other components in the cathode, leading to enhanced electron transport and effective trapping of soluble polysulfides. As a result, the sulfur cathode with the in-cell formed PEDOT shows substantially improved capacity, cycling stability, and rate performance compared with that using the commercial PEDOT. Furthermore, combined cyclic voltammetry (CV) and electrochemical impedance spectroscopy (EIS) results show that the conductivity of PEDOT changes drastically during the Li-S battery cycling process. In the potential range of 1.7~2.8 V for Li-S batteries, the conductivity of PEDOT is rather limited due to the electrochemical dedoping process. To utilize the high conductivity of PEDOT and increase its conductivity by the electrochemical doping, PEDOT is applied in LiFeO_4 (LFP) batteries which uses a potential range of 2~4.2 V. With the in-situ synthesized PEDOT, the LFP cathode shows a notable improvement in the specific capacity at the high current rate of 1 C.

Thirdly, a series of one-dimensional coordination polymers using 2,5-dihydroxy-1,4-benzoquinone (DHBQ) as the ligand and divalent metal ions (Ni, Co, Mn, Zn, and Cu) as the metal center have been synthesized and their electrochemical properties have been compared. It has been found that the coordination polymers using Ni, Co, Mn, and Zn ($\text{M-DHBQ}\cdot 2\text{H}_2\text{O}$) exhibit the redox activities of both metal and ligand in the potential range of 0.5~3 V vs. Li^+/Li , while the coordination polymer using Cu (Cu-DHBQ) only exhibits the redox activity of the ligand in the same potential range. In the potential range of 1.4~3 V vs. Li^+/Li where only the DHBQ ligand is redox active, Cu-DHBQ exhibits the highest utilization of the quinone groups among the as-synthesized coordination polymers. Moreover, the capacity fading mechanism of Cu-DHBQ cathode is identified as the dissolution of the discharged product or intermediate in the electrolyte

by UV-Vis analysis. By using the alginate binder (25 wt% in the cathode), which can strongly bind the electrode film and effectively trap the soluble species, the Cu-DHBQ cathode exhibits a high capacity of 261 mA h g⁻¹ (98.1% of the theoretical capacity) at the current rate of 20 mA g⁻¹, and can maintain a capacity of 194 mA h g⁻¹ after 200 cycles at 100 mA g⁻¹ with a capacity retention of 91.5%. Furthermore, our coordination approach is very versatile and can be extended to other ligand such as 2,5-dichloro-3,6-dihydroxy-1,4-benzoquinone (DHBQ-Cl) which has a higher discharge voltage than that of DHBQ. The Cu-DHBQ-Cl cathode shows a fast capacity fading, which might be caused by the collapse of the crystal structure after Li⁺ insertion. Nevertheless, our approach opens up a new avenue for the application of coordination polymers in energy storage. Finally, the stabilization of organic cathode through acid-base interaction with polymer binders has also been studied. It has been found that the binder approach for improving the cycling stability of organic cathode is only an auxiliary approach, whereas the polymerization approach, which includes the formation of conventional polymers, macrostructures, coordination polymers, covalent organic frameworks (COFs) and metal organic frameworks (MOFs), is be considered as the primary approach.

Finally, two diketopyrrolopyrrole (DPP) based conjugated polymers, namely diketopyrrolopyrrole-quaterthiophene copolymer (PDQT) and diketopyrrolopyrrole-bithiophene polymer (PDBT) have been explored as the cathode materials for Li-ion storage. The PDQT cathode shows a p-type charge storage mechanism with a theoretical capacity of 104.8 mA h g⁻¹ and an experimental capacity of 44.4 mA h g⁻¹ (corresponding to a high doping level of 42%), while the PDBT cathode shows a bipolar charge storage mechanism with a theoretical capacity of 124.8 mA h g⁻¹ and an experimental capacity of 17.1 mA h g⁻¹. The experimental average discharge voltages of PDQT and PDBT cathodes are ~3.8 and ~2.95 V, respectively, which are much higher than other conjugated polymer cathodes. Further optimization of the testing condition (e.g. nanocomposite formation between conjugated polymer cathode material and porous carbon, better electrolyte solvent which is stable over a broad potential range so that both the p- and n-doping reactions are reversible) is needed to increase the experimental capacity of PDBT.

Acknowledgements

First of all, I would like to express my sincere gratitude to my supervisor Prof. Yuning Li, for introducing the battery research area to me. This area is promising, exciting and meaningful yet challenging and competitive at the same time. Moreover, I want to thank my supervisor for his broad and deep knowledge, inspiration and encouragement, detailed and patient guidance throughout my PhD study regarding experimental design, data analysis and presentation, paper writing, and logical thinking. Without his input, the entire thesis would not have been possible. I also want to thank the Chem Eng Department, Waterloo Institute for Nanotechnology, and UWaterloo for providing me with the fundings for this PhD study.

Next, I want to thank the past and present members from Prof. Li's group who have helped me during the PhD study, Chenyang Guo, Dr. Jenner H. L. Ngai, Zhe Huang, Zhong Ma, Yonglin Wang, Yi Yuan, Dr. Arthur D. Hendsbee, Fengmei Li, Pankaj Kumar, Daniel Afzal, Xiaocheng Zhou, and Han Meng. I have had a great time working with them.

Furthermore, I want to thank all the other committee members, Prof. Zhibin Ye from Concordia University, Prof. Michael Pope, Prof. Jean Duhamel, and Prof. Xianshe Feng from University of Waterloo, for their valuable suggestions during my PhD comprehensive exam and PhD defense, and for spending time reviewing my PhD thesis.

Finally, I want to thank my parents and brother for their unconditional and endless love and encouragement. They always have faith in me and let me freely pursue my goals for my life.

Table of Contents

Examining Committee Membership	ii
Author's Declaration	iii
Statement of Contributions	iv
Abstract	vi
Acknowledgements	ix
List of Figures	xiv
List of Tables	xix
List of Schemes	xx
List of Abbreviations	xxi
Chapter 1. Introduction	1
1.1 Sulfur cathode	3
1.1.1 Redox mechanism of sulfur cathode	5
1.1.2 Challenges of sulfur cathode and corresponding strategies.....	7
1.1.2.1 The low electronic and ionic conductivity of sulfur	7
1.1.2.2 The large volume expansion during sulfur to Li ₂ S conversion.....	8
1.1.2.3 The use of lithium metal anode in Li-S batteries.....	8
1.1.3 Strategies to improve the cycling stability of sulfur cathode	10
1.1.3.1 Physical confinement by hierarchically structured carbon hosts.....	10
1.1.3.2 Solid electrolytes.....	11
1.1.3.3 Polysulfide adsorbers	13
1.2 Organic electrodes.....	16
1.2.1 Redox mechanisms of organic electrodes	17
1.2.2 Challenges of organic cathodes and corresponding strategies	18
1.2.2.1 Achieving high specific capacity (Q)	19

1.2.2.2 Achieving high output voltage (V)	20
1.2.3 Strategies to improve the cycling stability of organic cathodes	22
1.2.3.1 Polymerization or formation of macromolecular structures	22
1.2.3.2 Formation of organic salts	24
1.2.3.3 Nanocomposite formation with insoluble materials	26
1.2.3.4 Use of solid electrolytes	27
1.3 Research objectives	27
1.4 The structure of the thesis	29
Chapter 2. Characterization Techniques	31
2.1 Physical characterization	31
2.1.1 X-ray diffraction (XRD)	31
2.1.2 Thermal gravimetric analysis (TGA)	32
2.1.3 Ultraviolet-visible-near-infrared spectroscopy (UV-Vis-NIR)	34
2.1.4 Fourier transform infrared spectroscopy (FTIR)	35
2.1.5 Peel test	37
2.2 Electrochemical characterization	39
2.2.1 Coin cell fabrication	39
2.2.2 Cyclic voltammetry (CV)	40
2.2.3 Electrochemical impedance spectroscopy (EIS)	41
2.2.4 Galvanostatic charge/discharge	43
Chapter 3. Ionically Cross-Linked PEDOT:PSS as a Multifunctional Conductive Binder for High- Performance Lithium–Sulfur Batteries	45
3.1 Introduction	45
3.2 Experimental section	47
3.2.1 Materials and instrumentation	47

3.2.2 Detailed experimental procedures	47
3.3 Results and discussion.....	48
3.4 Conclusions	57
Chapter 4. Electropolymerized PEDOT for Enhancing the Performances of Sulfur and Lithium Iron Phosphate Cathodes.....	59
4.1 Introduction	59
4.2 Experimental section	60
4.2.1 Materials and instrumentation	60
4.2.2 Detailed experimental procedures	61
4.3 Results and discussion.....	64
4.3.1 e-Polymerization of EDOT via cyclic voltammetry	64
4.3.2 Optimization of e-polymerization of EDOT via chronoamperometry	68
4.3.3 Fabrication and characterization of Li–S batteries with the ePEDOT binder prepared via in-cell e-polymerization.....	71
4.3.4 Adhesion evaluation of ePEDOT:PSS by the 180° peel test.....	77
4.3.5 Investigation of doping/dedoping of PEDOT by CV and EIS	79
4.3.6 Electropolymerized PEDOT for lithium iron phosphate (LFP) cathode	84
4.4 Conclusions	89
Chapter 5. A Stable 2,5-Dihydroxy-1,4-benzoquinone (DHBQ) Based Organic Cathode Enabled by Coordination Polymer Formation and Binder Optimization	91
5.1 Introduction	91
5.2 Experimental section	92
5.2.1 Preparation of coordination polymers	92
5.2.2 Material characterizations and electrochemical measurements.....	93
5.3 Results and discussion.....	94
5.3.1 Synthetic route and material characterizations	94

5.3.2 Electrochemical performance of as-synthesized coordination polymers	97
5.3.3 Optimization on the electrochemical performance of Cu-DHBQ cathode.....	104
5.3.4 Study of the electrochemical reaction kinetics	116
5.3.5 Preparation of other structurally similar coordination polymers using different ligands	119
5.3.6 Stabilization of organic cathode by acid-base interaction with polymer binder	123
5.4 Conclusions	126
Chapter 6. Conjugated Diketopyrrolopyrrole (DPP) Polymer Based P-type and Bipolar-type Organic Cathodes.....	127
6.1 Introduction	127
6.2 Experimental section	128
6.2.1 Material synthesis	128
6.2.2 Electrochemical measurements	128
6.3 Results and discussion.....	129
6.3.1 Electrochemical performance of PDQT	129
6.3.2 Electrochemical performance of PDBT	136
6.3.3 Theoretical calculations	143
6.4 Conclusions	143
Chapter 7. Conclusions and Future Outlook.....	145
7.1 Conclusions	145
7.2 Future outlook	147
References	149

List of Figures

Figure 1.1 Schematic for the structure and working principle of a LIB.	2
Figure 1.2 Sulfur production, crystal structure, and the configuration of Li-S cell.	4
Figure 1.3 Different regions for the discharge/charge processes of sulfur cathode.	5
Figure 1.4 S/CMK-3 nanocomposite, S-PANI yolk-shell structure, La(NO ₃) ₃ additive for SEI formation on the Li anode, and layered Li-rGO composite film.	9
Figure 1.5 Mesoporous carbon nanoparticles and intertwined MWCNT film.	11
Figure 1.6 Solid electrolyte for Li-S batteries.	12
Figure 1.7 Chemical structures of PEDOT, PPY, and PANI.	13
Figure 1.8 Conductive polymers for sulfur cathode.	14
Figure 1.9 Representative nonconductive polymers for polysulfide trapping.	15
Figure 1.10 Metal oxides and sulfides for polysulfide trapping.	16
Figure 1.11 Redox mechanisms of different types of organic electrodes.	18
Figure 1.12 Chemical structures of para-dinitrobenzene and quinones with different molecular weights and specific capacities.	20
Figure 1.13 Chemical structures, charge/discharge curves, differential capacity curves, and the relationship between the first discharge potentials and the LUMO energy levels of AQ, BDTD, BFFD and PID.	22
Figure 1.14 Chemical structures of polymers and macromolecular structures synthesized from small organic molecules.	24
Figure 1.15 Representative organic salts with enhanced cycling stabilities.	25
Figure 1.16 Nanocomposite formation between small organic molecules and porous carbon.	26
Figure 1.17 The structure of PMA/PEG based electrolyte.	27
Figure 2.1 Instrumentation for XRD and an example of XRD data.	32
Figure 2.2 Instrumentation for the thermobalance of TGA, and examples DTG, DDTG and TGA data.	33

Figure 2.3 Theoretical principles and instrumentation for UV-Vis-NIR, and an example of UV-Vis data.	35
Figure 2.4 Instrumentation for FTIR and an example of FTIR data.....	37
Figure 2.5 Schematic for the peel test, and an example of peel force vs. distance curve obtained from the peel test.....	38
Figure 2.6 Schematic of the structure of a coin cell.....	39
Figure 2.7 Schematic and the potential vs. time curve for the CV testing, an example of the CV data, and an example showing the measurement of D_{Li^+} from CV curves.	41
Figure 2.8 An example of the EIS data and the corresponding equivalent circuit models for fitting the EIS data.	43
Figure 2.9 An example showing the galvanostatic cycling test.	44
Figure 3.1 Schematic representation of the PEDOT:PSS-Mg ²⁺ binder structure and NPS/SP/PEDOT:PSS-Mg ²⁺ electrode.	50
Figure 3.2 (a) TGA, and (b) SEM of nano-particulate sulfur (NPS).	50
Figure 3.3 Discharge–charge performance of NPS/SP/PVDF and NPS/SP/PEDOT:PSS-Mg ²⁺ electrodes.	54
Figure 3.4 EIS data of Li–S batteries with NPS/SP/PVDF and NPS/SP/PEDOT:PSS-Mg ²⁺ electrodes measured in the charge state.	57
Figure 4.1 Linear sweep voltammetry (LSV) curves of the electrolyte, 1 M LiTFSI in 1:1 (v/v) DOL/DME with 2 wt% LiNO ₃	65
Figure 4.2 CV and EIS data for the e-polymerization, and the characterization of as-prepared ePEDOT and commercial cPEDOT by UV-Vis-NIR.....	67
Figure 4.3 Comparison of the UV–Vis–NIR spectra of the ePEDOT prepared by the CV and CA methods.	68
Figure 4.4 Optimization of the e-polymerization by the chronoamperometry method.	70
Figure 4.5 Determination of the conversion for the e-polymerization by UV-Vis spectroscopy.	72
Figure 4.6 Chronoamperograms for the sulfur cathodes with Li-PSS or H-PSS binder.	73

Figure 4.7 Cyclic voltammograms of sulfur cathodes using different types of binders at a scan rate of 0.1 mV s ⁻¹	74
Figure 4.8 Cycling test of sulfur cathodes with and without ePEDOT, and rate performance of sulfur cathodes with ePEDOT:H-PSS or cPEDOT:PSS binder.	76
Figure 4.9 Comparison of lithium polysulfide dissolution in the electrolyte for the sulfur cathodes with different binders.	77
Figure 4.10 Peel test on the sulfur cathode films using cPEDOT:PSS or ePEDOT:H-PSS binder.	78
Figure 4.11 Optical images of sulfur cathode films before and after peel test, and tapes after peel test.	79
Figure 4.12 CV curves of sulfur cathode and ePEDOT:H-PSS.	81
Figure 4.13 Comparison of the CV curves of ePEDOT:H-PSS and cPEDOT:PSS in the electrolytes with and without LiNO ₃	81
Figure 4.14 Investigation of the conductivity difference of ePEDOT in the doped state (3.36 V) and dedoped state (1.7 V).	83
Figure 4.15 Investigation of the conductivity difference of ePEDOT at different potentials during the oxidation (doping) and reduction (dedoping) processes.	84
Figure 4.16 Cyclic voltammograms for a cell loaded with a 60 mM EDOT in 1:1:1 EC/EMC/DMC based electrolyte.	85
Figure 4.17 Optimization for the e-polymerization of EDOT on the carbon paper substrate by the CA method.	86
Figure 4.18 Photos of ePEDOT on carbon paper obtained by the CA method using the EDOT-containing electrolytes of different concentrations.	87
Figure 4.19 Application of ePEDOT in the LFP cathode.	88
Figure 5.1 FTIR, TGA, and XRD data of as-prepared coordination polymers.	95
Figure 5.2 CV testing of as-prepared coordination polymers.	98
Figure 5.3 Battery performance of as-synthesized coordination polymers involving the redox reactions of both metal and ligand.	101

Figure 5.4 Battery performance of as-synthesized coordination polymers involving the redox reaction of the ligand only.	103
Figure 5.5 Determination of the solubilities of DHBQ and Ni-, Co-, Mn-, Zn-, and Cu-coordination polymers in the electrolyte by UV-Vis spectroscopy.	105
Figure 5.6 CV curves of Cu-DHBQ cathodes with different binders at the binder content of 10 wt%.	108
Figure 5.7 EIS data, charge/discharge curves, and cycling performance of Cu-DHBQ cathodes with different types of binders at the binder content of 10 wt%.	110
Figure 5.8 Peel test on Cu-DHBQ cathode films with different types of binders.	111
Figure 5.9 UV-Vis spectra of cycled Cu-DHBQ cathodes in the charged state after 200 cycles at 100 mA g ⁻¹	112
Figure 5.10 Electrochemical performance of Cu-DHBQ cathode with different contents of alginate binder.	113
Figure 5.11 Photos showing the Li anode (top) and the separator (bottom) from disassembled cycled cells (after 200 cycles at 100 mA g ⁻¹ in the charged state).	115
Figure 5.12 Rate performance testing of Cu-DHBQ cathode with 25 wt% alginate binder.	115
Figure 5.13 Study of the electrochemical reaction kinetics by CV for the Cu-DHBQ cathode with 25 wt% alginate binder.	118
Figure 5.14 Structures and energy levels of DHBQ and DHBQ-Cl.	120
Figure 5.15 Characterizations of the Cu-DHBQ-Cl coordination polymer.	120
Figure 5.16 Comparison for the electrochemical performance of Cu-DHBQ and Cu-DHBQ-Cl.	122
Figure 5.17 UV-Vis spectra of Cu-DHBQ-Cl and Cu-DHBQ cells after the 1st discharge process.	123
Figure 5.18 CV curves of (a) 1,5-diaminoanthraquinone, and (b) 2,6-diaminoanthraquinone with a scan rate of 0.2 mV s ⁻¹	124
Figure 5.19 Chemical structures of binders containing acidic and neutral groups and the influence of these binders on the cycling performance of 1,5-diaminoanthraquinone cathode.	125

Figure 6.1 Optimization of the experimental condition for the CV testing of PDQT in 1 M LiPF ₆ in 1:1:1 EC/EMC/DMC (volume ratio) electrolyte.	131
Figure 6.2 CV curves of PDQT using the carbon paper substrate with different potential ranges.	132
Figure 6.3 Galvanostatic cycling performance of PDQT cathode in the potential range of 3~4.3 V.	135
Figure 6.4 CV curves of PDQT cathode in both the n-doping and p-doping potential ranges..	136
Figure 6.5 CV curves of PDBT cathode in both the n-doping and p-doping potential ranges..	137
Figure 6.6 Galvanostatic cycling performance of the PDBT cathode in the p-doping or n-doping region.	140
Figure 6.7 Energy levels of PDQT and PDBT.....	143

List of Tables

Table 1.1 Characteristics of representative intercalation cathode materials.	3
Table 1.2 An overview of the different strategies for solving the dissolution issue.	28
Table 3.1 Sulfur weight losses of cathode materials after Soxhlet extraction with CS ₂	52
Table 3.2 Electrode resistance (EIS) obtained from the equivalent circuit fitting of experimental data.	57
Table 4.1 Charges injected into the cells at different potentials during the e-polymerization.	70
Table 4.2 Features of unmodified and ePEDOT modified LFP cathodes.	88
Table 5.1 The assignment of the peaks in the FTIR spectra of as-synthesized coordination polymers.	96
Table 5.2 Molecular formula, molecular weight, theoretical and experimental water content, and the features about the TGA data of as-prepared coordination polymers.	97
Table 5.3 Molecular formula, molecular weight, and theoretical capacities of as-prepared coordination polymers.	100
Table 5.4 k_1 and k_2 values for the anodic current in the potential range of 2~2.4 V.	119
Table 6.1 Comparison of our work with other solution-processable conjugated polymer based cathodes.	141

List of Schemes

Scheme 4.1 Schematic showing the oxidation of EDOT and the doping of PEDOT via e-polymerization.	68
Scheme 4.2 Schematic illustrating the formation of ePEDOT in the sulfur cathode inside a Li-S cell by the in-cell e-polymerization.	71
Scheme 5.1 Schematic for the synthesis of M-DHBQ (M=Ni, Co, Mn, Zn, and Zn) coordination polymers.....	94
Scheme 6.1 Synthetic route to PDQT. ^a	129
Scheme 6.2 Electrochemical reaction schemes for the PDQT cathode.....	134
Scheme 6.3 Synthetic route to PDBT. ^b	137
Scheme 6.4 Electrochemical reaction schemes for the PDBT cathode.....	138

List of Abbreviations

Alginate	Alginic acid sodium salt
CA	Chronoamperometry
CMC	Sodium carboxymethyl cellulose
COF	Covalent organic frameworks
CP	Carbon paper, chronopotentiometry, conductive polymer, or coordination polymer
CV	Cyclic voltammetry
DHBQ	2,5-dihydroxy-1,4-benzoquinone
DME	1,2-dimethoxyethane
DOL	1,3-dioxolane
DPP	Diketopyrrolopyrrole
ePEDOT	electropolymerized EDOT
e-polymerization	Electrochemical polymerization
EDOT	3,4-ethylenedioxythiophene
EIS	Electrochemical impedance spectroscopy
FTIR	Fourier-transform infrared spectroscopy
ITO	Indium tin oxide
LFP	Lithium iron phosphate
LiPF ₆	Lithium hexafluorophosphate
LiTFSI	Lithium bis(trifluoromethanesulfonyl)imide
LSV	Linear sweep voltammetry

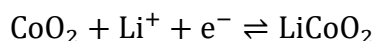
MOFs	Metal organic frameworks
PANI	Polyaniline
PEDOT:PSS	Poly(3,4-ethylenedioxythiophene) : polystyrene sulfonate
PDQT	Diketopyrrolopyrrole-quaterthiophene copolymer
PDBT	Diketopyrrolopyrrole-bithiophene polymer
PVDF	Poly(vinylidene fluoride)
PPy	Polypyrrole
TGA	Thermogravimetric analysis
UV-Vis-NIR	Ultraviolet-Visible-Near infrared spectroscopy
XRD	X-Ray diffraction

Chapter 1. Introduction

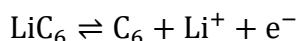
Due to the limited resources of fossil fuels (e.g. coal, gasoline and natural gas), and the greenhouse effect caused by the CO₂ emission associated with their burnings, the demand for renewable and clean energy resources has been increasing in recent decades. Wind, solar, tidal/wave and other renewable energies have been intensively explored due to their natural abundance and environmental friendliness. However, such renewable energy resources are intermittent, thus efficient electrical energy storage (EES) systems such as electric grids and batteries are needed to store and deliver the energy produced by them. Among various EES systems, rechargeable lithium-ion batteries (LIB) have been successfully applied in portable electronics, aerospace and electric vehicles (EVs) due to its high gravimetric and volumetric energy densities, and superior long cycle performance.^{1,2}

LIB was first commercialized by Sony in the early 1990s. The schematic for the structure and working principle of a LIB is shown in Figure 1.1. A LIB consists of an anode (e.g. C, Al, Ge, Si), a Li-intercalation compound cathode (e.g. LiCoO₂, LiMn₂O₄, LiNi_{0.33}Mn_{0.33}Co_{0.33}O₂, LiFePO₄), a separator, and electrolyte which transports Li⁺ ions between the cathodes and anodes. The graphite anode has a layered structure, while the Li-intercalation compound cathode has a similarly layered, spinel, olivine or tavorite structure.² Both electrodes are able to reversibly insert (a process called intercalation) and remove (a process called deintercalation) Li⁺ ions. During discharging, Li⁺ ions move from the anode to the cathode through the electrolyte inside the cell while the electrons flow through the external circuit in the same direction. The electrochemical reactions of a LIB are shown below:

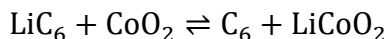
Half reaction in the cathode (taking CoO₂ as an example):



Half reaction in the anode (taking C as an example):



Overall reaction (discharging: from left to right, charging: from right to left):



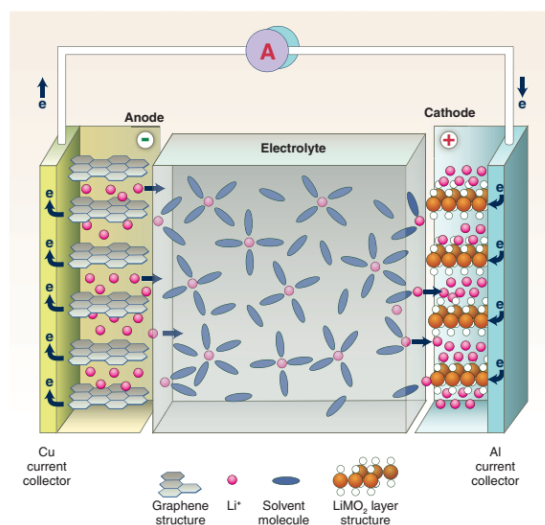


Figure 1.1 Schematic for the structure and working principle of a LIB. Reproduced with permission from Ref. 1.

Both anode and cathode materials can affect the specific energy of a LIB.^{2,3} After a few decades of intensive research on the cathode materials for LIB, the specific capacities of the cathode materials for the state-of-the-art LIBs are approaching their theoretical limits (Table 1.1). New cathode materials with larger specific capacities and higher discharge voltages are needed for the applications of LIBs in EVs and grid-scale energy storage. Moreover, the cost of the cathode materials needs to be considered to make the products (cell phones, cars, etc.) using LIBs more affordable to the general public. Cathode materials consisting of transition metals (e.g. Co, Ni, and Mn) requires a high cost for the mining of the respective raw materials from the earth's crust. Furthermore, the contents of these transition metals in the earth's crust are relatively low. Lastly, the environmental impact of the cathode materials is of high importance. Used LIBs which consist of transition metals can cause severe environmental pollution if they are released into the environment without any sophisticated chemical processing to eliminate the transition metals. With these considerations, a variety of new cathode materials with novel electrochemistry are being developed in recent years, which will be summarized in the next section.

Table 1.1 Characteristics of representative intercalation cathode materials. Reproduced with permission from Ref. 2.

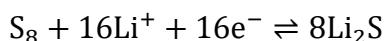
Crystal Structure	Compound	Specific Capacity (mA h g ⁻¹) (Theoretical/Experimental/Commercial)	Average Voltage (V)	Level of Development
Layered	LiTiS ₂	225/210	1.9	Commercialized
	LiCoO ₂	274/148/145	3.8	Commercialized
	LiNiO ₂	275/150	3.8	Research
	LiMnO ₂	285/140	3.3	Research
	LiNi _{0.33} Mn _{0.33} Co _{0.33} O ₂	280/160/170	3.7	Commercialized
	LiNi _{0.8} Co _{0.15} Al _{0.05} O ₂	279/199/200	3.7	Commercialized
	Li ₂ MnO ₃	458/180	3.8	Research
Spinel	LiMn ₂ O ₄	148/120	4.1	Commercialized
	LiCo ₂ O ₄	142/84	4.0	Research
Olivine	LiFePO ₄	170/165	3.4	Commercialized
	LiMnPO ₄	171/168	3.8	Research
	LiCoPO ₄	167/125	4.2	Research
Tavorite	LiFeSO ₄ F	151/120	3.7	Research
	LiVPO ₄ F	156/129	4.2	Research

1.1 Sulfur cathode

Being the fifth most common element by mass (weight content of 2.9%) in the earth,⁴ sulfur is abundant in nature. Sulfur is produced massively as a by-product in the natural gas processing and oil refining industry (Figure 1.2a).⁵ The annual production of sulfur world-wide is estimated to be 70 million tonnes.⁶ Sulfur has several solid allotropes, among which the most common one is cyclic octa-sulfur (S₈). Octa-sulfur melts at 115 °C and boils at 445 °C. At room temperature, octa-sulfur exists as the α-phase which has a “crankshaft” structure with the space group of Fddd-D_{2h}, as shown in Figure 1.2b.⁷ On increasing the temperature to 95 °C, octa-sulfur changes from α-phase to β-polymorph, where the structure of the S₈ ring is unchanged. Further increasing the temperature to 159 °C, the structure of octa-sulfur evolves into γ-phase, accompanied by a decreased density but increased viscosity due to the cleavage of S₈ rings and polymerization into

long chains. Molten sulfur exhibits the lowest viscosity around 155 °C before the beginning of polymerization.⁷ The sulfur cathode was first reported by Herbert and Ulam in 1962.⁸ A Li-S cell consists of a lithium metal anode, a separator, organic electrolyte, and a sulfur cathode (Figure 1.2c). The electrochemical reactions of a Li-S cell are shown below:

Half reaction in the cathode:



Half reaction in the anode:



Overall reaction (discharging: from left to right, charging: from right to left):

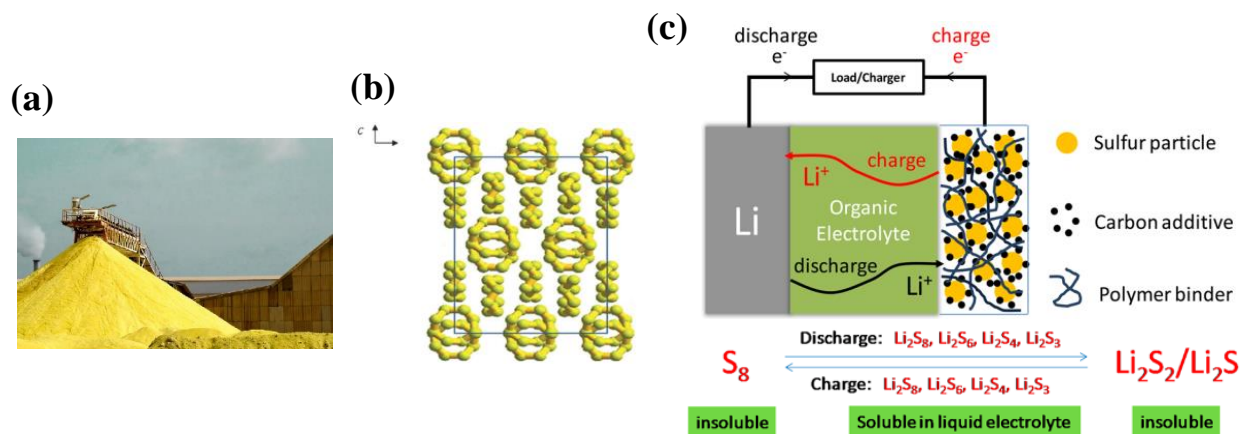
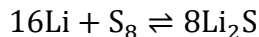


Figure 1.2 Sulfur production, crystal structure, and the configuration of Li-S cell. (a) Sulfur produced as a by-product in the natural gas processing and oil refining industry.⁵ (b) The “crankshaft” structure of orthorhombic α -sulfur with the unit cell marked in the outlined square. Reproduced with permission from Ref. 7. (c) Schematic of a Li-S cell and corresponding electrochemical reactions. Reproduced with permission from Ref. 9-10.

The average discharge voltage of the sulfur cathode (2.2 V vs. Li⁺/Li) is about 3/5 of those of intercalation cathodes, but the theoretical specific capacity of the sulfur cathode (1672 mA h g⁻¹) is six times of the latter. With the use of a lithium metal anode, the theoretical gravimetric and volumetric energy densities of Li-S batteries can reach 2500 Wh kg⁻¹ and 2800 Wh L⁻¹,

respectively, which are the second highest among all the cathodes reported so far. The natural abundance and environmental friendliness of sulfur together with the high specific energy of Li-S battery make Li-S battery a promising candidate for the next-generation rechargeable batteries for EVs and grid-scale energy storage.

1.1.1 Redox mechanism of sulfur cathode

Figure 1.3 shows the typical charge/discharge curves of the sulfur cathode. During discharge, sulfur reduction is a multistep electrochemical process that involves many lithium polysulfide intermediates with the general formula of Li_2S_n , $n = 2\sim 8$. It is generally accepted that long chain polysulfides such as Li_2S_8 and Li_2S_6 are produced first, and then the chain lengths of polysulfides are shortened with the formation of Li_2S_n ($n = 1\sim 4$) as the discharge continues. At the end of the discharge, lithium sulfide (Li_2S) is formed. Kawase *et al.* suggested that the electrochemical reduction of sulfur can be divided into four stages (Figure 1.3). The 1st stage is from point (1) to (3-1), the 2nd stage is from point (2-1) to (3-3), the 3rd stage is from point (3-1) to (4), and 4th stage is from point (3-4) to (5).¹¹

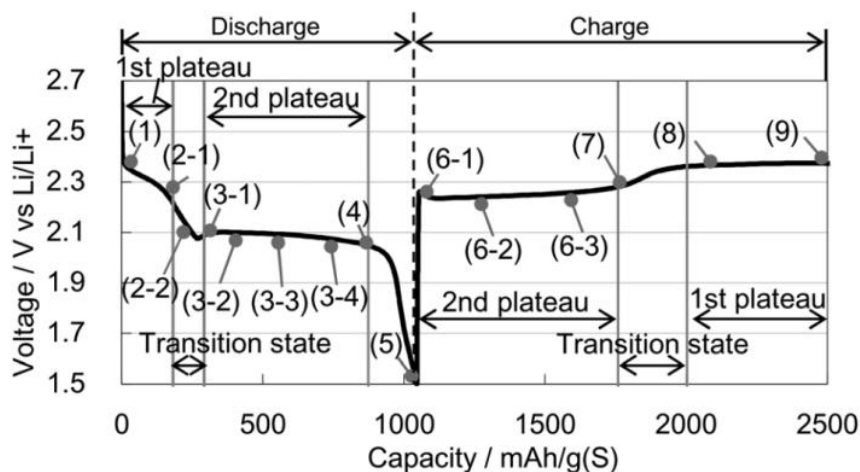
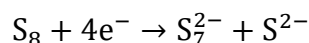
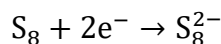
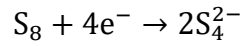
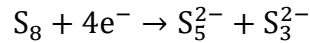
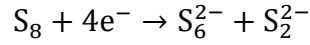


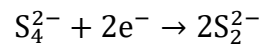
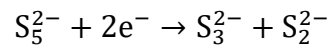
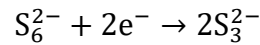
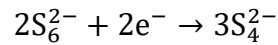
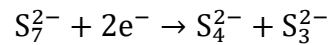
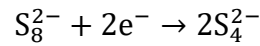
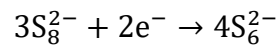
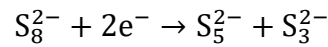
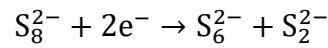
Figure 1.3 Different regions for the discharge/charge processes of sulfur cathode. Reproduced with permission from Ref. 11.

The electrochemical reactions in the 1st stage are:¹¹

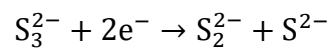




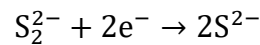
The electrochemical reactions in the 2nd stage are:¹¹



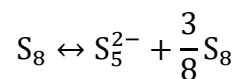
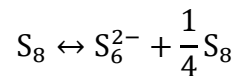
The electrochemical reaction in the 3rd stage is:¹¹

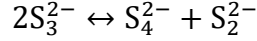
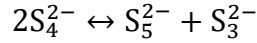
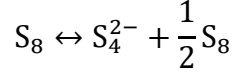


The electrochemical reaction in the 4th stage is:¹¹



In addition to electrochemical reactions shown above, chemical reactions (disproportionation) shown below can also occur in the discharge process of sulfur cathode:¹²





Despite a few decades of research, the exact reaction mechanism for sulfur cathode is still under debate. The intrinsic complexity of the electrochemical and chemical reactions of sulfur cathode, the difficulties in the separation and identification of pure polysulfide intermediates including S_8^{2-} , S_7^{2-} , S_6^{2-} , S_5^{2-} , S_4^{2-} , S_3^{2-} , $S_3^{\bullet-}$ and S_2^{2-} make the elucidation of the reaction mechanism rather difficult. Nonetheless, a number of in and ex-situ characterization techniques including high-performance liquid chromatography-mass spectrometry (HPLC-MS),^{11–13} electron spin resonance spectroscopy (ESR),¹² Inductively coupled plasma-optical emission spectrometer (ICP-OES),¹³ proton and lithium nuclear magnetic resonance spectroscopy (^1H and ^7Li -NMR),^{11,14,15} Operando UV-vis absorption spectroscopy,^{16–18} X-ray absorption spectroscopy (XAS),¹⁴ X-ray photoelectron spectroscopy (XPS),^{19,20} and X-ray diffraction (XRD)¹⁴ have been developed to probe the electrochemical reactions in Li-S batteries. Although the results revealed by different characterization techniques are drastically different from or even contradictory to each other, more fundamental and in-depth study on the reaction mechanism is needed to further improve the electrochemical performance of sulfur cathode for practical applications.

1.1.2 Challenges of sulfur cathode and corresponding strategies

Despite its great promise for future energy storage, the commercialization of sulfur cathode is hindered by several challenges which are discussed below:

1.1.2.1 The low electronic and ionic conductivity of sulfur

Sulfur is a poor conductor for electrons and Li^+ ions, which results in the low utilization of sulfur active material and slow electrochemical reaction kinetics when sulfur is used as an electrode material. To solve this challenge, Sulfur/Mesoporous Carbon (S/CMK-3) (Figure 1.4A)²¹, Sulfur/reduced Graphene Oxide (S/rGO)²², and Sulfur/Carbon Nanotubes (S/CNTs)²³ nanocomposites have been prepared. Benefiting from high surface areas and excellent electrical

conductivities of carbon nanomaterials, and small size of sulfur particles, these nanocomposites showed significantly enhanced utilization ($\geq 80\%$) of sulfur active material.

1.1.2.2 The large volume expansion during sulfur to Li_2S conversion

The densities of octa-sulfur and Li_2S are 2.07 and 1.66 g cm^{-3} , respectively, therefore a large volume expansion of $\sim 80\%$ is expected during the conversion of sulfur to Li_2S . The mechanical stress caused by such large volume change weakens the physical contact among sulfur, carbon additive and aluminum current collector, resulting in the pulverization of sulfur cathode and consequently rapid capacity decay. To solve this challenge, simple poly(ethylene glycol) (PEG) coating on sulfur particles²⁴, S-polyaniline (PANI) (Figure 1.4B)²⁵ and S- TiO_2 ²⁶ yolk-shell structures have been reported. Compared with the core-shell counterpart, the innovative yolk-shell structure with internal void space well accommodated the volume expansion of sulfur during discharge. As a result, a small capacity decay of 0.033% per cycle over $1,000$ cycles was obtained.

1.1.2.3 The use of lithium metal anode in Li-S batteries

Lithium metal anode is a promising candidate for high energy density batteries because of its ultrahigh specific capacity (3860 mA h g^{-1}) and low reduction potential (-3.04 V vs. standard hydrogen electrode).²⁷ However, the use of lithium metal as the electrode poses a number of challenges: i) the formation of lithium dendrites can puncture the separator and cause internal short-circuit; ii) the repetitive Li stripping/plating during the electrochemical cycling causes cracks and pulverization of the lithium anode, deteriorating its cycling stability; iii) lithium metal is highly reactive and can cause fire/explosion once exposed to air accidentally. To deal with this challenge, electrolyte additives such as LiNO_3 ,²⁸ $\text{La}(\text{NO}_3)_3$ (Figure 1.4C),²⁹ and LiF ³⁰ were found to promote the formation of stable protective solid electrolyte interphase (SEI) films on the surface of Li anode, artificial coating layers including Li_3N ,³¹ Al_2O_3 ,³² and nanocarbon³³ were found to not only prevent Li metal from contacting lithium polysulfides to avoid side reactions, but also effectively suppress the growth of lithium dendrites. Composite Li metal anode such as Li-rGO composite (Figure 1.4D) prepared by the infusion of molten Li metal into the nanoscale interlayers of a rGO film were capable of mitigating the volume change during Li stripping/plating, promoting uniform Li deposition, and providing an electrochemically and mechanically stable artificial interface to stabilize the as-formed SEI.³⁴

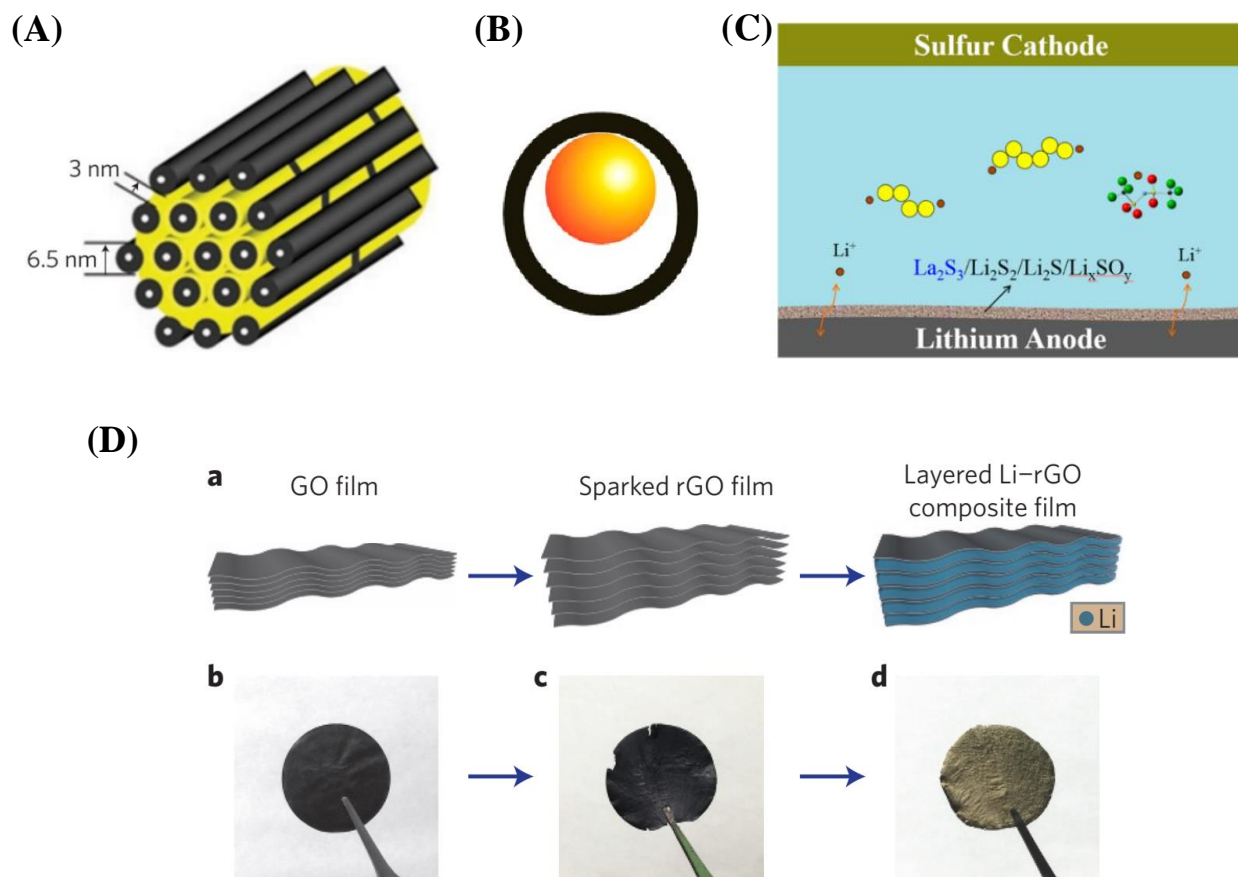


Figure 1.4 S/CMK-3 nanocomposite, S-PANI yolk-shell structure, $\text{La}(\text{NO}_3)_3$ additive for SEI formation on the Li anode, and layered Li-rGO composite film. (A) Schematic diagram of the S/CMK-3 nanocomposite, sulfur (yellow) is confined in the interconnected channel structures of mesoporous carbon, CMK-3 (black). Reproduced with permission from Ref. 21. (B) Schematic showing the S-PANI yolk-shell structure with internal void space. Reproduced with permission from Ref. 25. (C) Schematic showing the SEI formation on the surface of Li anode. The La_2S_3 contained in the SEI film is originated from the reactions among $\text{La}(\text{NO}_3)_3$ additive, lithium polysulfides and Li metal. Reproduced with permission from Ref. 29. (D) Fabrication of a layered Li-rGO composite film. (a) Schematic of the synthetic procedures. (b-d) Corresponding digital images. (b) GO film, (c) rGO film, and (d) Li-rGO film. Reproduced with permission from Ref. 34.

1.1.3 Strategies to improve the cycling stability of sulfur cathode

Improving the cycling performance is one of the focuses of this thesis, so the related strategies are discussed in detail, as shown below. Sulfur cathode is plagued with drastic capacity decay due to the dissolution and diffusion of lithium polysulfide intermediates in the electrolyte. A capacity retention far below 80% over 1000 cycles with sulfur cathode is often obtained due to this challenge. Lithium polysulfides (Li_2S_n , $n=3\sim 8$) are highly soluble in the electrolyte leading to a number of problems: i) driven by the concentration gradient force, during discharging the dissolved long-chain polysulfides diffuse from the sulfur cathode to the lithium anode where they are electrochemically reduced to soluble short-chain polysulfides remaining in the electrolyte and insoluble $\text{Li}_2\text{S}_2/\text{Li}_2\text{S}$ deposited on the surface of lithium anode, resulting in the loss of sulfur active material; ii) driven by the electric field, during recharging the soluble short-chain polysulfides migrate back to the sulfur cathode from the lithium anode causing the infamous “shuttle effect”, which decreases the coulombic efficiency; iii) the repetitive dissolution and redeposition of polysulfides in the cathode leads to the formation of large isolated sulfur and $\text{Li}_2\text{S}_2/\text{Li}_2\text{S}$ aggregates which do not participate in the electrochemical reactions any more due to the loss of electrical contact with conductive carbons; iv) the polysulfides migrated to the lithium anode can react with lithium metal forming cracks and pores on the surface of lithium metal, which destroys its structural integrity and worsens its cycling stability.¹⁰

This challenge is the focus of this thesis, and the various strategies to tackle this challenge will be discussed in detail below.

1.1.3.1 Physical confinement by hierarchically structured carbon hosts

Due to its excellent electrical conductivity and high surface area, a S/C composite prepared using a hierarchically structured carbon host can maximize the electrical contact between sulfur and carbon, therefore improving the electrical conductivity of the sulfur cathode on the whole and leading to enhanced utilization of sulfur. Moreover, the hierarchical structures including nanopores and nanochannels can function as physical confinement to contain polysulfides and prevent them from diffusion/dissolution into the electrolyte. Schuster et al. reported spherical ordered mesoporous carbon nanoparticles with bimodal pores of 3.1 and 6.0 nm and an ultra high surface area of $2445 \text{ m}^2 \text{ g}^{-1}$ (Figure 1.5a) as the host for sulfur.³⁵ The resultant S/C composite showed a high initial charge capacity of 1200 mA h g^{-1} and a capacity retention of 60.8% over 100 cycles at

1 C for the charge capacity. Li et al. systematically studied mesoporous carbons with tunable pore sizes from 3 to 22 nm as hosts for sulfur, and found that partial sulfur filling of the pores led to improved initial discharge capacity and cycle stability.³⁶ The mesoporous carbon host with the larger pore volume of 22 nm at the sulfur loading of 50 wt% and an additional surface coating with PEDOT:PSS afforded an initial capacity of 1390 mA h g⁻¹ and a capacity retention of 60.4% over 100 cycles at 0.1 C. A self-weaving multi-wall carbon nanotube (MWCNT) film was developed as the host for sulfur by Su et al.³⁷ The nanopores of the MWCNT film can absorb the electrolyte and localize the soluble polysulfides, thereby suppressing their migration. Without the use of any binder or current collector, the free-standing S/MWCNT cathode film exhibited superior rate performance (capacities of 1352 mA h g⁻¹ at 1 C and 1012 mA h g⁻¹ at 4 C) and cycling performance (a capacity retention of 67.7% over 100 cycles at 1 C).

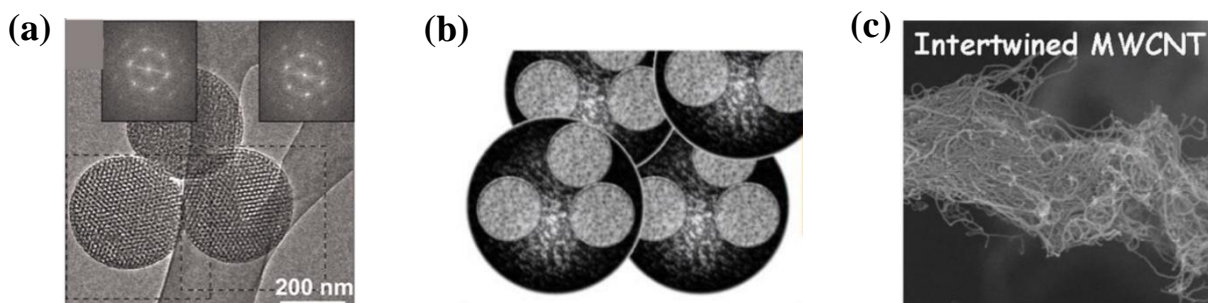


Figure 1.5 Mesoporous carbon nanoparticles and intertwined MWCNT film. (a) TEM image of spherical ordered mesoporous carbon nanoparticles showing the 2D-hexagonal structure. The pore size is bimodal, 3.1 and 6.0 nm. Reproduced with permission from Ref. 35. (b) SEM image of mesoporous carbon nanoparticles with tunable pore sizes in the range of 3 to 22 nm. Reproduced with permission from Ref. 36. (c) SEM image of an intertwined MWCNT film. Reproduced with permission from Ref. 37.

1.1.3.2 Solid electrolytes

Solid electrolytes are superior to liquid electrolytes in mitigating the dissolution of polysulfides, preventing lithium dendrite formation, and avoiding electrolyte leakage. However, solid electrolytes generally have low ionic conductivity and high interfacial contact resistance, resulting in low utilization of sulfur and unsatisfactory rate performance. The matrix of solid electrolytes can be either polymers or inorganic ceramics. Marmorstein et al. compared the

electrochemical performance of sulfur cathode with three solid polymer electrolytes, including poly(ethylene oxide) (PEO), poly(ethylene-methylene oxide) (PEMO) and poly(ethylene-glycol) dimethyl ether (PEGDME).³⁸ They found that the cell with PEGDME electrolyte showed a much lower capacity fade rate than the cells with the other two electrolytes. Hassoun et al. reported a specially designed solid polymer electrolyte, a hot-pressed PEO-lithium triflate (PEO-LiCF₃SO₃) membrane with finely dispersed nano-sized zirconia (ZrO₂) and lithium sulfide (Li₂S).³⁹ The ZrO₂ filler can improve the ionic conductivity of the polymer electrolyte and stabilize the lithium metal anode/electrolyte interface, while Li₂S can enhance the ionic conductivity and prevent the polysulfide dissolution. Fu et al. reported a bilayer solid electrolyte, a thin dense layer (20 μm) mechanically supported by a thick porous layer (50~100 μm), as shown in Figure 1.6a.⁴⁰ The thick porous layer provides continuous Li⁺/electron pathways for the sulfur cathode, while the thin dense layer blocks polysulfide diffusion and prevents Li dendrite formation. With this solid electrolyte design, the sulfur cathode can reach a high sulfur loading (> 7 mg cm⁻²) and a high average coulombic efficiency (> 99%). Yao et al. reported an all-solid-state Li-S cell which consists of a rGO@S-Li₁₀GeP₂S₁₂-acetylene black (AB) composite cathode, a bilayer solid electrolyte of Li₁₀GeP₂S₁₂ and 75% Li₂S-24% P₂S₅-1% P₂O₅, and a lithium metal anode, as shown in Figure 1.6b.⁴¹ At 60 °C, the as-designed all-solid-state cell delivers a high initial discharge capacity of 1629 mA h g⁻¹ at 0.05 C, and maintains a high capacity of 830 mA g⁻¹ after 750 cycles at 1 C.

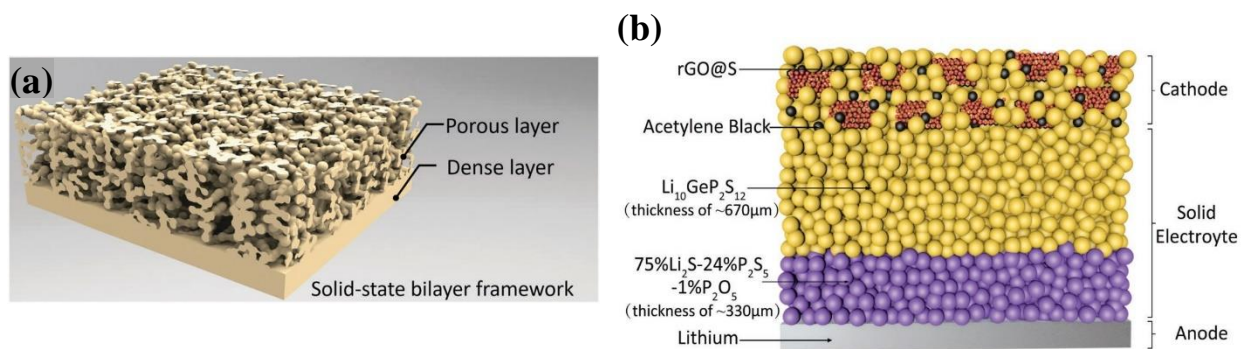


Figure 1.6 Solid electrolyte for Li-S batteries. (a) Schematic of the bilayer solid electrolyte. Reproduced with permission from Ref. 40. (b) Schematic of the all-solid-state Li-S cell. Reproduced with permission from Ref. 41.

1.1.3.3 Polysulfide adsorbers

Using adsorbers/trappers which have strong binding energies toward polysulfides to trap and confine them in the cathode is another effective strategy to impede the polysulfide shuttle. The adsorbers include polymers and metal oxides/sulfides.

Conductive polymers (Figure 1.7) have attracted great interest for applications with Li-S batteries as they can only enhance the electrical conductivity of the sulfur cathode, but also trap polysulfides to reduce the polysulfide shuttle due to the strong interaction between the hetero atoms (O, N, S) of conductive polymers and the lithium atoms of polysulfides.

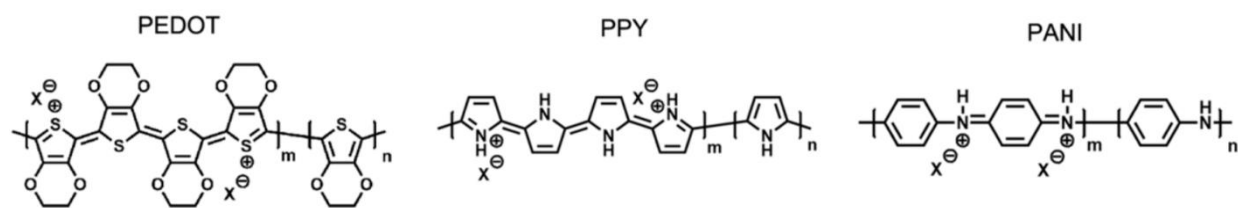
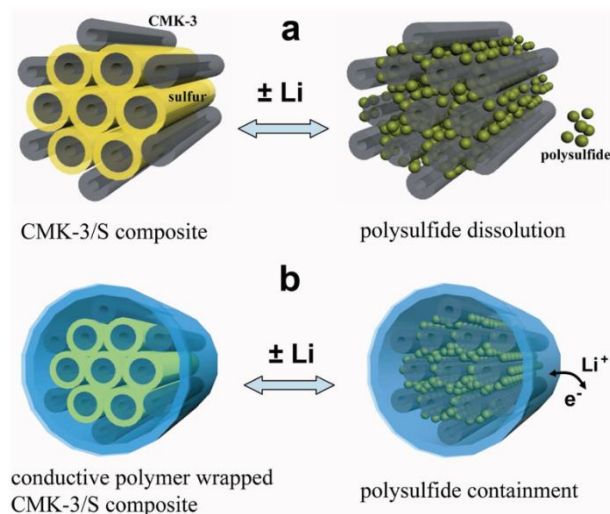


Figure 1.7 Chemical structures of PEDOT, PPY, and PANI. *m* and *n* indicate the doped and undoped parts in these polymers, and X⁻ indicates the counterion in the doped part. Reproduced with permission from Ref. 42.

Yang et al. employed PEDOT:PSS coating on the exterior surface of CMK-3/S particles to improve its electrochemical performance (Figure 1.8A).⁴³ It was found that the PEDOT:PSS coating led to the enhancement of the capacity retention from ~70% to ~80% over 100 cycles and 10% increase in the discharge capacity due to the effective trapping of polysulfides by PEDOT:PSS. By systematically studying the electrochemical performance of sulfur cathodes made from PEDOT-, PPY-, and PANI-coated hollow sulfur nanospheres (Figure 1.8B), Li et al. found that the capability of these polymers in improving the cycling stability and rate performance of sulfur cathode decreased in the order of PEDOT > PPY > PANI.⁴² Ab initio simulations showed that PEDOT had a much stronger binding affinity with the Li_{*x*}S ($0 < x \leq 2$) species than PPY and PANI. The strong binding of conductive polymers with polysulfides effectively reduced the polysulfide diffusion and thus contributed to the stable cycling performance.

(A)



(B)

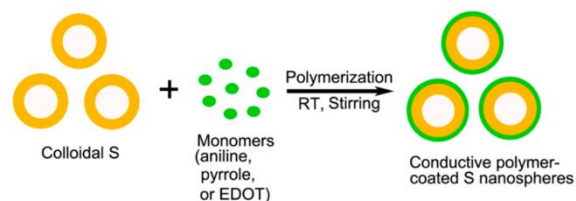


Figure 1.8 Conductive polymers for sulfur cathode. (A) Schematic of PEDOT:PSS-coated CMK-3/S composite for improving the electrochemical performance. Reproduced with permission from Ref. 43. (B) Schematic for the fabrication of conductive polymer-coated hollow sulfur nanospheres. Reproduced with permission from Ref. 42.

Non-conductive polymers which have strong absorption capability toward polysulfides have also been intensively studied. Some representative examples are given in Figure 1.9. The polar functional groups including hydroxyl (-OH), ether (-C-O-C-), carbonyl (-C=O), carboxylic (-COOH) and amine (-NH₂) in these polymers can bind with polysulfides strongly, as revealed by theoretical calculations.^{18,44} Most of these polymers were used as binders in Li-S batteries to replace the conventional poly(vinylidene fluoride) (PVDF) binder as PVDF fails to trap polysulfides. It is worth noting that stable cycling performance with a capacity retention of 85.6% over 200 cycles at 0.5 C was achieved with the poly(ethylenimine-hexamethylene diisocyanate) (PEI-HDI) binder.¹⁸ In addition to trapping polysulfides strongly, the excellent mechanical properties of some of these polymers such as gum arabic (GA),⁴⁵ PEI-HDI,¹⁸ and generation 3 polyamidoamine 4-carbomethoxy pyrrolidone dendrimer (G3CMP)⁴⁶ enable them to minimize the mechanical stress caused by the volume change of sulfur particles during charge/discharge and maintain the electrode integrity, which also contributes to the enhanced cycling performance.

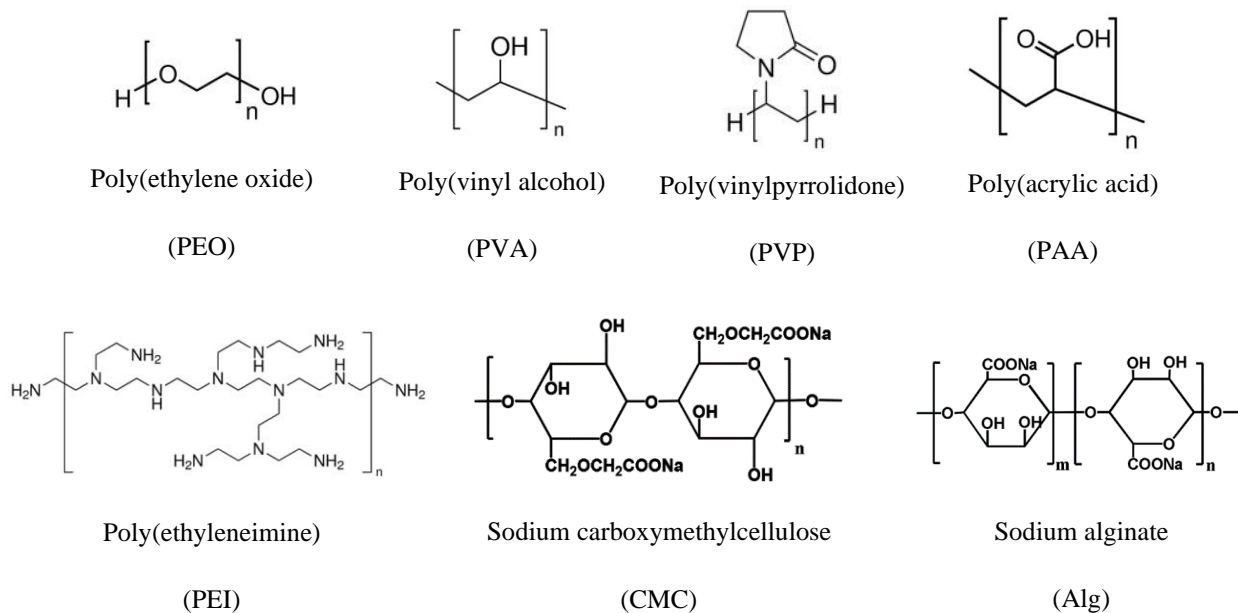


Figure 1.9 Representative nonconductive polymers for polysulfide trapping.

Metal oxides/sulfides including conductive ones (Ti_4O_7 , Ni_3S_2 , FeS , CoS_2),^{47–49} semi-conductive ones (VS_2 , TiS_2)⁴⁸ and non-conductive ones (MnO_2 , CeO_2 , Al_2O_3 , La_2O_3 , MgO , CaO)^{20,50,51} have been explored as effective additives for improving the performance of Li-S batteries. Pang et al. reported that conductive Ti_4O_7 cannot only enhance the electrical conductivity of sulfur cathode, but also strongly adsorb polysulfides to retard their diffusion in the electrolyte.⁴⁷ The $\text{Ti}_4\text{O}_7/\text{S}$ electrode shows a doubled capacity retention compared to a typical conductive carbon electrode. Tao et al. studied the effects of a series of non-conductive metal oxides including CeO_2 , Al_2O_3 , La_2O_3 , MgO and CaO on the performance of Li-S batteries, and found that MgO , CeO_2 and La_2O_3 resulted in higher capacity and better cycling stability over others (Figure 1.10c).⁵⁰ Polysulfide adsorption test, microstructure analysis and density functional theory (DFT) calculations revealed that the adsorption and the diffusion of polysulfides on the surface of non-conductive metal oxides needed to be balanced. Due to the poor conductivity of non-conductive metal oxides, the adsorbed polysulfides need to be transferred from the surface of metal oxide to the surface of conductive carbon for the electrochemical reactions to occur. Therefore, the diffusion of polysulfides on metal oxides is also important. In addition to effectively trapping polysulfides, some metal sulfides were found to exhibit electrocatalytic effects on polysulfide redox reactions.^{48,49} Zhou et al. compared the effects of a series of metal sulfides including Ni_3S_2 ,

FeS, CoS₂, VS₂ and TiS₂ on the battery performance of sulfur cathodes.⁴⁸ They found that VS₂, TiS₂ and CoS₂ showed higher binding energies with polysulfides and lower energy barriers for Li₂S oxidation, resulting in improved capacind cycling stability (Figure 1.10d).

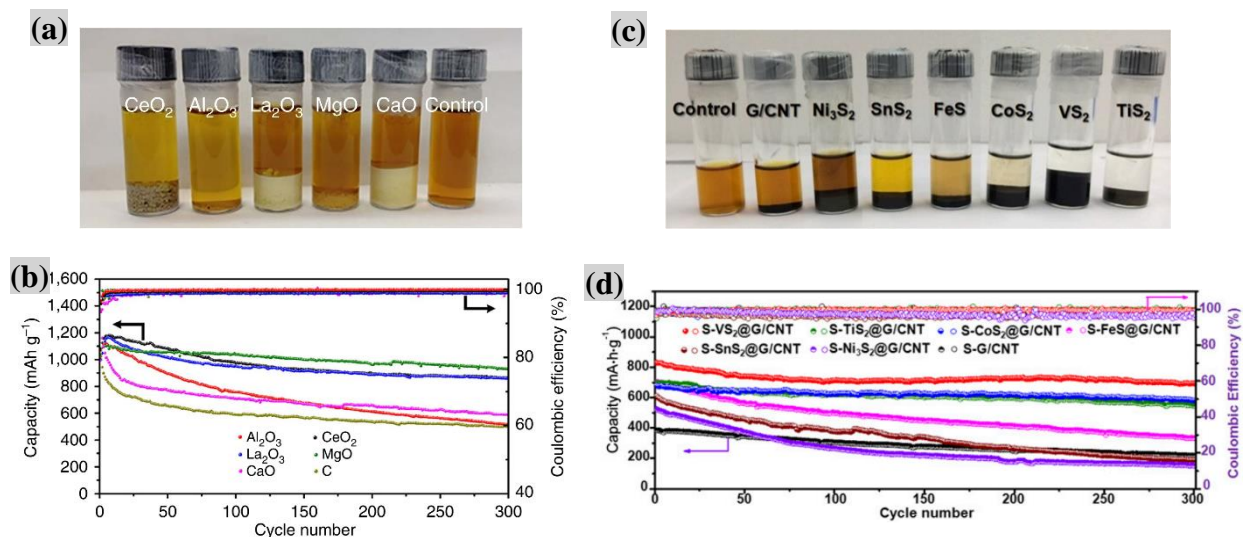


Figure 1.10 Metal oxides and sulfides for polysulfide trapping. (a) Digital images of Li₂S₈ (0.005 M) adsorption by metal oxides in DOL/DME (1:1, v:v) solution. Reproduced with permission from Ref. 50. (b) Cycling performance and coulombic efficiency of sulfur cathodes with metal oxides at 0.5 C. Reproduced with permission from Ref. 50. (c) Digital images of Li₂S₆ (0.005 M) adsorption by carbon and metal sulfides in DOL/DME solution. Reproduced with permission from Ref. 48. (d) Cycling performance and coulombic efficiency of sulfur cathodes with carbon and metal sulfides at 0.5 C. Reproduced with permission from Ref. 48.

1.2 Organic electrodes

Recently organic electrodes have attracted great research interest due to their high capacity (such as cyclohexanone⁵² with a theoretical capacity of 957 mA h g⁻¹, para-dinitrobenzene⁵³ with a theoretical capacity of 638 mA h g⁻¹), structural versatility (structural modification using various synthesis methods in organic chemistry), environmental benignity (organic electrodes only contain C, H, O, N, S, free of transition metals), renewability (organic electrodes can be produced from existing organic materials such as plants in nature), low cost (mass production of organic electrodes from existing organics through chemical or biochemical processes), mechanical flexibility (many organic electrodes can be easily processed into foldable films), and versatility

(applications of organic electrodes in various metal-ion batteries including lithium-ion, sodium-ion, potassium-ion, zinc-ion, magnesium-ion, calcium-ion and aluminum-ion).⁵⁴

1.2.1 Redox mechanisms of organic electrodes

Based on the redox mechanisms, organic electrodes can be categorized into three types: n-type, p-type and bipolar-type (Figure 1.11).⁵⁴ For n-type electrodes, they undergo reduction first, during which they gain electrons to become negatively charged and positive lithium ions are associated with them to render them electroneutral. n-Type electrodes include carbonyl, imine or phenazine, nitrile, organosulfide, azo, anhydride and phenoxy/galvinoxyl radical. For p-type electrodes, they undergo oxidation first, during which they lose electrons to become positively charged and the anions from the electrolyte are associated with them to render them electroneutral. p-type electrodes include conjugated thiophene and N-heterocycle. For bipolar-type electrodes, they undergo the reactions experienced by both n- and p-type electrodes. Bipolar-type electrodes include polyaniline, nitroxide radical such as 2,2,6,6-tetramethylpiperidiny-N-oxyl (TEMPO) derived nitroxide, 2,2,5,5-tetramethylpyrrolidin-N-oxyl (PROXYL) derived nitroxide and nitronyl nitroxide. Generally, p-type electrodes exhibit higher redox potentials (> 3 V vs. Li^+/Li) than n-type electrodes (redox potential $0\sim 3$ V vs. Li^+/Li). Therefore, p-type electrodes are often used as the cathodes. N-type electrodes can be used as either cathodes or anodes depending on their redox potentials. Those with the redox potentials in the range of $1.5\sim 3$ V vs. Li^+/Li are used as the cathodes, while the others with the redox potentials in the range of $0\sim 1.5$ V vs. Li^+/Li are used as the anodes.

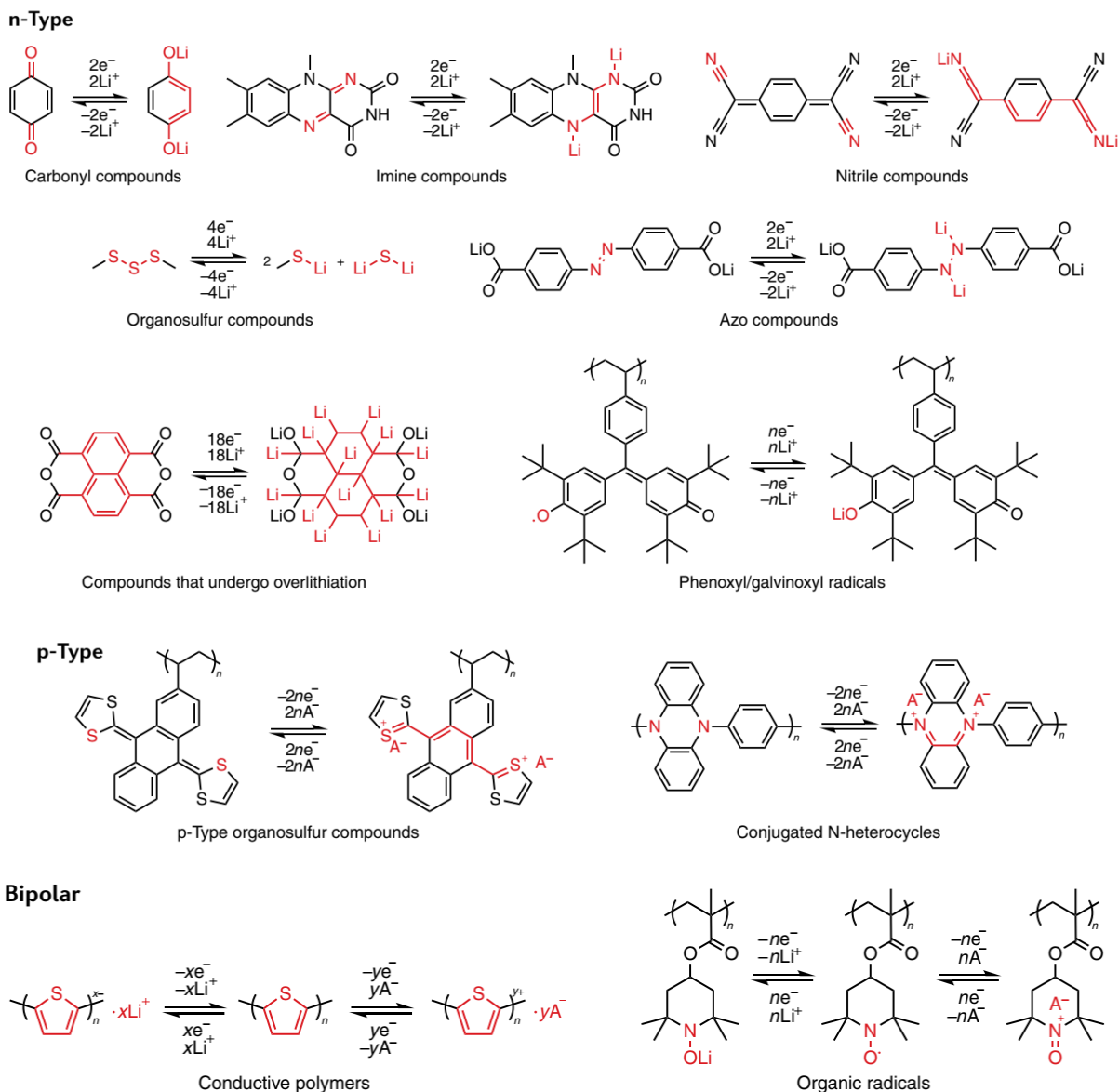


Figure 1.11 Redox mechanisms of different types of organic electrodes. Reproduced with permission from Ref. 54.

1.2.2 Challenges of organic cathodes and corresponding strategies

Organic cathodes generally have lower energy densities compared with sulfur and inorganic intercalation cathodes.

Energy density (E , unit: Wh kg^{-1}) of an electrode material can be calculated with Equation 1.1:

$$E = Q \times V \quad (\text{Equation 1.1})$$

where Q is the specific capacity (unit: mA h g⁻¹), V is the output voltage (unit: V).

Challenges have been encountered in achieving high Q and high V for organic batteries.

1.2.2.1 Achieving high specific capacity (Q)

As shown in Equation 1-1, achieving high specific capacity is essential for enhancing energy density. The specific capacity of an electrode material can be calculated, as shown below:

$$Q = \frac{n \cdot F}{3.6 \cdot M} = \frac{26801 \cdot n}{M} \quad (\text{Equation 1.2})$$

where Q is the specific capacity (unit: mA h g⁻¹), n is the number of electrons transferred per one molecule of the electrode material, F is the Faraday constant (96485 C mol⁻¹), M is the molecular weight of the electrode material (unit: g mol⁻¹). Based on Equation (1.2), Q is proportional to $\frac{n}{M}$. It is imperative to increase n while keeping M as low as possible. Recently, the aromatic nitro group (-NO₂) with an n value of two has been demonstrated as a reversible electroactive group for organic electrodes.⁵³ For the carbonyl group (-C=O), n equals one. Since n is a fixed number for a specific type of electroactive group, the challenge is to keep M as low as possible for achieving high capacity. 1,4-Benzoquinone (BQ) is quite soluble in the liquid electrolyte (usually 1:1 DOL/DME based, v:v) to the extent that it immediately dissolves in the electrolyte when it contacts the electrolyte solvents. Therefore, BQ cathode suffers from low utilization of the active material and fast capacity decay. It has been reported that the formation of macrostructures such as dibenzo[b,i]thianthrene-5,7,12,14-tetraone (DTT),⁵⁵ quinone-based polymers such as poly(benzoquinonyl sulfide) (PBQS),⁵⁶ lithium salt of poly(2,5-dihydroxy-p-benzoquinonyl sulfide) (Li₂PDHBQS)⁵⁷ and poly(anthraquinonyl sulfide) (PAQS)⁵⁸ can suppress the dissolution issue (Figure 1.12). However, these approaches inevitably introduce inactive structures into the BQ structure, which increases M while n is unchanged. As a result, the specific capacities of these quinones are much lower than that of BQ (Figure 1.12). Modification of the BQ structure with electro-donating such as 2,5-dimethoxy-1,4-benzoquinone (CH₃O-BQ),⁵⁹ or electron-withdrawing groups such as 2,5-bis(trifluoromethyl)-1,4-benzoquinone (CF₃-BQ)⁶⁰ and tetrachloro-1,4-benzoquinone (Cl-BQ)⁶¹ has been reported to tune the charge/discharge voltage of BQ (Figure 1.12). This approach also increases M while n stays the same, resulting in decreased specific capacities.

In summary, to achieve high specific capacity, special attention should be paid to keep the molecular weights (M) of organic electrode materials as low as possible when structural modification is applied to organic molecules.

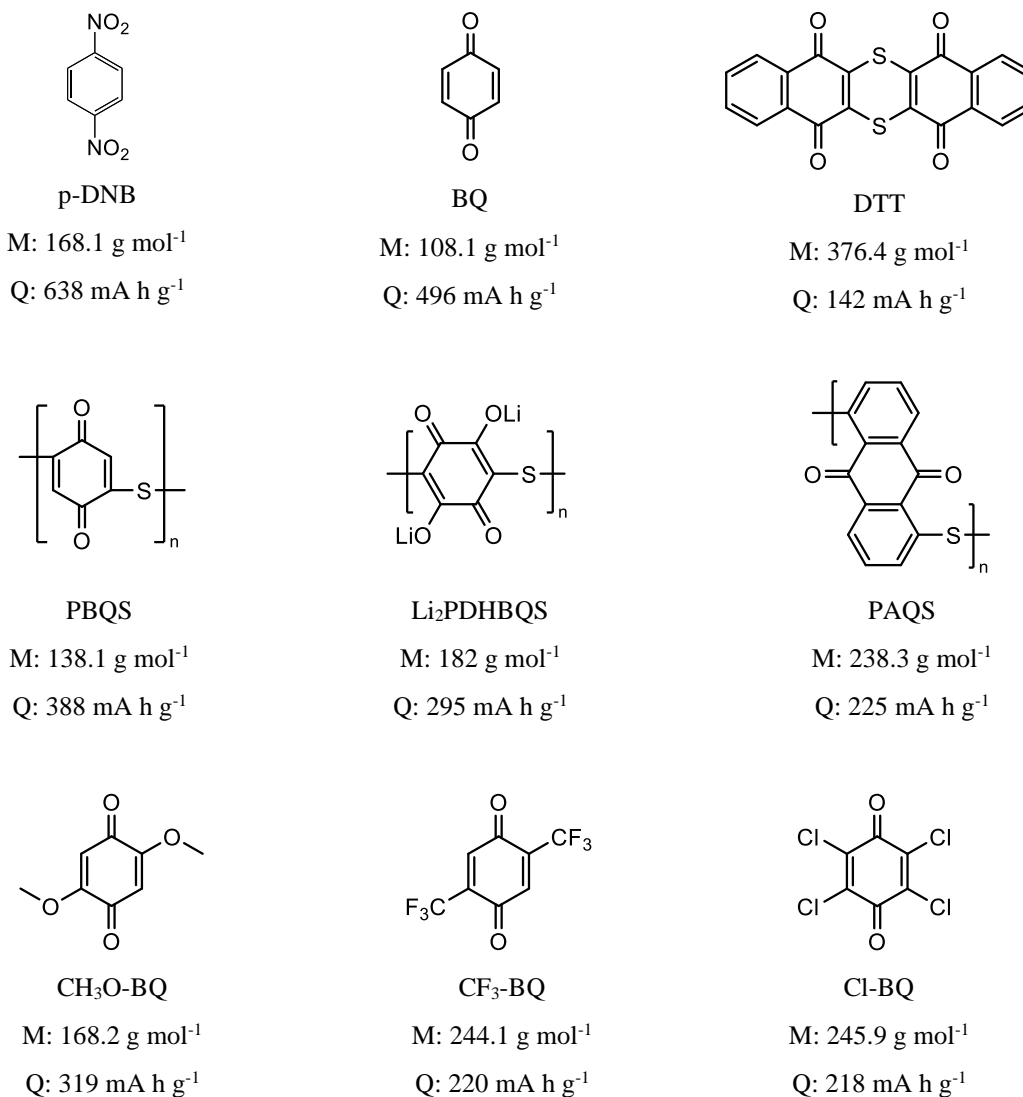


Figure 1.12 Chemical structures of para-dinitrobenzene and quinones with different molecular weights and specific capacities.

1.2.2.2 Achieving high output voltage (V)

Based on Equation 1.1, increasing the output voltage is also necessary for improving energy density. The output voltage is the difference between the cathode and the anode working potentials. It has been reported that the discharge potentials of organic cathode materials are closely related with their lowest unoccupied molecular orbital (LUMO) energy levels which can

be adjusted by the introduction of electron-withdrawing or -donating groups into their molecular structures.^{55,60–63} For the absolute vacuum scale (AVS), the Li^+/Li redox potential is -1.4 V corresponding to -1.4 eV for the one-electron-transferred reaction while the LUMO levels of organic cathode materials are much lower than -1.4 eV, indicating that the organic cathode materials gain electrons and are reduced during the discharge process. Therefore, the lower the LUMO levels of the organic cathode materials, the higher the discharge potentials. Liang et al. designed three AQ-based molecules with different electron-withdrawing aromatic heteroatoms (S, O and N), benzo[1,2-b:4,5-b']dithiophene-4,8-dione (BDTD), benzofuro[5,6-b]furan-4,8-dione (BFFD) and pyrido[3,4-g]isoquinoline-5,10-dione (PID), as shown in Figure 1.13A.⁶³ From the differential capacity curves (Figure 1.13B), it can be seen that the first-stage discharge potentials increase in the order of AQ (2.27 V) < BDTD (2.52 V) < BFFD (2.61 V) < PID (2.71 V), which follows the same trend of the absolute values of LUMO levels (Figure 1.13D).⁶³ The results also imply that there is a linear relationship between the first-stage discharge potentials and LUMO levels of organic cathode materials with analogous structures. For BQ based organic electrode materials, it has been reported that introduction of electron-withdrawing groups such as $-\text{CF}_3$, $-\text{CN}$, $-\text{F}$ and $-\text{Cl}$ increased the average discharge potentials by 0.3-0.6 V vs. Li^+/Li , while electron-donating groups such as $-\text{CH}_3$, $-\text{OCH}_3$, $-\text{Ph}$ and $-\text{OLi}$ lowered the average discharge potentials by 0.1-0.9 V vs. Li^+/Li .⁶⁴ It should be noted that the structural modification of organic cathode materials with electro-withdrawing groups aiming at increasing the discharge potentials (V) and energy densities (E) inevitably increases their molecular weights (M) which results in lowered specific capacities (Q) and energy densities. Therefore, smart design of organic electrode materials is needed to ensure that the gain in energy densities resulted from increased discharge potentials can compensate for the loss in energy densities resulted from decreased specific capacities.

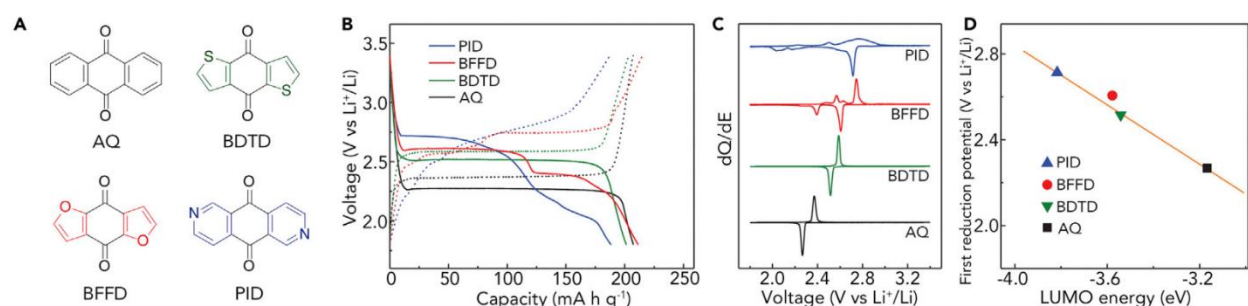


Figure 1.13 Chemical structures, charge/discharge curves, differential capacity curves, and the relationship between the first discharge potentials and the LUMO energy levels of AQ, BDTD, BFFD and PID. (A) Structures. (B) Charge/discharge profiles. (C) Differential capacity profiles derived from the curves shown in (B). (D) The relationship between the first discharge (reduction) potentials and the calculated LUMO levels. Figures 1.13(A-D) are reproduced with permission from Ref. 63.

1.2.3 Strategies to improve the cycling stability of organic cathodes

Improving the cycling performance of sulfur and organic cathodes is one of the focuses of this thesis, so the related strategies are discussed in detail. Similar to sulfur cathode, the cycling stability of organic cathodes is generally poor due to the high solubilities of organic cathode materials and their charge/discharge intermediates in the liquid electrolyte. Several strategies have been developed to solve the dissolution issue, including polymerization/formation of extended structures, formation of organic salt, hybridization with carbon and solid electrolyte, which will be discussed in detail in the following sections.

1.2.3.1 Polymerization or formation of macromolecular structures

Polymerization or formation of macromolecular structures has proven to be an effective strategy to improving the cycling stability of organic cathodes. Compared with small molecules, polymers or macromolecules with extended structures are less soluble in the liquid electrolyte. Song et al. synthesized two new polyanthraquinones, namely poly(1,4-anthraquinone) (P14AQ) and poly(1,5-anthraquinone) (P15AQ), and compared their cycling performances with those of a small molecule-1,4-anthraquinone (AQ) and another polymer-poly(anthraquinonyl sulfide) (PAQS).⁶⁵ As shown in Figure 1.14a, the discharged product of AQ is soluble in the liquid electrolyte where the discharged products of PAQS and P14AQ are insoluble, demonstrating the

effectiveness of polymerization in overcoming the dissolution issue. The capacity retentions of the polymers PAQS, P14AQ and P15AQ after 100 cycles at 0.2 C are 98.4, 98.3 and 67.6%, respectively, which are much higher than that (17.8%) of the small molecule AQ (Figure 1.14a). Long-term cycling test shows that P14AQ exhibits superior cycling stability with capacity retentions of 98.1 and 99.4% after 1000 cycles at 1 and 2 C, respectively. In addition to polymerization, formation of extended structures such as pillar[5]quinone (P5Q)⁶⁶ and Vat Green 8 (VG 8)⁶⁷, shown in Figure 1.14b-c, is another method to reduce the solubilities of the materials in the liquid electrolyte. Improved cycling stabilities were obtained with these macromolecules of extended structures. Recently, covalent organic frameworks (COFs), a special class of polymers with periodic skeletons and ordered nanopores, have attracted considerable research interest for their potential application in rechargeable batteries. As battery electrode materials, COFs have several advantages including tunable electronic properties, ability to accommodate ions such as Li⁺ and Na⁺ in the nanopores without prominent volume change, and facilitated transport of ions in the nanopores. Shi et al. reported the design and battery application of a COF with triquinoxalinylene and benzoquinone units (TQBQ) in the skeletons (TQBQ-COF), as shown in Figure 1.14d.⁶⁸ In addition to high-rate capability of 134.3 mA h g⁻¹ (26.1% of the theoretical capacity) at 10.0 A g⁻¹ (19.4 C) resulted from enhanced electronic and ionic conduction, the as-designed TQBQ-COF electrode exhibits excellent cycling stability with a capacity retention of 96% after 1000 cycles at 1.0 A g⁻¹ (1.9 C) in sodium-ion batteries.⁶⁸

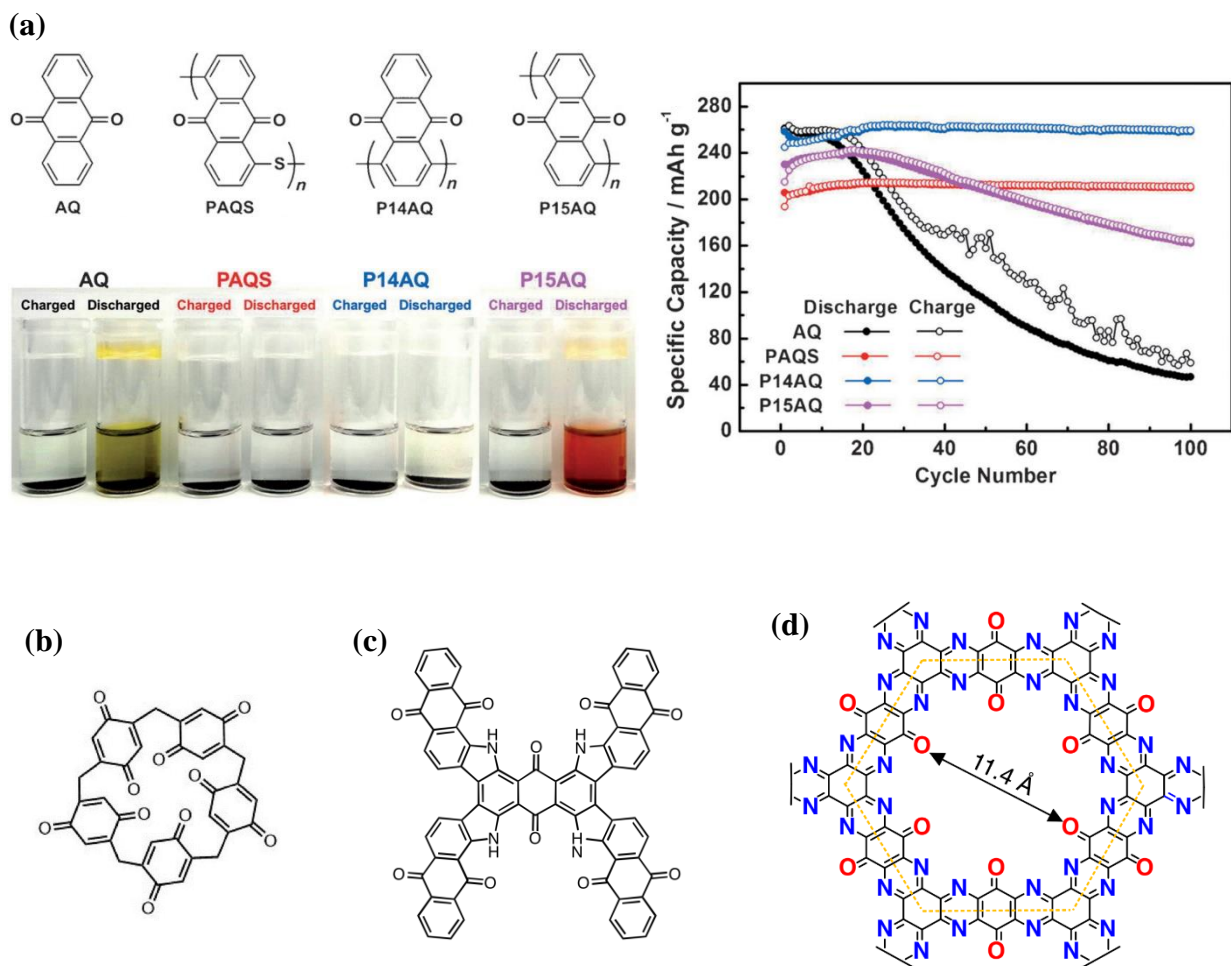


Figure 1.14 Chemical structures of polymers and macromolecular structures synthesized from small organic molecules. (a) Structures of AQ, PAQS, P14AQ and P15AQ. Photographs showing the dissolution behaviors of the materials and their discharged products in the liquid electrolyte. Cycling performance of the materials at 0.2 C. Reproduced with permission from Ref. 65. Structures of (b) P5Q, (c) VG 8, and (d) TQBQ-COF (reproduced with permission from Ref. 68).

1.2.3.2 Formation of organic salts

Formation of organic salt is another effective strategy to reduce the solubilities of organic cathode materials in the liquid electrolyte. The most common liquid electrolyte for organic cathodes uses aprotic solvents, normally DOL/DME (1:1, v:v). The introduced salt groups are highly polar (ionic bond) and have poor solubilities in aprotic solvents. The salt groups reported so far include -OM, -COOM, and -SO₃M (M represents Li or Na). The disodium salt of 2,5-

dihydroxy-1,4-benzoquinone (Na_2DHBQ) showed excellent cycling stability with a capacity retention of 76.7% after 300 cycles at 1 C.⁶⁹ Similarly, enhanced cycling stabilities with capacity retentions of 90% after 50 cycles at 0.05 C and 95% after 50 cycles at 0.1 C were seen with the tetralithium salt of 2,3,5,6-tetrahydroxy-1,4-benzoquinone (Li_4THBQ)^{70,71} and the dilithium salt of 1,5-dihydroxyanthraquinone (Li_2DHAQ)⁷², respectively. It is worth noting that for the compounds containing lithium enolate groups ($-\text{OLi}$), coordination bonding ($\text{O}\cdots\text{Li}\cdots\text{O}$) may exist resulting in the formation of coordination polymers with periodic frameworks, as suggested by Xiang et al.⁷³ Recently, azo compounds ($-\text{N}=\text{N}-$) were identified as a new type of organic electrode materials for alkali-ion batteries by Luo et al.^{74,75} They found that the cycling stabilities of azo compounds increases on increasing the number of carboxylate groups ($-\text{COOM}$). The azobenzene (AB) electrode lost more than 50% of the capacity after the first cycle due to the high solubility of AB in the electrolyte. On adding two carboxylate groups to the structure of AB, the resultant azobenzene-4,4'-dicarboxylic acid sodium salt (ADASS) electrode exhibited exceptional cycling stability with a capacity retention of 86.6% after 2000 cycles at 20 C due to the substantially reduced solubility in the electrolyte.⁷⁴ Sulfonate group ($-\text{SO}_3\text{Na}$) was also reported to enhance the cycling stability of organic electrode materials.^{76,77} Compared with indigo, indigo carmine (5,5'-indigodisulfonic acid sodium salt) showed improved cycling stability with a capacity retention of more than 90% after 40 cycles at 0.09 C in both Li-ion and Na-ion batteries.⁷⁶

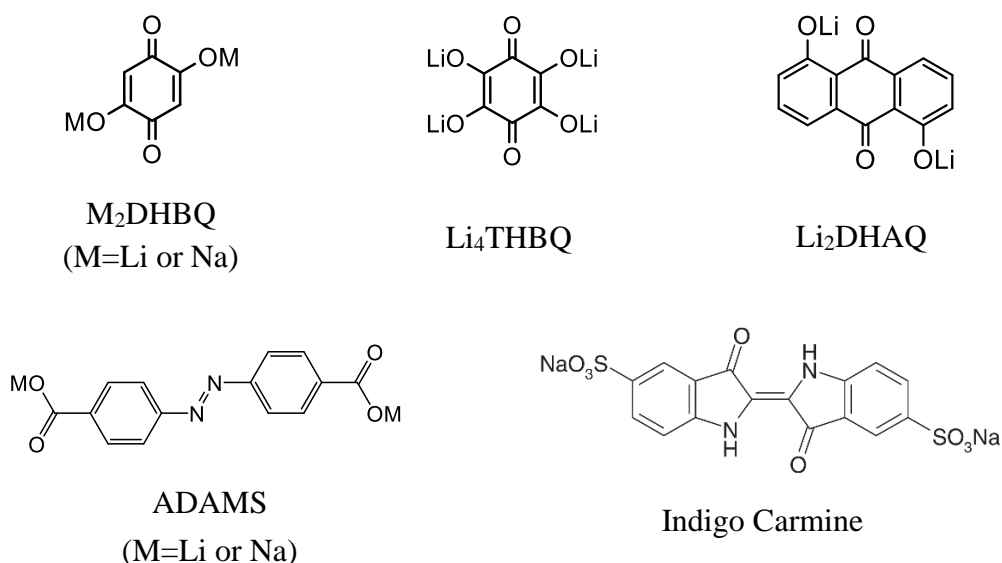


Figure 1.15 Representative organic salts with enhanced cycling stabilities.

1.2.3.3 Nanocomposite formation with insoluble materials

Similar to the sulfur cathode, nanocomposite formation between organic electrode materials and insoluble materials such as graphene, CNTs, porous carbon and metal oxides has proven effective in alleviating the dissolution issue. The capacity retention of P5Q electrode in Na-ion batteries was increased from 27% after 100 cycles at 0.1 C to 69% after 300 cycles at 0.1 C by the encapsulation of P5Q with mesoporous conductive carbon (CMK-3) at the P5Q loading of 33.3%.⁷⁸ The capacity retention of 2,2'-bis(3-hydroxy-1,4-naphthoquinone) (H_2BHNQ) electrode in Li-ion batteries was improved from 26.3% to 65.7% after 50 cycles at 0.1 C by the encapsulation of H_2BHNQ with CMK-3 at the H_2BHNQ loading of 50% (Figure 1.16a).⁷⁹ In addition to the encapsulation of organic electrode materials in the pores of porous carbons by physisorption^{78–80} and nanocomposite formation with graphene/CNTs via π - π interaction⁸¹, chemically grafting organic electrode materials onto functionalized carbons was also reported.⁸² By chemically grafting 2,3-diamino-1,4-naphthoquinone (DANQ) molecules onto the surfaces of carboxylate group (-COOH) functionalized carbon fibers via peptide bond formation, as shown in Figure 1.16b, the capacity retention of DANQ electrode in Li-ion batteries was improved from 34% after 50 cycles at 98% after 100 cycles at 0.2 C.⁸² It is worth mentioning that the rate performance of the materials is also enhanced when conductive materials are used for preparing the nanocomposite. Nanocomposite formation with metal oxides was also reported. Yang et al. reported an elaborately designed 1,4-benzoquinone@TiO₂ structure to mitigate the dissolution issue.⁸³ Enhanced capacity retention of 80.7% after 100 cycles at 0.1 C was obtained.

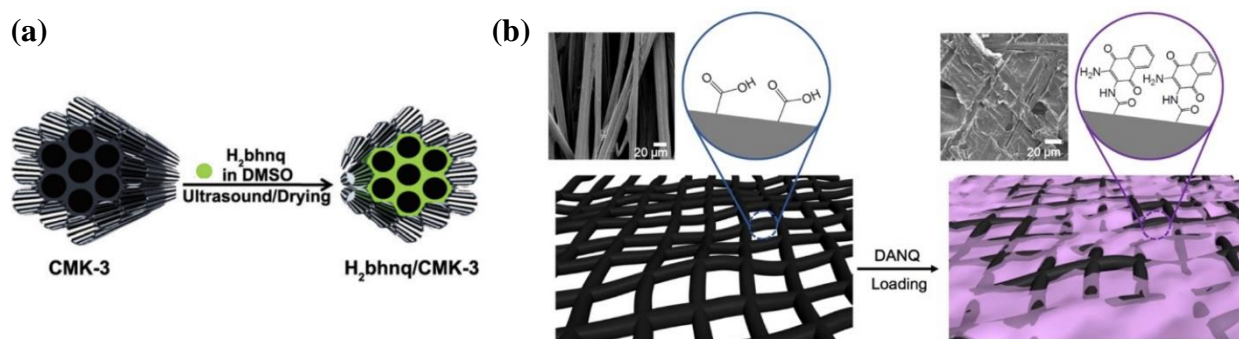


Figure 1.16 Nanocomposite formation between small organic molecules and porous carbon. (a) Schematic of the encapsulation of H_2BHNQ molecules in the nanopores of CMK-3 by the wet impregnation method. Reproduced with permission from Ref. 79. (b) Chemically grafting DANQ molecules onto functionalized carbon fibers. Reproduced with permission from Ref. 82.

1.2.3.4 Use of solid electrolytes

For organic electrodes, the dissolution of organic molecules in the liquid electrolyte can be substantially suppressed by using solid electrolyte. With a quasi-solid gel polymer electrolyte, poly(methacrylate) (PMA)/poly(ethylene glycol) (PEG)-LiClO₄-DMSO (Figure 1.17), the calix[4]quinone (C4Q) cathode showed enhanced cycling performance with a capacity retention of 89.8% after 100 cycles at 0.2 C and room temperature.⁸⁴ Later on, the same group developed a PMA/PEG based solid electrolyte, namely PMA/PEG-LiClO₄-3 wt% SiO₂. Using the as-developed solid electrolyte, the P5Q cathode exhibited stable cycling performance with a capacity retention of 94.7% after 50 cycles at 0.2 C and room temperature.⁸⁵ By contrast, the P5Q cathode showed rapid capacity decay with the loss of ~45% of the initial capacity after only three cycles when the liquid electrolyte of 1 M LiPF₆ in 1:1 (v:v) ethylene carbonate (EC)/diethyl carbonate (DEC) was used, which demonstrated the advantages of solid electrolyte over liquid electrolyte in improving the cycling stability of organic electrodes.

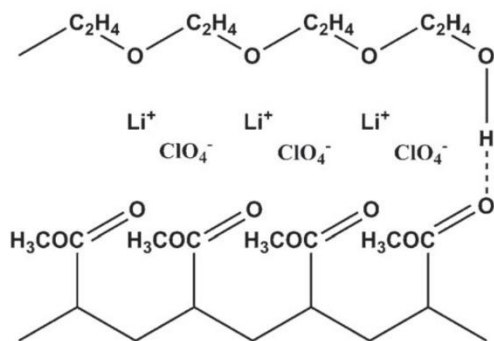


Figure 1.17 The structure of PMA/PEG based electrolyte. Reproduced with permission from Ref. 84.

1.3 Research objectives

An overview of the different approaches for solving the dissolution issue is shown in Table 1.2.

Table 1.2 An overview of the different strategies for solving the dissolution issue.

	Advantages	Disadvantages
Nanocomposite formation with porous carbons	<ul style="list-style-type: none">i) Can trap the soluble species in the nanoporesii) Can improve the electrical conductivity of electrode due to the high conductivity of porous carbon	<ul style="list-style-type: none">i) Cannot completely solve the dissolution issue and the soluble species still diffuse out of electrodeii) The weight ratio of active material to porous carbon cannot exceed ~70% to make this approach effective, which lowers the energy density of electrode
Polymerization (conventional polymers, macrostructures, coordination polymers, COFs, MOFs)	Completely solve the dissolution issue	<ul style="list-style-type: none">i) Not applicable to the sulfur cathodeii) May introduce non-electroactive units into the structures of organic electrodesiii) Instabilities of some MOFs after Li insertion
Adding adsorbers (metal oxides, sulfides, polymer binders) for trapping soluble species	Can effectively trap the soluble species	May need to use a large amount of adsorbers to make this approach effective, which lowers the energy density of the electrode
Formation of organic salts	Can substantially reduce the solubilities of organic electrodes in the liquid electrolytes	<ul style="list-style-type: none">i) Not applicable to the sulfur cathodeii) Not as effective as the polymerization approach
Using solid electrolyte	Completely solve the dissolution issue	<ul style="list-style-type: none">i) Low ionic conductivity of solid electrolyte and may require high temperature to make the battery workii) Compatibility of solid electrolyte with organic electrode and Li anode

The main objective of this thesis is to improve the battery performance (mainly the cycling stability) of sulfur and organic cathodes by using polymers.

- The trapping ability toward soluble polysulfides and the mechanical strength of separated or lightly interacted polymer chains are limited. By using a robustly crosslinked PEDOT:PSS binder, these two aspects are expected to be strengthened, which can result in improved cycling stability for the sulfur cathode.
- Physical mixing of commercial PEDOT binder with other electrode components such as Super P and sulfur particles cannot afford a tight contact among these electrode components. And whether the conductivity of conductive polymers stays unchanged during the electrochemical cycling of Li-S batteries is known. An in-cell (or in-situ) electrochemical polymerization method is expected to generate a tight contact among the different electrode components, which can result in improved trapping effect toward polysulfides and facilitated electron transport. Revealing potential dependence of the conductivity for conductive polymers is of utmost importance while using these materials to improve the electrical conductivity of the electrodes.
- Formation of coordination polymers or metal organic frameworks by using transition metal ions and small organic molecules is an established area. But whether these compounds including both the metal and the ligand are electroactive or not is unknown. How to improve the cycling stability of organic electrodes using the afore-mentioned approaches is also very important.
- Conjugated polymer electrodes are a special organic electrode with the merits of solution processability, mechanical flexibility and high-rate capability. The discharge voltages and capacities of conjugated polymer electrodes reported so far are very low. How to improve these two aspects for conjugated polymer electrodes are crucial.

1.4 The structure of the thesis

This thesis consists of seven chapters. Chapter 1 introduces the general backgrounds and recent progress in sulfur and organic cathodes, and motivation of the thesis. Chapter 2 presents a summary of the theoretical principles and instrumentation of the various characterization techniques which have been used in the thesis. In Chapter 3, a crosslinked PEDOT:PSS-Mg²⁺ binder is developed to improve the cycling stability and rate performance of sulfur cathode. In Chapter 4, a novel in-cell electro-polymerization method is developed to incorporate a conductive polymer (PEDOT) into the sulfur cathode and discusses the conductivity changes of conductive

polymers during battery cycling. The electrochemical performances of a series of coordination polymers are compared in Chapter 5. The polymers were synthesized with divalent metal ions (Ni^{2+} , Co^{2+} , Mn^{2+} , Zn^{2+} , and Cu^{2+}) and 2,5-dihydroxy-1,4-benzoquinone (DHBQ). The results indicate that these polymers improve the performance of DHBQ electrode. Moreover, stable cycling for the Cu-DHBQ cathode is achieved by binder optimization. Two diketopyrrolopyrrole (DPP) based conjugated polymer cathodes are developed in Chapter 6. These polymers are diketopyrrolopyrrole-quaterthiophene copolymer (PDQT) and diketopyrrolopyrrole-bithiophene polymer (PDBT), which show p-type and bipolar-type charge storage mechanisms, respectively. A summary of the main findings of the thesis is provided in Chapter 7, where future research directions are suggested.

Chapter 2. Characterization Techniques

In this chapter, the basic principles and the instrumentation for the main characterization techniques adopted to characterize the physicochemical properties of electrode materials and evaluate their electrochemical performance are described.

2.1 Physical characterization

2.1.1 X-ray diffraction (XRD)

When an X-ray is shined on a crystal, it diffracts in a unique pattern characteristic of the structure of the crystal. The diffraction pattern originates from the powders of a material in powder XRD while it is from the individual crystal of a material in single crystal XRD. X-rays are partially scattered by the atoms when they strike the surface of a crystal. The part of the X-ray that is not scattered will pass through to the next layer of atoms, where again part of the X-ray is scattered and part of the X-ray passes through to the next layer. This causes an overall diffraction pattern, similar to how a grating diffracts a beam of light. The sample must be crystalline and the spacing (d) between atomic layers must be close to the radiation wavelength for an X-ray to diffract. If the beams diffracted by the two different atomic layers are in phase, constructive interference occurs and the diffraction pattern shows a peak, while destructive interference occurs and there is no peak if they are out of phase. Diffraction peaks appear only when $\sin\theta = \frac{n\lambda}{2d}$ (Bragg's Law), where θ is the angle of incidence of the X-ray, n is an integer, λ is the wavelength of the X-ray, and d is the spacing between atomic layers. A highly ordered structure is needed for the diffraction to occur, therefore only crystalline materials show diffraction patterns while amorphous materials do not. Since the diffraction patterns are unique, the samples can be identified by referring to databases of diffraction patterns such as International Centre for Diffraction Data (ICDD) and Joint Committee for Powder Diffraction Standards (JCPDS). The purity of a sample can be determined from its diffraction pattern since the contaminants would show additional peaks if there are any. The particle size of the powder can be determined using the Scherrer formula, $t = \frac{K\lambda}{\beta\cos\theta}$, where t is the mean size of the ordered (crystalline) domains and may be different from the grain size, K is a dimensionless shape factor with a value close to unity (K has a typical value of ~ 0.9 and varies with the shape of the crystallite, λ is the wavelength of the X-ray, β is the line broadening corresponding to the full width at half maximum (FWHM) after subtracting the instrumental line

broadening and sometimes denoted as $\Delta(2\theta)$, and θ is the Bragg angle. The instrumentation of an X-ray diffractometer⁸⁶ is shown in Figure 2.1a, an example of the XRD data⁷³ is shown in Figure 2.1b.

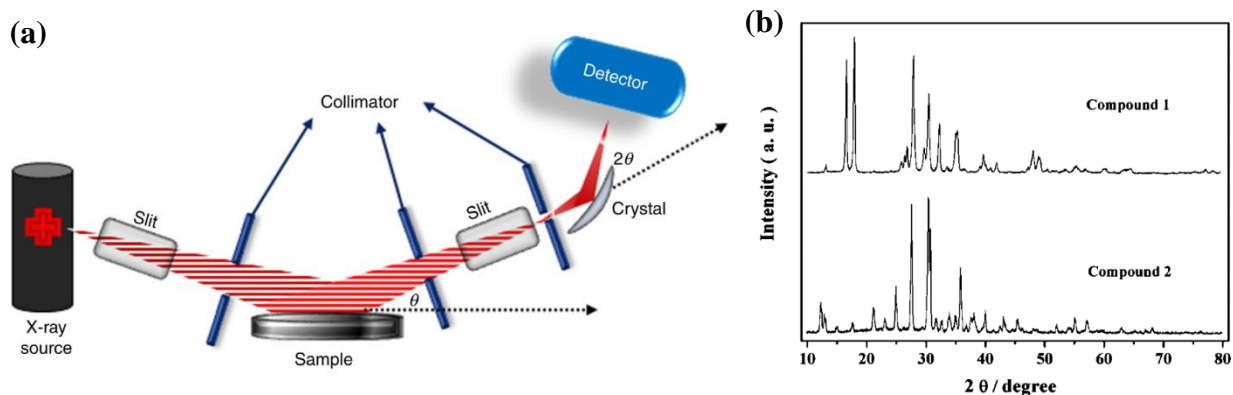


Figure 2.1 Instrumentation for XRD and an example of XRD data. (a) Instrumentation of an X-ray diffractometer. Reproduced with permission from Ref. 86. (b) XRD patterns of compounds 1 [$\text{Li}_2(\text{C}_6\text{H}_2\text{O}_4)$] and 2 [$\text{Li}_2(\text{C}_6\text{H}_2\text{O}_4) \cdot 2\text{H}_2\text{O}$]. Reproduced with permission from Ref. 73.

2.1.2 Thermogravimetric analysis (TGA)

Thermogravimetric analysis (TGA) is a thermal analytical technique where the mass change of a sample as a function of time or temperature is monitored while the sample is being treated with a controlled temperature program in a controlled gas atmosphere.⁸⁷ The temperature program includes heating at a constant heating rate (e.g. $10\text{ }^\circ\text{C min}^{-1}$), an isothermal regime for a certain period of time, and a non-linear temperature change.⁸⁷ The gas atmosphere includes inert (e.g. N_2 , Ar) and reactive gases (e.g. air, O_2 , 8-10% H_2 in N_2).⁸⁸ The TGA experiment is conducted with a thermogravimetric analyser which is equipped with a high-precision thermobalance. There are three different designs for the thermobalance, top loading, bottom loading or hang down, side loading, as shown in Figure 2.2a-c.⁸⁹ The balance and the thermocouple can accurately measure mass and temperature, respectively. A protective tube is used to isolate both heating element and cooling coil from the sample pan. TGA can provide information on phase transition, thermal/oxidative stability, composition of a mixture, and product lifetime. The TGA data (known as thermogram) is normally represented as percent weight versus temperature. The first derivative

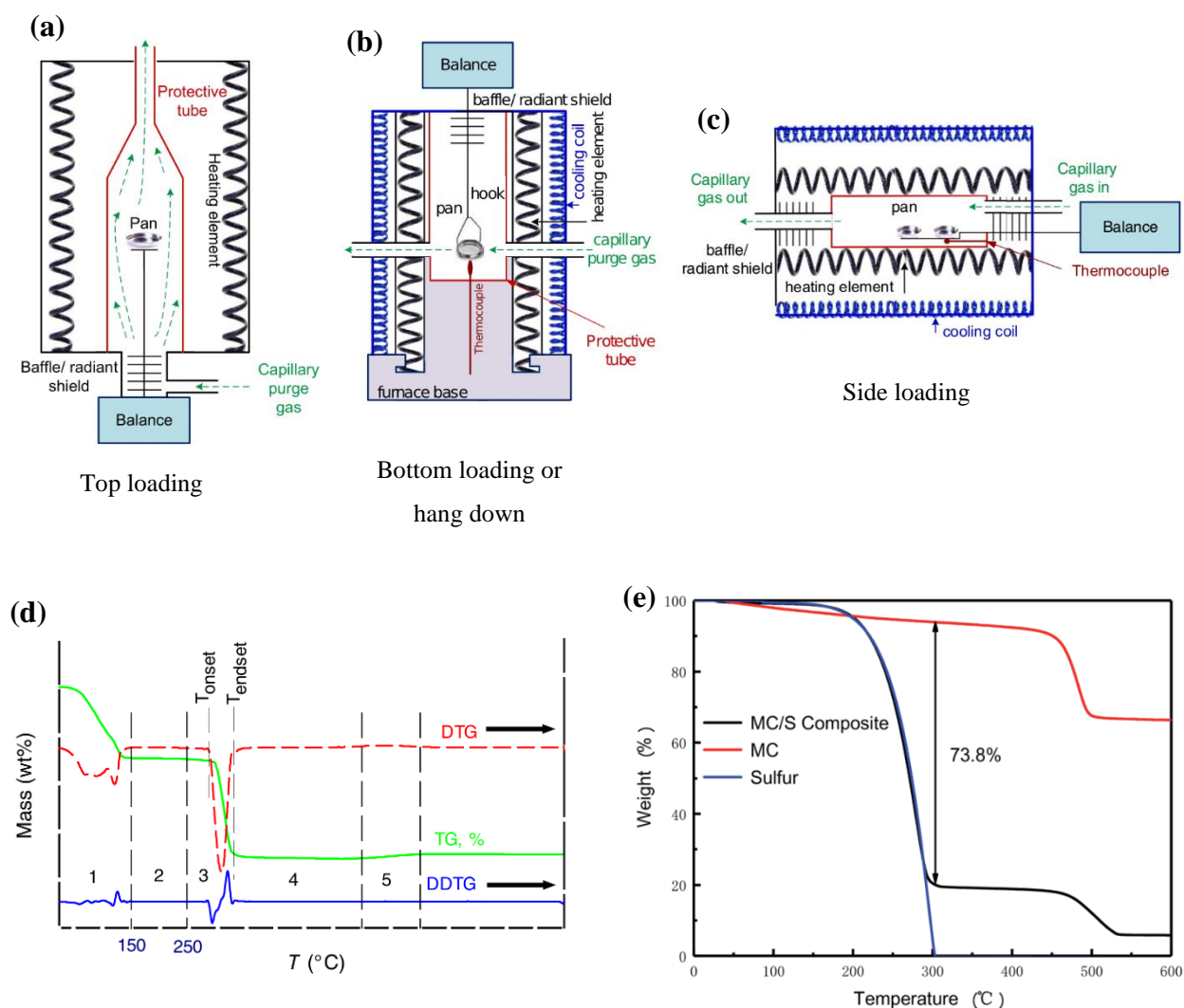


Figure 2.2 Instrumentation for the thermobalance of TGA, and examples DTG, DDTG and TGA data. Three different designs of thermobalance: (a) top loading, (b) bottom loading or hang down, and (c) side loading. Reproduced with permission from Ref. 89. (d) Thermogram (TG curve, green), first derivative of thermogram (DTG curve, red), second derivative of thermogram (DDTG curve, blue) of $Mn(CH_3COO)_2 \cdot 4H_2O$ heated up to 900 °C in air. Reproduced with permission from Ref. 89. (e) TGA curves of the mesoporous carbon/sulfur (MC/S) composite, MC and sulfur. Reproduced with permission from Ref. 90.

of a TGA thermogram, known as DTG, can be used to identify the onset decomposition temperature, inflection point, and end decomposition temperature.^{89,91} An example showing the

TGA and DTG curves is given in Figure 2.2d.⁸⁹ By equipping TGA with evolved gas analysis (EGA) such as mass spectroscopy (MS) and Fourier transform infrared spectroscopy (FTIR), it is possible to identify the chemical nature of the evolved gas and correlate the results with the observed mass change.^{88,92} In addition to characterizing the thermal stabilities of electrode materials, TGA can also be used to determine the sulfur content of a S/C composite.⁹⁰

2.1.3 Ultraviolet-visible-near-infrared spectroscopy (UV-Vis-NIR)

Ultraviolet-visible-near-infrared (UV-Vis-NIR) spectroscopy, performed in the wavelength range of 200-3300 nm, is a powerful analytical technique to probe the optical and electronic properties of liquids and solids (thin films and powders). Figure 2.3a is a summary of the phenomena that can occur when a sample is illuminated or irradiated (infrared range).⁹³ When luminescence, scattering and reflection are negligible or eliminated by the control experiment,⁹³ the Lambert–Beer law can be applied: $A = \log_{10} \frac{I_0}{I} = \epsilon cL$, where A is the absorbance, I_0 is the power (intensity) of the incident light, I is the power of the transmitted light, L is the path length of light through the sample in cm, c is the analyte concentration in mol L⁻¹, ϵ is the molar absorptivity or extinction coefficient in L mol⁻¹ cm⁻¹. UV-Vis-NIR spectroscopy includes two modes, transmittance and reflectance. A UV-Vis-NIR experiment is conducted with a spectrophotometer. Three common instrumental designs for spectrophotometers are shown in Figure 2.3b-d.⁹⁴ In a single-beam instrument (Figure 2.3b), the radiation passed through the filter enters either the reference or the sample cell before striking the photodetector. In a double-beam-in-space instrument (Figure 2.3c), the radiation passed through the filter is split into two beams that simultaneously pass through the reference and the sample cells before striking two matched photodetectors. In a double-beam-in-time instrument (Figure 2.3d), the radiation passed through the filter alternately enters the reference and the sample cells before striking a single photodetector.⁹⁴ An example of UV-Vis data is shown in Figure 2.3e, which is the UV-Vis spectrum of lithium polysulfide (Li₂S₆).⁹⁵

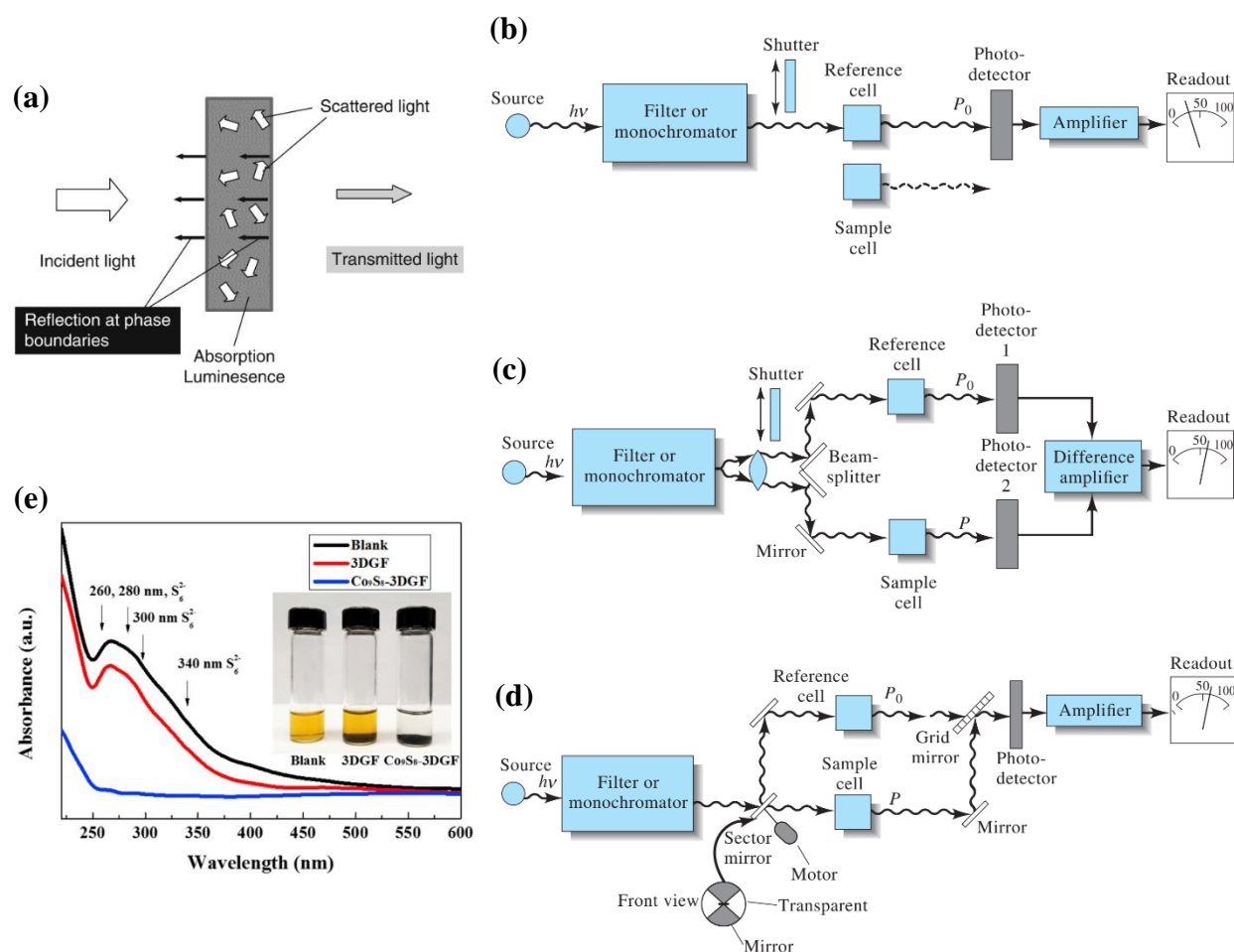


Figure 2.3 Theoretical principles and instrumentation for UV-Vis-NIR, and an example of UV-Vis data. (a) Schematic illustrating the interaction of light with matter. Reproduced with permission from Ref. 93. Three instrumental designs for spectrophotometers: (b) single beam, (c) double beam in space, (d) double beam in time. Reproduced with permission from Ref. 94. (e) UV-Vis spectra of blank Li_2S_6 solution, and Li_2S_6 solutions with three-dimensional graphene foam (3DGF) and Co_9S_8 -3DGF. Reproduced with permission from Ref. 95.

2.1.4 Fourier transform infrared spectroscopy (FTIR)

Infrared spectroscopy (IR) is a technique used to identify the structures of molecules or quantify the amounts of molecules based on the characteristic absorption spectra of molecules under IR radiation. The IR region includes near-infrared ($12800\sim 4000\text{ cm}^{-1}$), mid-infrared

(4000~200 cm^{-1}), and far-infrared (200~10 cm^{-1}). The most used region in IR spectroscopy is the mid-infrared region (4000~670 cm^{-1}).⁹⁴ The spectrum in IR spectroscopy is caused by molecular vibrations or rotations whereas that in UV-Vis spectroscopy is caused by electronic transitions. The absorption of IR radiation causes a molecule to undergo a net change in dipole moment as it vibrates or rotates. Vibrations of molecules can be categorized into stretching and bending. There are three types of IR spectrometers, dispersive type with a grating monochromator, non-dispersive type with a filter or an absorbing gas for the analysis of atmospheric gases, and Fourier transform (FT) type with an interferometer.⁹⁴ Compared with the other two types, the FT-type has the advantages of fast speed, reliability, high signal-to-noise ratio, and convenience. The main difficulty with the dispersive IR is the slow scanning process. By using an interferometer, the FTIR can measure all the infrared frequencies simultaneously rather than individually on the order of one second or so. The as-measured interferogram was decoded to give the plot of intensity at each individual frequency using the well-known mathematical technique (fast Fourier transformation, FFT) with a computer. The layout of a FTIR spectrometer is shown in Figure 2.4a, and the schematic of the sample analysis process using a FTIR spectrometer is shown in Figure 2.4b.⁹⁶ An example of FTIR spectra is shown in Figure 2.4c.⁹⁷

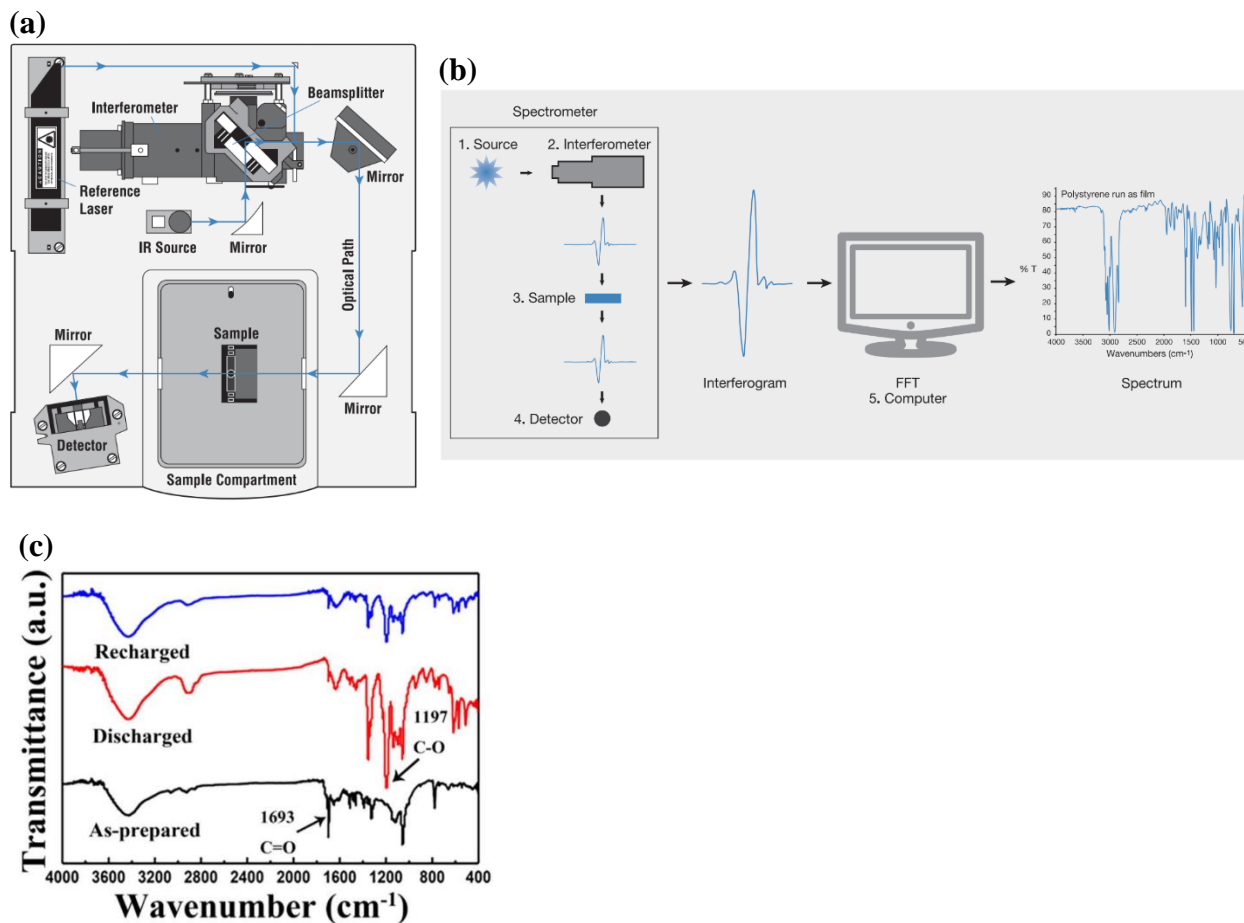


Figure 2.4 Instrumentation for FTIR and an example of FTIR data. (a) The layout of a FTIR spectrometer. Reproduced with permission from Ref. 96. (b) Schematic of the sample analysis process with a FTIR spectrometer. Reproduced with permission from Ref. 96. (c) FTIR spectra of the 5,7,12,14-tetraaza-6,13-pentacenequinone (TAPQ) electrodes in three states: as-prepared, discharged, recharged. Reproduced with permission from Ref. 97.

2.1.5 Peel test

Peel test is a commonly used method to measure the adhesive strength of an adhesive material. The adhesive strength, sometimes referred to as the “stickiness”, describes the ability of an adhesive to stick to a surface and bond two surfaces together. The adhesive strength (unit: N mm^{-1}) is defined as the average load per unit width of bond line required to gradually separate a flexible member from a rigid member over adhered surfaces. A schematic for the peel test is shown

in Figure 2.5a.⁹⁸ Standard methods for peel test include T-peel (Figure 2.5b)⁹⁹, 90° peel, 180° peel (Figure 2.5c)⁹⁹, roller, and climbing drum.⁹⁸ In the battery research area, the peel test can be used to evaluate the binding properties of polymer binders.¹⁰⁰⁻¹⁰³ As shown in Figure 2.5d, by performing a 180° peel test on an electrode film, the adhesive strength of a polymer binder can be measured.¹⁰³ A typical plot of peel force versus distance obtained from the peel test is shown in Figure 2.5e.¹⁰³

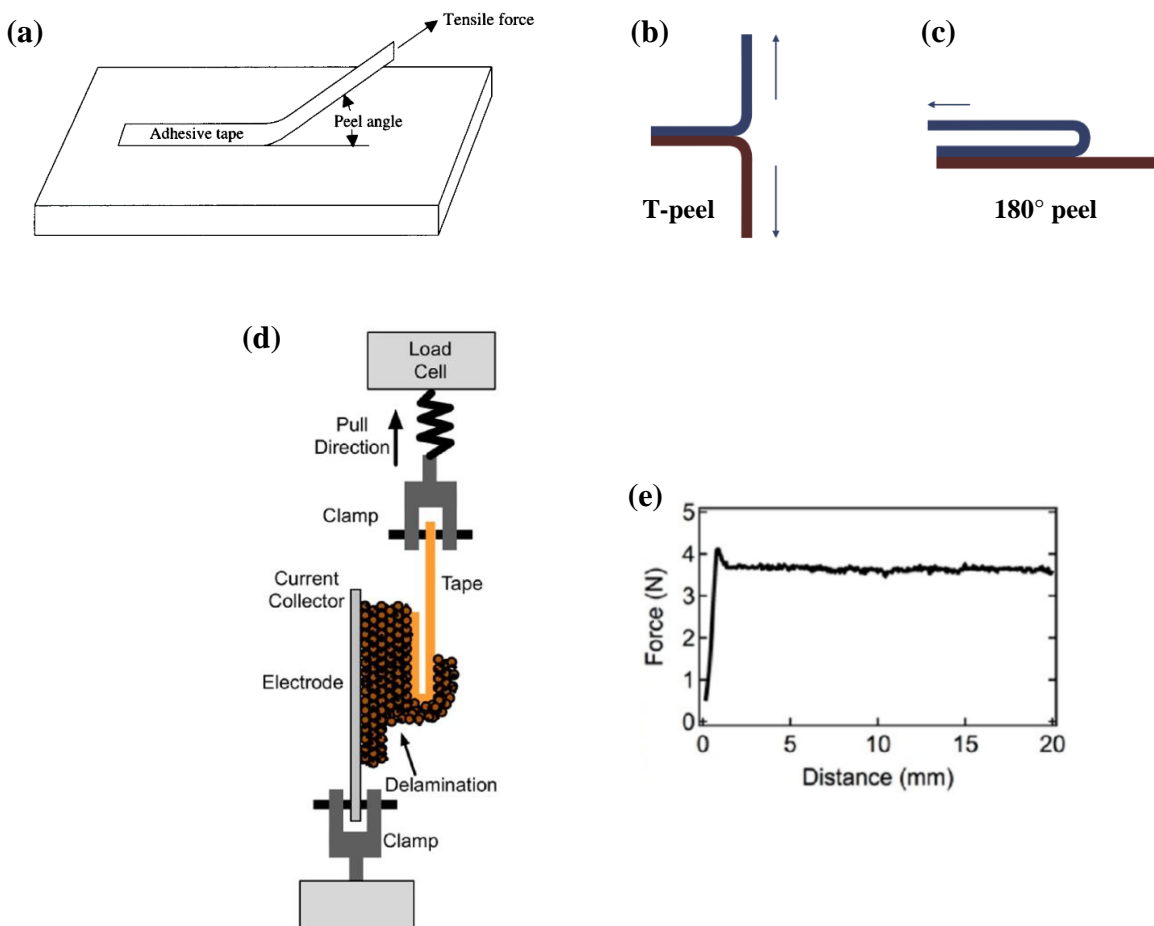


Figure 2.5 Schematic for the peel test, and an example of peel force vs. distance curve obtained from the peel test. (a) Schematic for the peel test. Reproduced with permission from Ref. 98. (b) T-peel test. Reproduced with permission from Ref. 99. (c) 180° peel test. Reproduced with permission from Ref. 99. (d) Schematic of the 180° peel test on an electrode film. Reproduced with permission from Ref. 103. (e) A typical plot of peel force versus distance obtained from the peel test. Reproduced with permission from Ref. 103.

2.2 Electrochemical characterization

2.2.1 Coin cell fabrication

The structure of a coin cell is shown in Figure 2.6. A coin cell consists of (from bottom to top) a bottom cap, a cathode (sulfur or organic materials), a separator (polypropylene membrane), electrolyte (e.g. 1 M LiTFSI in 1:1 DOL/DME), an anode (lithium metal), a spacer, a spring, and a top cap. CR2016, 2025 and 2032 are three commonly used coin cell types for lab-scale testing. CR2032 means the diameter and the thickness of the cell are 20 and 3.2 mm, respectively. For preparing the cathode films, the active material (sulfur or organic materials), conductive carbon and polyvinylidene fluoride (PVDF) binder (at a weight ratio of 5:4:1 or 6:3:1) are mixed in N-methyl-2-pyrrolidone (NMP) solvent to produce a homogeneous slurry. The solid content of the slurry is carefully controlled to ensure the viscosity of the slurry is suitable for coating. Then the slurry is spread uniformly on a carbon-coated aluminum foil by a doctor blade. The coating thickness or wet film thickness is controlled to get the desired areal loading of the active material ($1\sim3\text{ mg cm}^{-2}$) after drying. After coating, the electrode film is dried in an oven at $50\text{ }^{\circ}\text{C}$ overnight. The circular electrode disc with a diameter of 12 mm is punched out from the dried electrode. Then the different coin cell parts are aligned properly (Figure 2.6) and sealed with a battery crimper. The coin cell assembly process is conducted in an argon-filled glovebox with O_2 and H_2O contents below 0.1 ppm.

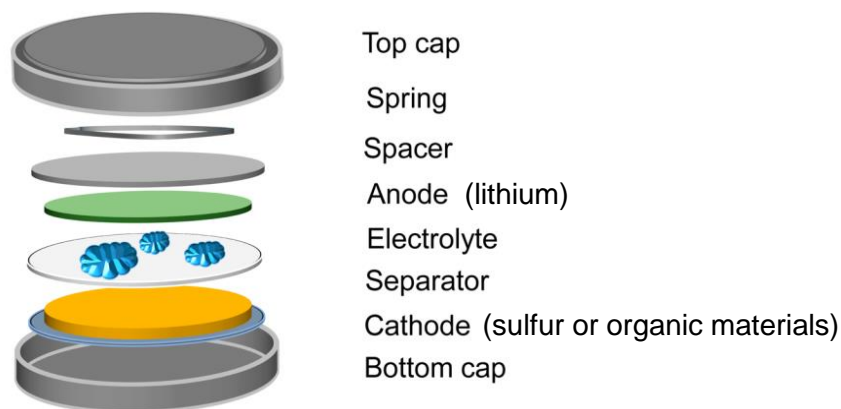


Figure 2.6 Schematic of the structure of a coin cell. Reproduced with permission from Ref. 104.

2.2.2 Cyclic voltammetry (CV)

Cyclic voltammetry is a potentiodynamic electrochemical technique in which the current at the working electrode is plotted against the potential at the working electrode (the applied voltage) to give the cyclic voltammogram trace. The schematic of an electrochemical cell for the CV experiment is shown in Figure 2.7a.¹⁰⁵ In a CV experiment, the electrode potential measured between the working and reference electrodes ramps linearly versus time in a cyclic manner (Figure 2.7b). The rate of potential change versus time is termed as scan rate (unit: V s⁻¹). The current is measured between the working and counter electrodes. During the forward scan from A to D, a linearly increasing potential is applied. Once the oxidation potential of the analyte is reached, the analyte starts to be oxidized causing an anodic current (corresponding to the segment A→C in Figure 2.7c). Upon increasing the applied potential, the anodic current is decreasing due to the depletion of the analyte leading to decreased concentration (corresponding to the segment C→D in Figure 2.7c). If the redox couple is reversible, during the reverse scan from D to G, the oxidized analyte is reduced generating a cathodic current (corresponding to the segment D→G in Figure 2.7c). The more reversible the redox couple is, the more similar in shape the oxidation peak is compared with the reduction peak.

In the battery research area, the CV data can provide rich information on onset potential, peak potential, peak shape, and peak area, which is helpful for the mechanistic understanding of the electrochemical processes. By varying the scan rate during a CV measurement, the Li⁺ diffusion coefficient (D_{Li^+}) of the sulfur or organic cathode can be calculated using the Randles–Sevcik equation: $I_p = 268600n^{\frac{3}{2}}AD_{Li}^{\frac{1}{2}}C_{Li}v^{\frac{1}{2}}$, where I_p is the current maximum in A, n is the number of electrons transferred in the redox process, A is the electrode area in cm², D_{Li} is the diffusion coefficient of Li⁺ in cm² s⁻¹, C_{Li} is the bulk concentration of Li⁺ in mol cm⁻³, v is the scan rate in V s⁻¹. An example showing the features of CV curves under different scan rates is given in Figure 2.7d.¹⁰⁶

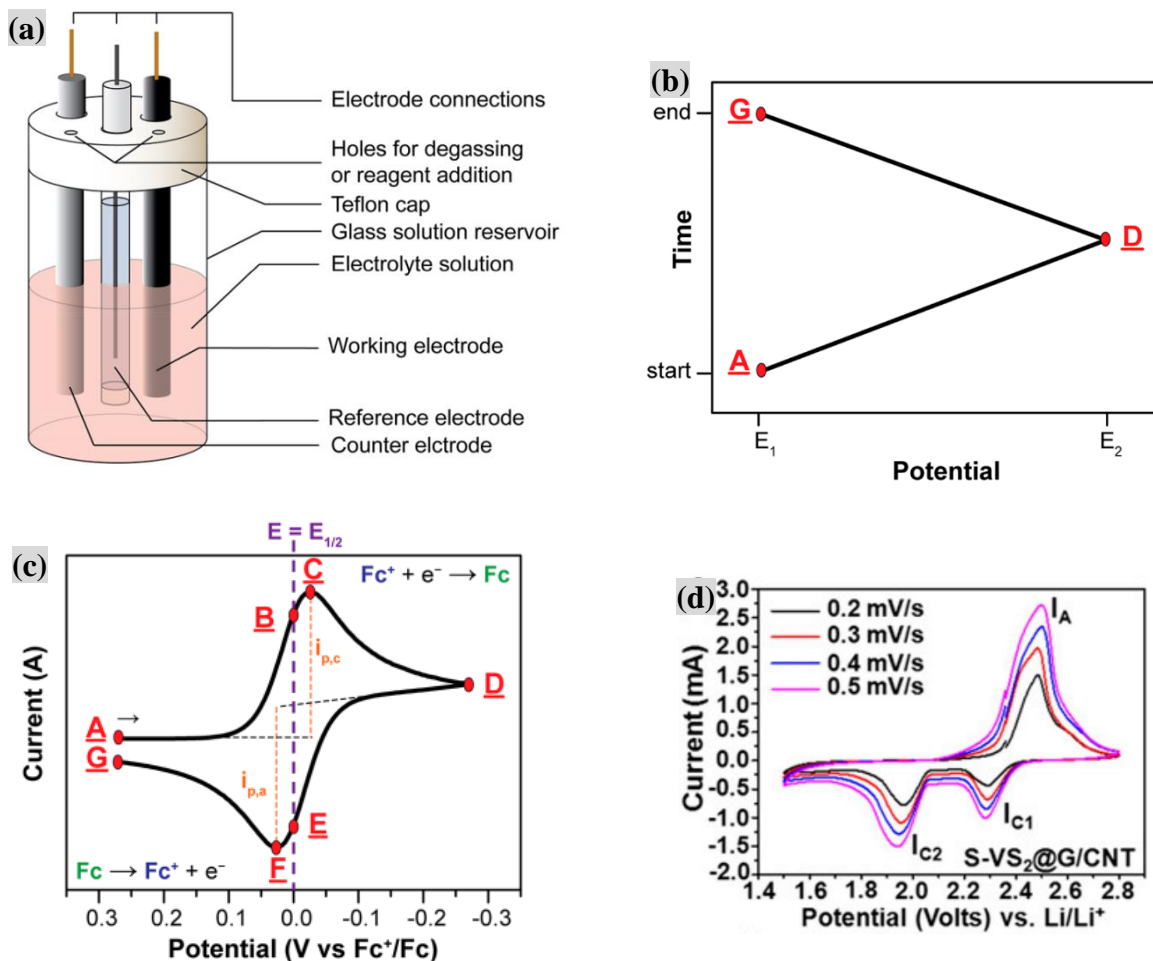


Figure 2.7 Schematic and the potential vs. time curve for the CV testing, an example of the CV data, and an example showing the measurement of D_{Li^+} from CV curves. (a) Schematic of an electrochemical cell for CV experiment. (b) Applied potential vs. time for CV experiment. (c) Cyclic voltammogram for the redox couple (Fc^+/Fc) at the concentration of 1 mM and scan rate of 100 mV s^{-1} . Figures (a-c) are reproduced with permission from Ref. 105. (d) CV curves of the $S-VS_2@G/CNT$ electrode at various scan rates. Reproduced with permission from Ref. 106.

2.2.3 Electrochemical impedance spectroscopy (EIS)

The term impedance refers to the frequency dependent resistance to current flow of a circuit element, e.g. resistor, capacitor, inductor. Impedance $Z_w = \frac{E_w}{I_w}$. The information that an alternating current (AC) technique can provide is much richer than a direct current (DC) or single frequency technique. EIS is able to distinguish between two or more electrochemical processes, identify

diffusion-limited processes, and provide the information on the capacitive behaviors of the system. During EIS measurement, a small sinusoidal perturbation (potential or current) of a fixed frequency is applied, then the response is measured and the impedance at each frequency is computed. The measurement is repeated for a wide range of frequencies, and then the data is plotted and analyzed. The impedance Z is often written as a complex quantity, $Z_{\text{total}} = Z_{\text{real}} + Z_{\text{imaginary}}$. EIS data can be represented as a Bode plot or Complex Plan (Nyquist) plot. In the Nyquist plot, the imaginary part ($Z_{\text{imaginary}}$ or $-Z''$) of the impedance versus the real part (Z_{real} or Z') of the impedance is plotted. Electrochemical cells can be modeled using an equivalent circuit of a number of electrical circuit elements. The EIS response of an equivalent circuit can be compared with the actual EIS data of an electrochemical cell (curve fitting). For an electrochemical cell, double layer capacitance (C_{dl}), electron or charge transfer resistance (R_{ct}), electrolyte resistance (R_e), and Warburg diffusion impedance (W_o) are typically added into the equivalent circuit. Constant phase element (CPE) is used to replace capacitor to model the non-ideal electrode due to the porosity and roughness of the electrode. For cycled sulfur cathode, due to the formation of a solid electrolyte interphase (SEI) and insoluble $\text{Li}_2\text{S}_2/\text{Li}_2\text{S}$ layer on the cathode surface, R_{surf} (or R_{interf}) is often included in the equivalent circuit to depict the surface (or interfacial) resistance for the diffusion of Li^+ through the SEI and the $\text{Li}_2\text{S}_2/\text{Li}_2\text{S}$ layer. An example showing the EIS data and corresponding equivalent circuit is given in Figure 2.8.¹⁰⁷

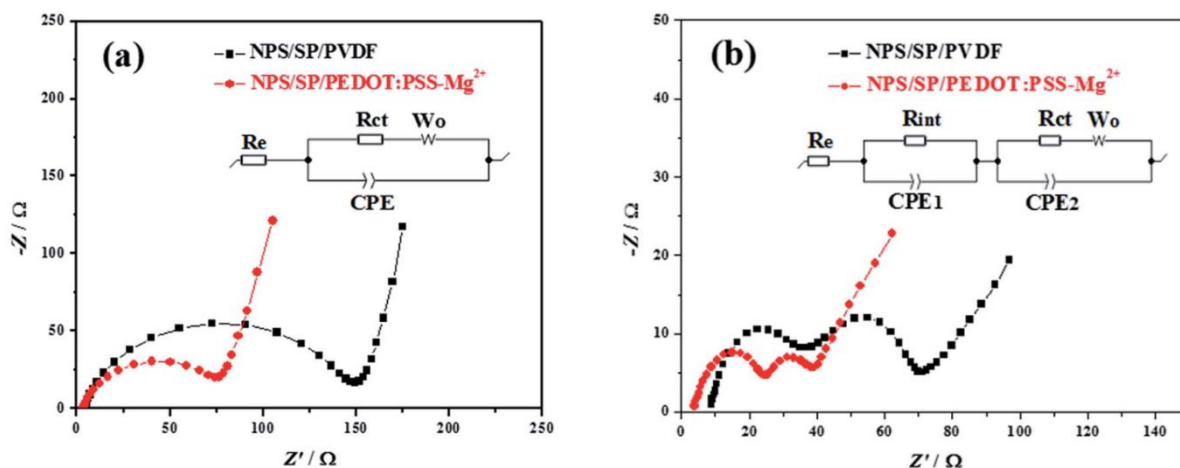


Figure 2.8 An example of the EIS data and the corresponding equivalent circuit models for fitting the EIS data. EIS data of Li-S batteries with NPS/SP/PVDF and NPS/SP/PEDOT:PSS-Mg²⁺ electrodes measured in the charge state: (a) fresh cell and (b) after 10 cycles. The inserts are the equivalent circuits. Reproduced with permission from Ref. 107.

2.2.4 Galvanostatic charge/discharge

Galvanostatic charge/discharge is the most common method to evaluate the electrochemical performance of electrode materials. In this mode, a voltage window is defined (e.g. 1.7~2.8 V for the sulfur cathode) for the test, and then the battery is discharged/charged at a constant current within this voltage window. Three types of plots are typically obtained from galvanostatic charge/discharge. The first one is the plot of voltage versus specific capacity, termed as voltage profile, which can give the information on the different electrochemical processes. Take the sulfur cathode as an example, the plateau at ~2.3 V in the discharge curve corresponds to the conversion of $S_8 \rightarrow Li_2S_4$ while the plateau at ~2.1 V in the discharge curve corresponds to the conversion of $Li_2S_4 \rightarrow Li_2S_2/Li_2S$. The second one is the plot of specific capacity versus cycle number, which can give the information on the cycling stability of an electrode. The third one is the plot of specific capacity versus cycle number at different cycling rates. This plot is obtained by testing the cell at different rates (e.g. 0.1, 0.2, 0.5, 1, 2, 5, 10 C) but with an equal number of cycles. From this plot, the rate performance of a material can be evaluated, which is important for

screening new materials with fast charging/discharging property for commercial applications. An example of these three typical plots is shown in Figure 2.9.¹⁰⁷

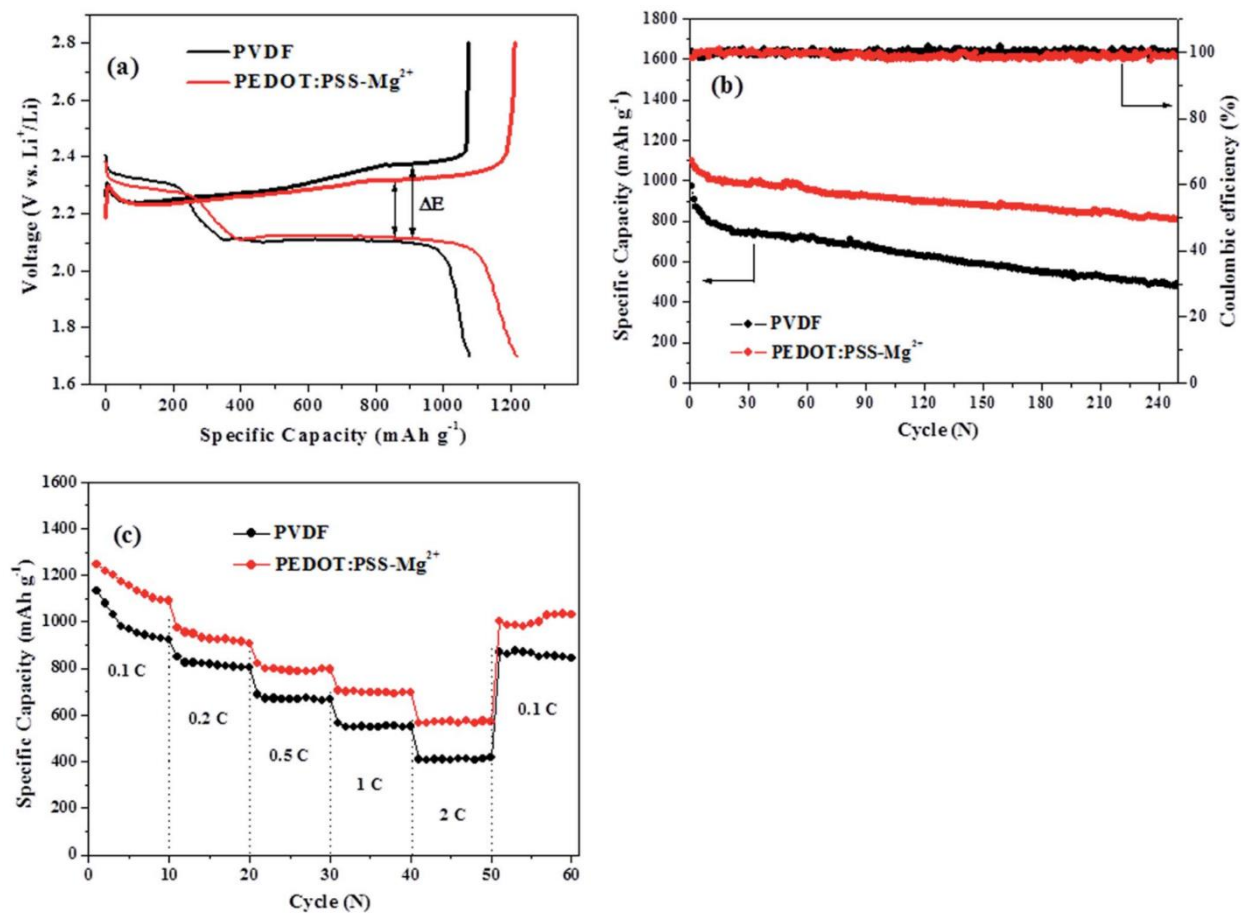


Figure 2.9 An example showing the galvanostatic cycling test. Electrochemical performance of NPS/SP/PVDF and NPS/SP/PEDOT:PSS-Mg²⁺ electrodes: (a) discharge–charge voltage vs. specific capacity profile, (b) cycling performance at 0.5 C, (c) rate performance from 0.1 to 2 C. Reproduced with permission from Ref. 107.

Chapter 3. Ionically Cross-Linked PEDOT:PSS as a Multifunctional Conductive Binder for High-Performance Lithium–Sulfur Batteries

3.1 Introduction

The very high theoretical specific capacity of the sulfur cathode (1675 mA h g^{-1}) allows lithium–sulfur (Li–S) batteries to reach a theoretical energy density of 2600 W h kg^{-1} , which is 6 times that of lithium-ion batteries (LIBs) based on intercalation compounds such as LiCoO_2 and LiFePO_4 .^{108–110} In addition, sulfur is inexpensive, environmentally benign and abundant, making it one of the most promising candidate cathode materials for next-generation high performance batteries.

A typical Li–S battery cathode consists of four components: sulfur, conductive carbon additive, binder, and current collector. The binder is an important ingredient, which binds sulfur and conductive carbon together with the current collector to maintain the structural integrity of the cathode. Compared with other cathode components, the binder has been paid much less attention for the improvement of Li–S battery performance. Poly(vinylidene fluoride) (PVDF) and poly(ethylene oxide) (PEO) are the most commonly used binders for Li–S battery cathodes.¹¹¹ However, these binders are suboptimal for achieving high cycling stability and high capacity of Li–S batteries because (i) they have linear polymer chains and weaker interchain interaction and cannot cushion the large volume change during discharge/charge cycling to retain the structural integrity of the cathode; (ii) they have relatively weak affinity to polysulfides and cannot effectively prevent the shuttling of polysulfides; (iii) they are electrical insulators and make no contribution to the electron transfer. In particular, for high sulfur loading cathode composites ($\text{S}\% \geq 70 \text{ wt}\%$), which are mandatory for high energy density Li–S batteries,^{112,113} the combined amount of the conductive component and binder used would be 20 wt% or less. Therefore, a high-performance binder with high binding strength as well as high electrical conductivity would be ideal. Recently, some efforts have been made to develop new binders to replace PVDF and PEO. For example, Li et al.⁴⁵ used gum arabic (GA) polymer as the binder to improve the capacity and stability. Bhattacharya et al.⁴⁶ reported a polyamidoamine (PAMAM) dendrimer-based binder, which can encapsulate sulfur more effectively. Chen et al.¹⁸ designed a multifunctional cross-linked binder of PEI-HDI with a 3D network structure for stable Li–S batteries. Although these new binders showed better performance than PVDF and PEO, they are electrical insulators and do

not contribute to the improvement of the electrical conductivity of the cathode composite. A few electrically conductive binders such as (reduced) graphene oxide-poly(acrylic acid) (GOPAA),¹¹⁴ PEDOT:PSS,¹¹⁵ PEDOT:PSS-PAA,¹¹⁶ and poly(9,9-dioctylfluorene-co-fluorenone-co-methylbenzoic ester) (PFM)¹¹⁷ have been reported to improve the cathode performance of Li-S batteries. However, Li-S batteries with these conductive binders have not demonstrated both high capacity and high cycling stability for high sulfur loading ($S \geq 70$ wt%) Li-S batteries.

PEDOT:PSS is the most studied and widely used conductive polymer as the electrode for various electronic and electrical devices such as organic thin film transistors, organic photovoltaics, and batteries because it is solution-processable and both electrically (with electrical conductivity of up to 4600 S cm^{-1} and higher)^{118,119} and ionically (with the mobility of K^+ ions of up to $2.2 \times 10^{-3} \text{ cm}^2 \text{ V}^{-1} \text{ s}^{-1}$)¹²⁰ highly conductive. In addition, it has been reported that the oxygen atoms in PEDOT:PSS can strongly bond polysulfides,⁴² which would be beneficial for the improvement of the cathode cycling stability. Despite these advantages, previous studies showed that when PEDOT:PSS alone was used as a binder, very limited improvements in the cathode capacity and cycling stability were obtained.¹¹⁵ A combination of PEDOT:PSS and poly(acrylic acid) (PAA) could improve both the capacity and cycling stability of the cathode.¹¹⁶ It was suggested that PEDOT:PSS facilitated electron transfer and prevented lithium polysulfide dissolution, while PAA improved the swelling properties of the cathode, leading to better lithium ion conduction. An impressive initial specific capacity of 1121 mA h g^{-1} was achieved, but the specific capacity still dropped rather rapidly to 834 mA h g^{-1} (74% of the initial capacity) after 80 cycles.

In this work, we used a very convenient approach to crosslinking PEDOT:PSS to improve the structural stability of the PEDOT:PSS network formed in the Li-S battery cathode. Specifically, we used the divalent Mg^{2+} ion as a cross-linker for PSS in PEDOT:PSS to form a 3-D network binder, PEDOT:PSS- Mg^{2+} , for the Li-S battery cathode. The Li-S batteries using this PEDOT:PSS- Mg^{2+} binder achieved a high initial capacity of 1097 mA h g^{-1} and significantly improved cycling stability with capacity retention of 74% after 250 cycles at 0.5C. Moreover, water was used as the solvent for preparing the cathode, making the fabrication process environmentally friendly.

3.2 Experimental section

3.2.1 Materials and instrumentation

PEDOT:PSS (Clevios PH 1000, 1.2 wt%, with a PEDOT:PSS weight ratio of 1 : 2.5) was obtained from Heraeus, Germany. Magnesium nitrate ($\text{Mg}(\text{NO}_3)_2$, 99%) was supplied by EM Science, Germany. Carbon paper (CP) (TGP-H-090; 0.28 mm) was obtained from Toray, Japan. Super P (SP; 99%) conductive carbon powder was obtained from Timical, Switzerland. All the chemicals were used without further purification. UV-vis spectra were measured with a Shimadzu UV-2501PC spectrometer. The conductivity measurements of PEDOT:PSS and PEDOT:PSS- Mg^{2+} films on glass substrates were conducted using a four-point probe technique with a Signatone Pro-4 and Keithley 2400 source meter.

3.2.2 Detailed experimental procedures

Synthesis of NPS: Nano-particulate sulfur (NPS) was synthesized by a previously reported method.⁴⁴ Aqueous solutions of 80 mM $\text{Na}_2\text{S}_2\text{O}_3$ (50 mL) and 0.4 M PVP (the concentration was based on the repeat unit of PVP) (50 mL) were mixed at room temperature. Then, concentrated hydrochloric acid (0.4 mL, 37%) was added under stirring. After 2 h, the obtained reaction mixture was centrifuged at 4000 rpm for 15 min to isolate the precipitated particles, which were washed with deionized water 5 times and dried in air and then under vacuum at room temperature to give the NPS product. The sulfur content of the NPS is ~99% as determined by thermogravimetric analysis (TGA). The average diameter of the NPS is ~110 nm as estimated from the SEM image.

Preparation of PEDOT:PSS and PEDOT:PSS- Mg^{2+} films: PEDOT:PSS film was prepared by spin coating PEDOT:PSS aqueous solution (1.2 wt%) on glass substrates and dried at 120 °C in a vacuum oven. PEDOT:PSS- Mg^{2+} film was prepared by adding a few drops of $\text{Mg}(\text{NO}_3)_2$ solution (11 mM) onto PEDOT:PSS film, waiting for 1 min, then spin-coating, and then drying at 120 °C in a vacuum oven.

Preparation of cathodes: NPS (0.21 g) was uniformly dispersed in 1.2 wt% PEDOT:PSS aqueous solution (2.3 mL containing ~27.6 mg of PEDOT:PSS) in an ultrasonic bath for 30 min. Then SP (0.06 g) was added and the mixture was homogenized in an ultrasonic bath for an additional 40 min. Subsequently, 0.5 M $\text{Mg}(\text{NO}_3)_2$ solution (50 mL containing 3.7 mg of $\text{Mg}(\text{NO}_3)_2$) was added and the mixture was sonicated for another 30 min. The obtained slurry was blade coated on a CP current collector and dried briefly in air before being transferred to a vacuum oven and heated at

50 °C for 12 h to form the NPS/SP/PEDOT:PSS-Mg²⁺ (NPS/SP/PEDOT:PSS-Mg²⁺ = 70 : 20 : 10 by weight) cathode. The NPS/SP/PVDF cathode using PVDF as the binder was prepared similarly by blade coating a slurry made by mixing NPS, SP, and PVDF at weight ratios of 70 : 20 : 10 in N-methylpyrrolidone (NMP). The cathodes were cut into circular disks with a diameter of 12 mm for the battery assembly. All the cathodes have an areal sulfur loading of 1~1.2 mg cm⁻².

Battery assembly and electrochemical measurements: CR2025 coin cells were assembled in an argon-filled glove box using a CP coated with either the NPS/SP/PEDOT:PSS-Mg²⁺ or NPS/SP/PVDF composite described above as the cathode. Lithium foil, a Celgard 2500 film, and 1 M LiTFSI (LiN(SO₂CF₃)₂) in a 1 : 1 volume of DOL/DME solvent with 2 wt% LiNO₃ (50 μL per cell) were used as the anode, separator, and electrolyte, respectively. Discharge–charge measurements were carried out in a voltage window of 1.7–2.8 V at different current densities at room temperature with a LAND battery tester. The capacities were calculated based on the mass of sulfur in the cathode materials. Electrochemical impedance spectroscopy (EIS) of fresh and cycled (for 10 cycles) batteries in the charged state was conducted on an SP-300 electrochemical workstation (Bio-Logic Science Instrument).

Li₂S₆ adsorption testing of SP, SP/PVDF, SP/PEDOT:PSS, and SP/PEDOT:PSS-Mg²⁺: Li₂S₆ was synthesized by reacting elemental sulfur with Li₂S in a stoichiometric ratio of 5 : 1 in DOL/DME (v/v, 1/1) in a sealed vessel at 80 °C.¹²¹ SP/PVDF, SP/PEDOT:PSS and SP/PEDOT:PSSMg²⁺ composite slurries were prepared as described above for the fabrication of the cathode composites, where the SP/polymer weight ratio was kept at 2 : 1. The slurries were dried in air and then under vacuum at 50 °C for 12 h. After drying, the composites were ground into fine powders in an agate mortar. Next, SP/PVDF composite (10 mg SP + 5 mg PVDF), SP/PEDOT:PSS (10 mg SP + 5 mg PEDOT:PSS), and SP/PEDOT:PSS-Mg²⁺ composite (10 mg SP + 5 mg PEDOT:PSS-Mg²⁺) were added to 3.5 mL of 0.5 mM Li₂S₆ solution, respectively. The mixtures were well mixed by shaking the vials. After being kept for 24 h at room temperature, the clear supernatants were taken for the UV-vis absorption measurements. As a comparison, the Li₂S₆ adsorption of a same amount of SP (10 mg) was also tested.

3.3 Results and discussion

PEDOT:PSS is a commercially available water-soluble polymer, whose chemical structure is shown in Figure 3.1a. A PEDOT:PSS aqueous dispersion consists of PEDOT nanoparticles

wrapped by PSS (polystyrenesulfonic acid), which was added when PEDOT:PSS was synthesized, in order to solubilize PEDOT.^{118,120} PSS is also a dopant, giving away some of its protons to PEDOT to form the PEDOT:PSS complex, which is highly conductive in the solid state. The PEDOT:PSS dispersion, Clevis PH 1000, used in this study can provide films with high electrical conductivity of up to 1000 S cm^{-1} . The PSS:PEDOT weight ratio in this dispersion is 2.5 : 1, indicating that the sulfonic acid $-\text{SO}_2\text{OH}$ groups in PSS is in a large excess. Therefore, we may utilize the extra $-\text{SO}_2\text{OH}$ groups to crosslink the PSS polymer chains. Since PSS molecules strongly interact with PEDOT molecules, cross-linking of PSS could fasten the PEDOT chains to form a robust conductive PEDOT:PSS 3D network. To crosslink the PSS, we chose the divalent cation, Mg^{2+} , as the crosslinker (Figure 3.1). To prepare the cathode material, nano-particulate sulfur (NPS) with an average diameter of $\sim 110 \text{ nm}$ (Figure 3.2) was used as the active cathode material. At room temperature, NPS and a conductive carbon, Super P (SP), were uniformly dispersed in a PEDOT:PSS aqueous solution (1.2 wt%) by ultrasonication and then a small amount of $\text{Mg}(\text{NO}_3)_2$ was added. The mixture was further sonicated to obtain a stable, uniform dispersion with NPS/SP/PEDOT:PSS/ $\text{Mg}(\text{NO}_3)_2$ weight ratio of 70 : 20 : 9 : 1. During mixing, $\text{Mg}(\text{NO}_3)_2$ would react with the $-\text{SO}_2\text{OH}$ groups of PSS, producing the $-\text{SO}_2\text{O}-\text{Mg}-\text{O}-\text{SO}_2-$ linkages resulting in an immediate increase in viscosity. A trace amount of by-product HNO_3 would form, which could be evaporated during drying. Therefore, in the dried film only the Mg^{2+} ion of $\text{Mg}(\text{NO}_3)_2$ would remain, which takes up only 2 wt% of the binder or merely 0.2 wt% of the total cathode material. Even with such a small amount of Mg^{2+} , the Mg^{2+} /PSS repeat unit molar ratio would be ~ 4.3 , which would be sufficient to achieve a high cross-linking density. The as-prepared slurry was blade-coated on Al foil and then dried in a vacuum oven at $50 \text{ }^\circ\text{C}$ for 12 h. The formed NPS/SP/PEDOT:PSS- Mg^{2+} layer was peeled off and subjected to Soxhlet extraction with CS_2 , which is a good solvent for elemental sulfur, to evaluate the sulfur retention ability of this new

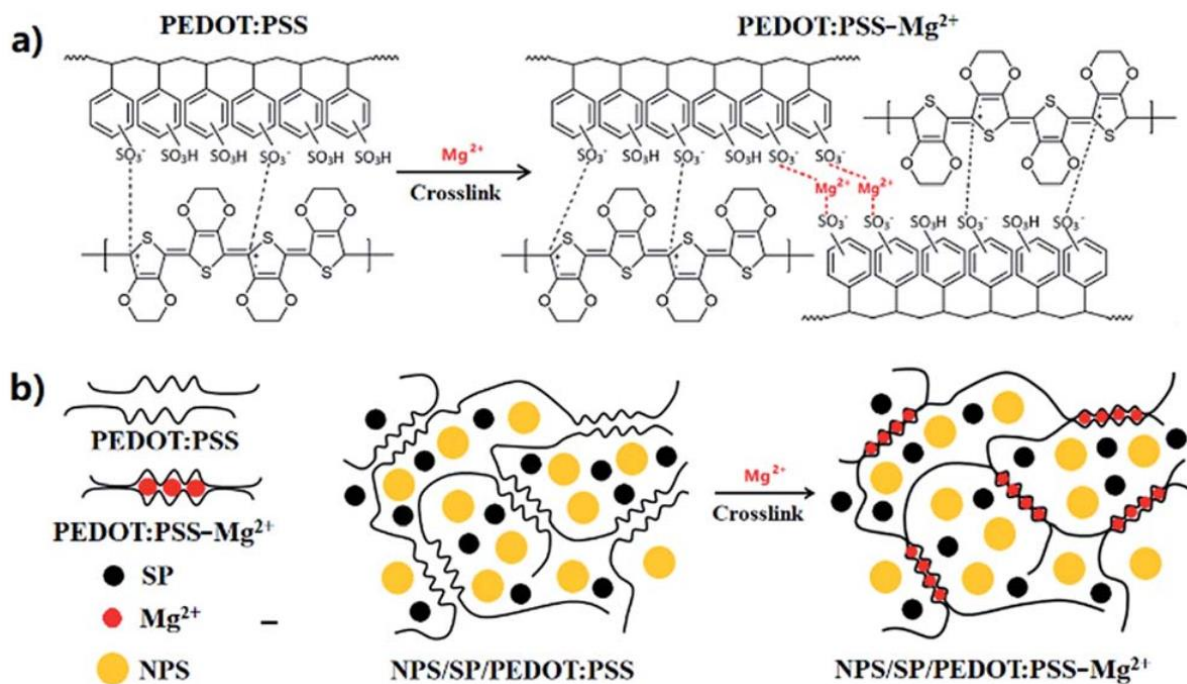


Figure 3.1 Schematic representation of the PEDOT:PSS-Mg²⁺ binder structure and NPS/SP/PEDOT:PSS-Mg²⁺ electrode. The coordination of Mg²⁺ by the SO₃⁻ is the main process in the gel formation and polymer–metal framework stabilization.

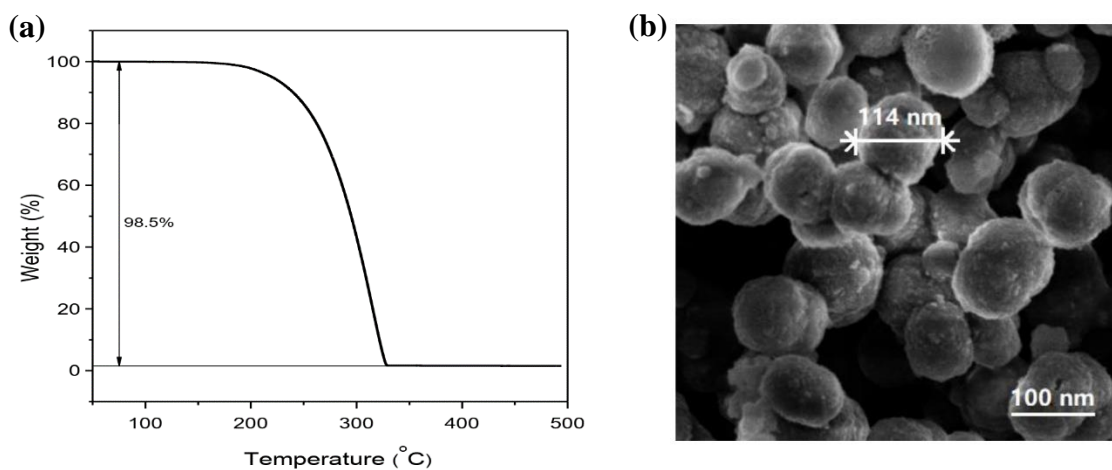


Figure 3.2 (a) TGA, and (b) SEM of nano-particulate sulfur (NPS).

cathode binder. As comparative references, NPS/SP/PVDF and NPS/SP/PEDOT:PSS (without addition of $\text{Mg}(\text{NO}_3)_2$) samples were also prepared and tested. After extensive extraction for 5 h with boiling CS_2 , the NPS/SP/PEDOT:PSS- Mg^{2+} sample retained 14% of the initially loaded sulfur (Table 3.1). On the other hand, sulfur in the NPS/SP/PVDF or the NPS/SP/PEDOT:PSS sample was completely lost after extraction for 5 h. The improved solvent resistance of the NPS/SP/PEDOT:PSS- Mg^{2+} sample against sulfur loss indicates that the PEDOT:PSS- Mg^{2+} binder has a stronger ability to retain elemental sulfur, as a result of the cross-linked binder network. The slurry of NPS + SP + PEDOT:PSS- $\text{Mg}(\text{NO}_3)_2$ or NPS + SP + PVDF cathode material was then coated on a carbon paper (CP) current collector substrate. The coated substrate was dried in a vacuum oven at 50 °C for 12 h, cut into discs, and assembled into CR2025 coin cells to evaluate the electrochemical performance. As aforementioned, with addition of $\text{Mg}(\text{NO}_3)_2$ the viscosity of the NPS + SP + PEDOT:PSS + $\text{Mg}(\text{NO}_3)_2$ slurry increased notably probably due to the electrostatic interaction of Mg^{2+} cations with the pendent $-\text{SO}_2\text{O}^-$ anions of neighboring PSS chains. The appropriately increased viscosity makes this aqueous slurry stable and facilitates its coating on the CP current collector substrate to form a smooth and uniform cathode composite film. In contrast, the slurry of NPS + SP + PEDOT:PSS without the addition of $\text{Mg}(\text{NO}_3)_2$ could not form a stable slurry, rapidly forming precipitates as soon as agitation was stopped. This posed a challenge to coat the slurry on the CP current collector and no properly working battery with the NPS/SP/PEDOT:PSS cathode was obtained in this study. To examine whether the Mg^{2+} -crosslinking affects the conductivity of PEDOT:PSS or not, PEDOT:PSS and cross-linked PEDOT:PSS- Mg^{2+} films (thickness ~80 nm) were prepared and their conductivities were evaluated using a four-point probe method. The average conductivity of PEDOT:PSS films was measured to be 833 S cm^{-1} . After cross-linking by Mg^{2+} , the average conductivity dropped to 668 S cm^{-1} which corresponds to a ~20% decrease. Therefore, the cross-linked PEDOT:PSS- Mg^{2+} films remained highly conductive.

Table 3.1 Sulfur weight losses of cathode materials after Soxhlet extraction with CS₂.

Sample	Weight		Total weight loss	Sulfur weight loss
	Before Soxhlet extraction	After 5 h Soxhlet extraction		
70% NPS/20% SP/10% PVDF	1.0000 g	0.2980 g	70%	100%
70% NPS/20% SP/10% PEDOT:PSS	1.0004 g	0.2998 g	70%	100%
70% NPS/20% SP/10% PEDOT:PSS-Mg ²⁺	1.0010 g	0.3984 g	60%	86%

Figure 3.3a presents the cathode capacity versus voltage profiles during the second discharge/charge cycle of batteries with NPS/SP/PEDOT:PSS-Mg²⁺ and NPS/SP/PVDF cathodes. The NPS/SP/PVDF cathode shows a specific capacity of 1079 mA h g⁻¹ at a discharge rate of 0.1C. Its discharge curve exhibits a typical two-step reduction process with the formation of long lithium polysulfide species (Li₂S_x, x = ~3–8) in the first plateau at ~2.3 V and lithium disulfide (Li₂S₂) and lithium sulfide (Li₂S) in the second plateau at ~2.1 V.^{10,122–125} During the charging process, Li₂S was oxidized to form Li₂S₂ at ~2.2–2.3 V, Li₂S_{3–8} at ~2.3 V and then the final product sulfur (S₈) at ~2.4 V. The NPS/SP/PEDOT:PSS-Mg²⁺ cathode shows a significantly increased specific capacity of 1219 mA h g⁻¹. It also appears that the NPS/SP/PEDOT:PSS-Mg²⁺ cathode exhibits a higher specific capacity (~270 mA h g⁻¹) than the NPS/SP/PVDF electrode (~220 mA h g⁻¹) at the end of the first discharge plateau (Figure 3.3a). This result indicates that the reduction reactions to form the soluble polysulfides (Li₂S_{3–8}) were facilitated by the PEDOT:PSS-Mg²⁺ binder, which might be due to the improved electrical conductivity due to the presence of the conductive PEDOT:PSS-Mg²⁺ binder as well as the stronger interaction of this new binder with soluble polysulfides (to be discussed below). The second discharge plateau at ~2.1 V to form Li₂S₂ and Li₂S is also much longer for the NPS/SP/PEDOT:PSS-Mg²⁺ cathode, indicating that a larger amount of soluble polysulfides were involved in this reduction step. This may be contributed by (1) improved charge transfer by the presence of this conductive binder, (2) the suppressed diffusion of soluble polysulfides (Li₂S_x, where x > 2) due to the 3D network structure and the strong polysulfide-adsorbing ability of the PEDOT:PSS-Mg²⁺ binder. It is noteworthy that a smaller voltage hysteresis (ΔE) was observed for the NPS/SP/PEDOT:PSS-Mg²⁺ cathode, which also suggests that introduction of this conductive binder into the Li–S cathode can promote the reduction of the intermediate polysulfides to Li₂S₂/Li₂S.¹²⁶

The cycling stabilities of cathodes with the PVDF binder and PEDOT:PSS-Mg²⁺ binder at a discharge–charge current rate of 0.5C are shown in Figure 3.3b. The cathode with the PVDF binder shows an initial specific capacity of 973 mA h g⁻¹ and a rapid decrease in capacity to 795 mA h g⁻¹ after only 10 cycles. The capacity further dropped to 495 mA h g⁻¹ after 250 cycles, corresponding to a capacity retention of 51%. On the other hand, the cathode with the PEDOT:PSS-Mg²⁺ binder shows a significantly improved initial specific capacity of 1097 mA h g⁻¹, which is 13% higher than that of the cathode with the PVDF binder. The discharge capacity is maintained at a high value of 807 mA h g⁻¹ after 250 cycles, corresponding to a capacity retention of 74%. As discussed previously, the higher sulfur utilization and better capacity retention of the cathode using the PEDOT:PSS-Mg²⁺ binder compared to the PVDF binder are most likely due to the highly conductive, crosslinked 3-D network structure and strong polysulfide-adsorbing ability of the PEDOT:PSS-Mg²⁺ binder. Moreover, the coulombic efficiency of the NPS/SP/PEDOT:PSS-Mg²⁺ electrode is maintained at > 98% after 250 cycles. The capacities at various C-rates of 0.1C, 0.2C, 0.5C, 1C and 2C of the NPS/SP/PEDOT:PSS-Mg²⁺ and NPS/SP/PVDF cathodes were measured and the results are shown in Figure 3.3c. A highly reversible capacity of 1033 mA h g⁻¹ after 60 cycles was obtained when the C-rate was set back to 0.1C for the cathode with the PEDOT:PSS-Mg²⁺ binder. Highly reversible capacities of ~790 mA h g⁻¹ at 1C and 576 mA h g⁻¹ at 2C were also achieved. As a comparison, the electrode with the PVDF binder exhibits a capacity of 846 mA h g⁻¹ after 60 cycles when the C-rate was set back to 0.1C. At higher C-rates, the capacities decreased to ~550 mA h g⁻¹ at 1C and ~410 mA h g⁻¹ at 2C. Clearly the battery based on the NPS/SP/PEDOT:PSS-Mg²⁺ cathode demonstrated higher specific capacities at all the tested current densities, which results from the improved conductivity and structural stability of the cathode composite due to the use of the PEDOT:PSS-Mg²⁺ binder.

Furthermore, the lithium polysulfide-adsorbing ability of the PEDOT:PSS-Mg²⁺ binder was studied by using UV-vis spectroscopy. Li₂S₆ was chosen as a representative long chain lithium polysulfide, which was synthesized by the reaction of sulfur with Li₂S in a stoichiometric ratio in a mixture solvent of 1,3-dioxolane (DOL)/1,2-dimethoxyethane (DME) (v/v, 1/1).¹²¹ Specifically, an SP/PEDOT:PSS-Mg²⁺ composite with a carbon/polymer weight ratio of 2 : 1 was added to the Li₂S₆ solution and kept for 24 h at room temperature before the clear supernatant was taken out for the UV-vis absorption measurement. For comparison, SP, SP/PVDF composite, and SP/PEDOT:PSS composite were also tested similarly. As shown in Figure 3.3d, the blank Li₂S₆

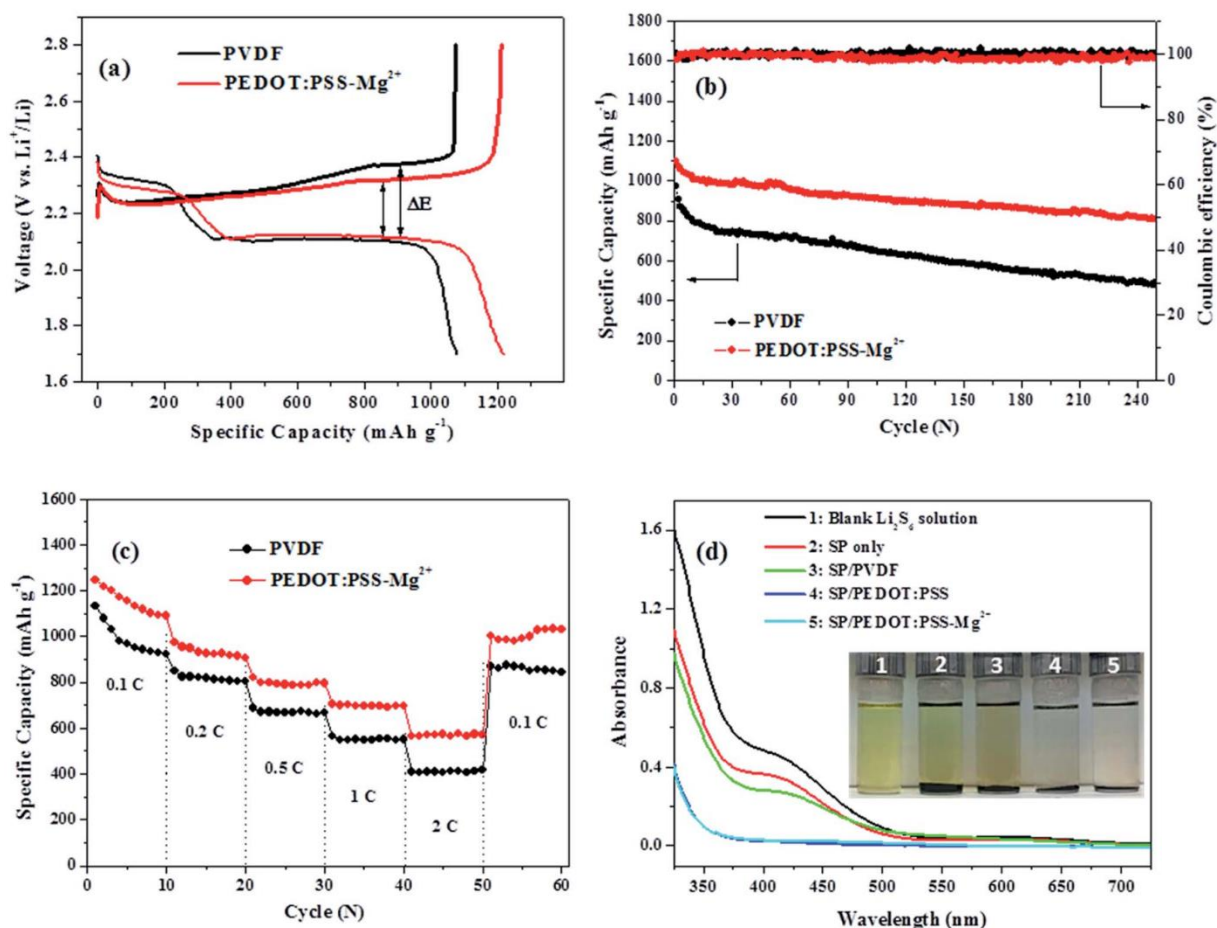


Figure 3.3 Discharge-charge performance of NPS/SP/PVDF and NPS/SP/PEDOT:PSS-Mg²⁺ electrodes. (a) typical discharge-charge voltage vs. capacity profile; (b) cycling performance at 0.5C; (c) rate performance from 0.1C to 2C. (d) UV-vis absorption spectra and photos of the Li₂S₆ solutions in 1,3-dioxolane (DOL)/1,2-dimethoxyethane (DME) (v/v, 1/1) before (blank) and after addition of SP, SP/PVDF, SP/PEDOT:PSS, and SP/PEDOT:PSS-Mg²⁺.

solution showed a shoulder peak at ~400 nm, which is in agreement with that reported in the literature.^{18,121,125} The solution mixed with SP showed a lighter color and its UV-vis spectrum also displayed a decrease in the absorption intensity, indicating that SP has some effect on the adsorption of Li₂S₆. For the sample mixed with SP/PVDF, a further slight drop in the absorption intensity was observed. On the other hand, the solutions mixed with SP/PEDOT:PSS and SP/PEDOT:PSS-Mg²⁺ showed much lighter colors and their UV-vis spectra exhibited a complete

disappearance of absorption at ~400 nm, indicating that almost all the Li_2S_6 species were adsorbed. These results strongly support that the SP/PEDOT:PSS and SP/PEDOT:PSS- Mg^{2+} composites have excellent Li_2S_6 (and probably other lithium polysulfides) adsorption ability, which agrees with the theoretical calculation results that the oxygen atoms in PEDOT can strongly bind lithium polysulfides.⁴² The results also confirmed that the presence of the crosslinking Mg^{2+} ions in SP/PEDOT:PSS- Mg^{2+} does not negatively affect its ability for adsorbing the lithium polysulfides compared to SP/PEDOT:PSS. Therefore, the above UV-vis absorption results further demonstrated that the observed better cycling stability of the NPS/SP/PEDOT:PSS- Mg^{2+} cathode compared to the NPS/SP/PVDF cathode is attributed in part to the stronger lithium polysulfide adsorption ability of the PEDOT:PSS- Mg^{2+} binder than PVDF.

To further examine the contributions of the PEDOT:PSS- Mg^{2+} binder to the enhancement of the battery performance, electrochemical impedance spectroscopy (EIS) measurements were performed on the fresh and cycled batteries with PEDOT:PSS- Mg^{2+} and PVDF binders in the charged state (Figure 3.4). The Nyquist plot of each fresh battery exhibits a semicircle in the high frequency region and an inclined line in the low frequency region (Figure 3.4a), which can be deconvoluted into an equivalent Randles circuit¹²⁷ shown in the inset of Figure 3.4a. The intercept of the semicircle with the Z_{real} (the real part of impedance) axis in the high frequency region corresponds to the resistance of the electrolyte solution (R_e). The semicircle is ascribed to the charge-transfer resistance (R_{ct} , the diameter of the semicircle) and related capacitance (CPE, constant phase element) at the cathode. The inclined line in the low frequency region is associated with the Li^+ diffusion, namely, the Warburg impedance (W_o). As shown in Table 3.2, the fresh battery with the NPS/SP/PEDOT:PSS- Mg^{2+} cathode exhibits a much lower R_{ct} (43.1 Ω) compared to that with the NPS/SP/PVDF cathode (78.0 Ω), indicating that the charge transfer resistance decreased significantly when the conductive PEDOT:PSS- Mg^{2+} binder was used. Since R_{ct} is related to the electronic conduction of the conductive network of the cathode as well as the faradaic charge transfer at the interface of the conductive network and the electrolyte,^{128,129} the results strongly indicate that the use of the conductive PEDOT:PSS- Mg^{2+} binder is very effective to reduce the R_{ct} . After cycling, both batteries showed two semicircles (Figure 3.4b), where the semicircle in the high-to-middle frequency region (right) is due to the charge-transfer resistance (R_{ct}) and capacitance (CPE_2) of the cathode, while the semicircle in the high frequency region (left) can be ascribed to the interfacial contact resistance (R_{int})/capacitance (CPE_1) between the

electrolyte and the cathode.^{127,129,130} The semicircle that newly appeared in the high frequency region is mainly due to the formation of an insulating layer (sulfur and some non-oxidized insoluble $\text{Li}_2\text{S}_2/\text{Li}_2\text{S}$ after charging) on the surface of the cathode current collector (CP). The absence of this semicircle in the Nyquist plots for the fresh batteries is probably due to the fact that part of the CP surface was not covered by the active cathode composite and was able to be in direct contact with the electrolyte solution. The battery with the NPS/SP/PEDOT:PSS- Mg^{2+} cathode showed a lower R_{int} of 13.4Ω than that of the battery with the NPS/SP/PVDF cathode (17.3Ω), indicating that the PEDOT:PSS- Mg^{2+} binder in the newly formed layer on the CP surface after cycling can effectively reduce the resistance of this interlayer. Another possible contribution for the appearance of the high-frequency semicircle after cycling might be the deposition of insoluble $\text{Li}_2\text{S}_2/\text{Li}_2\text{S}$ on the anode (Li) surface as a result of the diffusion of polysulfides from the cathode, followed by reduction by Li. Therefore, the lower R_{int} observed for the battery with the NPS/SP/PEDOT:PSS- Mg^{2+} cathode might also partially result from the stronger ability of the PEDOT:PSS- Mg^{2+} binder to trap soluble polysulfides within the cathode. For both batteries, the R_{ct} decreased notably, revealing that the surface electrochemical activity is initiated during the discharge–charge processes.¹²⁷ As observed for their fresh batteries, the R_{ct} of the cycled battery with the NPS/SP/PEDOT:PSS- Mg^{2+} cathode (12.4Ω) is still much lower than that of the battery with the NPS/SP/PVDF cathode (24.7Ω), which again manifests the enhanced charge transfer by the conductive PEDOT:PSS- Mg^{2+} binder. It is also noticed that the R_{e} of the battery with the NPS/SP/PVDF cathode obviously increased from 3.6Ω to 8.4Ω after cycling, which might be caused by the increased viscosity of the electrolyte solution and thus lowered ion mobility due to the presence of unreacted polysulfides in the electrolyte.¹²⁷ For the battery with the NPS/SP/PEDOT:PSS- Mg^{2+} cathode, the R_{e} remained almost the same (from 3.3Ω to 3.5Ω) after cycling, which can be accounted for by the presence of much less unreacted polysulfides in the electrolyte as supported by the UV-vis absorption spectroscopy experiments (Figure 3.4d). Overall, the impedance of the NPS/SP/PEDOT:PSS- Mg^{2+} cathode is significantly decreased owing to the application of the conductive cross-linked PEDOT:PSS- Mg^{2+} binder, which supports the improved discharge–charge performance as shown in Figure 3.3.

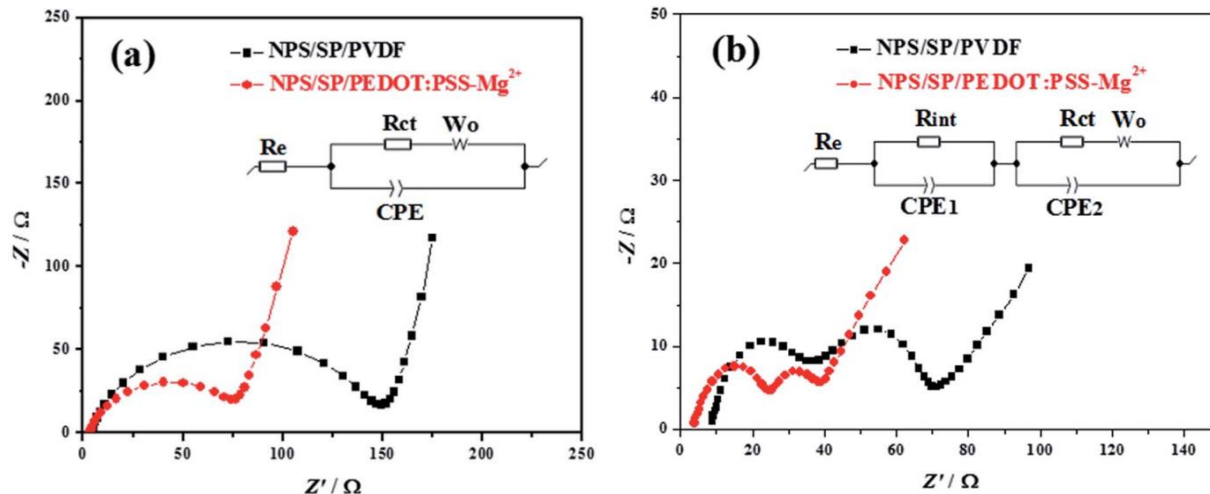


Figure 3.4 EIS data of Li-S batteries with NPS/SP/PVDF and NPS/SP/PEDOT:PSS-Mg²⁺ electrodes measured in the charge state. (a) fresh cells and (b) after 10 cycles.

Table 3.2 Electrode resistance (EIS) obtained from the equivalent circuit fitting of experimental data.

Cathode	Cycle	R _e (Ω)	R _{ct} (Ω)	R _{int} (Ω)
NPS/SP/PVDF	Fresh cell	3.6	78.0	—
	10 th	8.4	24.7	17.3
NPS/SP/PEDOT:PSS-Mg ²⁺	Fresh cell	3.3	43.1	—
	10 th	3.5	12.4	13.4

3.4 Conclusions

In summary, a multi-functional PEDOT:PSS-Mg²⁺ binder formed by cross-linking PEDOT:PSS with Mg²⁺ was developed for the sulfur cathode in Li-S batteries. This new binder has high electrical conductivity, a robust 3-D network structure achieved by the cross-linking of PSS with Mg²⁺ ions, and a strong binding ability toward lithium polysulfides due to the strong interaction between the oxygen atoms in PEDOT and lithium polysulfides. These functionalities can increase the conduction and charge transfer reactions, cushion the drastic volume change during discharge/charge cycling, and trap the soluble lithium polysulfides in the cathode. The Li-

S battery with a cathode using this new binder exhibited an initial capacity of 1097 mA h g⁻¹ and capacity retention of 74% over 250 cycles at 0.5C, which are significant improvements compared with the Li-S battery using a conventional PVDF binder. Moreover, the preparation of the cathode slurry and the subsequent cathode fabrication using the PEDOT:PSS-Mg²⁺ binder uses water present in the PEDOT:PSS dispersion as the only dispersing solvent, which eliminates the use of any organic solvent, making the fabrication of Li-S batteries more environmentally friendly. Therefore, this study demonstrated that the cross-linked PEDOT:PSS-Mg²⁺ is a very promising new binder for high-performance Li-S batteries.

Chapter 4. Electropolymerized PEDOT for Enhancing the Performances of Sulfur and Lithium Iron Phosphate Cathodes

4.1 Introduction

Sulfur cathode is a promising candidate to replace the conventional cathodes based on intercalation compounds such as LiCoO_2 and $\text{LiNi}_x\text{Co}_y\text{Mn}_z\text{O}_2$ and LiFePO_4 . Nanocomposite formation with inorganic conductors, such as CMK-3,²¹ CNTs,³⁷ graphene,¹³¹ and Mxene,¹³² has significantly improved the performance of sulfur cathode. Organic conductors or conductive polymers (CPs), such as poly(3,4-ethylenedioxythiophene) (PEDOT), polypyrrole (PPy), and polyaniline (PANI), have also attracted considerable attention for enhancing the performance of sulfur cathode. CPs have numerous advantages including mild synthesis and processing conditions, chemical and structural diversity, high conductivity (up to $\sim 10^2\text{--}10^3 \text{ S cm}^{-1}$), and excellent mechanical properties.^{133,134} Moreover, some CPs such as PEDOT and PPy possess abundant polar heteroatoms (oxygen and nitrogen, respectively), which have better polysulfide absorption capabilities compared to non-polar carbon-based conductors.¹³⁵ CPs have been employed in Li-S batteries as cathode binders,^{116,136,137} and conductive coatings on sulfur particles,¹³⁸ sulfur/carbon composites,^{139,140} the top surface of sulfur cathodes,^{141,142} current collectors¹⁴³ and separators.^{143,144} Improved stability and in some cases enhanced rate performance of the sulfur cathode have been achieved due to the incorporation of CPs.

Electropolymerization (e-polymerization) has been a widely adopted method to produce various CPs due to its simplicity and ease of implementation. A rechargeable battery, which is essentially an electrochemical device, may be used as a reactor for the in-situ polymerization of a monomer to form a CP inside the battery. This “in-cell” (inside a battery) polymerization method would greatly simplify the incorporation of a CP into a battery and result in more tightly integrated interfaces with other components of the battery. Recently, in-cell ring-opening polymerization of a liquid electrolyte solvent to form a solid or gel polymer electrolyte was reported, which significantly lowered the interfacial resistances and promoted uniform lithium deposition.^{145–148} However, the utilization of in-cell e-polymerization to form a CP inside a battery has not been reported yet.^{145–148}

In this chapter, the in-cell e-polymerization of 3,4-ethylenedioxythiophene (EDOT) to form a CP, ePEDOT, as a binder at the cathode inside a Li–S battery was demonstrated. The battery with ePEDOT:PSS (poly(styrene sulfonate)) showed enhanced specific capacity and cycling stability in comparison to the battery with the commercial PEDOT:PSS (cPEDOT:PSS) binder, which is attributed to the tightly integrated interfaces of ePEDOT:PSS with other components in the sulfur cathode. Our study demonstrated the feasibility of using in-cell e-polymerization to produce CPs in rechargeable batteries to boost the battery performance.

Moreover, our study revealed that the initially doped conductive PEDOT is de-doped to become less conductive during the battery discharging process and could not be fully re-doped during the following charging process within the typical potential window of 1.7–2.8 V for Li–S batteries. Our finding has provided new insights into the role of CPs during battery cycling, where the CPs may not contribute to the improvement of the electrical conductivity of the cathode as significantly as expected previously.

Lastly, the electropolymerized PEDOT was applied in the lithium iron phosphate (LiFePO₄, LFP) cathode. Reduced polarization and improved specific capacity were obtained at the high rate of 1 C after the ePEDOT modification.

4.2 Experimental section

4.2.1 Materials and instrumentation

Sublimed sulfur (Fluka), Super P (TIMCAL), carbon paper (Toray, TGP-H-060), transparent and conductive indium-doped tin oxide (ITO) coated glass substrates (Delta Technologies), poly(4-styrenesulfonic acid) (H-PSS, Sigma-Aldrich, Mw ~75000, 18 wt% in H₂O), 3,4-ethylenedioxythiophene (EDOT, Sigma-Aldrich), high conductivity commercial PEDOT:PSS (cPEDOT:PSS) (PH 1000, 1.1 wt% dispersion in H₂O, Ossila), and the battery electrolyte, 1 M LiTFSI in 1 : 1 (v : v) 1,3-dioxolane(DOL)/1,2-dimethoxyethane (DME) with 2 wt% LiNO₃ was purchased from Suzhou Fosai and used as received. Poly(4-styrenesulfonate) lithium salt (Li-PSS) was prepared by neutralizing H-PSS with lithium hydroxide. EDOT was dissolved in the electrolyte (1 M LiTFSI in 1 : 1 (v : v) DOL/DME with 2 wt% LiNO₃) to prepare a 60 mM EDOT-containing electrolyte solution. Cyclic voltammetry (CV) and chronoamperometry (CA) measurements were performed using a CHI 604E electrochemical workstation or a VMP3 Bio-Logic potentiostat. The electrochemical impedance spectroscopy (EIS)

measurement was carried out using a VMP3 Bio-Logic potentiostat with a 5 mV amplitude in the frequency range from 100 kHz to 100 mHz. The EIS data were fitted using the ZView software. The ultraviolet–visible–near infrared (UV–Vis–NIR) spectra were recorded using an Agilent Cary 7000 spectrophotometer. Galvanostatic cycling of batteries was performed using a LAND CT2001A battery tester. The peel test was performed using a Universal Macro-Tribometer (UNMT-2MT, Centre for Tribology Inc.) equipped with a 1 kg load cell.

4.2.2 Detailed experimental procedures

General procedures for fabricating coin cells. CR2032 coin cells composed of the cathode (on ITO, carbon paper, or carbon-coated Al substrate), Celgard 2500 separator, electrolyte, and lithium foil anode were assembled inside an argon (Ar)-filled glovebox with both O₂ and H₂O levels below 0.1 ppm. Characterization and e-polymerization of the cells were carried out outside the glove box under ambient conditions. Some of the cells were disassembled inside the Ar-filled glovebox for further experiments.

Electrolyte stability studies using linear sweep voltammetry (LSV). A coin cell composed of carbon paper, a lithium foil, and 40 mL of the electrolyte (1 M LiTFSI in 1 : 1 (v : v) DOL/DME with 2 wt% LiNO₃) was assembled inside an Ar-filled glovebox. The cell was scanned in the LSV mode from the open circuit potential (OCP) to 5 V vs. Li/Li⁺ at a scan rate of 1 mV s⁻¹.

In-cell e-polymerization of EDOT on the ITO electrode via CV and characterization of the as-prepared ePEDOT using UV–Vis–NIR spectroscopy. An ITO-coated glass substrate was paired with a lithium foil to construct a coin cell, which was filled with 20 mL of 60 mM EDOT-containing (or EDOT-free for comparison) electrolyte. The edges of the ITO substrate were wrapped with a small piece of an Al foil to make the electrical contact with the cathode case. The cell was scanned in the CV mode in a potential range of 3–4.2 V vs. Li/Li⁺ at a scan rate of 20 mV s⁻¹ for ten cycles to carry out e-polymerization. The EIS spectrum of the cell was measured immediately after each CV cycle. The cell was disassembled, and the ITO substrate onto which ePEDOT was deposited was taken out, washed with DME and isopropanol, and dried with N₂ gas, followed by the UV–Vis–NIR spectroscopy measurement. The as-prepared ePEDOT was dedoped by covering the film with ethylenediamine and heating it at 90 °C on a hot plate for 20 min. The film was washed with DI water, dried under a nitrogen flow, and measured using UV–Vis–NIR

spectroscopy again. For comparison, the cPEDOT:PSS film on the ITO substrate was prepared by drop-casting using the commercial PEDOT:PSS solution. The cPEDOT:PSS film was dedoped in the same way as ePEDOT.

e-Polymerization on the carbon paper electrode by CA. A carbon paper substrate was paired with a lithium foil to construct a coin cell, which was filled with 40 mL of 60 mM EDOT-containing electrolyte. A constant potential chosen in the range from 3.8 to 4.4 V vs. Li/Li⁺ was applied to the cell for 800 s to carry out e-polymerization.

E-Polymerization on the carbon-coated Al electrode by CA and determination of the yield for the e-polymerization. A mixture of Super P and H-PSS in a weight ratio of 4 : 1 was ground in a water/ethanol (w : w = 9 : 1) mixture to form a uniform slurry, which was coated on a carbon-coated Al foil by doctor blading. The substrate was dried at 50 °C overnight and then cut into disks (~12 mm in diameter), which were used to assemble coin cells with Celgard 2500, a lithium foil, and 20 mL of 60 mM EDOT-containing electrolyte for each cell. The cells were subjected to e-polymerization using the CA method at 4.1 V for 800 s. After e-polymerization, the cell was disassembled, and all the cell parts were soaked in 3 mL of DME. Then, a known amount of the supernatant was evacuated using a Rotovap to remove the majority of the DME solvent. The residue was diluted with 3 mL of deionized water, which was subjected to the UV-vis absorption measurement. The amount of unreacted EDOT in the cell after polymerization was then calculated using the pre-determined molar absorptivity of EDOT.

To collect the CV data, the cell containing the e-polymerized ePEDOT:H-PSS was measured directly without being disassembled in the potential range of 1.7–3.9 V vs. Li/Li⁺ at a scan rate of 1 mV s⁻¹. For comparison, a Super P/cPEDOT:PSS (weight ratio of 4 : 1) substrate was also fabricated by coating the slurry on a carbon-coated Al foil to assemble a coin cell with the EDOT-free electrolyte. The cell was tested using the same potential range and scan rate.

Preparation and characterization of Li-S batteries. A S/Super P composite was prepared by mixing sublimed sulfur with Super P in a weight ratio of 65 : 35 in an agate mortar, followed by heating at 155 °C for 17 h in a sealed Teflon-lined stainless steel container. The S/Super P composite, additional Super P, and Li-PSS or H-PSS binder in a weight ratio of 77 : 13 : 10 were ground in a water/ethanol (w : w = 9 : 1) mixture to form a uniform slurry, which was coated on a carbon-coated Al foil by doctor blading. For comparison, a sulfur cathode containing

10 wt% cPEDOT:PSS as the binder was also prepared using the same method. The electrode films were then dried at 50 °C overnight and cut into disks with a diameter of 12 mm. The weight ratio of sulfur : Super P : binder in the cathode was 5 : 4 : 1. The areal sulfur loading in the electrode was 0.9–1.1 mg cm⁻². Coin cells were then assembled using the above cathode, 20 mL of the electrolyte (with or without EDOT) for each cell, and the lithium foil anode. The e-polymerization of EDOT inside the cell was performed using the CA method at 4.10 V vs. Li/Li⁺ for 800 s. The EIS data of the cell were acquired before and immediately after e-polymerization. The CV data of sulfur cathodes were measured in the potential range of 1.7–2.8 V at a scan rate of 0.1 mV s⁻¹. Galvanostatic cycling of Li–S cells was performed in the potential range of 1.7–2.8 V at room temperature.

180° peel tests on ePEDOT:H-PSS and cPEDOT:PSS binders. Sulfur cathodes using the ePEDOT:H-PSS or cPEDOT:PSS binder were prepared as described above. The cathode film disk (diameter: 12 mm) was attached to a glass slide using a double-sided tape. Then, a one-sided tape (width: 8 mm) was firmly attached to the cathode film. Then, the tape was pulled at an angle of 180° with a constant speed of 100 μm s⁻¹ using a mechanical tester. The middle square part (8 mm × 8 mm) of the cathode film was used to obtain the load force vs. displacement curve. Before and after the peel test, optical images of the cathode film and the tape were taken using a microscope for comparison.

Study of the conductivity–potential dependence of ePEDOT using combined CV and EIS. An ITO substrate was paired with a lithium foil to fabricate a coin cell, which was filled with 20 mL of 60 mM EDOT-containing electrolyte. e-Polymerization was performed using the CA method at 4.10 V vs. Li/Li⁺ for 800 s. Then, the cell was subjected to CV cycling between 1.7 and 3.36 V vs. Li/Li⁺ for 20 cycles until the CV diagram was stabilized. Afterwards, four more CV cycles were applied to the same cell. During each cycle, the cell was switched from the CV testing mode to the EIS testing mode at potentials of 1.7 and 3.36 V, respectively. Finally, such testing was conducted for an additional CV cycle by switching from the CV to the EIS mode at more potential points of 1.7, 2.34, 2.43, 2.8, and 3.36 V during the oxidation process and 2.8, 2.28, 1.93, and 1.7 V during the reverse reduction process. All the obtained EIS spectra were fitted to obtain the R_{ct} values using ZView. The CV and EIS measurements and automatic switching from CV to EIS were performed using a VMP3 Bio-Logic potentiostat.

E-polymerization of EDOT on the surface of lithium iron phosphate (LFP) cathode. LFP cathode film was prepared by a slurry coating process using LFP, Super P and PVDF in a weight ratio of 8:1:1. The areal loading of LFP was 2.7 mg cm^{-2} . The e-polymerization was conducted in a similar way as that on the sulfur cathode except that the electrolyte was replaced with 1 M LiPF_6 in 1:1:1 (volume ratio) ethylene carbonate (EC)/ethyl methyl carbonate (EMC)/dimethyl carbonate (DMC), which is a standard electrolyte for LFP cathode.

4.3 Results and discussion

4.3.1 e-Polymerization of EDOT via cyclic voltammetry

Cyclic voltammetry (CV) and chronoamperometry (CA)^{149,150} are two commonly used electrochemical methods for the preparation of PEDOT and other CPs. First, the CV method was employed in this study. Prior to e-polymerization, the electrochemical stability of the electrolyte (1 M LiTFSI in 1 : 1 (v : v) DOL/DME with 2 wt% LiNO_3) was examined using the linear sweep voltammetry (LSV) method using a coin cell with carbon paper and a lithium foil as electrodes in the potential range from the open circuit potential to 5 V vs. Li^+/Li . As shown in Figure 4.1, the current starts to increase abruptly at 4.56 V due to electrolyte decomposition, which signifies the upper potential limit for e-polymerization.

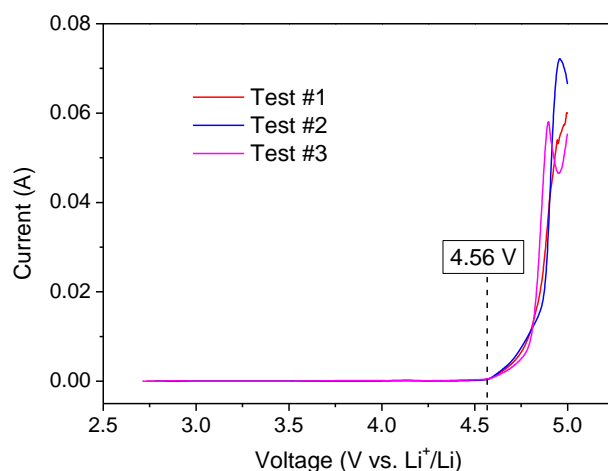


Figure 4.1 Linear sweep voltammetry (LSV) curves of the electrolyte, 1 M LiTFSI in 1:1 (v/v) DOL/DME with 2 wt% LiNO₃. Carbon paper was used as the working electrode. Three tests were performed.

Next, a conductive ITO-coated glass substrate was paired with a lithium foil in a coin cell for e-polymerization of EDOT, in which the transparent ITO substrate would allow the UV–vis measurement of the formed polymer, ePEDOT. A 60 mM EDOT solution was prepared by adding EDOT to 1 M LiTFSI in 1 : 1 (v : v) DOL/DME with 2 wt% LiNO₃. The coin cell loaded with the EDOT-containing electrolyte was scanned in a potential window between the open circuit voltage (~3 V) and 4.2 V vs. Li⁺/Li in the CV mode at a scan rate of 20 mV s⁻¹ for up to 10 cycles. For comparison, another coin cell loaded with the EDOT-free electrolyte was tested under the same conditions. The cyclic voltammograms for the 1st cycles of the two cells are shown in Figure 4.2a. A notable oxidation process is observed for the cell using the EDOT-containing electrolyte, in stark contrast to the irresponsive flat line obtained for the cell containing the EDOT-free electrolyte. For the cell with the EDOT-containing electrolyte, the current starts to increase sharply when the potential is above ~4.1 V, indicating the start of the oxidation (e-polymerization) of EDOT. It is noteworthy that the current is higher during the early reverse scan than that during the forward scan, leading to a crossover at 3.99 V. This phenomenon indicates that the deposition of the polymer proceeds through a nucleation-and-growth mechanism, which has been observed in e-polymerizations for preparing various CPs.^{151,152} The electrochemical impedance spectroscopy (EIS) spectra of the electrode after different numbers of CV cycles are shown in Figure 4.2b. Before e-polymerization, Warburg diffusion behaviour (an oblique line) dominates in the EIS

spectrum. Once the deposition of PEDOT begins, a semicircle together with an oblique tail shows up. By fitting the EIS spectra using the equivalent circuit model shown in Figure 4.2c, R_s , R_{ct} , W_o and CPE, which represent the solution resistance, charge transfer resistance, Warburg diffusion impedance and constant phase element, respectively, can be obtained.^{153,154} The R_{ct} values after different numbers of CV cycles are plotted in Figure 4.2c. As R_{ct} is strongly related to the conductivity of the electrode, the change in R_{ct} can be related to the deposition of the PEDOT layer on the ITO substrate. As the number of CV cycles is increased from 1 to 5, the R_{ct} continuously drops from 244 to 61 Ω , i.e., the conductivity increases. This can be explained by the gradual growth of PEDOT from the initially formed isolated PEDOT nuclei to the final continuous PEDOT film on the ITO substrate, leading to a gradual increase in conductivity with increasing the number of CV cycles.¹⁵⁵ The R_{ct} of the electrode at the 10th CV cycle is similar to that measured at the 5th CV cycle, which indicates that the polymerization is almost completed after 5 CV cycles to form the polymer ePEDOT. The ePEDOT-bearing ITO substrate after 10 CV cycles was taken out of the coin cell, washed with DME and isopropanol, dried with N_2 gas, and subjected to the UV–Vis–NIR spectroscopy measurement. As shown in Figure 4.2d, the as-prepared ePEDOT shows a strong, flat absorption profile starting from 540 nm and extending into the near-IR region, indicating the formation of doped PEDOT on the ITO substrate. The broad bands centered at 970 nm and from 1360 to 2000 nm are attributed to the polaron (radical cation) and bipolaron (dication) charge carriers, respectively.^{156–158} Next, the as-prepared ePEDOT on the ITO substrate was dedoped by treatment with ethylenediamine. The dedoped ePEDOT shows a distinct peak at 572 nm, which can be ascribed to the characteristic p–p* electronic transition of the neutral PEDOT,¹⁵⁸ as well as decreased polaron and bipolaron absorption bands. For comparison, the UV–Vis–NIR spectra of the doped (as-coated) and dedoped cPEDOT:PSS were also measured (Figure 4.2d). The as-coated cPEDOT:PSS on the ITO substrate exhibits a sloping absorption curve from 350 to 2000 nm, indicating that bipolarons are the main charge carriers. The difference in the distribution of polarons and dipolarons between the as-prepared ePEDOT and the coated cPEDOT:PSS may be due to the difference in counterion (TFSI⁻ vs. PSS⁻) and polymer molecular weight. The dedoped cPEDOT showed a p–p* electronic transition peak at 615 nm, an intensified polaron absorption band centered at 982 nm, and a weakened bipolaron band from 1360 to 2000 nm, which is consistent with the literature.^{156,157} The aforementioned UV–Vis–NIR data confirm the formation of doped PEDOT, ePEDOT, after e-polymerization.

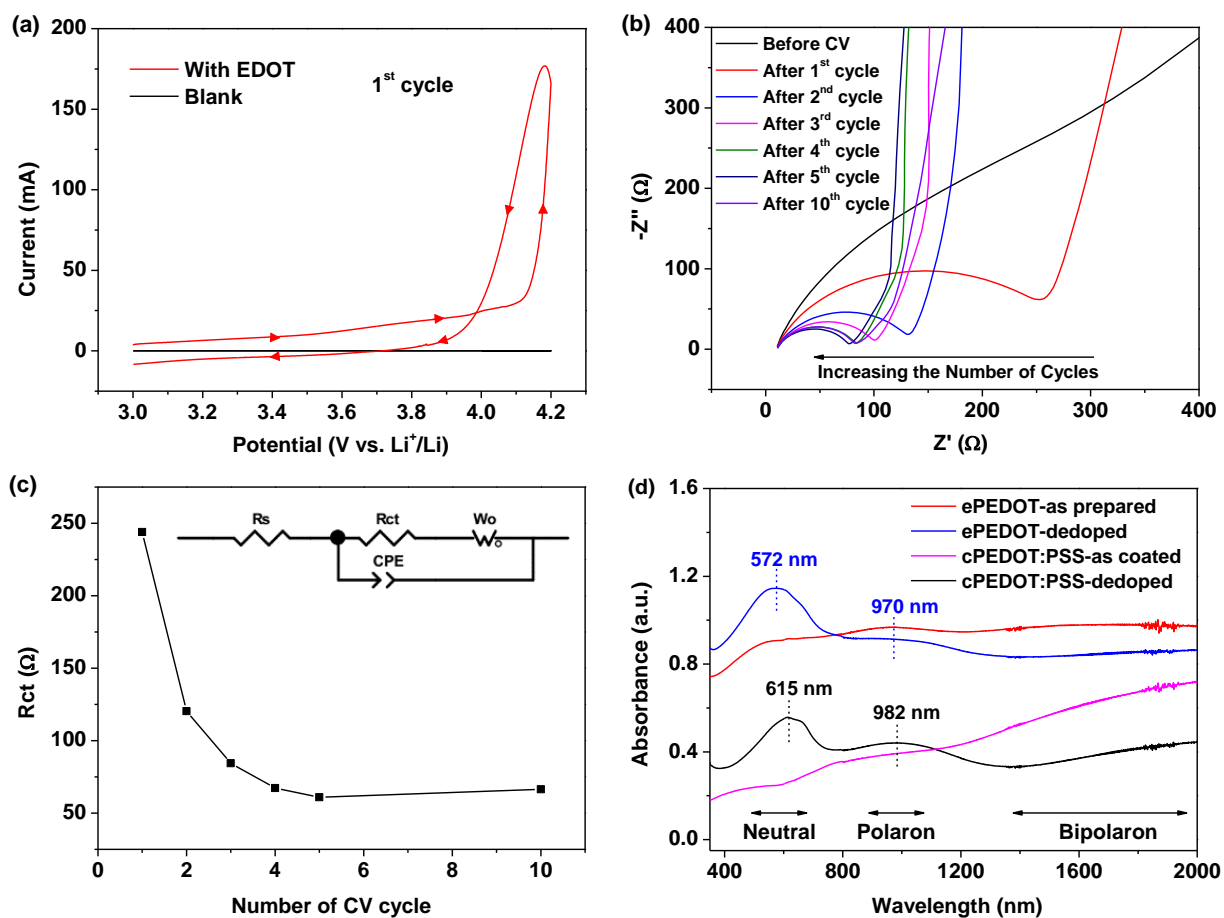
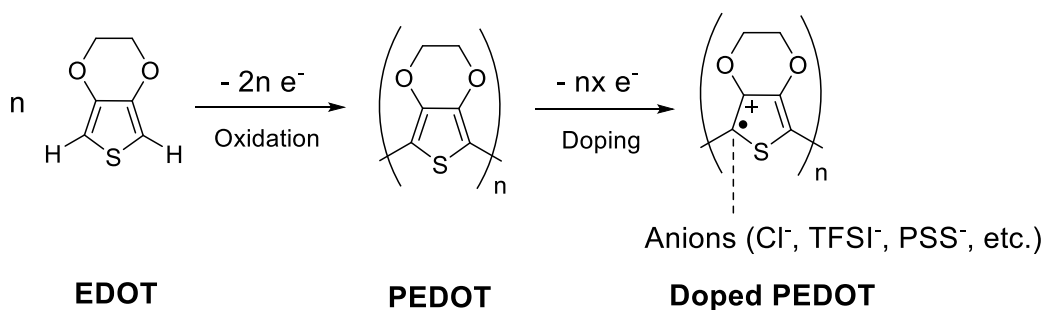


Figure 4.2 CV and EIS data for the e-polymerization, and the characterization of as-prepared ePEDOT and commercial cPEDOT by UV-Vis-NIR. (a) CV curves of the two-electrode coin cells with the EDOT-containing or EDOT-free (blank) electrolyte for the 1st cycle scanned between 3 and 4.2 V at a scan rate of 20 mV s⁻¹. The arrows indicate the scan direction. An ITO-coated glass substrate was used. (b) EIS spectra of the same coin cell shown in (a) with the EDOT-containing electrolyte before and after CV scanning for different numbers of cycles. (c) The change of R_{ct} with increasing the number of CV cycles. The inset shows the equivalent circuit for the fitting of EIS data shown in (b). (d) UV-Vis-NIR spectra of the as-prepared and dedoped ePEDOT, and the as-coated and dedoped cPEDOT:PSS on ITO-coated glass substrates, where the ePEDOT was e-polymerized by the CV method (between 3 and 4.2 V for 10 cycles with a scan rate of 20 mV s⁻¹).

3.3.2 Optimization of e-polymerization of EDOT via chronoamperometry

Scheme 4.1 shows the oxidation of EDOT and the doping of PEDOT via e-polymerization. It should be noted that in real cases the oxidation of monomer and the doping of polymer occur simultaneously. The portion of the repeat units which are oxidized during the p-doping is known as the doping level (x).



Scheme 4.1 Schematic showing the oxidation of EDOT and the doping of PEDOT via e-polymerization.

As shown in Figure 4.3, the ePEDOT prepared by the CV and CA methods are very similar as the UV–Vis–NIR spectra of the ePEDOT prepared by these two methods are almost identical.

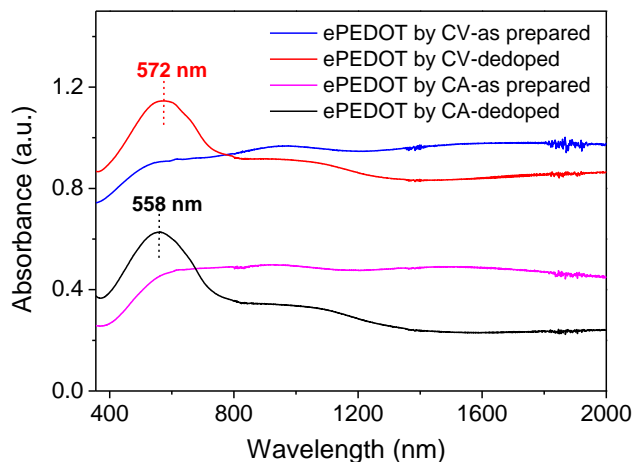


Figure 4.3 Comparison of the UV–Vis–NIR spectra of the ePEDOT prepared by the CV and CA methods. The conditions for the CV and CA methods are 3~4.2 V for 10 cycles with a scan rate of 20 mV s^{-1} and 4.1 V for 800 s, respectively.

To have better control over the e-polymerization process, the chronoamperometry (CA) technique was adopted since the amount of charge injected into the cell for polymerization can be precisely controlled by the applied potential and time. A carbon paper substrate, which has a porous structure for growing a larger amount of ePEDOT, was used to replace the ITO-coated glass substrate. A constant potential of 3.80, 3.90, 4.00, 4.05, 4.10, 4.15, 4.20, 4.30, or 4.40 V was applied to coin cells containing 60 mM EDOT in the electrolyte for 800 s. The current vs. time responses at different potentials (chronoamperograms) are shown in Figure 4.4a. The current remains low at a potential below 3.90 V, indicating that the applied potentials are inadequate to initiate the polymerization. At a potential of 4.00 V, the curve starts to show a very broad peak between 200 s and 400 s. The peak becomes sharper and earlier with further increasing the potential to 4.10 V, which agrees with the CV data (Figure 4.2a). As the potential exceeds 4.15 V, two peaks start to appear with both becoming sharper and earlier with increasing potentials. The features of these CA curves are similar to those observed in the electrosynthesis of PEDOT¹⁵⁸ and poly(anthraquinone) derivatives¹⁵⁹ reported previously. The area under the current vs. time curve is used to obtain the amount of charge injected into the cell during the e-polymerization (Table 4.1). The charge vs. potential plot is shown in Figure 4.4b. As 40 mL of the EDOT-containing electrolyte was used for each cell, the maximum charge required for the polymerization (oxidation) of all the monomers and the p-doping of the resultant polymers at a doping level of 0.4 is 0.55 C. The typical doping level for electropolymerized CPs is between 0.25 and 0.4.¹⁶⁰ From Figure 4.4b, the effective charge injected into the cell for e-polymerization at 4.10 V is 0.56 C, which is close to the calculated value. A larger amount of charge injected at a higher potential (> 4.10 V) may over-oxidize or over-dope the polymer, which possibly leads to the appearance of the 2nd peak in the corresponding chronoamperograms (Figure 4.4a). The optical images of a series of carbon papers with ePEDOT deposited at different potentials (Figure 4.4c) clearly show that a potential higher than 4.10 V would result in non-uniform deposition of the polymers (large polymer aggregates). Based on the aforementioned results, a potential of 4.10 V vs. Li/Li⁺ and a reaction time of 800 s are chosen as the optimal conditions for the e-polymerization of EDOT using the CA method.

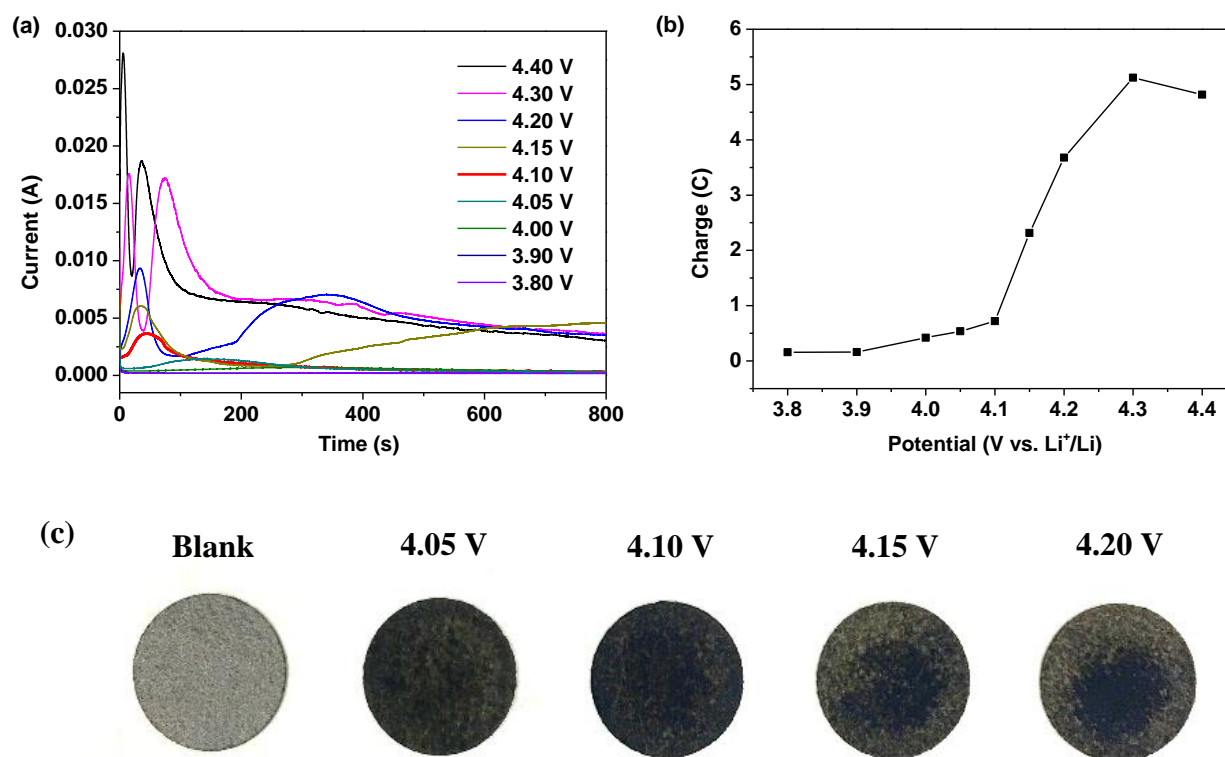


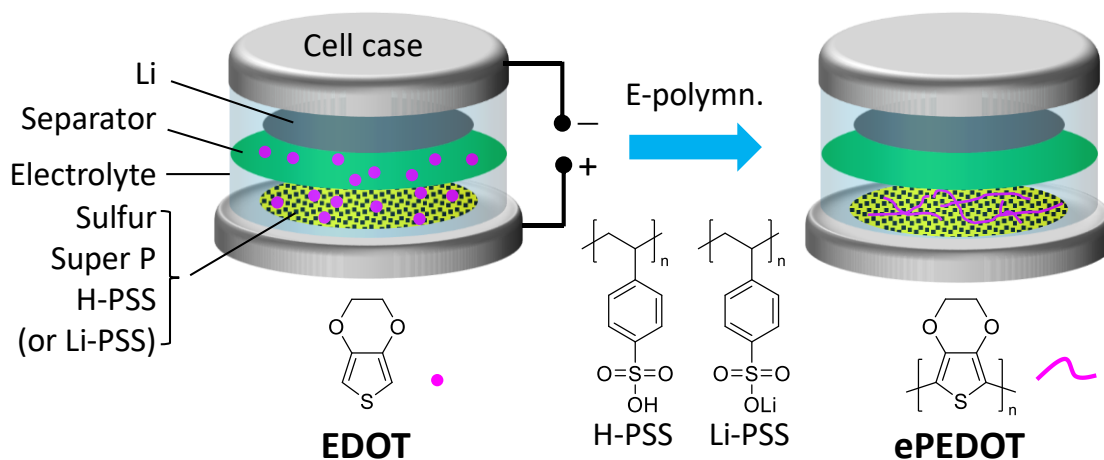
Figure 4.4 Optimization of the e-polymerization by the chronoamperometry method. (a) Chronoamperograms for the e-polymerization of EDOT at different potentials from 3.8 to 4.4 V. Carbon paper substrates were paired with lithium foils to construct two-electrode coin cells. (b) Total charges injected into the coin cells at different potentials for 800 s. (c) Photos of carbon papers with e-PEDOT synthesized at different potentials.

Table 4.1 Charges injected into the cells at different potentials during the e-polymerization.

Potential (V vs. Li ⁺ /Li)	3.80	3.90	4.00	4.05	4.10	4.15	4.20	4.30	4.40
Total charge (C)	0.16	0.16	0.42	0.54	0.72	2.32	3.68	5.12	4.82
Effective charge (C)	0	0	0.26	0.38	0.56	2.16	3.52	4.96	4.66

4.3.3 Fabrication and characterization of Li-S batteries with the ePEDOT binder prepared via in-cell e-polymerization

A schematic illustrating the formation of ePEDOT on the sulfur cathode via the in-cell e-polymerization method is shown in Scheme 4.2.



Scheme 4.2 Schematic illustrating the formation of ePEDOT in the sulfur cathode inside a Li-S cell by the in-cell e-polymerization.

The yield of e-polymerization by the CA method was determined with UV-Vis microscopy, as shown in Figure 4.5. At first, a sulfur-free Super P/H-PSS (weight ratio of 4 : 1) substrate was prepared by coating the slurry on a carbon-coated Al foil, which has similar structure and composition to those of the sulfur cathode. The substrate was assembled into a coin cell by pairing with a lithium foil and using 20 mL of 60 mM EDOT-containing electrolyte. e-Polymerization was performed in the CA mode at 4.10 V vs. Li/Li⁺ for 800 s. The cell was disassembled and all the parts were washed with DME to dissolve the unreacted EDOT for the UV-Vis measurement. The EDOT monomer shows an absorption peak at 255 nm (Figure 4.5a). The molar absorptivity of EDOT was determined as 8458 L mol⁻¹ cm⁻¹. The average EDOT monomer conversion was 86%.

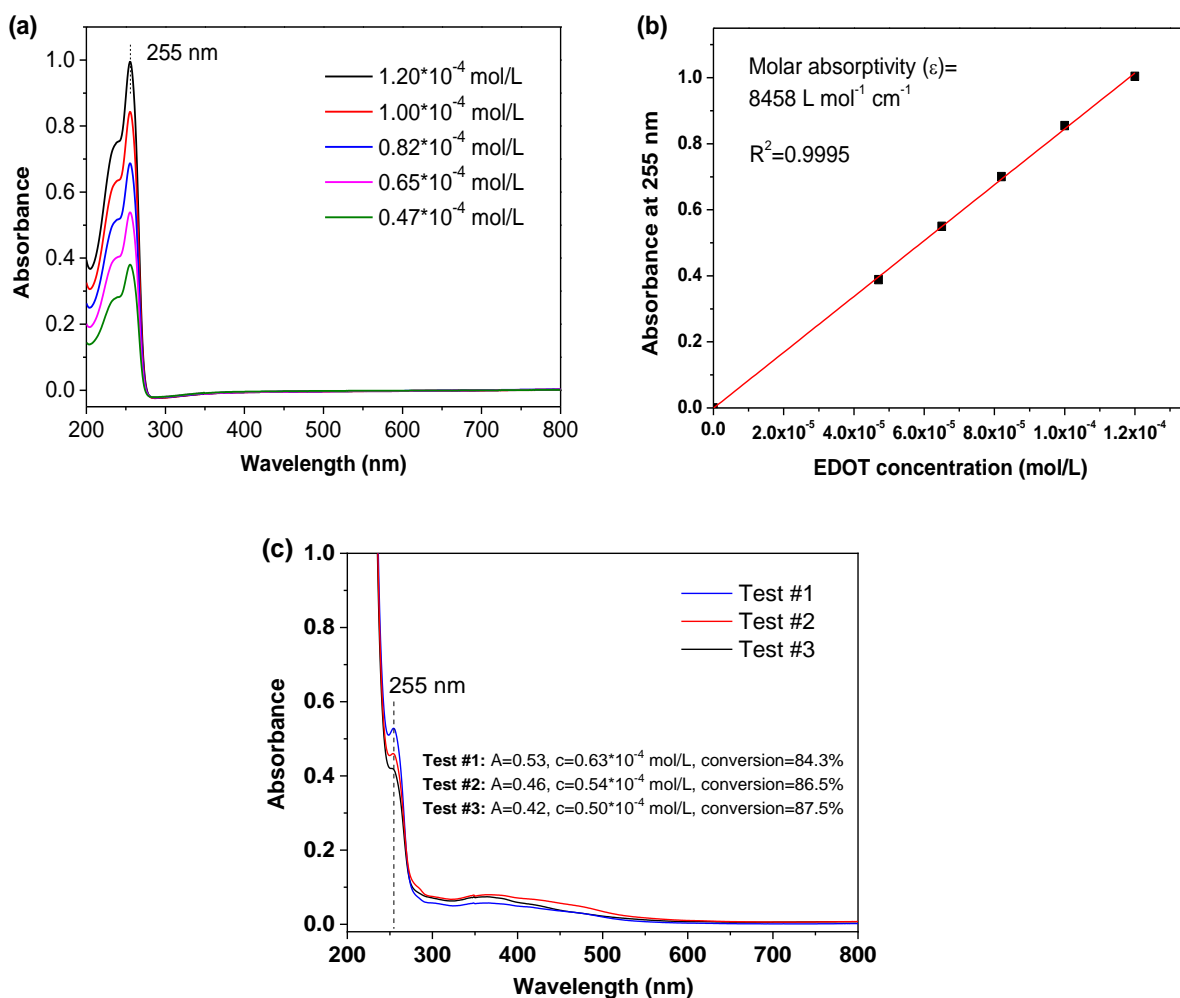


Figure 4.5 Determination of the conversion for the e-polymerization by UV-Vis spectroscopy. (a) UV-Vis spectra of a series of EDOT aqueous solutions with different concentrations. (b) Linear plot of the absorbance (at 255 nm) of EDOT at different concentrations. (c) UV-Vis spectra of the diluted electrolyte solutions after e-polymerization at 4.10 V vs. Li/Li^+ for 800 s using the CA method with the electrodes having Super P/H-PSS (weight ratio of 4:1) on carbon-coated Al substrates. Three tests were performed to obtain an average EDOT monomer conversion.

Next, poly(4-styrenesulfonic acid) (H-PSS) or poly(lithium 4-styrenesulfonate) (Li-PSS) is used as a pre-binder in the sulfur cathode, which is expected to form a doped ePEDOT:PSS that is similar to the commercial one, cPEDOT:PSS, in the cathode. The Li-S batteries with the 60 mM EDOT-containing electrolyte were assembled and in-cell e-polymerized using the CA method at 4.10 V for 800 s. As shown in Figure 4.6, the chronoamperograms of the sulfur cathodes are similar

to those obtained using carbon paper (without sulfur) as the substrate since sulfur is inert under the e-polymerization (4.1 V vs. Li/Li⁺) conditions, suggesting the successful formation of ePEDOT at the sulfur cathode.

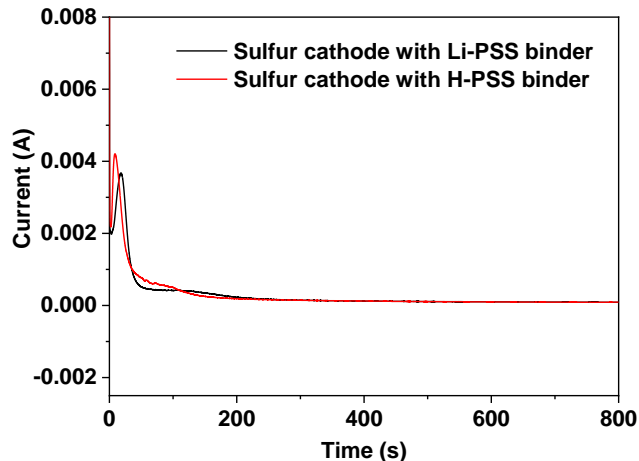


Figure 4.6 Chronoamperograms for the sulfur cathodes with Li-PSS or H-PSS binder. The Li-S cells were held at 4.10 V vs. Li/Li⁺ for 800 s.

As a comparison, Li-S batteries using the EDOT-free electrolyte were also fabricated. The CV curves of the sulfur cathodes using H-PSS or Li-PSS binder with and without ePEDOT, and cPEDOT:PSS binder are shown in Figure 4.7a–e. Comparing the two cells with only H-PSS and Li-PSS binders (Figure 4.7a and b), the former shows a very weak and delayed 2nd reduction peak, which corresponds to the conversion of lithium polysulfides to Li₂S₂ and Li₂S₂ to Li₂S, in the 1st and 2nd cycles. In the subsequent cycles, this peak becomes stronger, but the peak position shifts to a much lower potential compared to the Li-PSS based cell. This indicates that the sulfonic acid (–SO₃H) groups in H-PSS may strongly interact with lithium polysulfides and impede their further reduction (a delayed second reduction peak). In other words, this suggests that the –SO₃H groups may have a better trapping capability than the lithium sulfonate (–SO₃Li) groups in Li-PSS. After e-polymerization, the cell with the resultant ePEDOT:H-PSS (Figure 4.7c) shows similar CV profiles with delayed second reduction peaks compared to the cell with the H-PSS binder. Interestingly, after e-polymerization, the cell with the ePEDOT:Li-PSS binder (Figure 4.7d) also displays delayed second reduction peaks, resembling closely those of the cells with H-PSS and ePEDOT:H-PSS binders (Figure 4.7a and c). This may be attributed to the generation of protons (during the e-polymerization of EDOT) that convert some of the –SO₃Li groups into –SO₃H groups

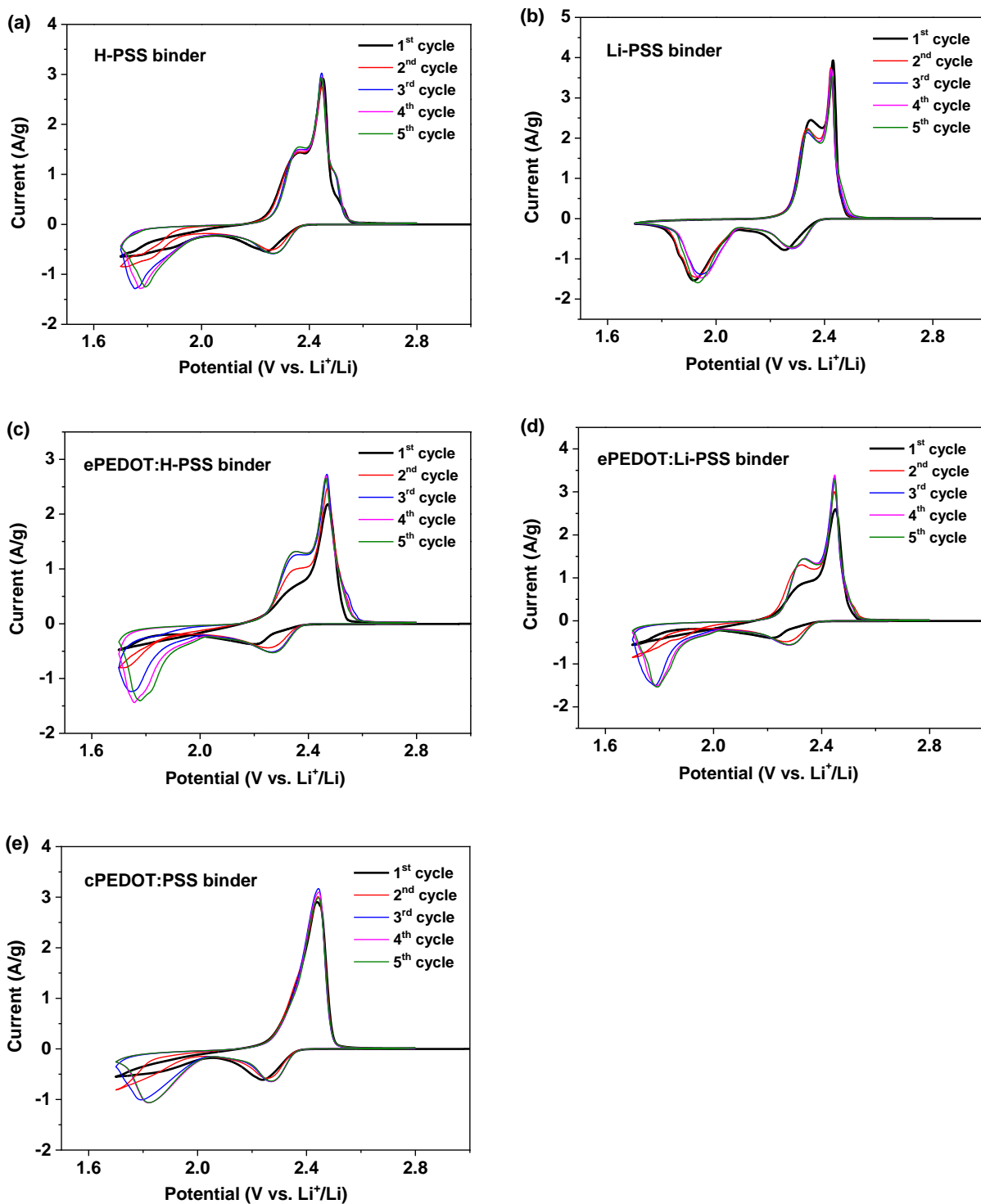


Figure 4.7 Cyclic voltammograms of sulfur cathodes using different types of binders at a scan rate of 0.1 mV s^{-1} . (a) H-PSS, (b) Li-PSS, (c) ePEDOT:H-PSS, (d) ePEDOT:Li-PSS, and (e) cPEDOT:PSS.

that have a stronger trapping effect on lithium polysulfides. Delayed second reduction peaks in the 1st and 2nd cycles are also observed for the commercial cPEDOT:PSS binder (Figure 4.7e) since cPEDOT:PSS is acidic (pH ~2 for the 1.1 wt% aqueous dispersion).

The 3rd and 100th charge/discharge profiles of the sulfur cathodes at 0.2 C are compared in Figure 4.8a. The galvanostatic cycling performance of sulfur cathodes using different binders is shown in Figure 4.8b. The initial capacities of sulfur cathodes with the ePEDOT:H-PSS and ePEDOT:Li-PSS binders are very close, i.e. 1142 and 1147 mA h g⁻¹, respectively. These values are almost identical to those of the cathodes with the H-PSS (1141 mA h g⁻¹) and Li-PSS (1145 mA h g⁻¹) binders, respectively. However, the cell with the Li-PSS binder shows an abrupt decay in capacity in the first few cycles compared to the cell with the H-PSS binder. This might be explained by the weaker trapping capability of the Li-PSS binder to lithium polysulfides than the H-PSS binder as discussed previously. After the 3rd cycle, the cell with H-PSS decays at a faster rate than the cell with Li-PSS, while both cells show exactly the same specific capacity of 596 mA h g⁻¹ at the 100th cycle. The faster decay of the cell with H-PSS between the 3rd cycle and the 100th cycle might be due to the fact that even though H-PSS has a stronger affinity to lithium polysulfides, the latter can still gradually escape from the cathode to the bulk electrolyte, resulting in a reduction in sulfur utilization. Consequently, the capacity retentions of the H-PSS and Li-PSS based cells after 100 cycles with respect to their initial specific capacities are very similar, i.e. 52% and 51%, respectively. On the other hand, the cells with the ePEDOT:H-PSS and ePEDOT:Li-PSS binders show much improved cycling stability with capacity retentions of 62% and 56%, respectively. The results demonstrate that ePEDOT has an additional benefit to the suppression of the polysulfide shuttle effect due to its strong polysulfide absorption capability.⁴² The sulfur cathode using the commercial cPEDOT:PSS binder shows an initial capacity of 1059 mA h g⁻¹ and a capacity retention of 53% after 100 cycles, both of which are lower than those of the batteries with the ePEDOT:H-PSS and ePEDOT:Li-PSS binders, indicating that ePEDOT formed via in-cell e-polymerization leads to an improved initial specific capacity and better cycling stability. Moreover, the cell with the ePEDOT:H-PSS binder also results in improved rate performance compared to that with the cPEDOT:PSS binder (Figure 4.8c). Especially at 0.5 C, the cell with the ePEDOT:H-PSS binder delivers a capacity of 733 mA h g⁻¹, which is much higher than that (579 mA h g⁻¹) with the cPEDOT:PSS binder. The improved specific capacity, cycling stability, and rate performance of the cells with the ePEDOT:H-PSS and ePEDOT:Li-PSS binders might originate

from the tightly integrated interfaces between ePEDOT and Super P (the conductive sites where e-polymerization occurs), where the trapped lithium polysulfides are in close proximity to Super P for more efficient charge transfer.

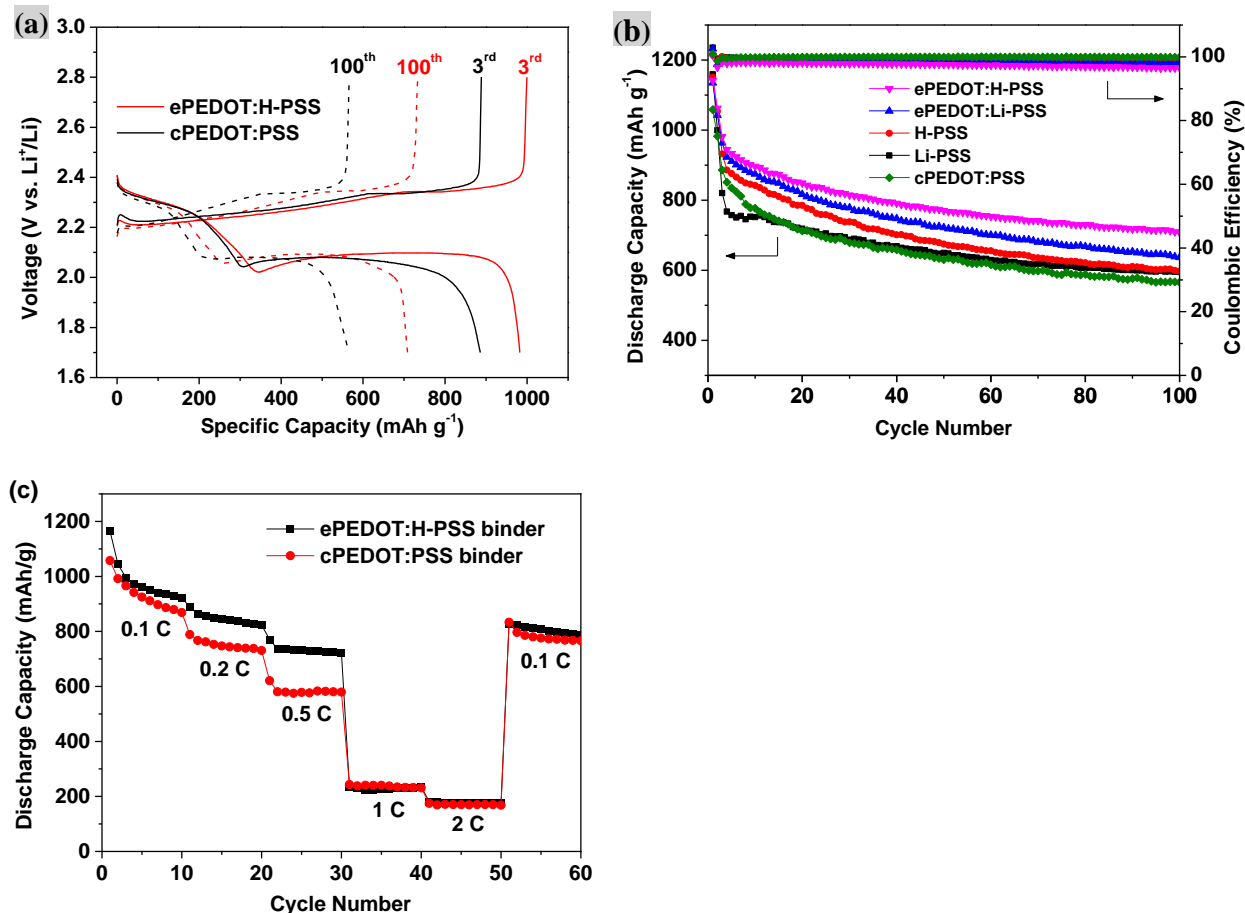


Figure 4.8 Cycling test of sulfur cathodes with and without ePEDOT, and rate performance of sulfur cathodes with ePEDOT:H-PSS or cPEDOT:PSS binder. (a) Charge/discharge profiles of sulfur cathodes using ePEDOT:H-PSS or cPEDOT:PSS binder at 0.2 C. (b) Cycling performance of sulfur cathodes using ePEDOT:H-PSS, ePEDOT:Li-PSS, H-PSS, Li-PSS, and cPEDOT:PSS binders. The batteries were activated at 0.1 C for 2 cycles and cycled at 0.2 C afterwards. (c) Rate performance of sulfur cathodes using ePEDOT:H-PSS and cPEDOT:PSS binders.

To further confirm the trapping capability of PEDOT toward lithium polysulfides, the cells using the sulfur cathodes with different binders were disassembled after 100 cycles in the charged state, and all the cell components were soaked in 5 mL of DOL/DME. Then, the UV-Vis spectra of the supernatants were recorded, as shown in Figure 4.9. Compared with the sulfur cathode using

the H-PSS binder, those using ePEDOT:PSS and cPEDOT:H-PSS binders show a notable reduction in the absorbance of lithium polysulfides (260, 280 and 310 nm for Li_2S_6 ,⁹⁵ 420 nm for Li_2S_4 ¹⁶¹), suggesting that both ePEDOT and cPEDOT have excellent polysulfide trapping abilities. Considering the ease of fabrication and the enhanced cell performance, the in-cell e-polymerized ePEDOT:H-PSS and ePEDOT:Li-PSS binders are advantageous over the cPEDOT:PSS binder.

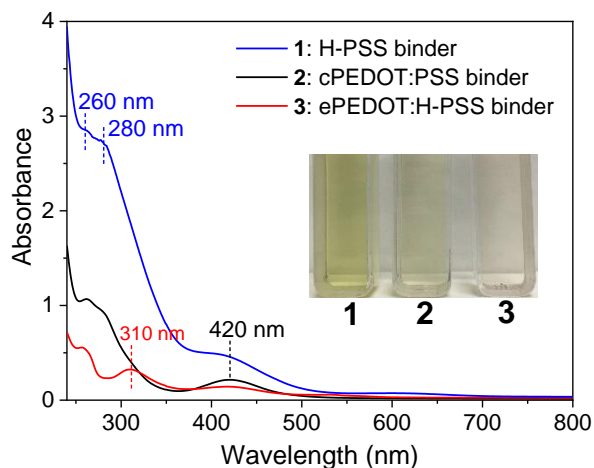


Figure 4.9 Comparison of lithium polysulfide dissolution in the electrolyte for the sulfur cathodes with different binders. The inset shows the photos of supernatants (polysulfide solutions) in the cuvettes.

4.3.4 Adhesion evaluation of ePEDOT:PSS by the 180° peel test

As a glue for bonding conductive carbon particles and sulfur particles and for bonding the entire cathode film to the Al current collector underneath, the binder is an important component of Li-S batteries. The adhesion strengths of cPEDOT:PSS and ePEDOT:H-PSS binders were evaluated by the 180° peel test using a mechanical tester (Figure 4.10a). The load force vs. displacement curves are shown in Figure 4.10b and c. The adhesion strengths (calculated by dividing the load force with the width of the tape) of ePEDOT:H-PSS and cPEDOT:PSS binders are 0.039 ± 0.008 and $0.028 \pm 0.003 \text{ N mm}^{-1}$, respectively, indicating that the ePEDOT:H-PSS binder has better adhesion compared to the cPEDOT:PSS binder. The optical images of the cathode film and the tape before and after the peel test were also compared. As shown in Figure 4.11, before the peel test, the sulfur cathode film using the cPEDOT:PSS or ePEDOT:H-PSS adhesive is completely covered on the carbon-coated aluminum foil. After the peel test, large pieces were peeled off from the sulfur cathode with the cPEDOT:PSS binder, while only small pieces were

peeled off from the one with the ePEDOT:H-PSS binder, which further confirmed that the adhesion of the ePEDOT:PSS binder is superior to that of the cPEDOT:H-PSS binder. The better adhesion strength of the ePEDOT:H-PSS binder can also explain its better battery performance than the cPEDOT:PSS binder.

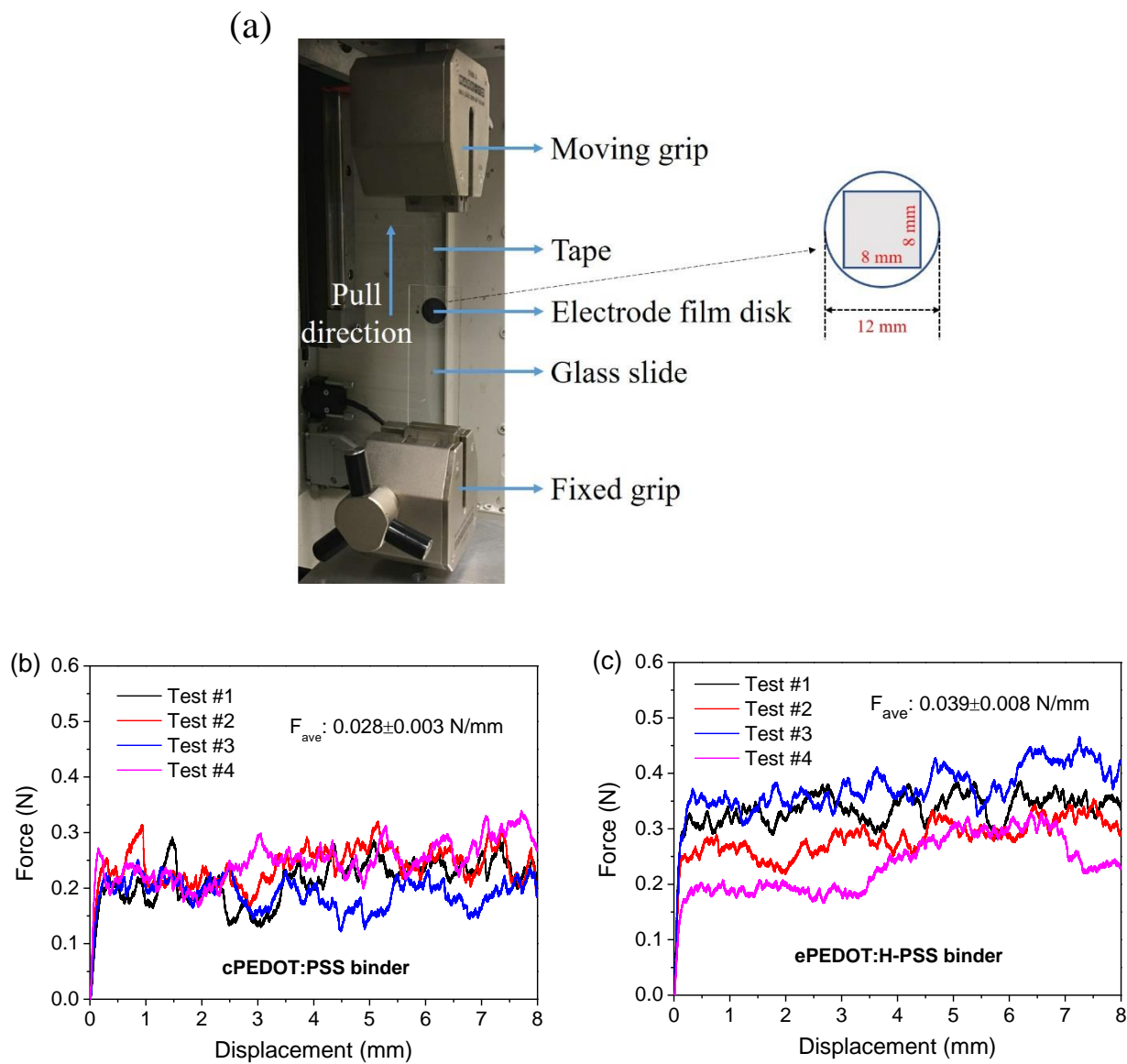


Figure 4.10 Peel test on the sulfur cathode films using cPEDOT:PSS or ePEDOT:H-PSS binder. (a) Photos of the mechanical tester for peel test. Load force vs. displacement curves for sulfur cathode films using (b) cPEDOT:PSS binder and (c) ePEDOT:H-PSS binder.

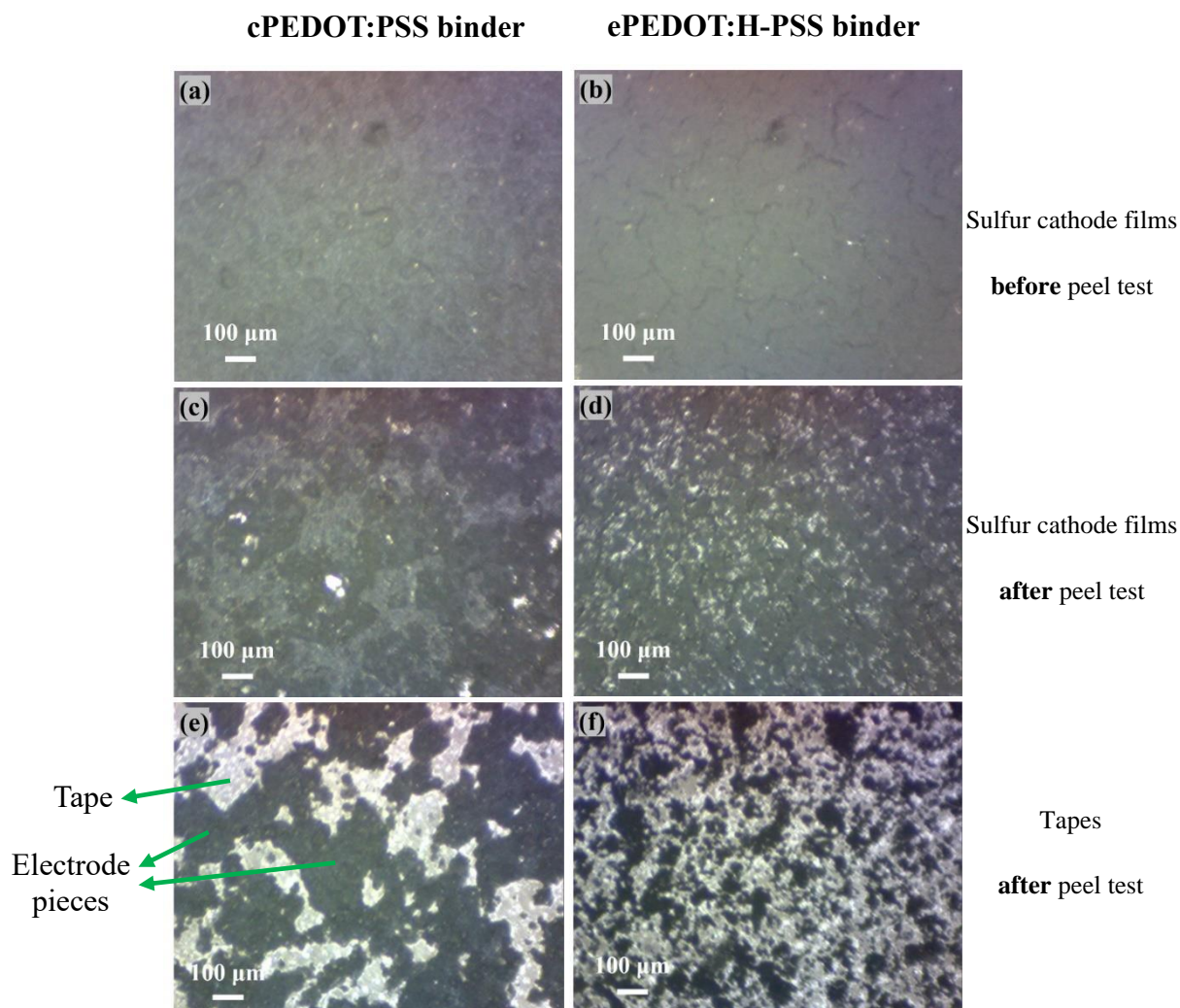


Figure 4.11 Optical images of sulfur cathode films before and after peel test, and tapes after peel test. Sulfur cathode film with the cPEDOT:PSS binder (a) before peel test, (c) after peel test, and (e) tape after peel test. Sulfur cathode film with the ePEDOT:H-PSS binder (b) before peel test, (d) after peel test, and (f) tape after peel test.

4.3.5 Investigation of doping/dedoping of PEDOT by CV and EIS

CPs are conductive in the doped state, while they are semiconducting or insulating in the undoped (or dedoped) state. When CPs are used in rechargeable lithium batteries, the enhanced battery performance has been often linked to the high conductivity of CPs in the literature. However, the initially doped and conductive CPs may be electrochemically dedoped and become less conductive or even insulating during the battery cycling process. This potential issue has not

been discussed and investigated in previous studies. On the other hand, the CV data of CPs reported in the literature, which can reveal the doping and dedoping behaviours at different potentials, have been reported with reference electrodes such as the SCE and Ag/AgCl that are different from Li^+/Li and in electrolytes that are different from conventional battery electrolytes, which makes it rather difficult to gauge the doping and dedoping behaviours of CPs when CPs are employed in lithium batteries. Here we investigated the aforementioned issue that might be associated with ePEDOT:H-PSS during the discharge/charge processes of Li-S batteries via CV and EIS measurements. A sulfur cathode was prepared using Li-PSS as the binder in order to rule out the influence of the binder (H-PSS) on the CV profiles as discussed earlier, while an electrode with Super P/ePEDOT:H-PSS (sulfur-free) on the carbon-coated Al substrate was prepared in order to obtain the intrinsic redox characteristics of ePEDOT:H-PSS. The CV curves of both electrodes were measured using Li^+/Li as the reference electrode in the same LiTFSI-based electrolyte for a direct comparison (Figure 4.12a). The electrochemical reaction associated with each peak is shown in Figure 4.12b. For the sulfur cathode, the two reduction (discharge) peaks at 2.28 and 1.93 V are attributed to the conversion of S_8 to lithium polysulfides (Li_2S_n , $n = 4-8$) and lithium polysulfides to $\text{Li}_2\text{S}_2/\text{Li}_2\text{S}$, respectively. The two oxidation (charge) peaks at 2.34 and 2.43 V are attributed to the conversions of $\text{Li}_2\text{S}_2/\text{Li}_2\text{S}$ to lithium polysulfides and lithium polysulfides to S_8 , respectively. For ePEDOT:H-PSS, the broad reduction peak at 2.53 V and the oxidation peak at 3.01 V correspond to the dedoping and doping processes, respectively (Figure 4.12b). The peak at 3.54 V is due to the oxidation of lithium nitrite (LiNO_2) that is generated by the reaction of lithium nitrate with lithium metal,^{162,163} which disappeared when a LiNO_3 -free electrolyte was used (Figure 4.13). From the CV curve of ePEDOT:H-PSS (Figure 4.12a), it can be seen that doping starts at 2.42 V, reaches a peak at 3.01 V, and finishes at 3.36 V, while dedoping starts at 2.86 V, reaches a peak at 2.53 V, and finishes at 1.95 V. This suggests that the dedoping of ePEDOT:H-PSS occurs simultaneously with the discharge of the sulfur cathode and that ePEDOT:H-PSS becomes mostly dedoped after the sulfur cathode is discharged to 1.7 V. After recharging the sulfur cathode to 2.8 V, the doping level of ePEDOT:H-PSS can only be partially restored with respect to its original state. Therefore, ePEDOT:H-PSS may only be highly conductive and contribute to the improvement^{nt} of the conductivity of the sulfur cathode during the 1st discharging process of the sulfur cathode. In the subsequent 1st charging process in the typical voltage range of 1.7–2.8 V, ePEDOT:H-PSS cannot be fully doped. Therefore, ePEDOT:H-PSS would make smaller

contributions to the improvement of the conductivity of the cathode in the subsequent discharge/charge cycles. Since cPEDOT:PSS shows similar reduction/oxidation profiles compared to ePEDOT:H-PSS (Figure 4.13), the dedoping of cPEDOT:PSS is also likely to occur when it is used in the sulfur cathode during the discharging/charging processes.

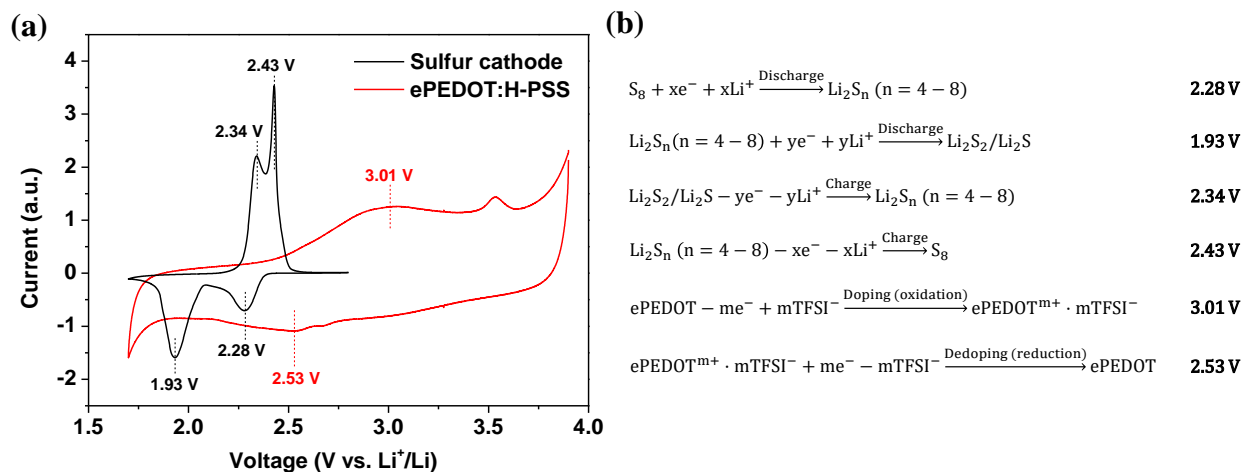


Figure 4.12 CV curves of sulfur cathode and ePEDOT:H-PSS. The sulfur cathode was made using Li-PSS as the binder, while ePEDOT:H-PSS was formed on the Super P/H-PSS substrate via in-cell e-polymerization using the CA method at 4.10 V for 800 s. The potential ranges for sulfur cathode and ePEDOT:H-PSS are 1.7-2.8 and 1.7-3.9 V, respectively.

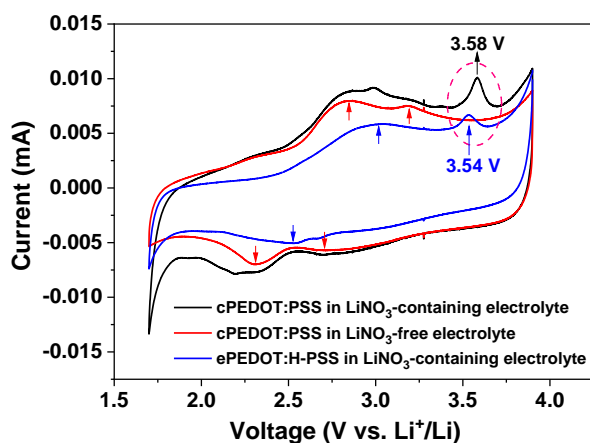


Figure 4.13 Comparison of the CV curves of ePEDOT:H-PSS and cPEDOT:PSS in the electrolytes with and without LiNO_3 . The ePEDOT was deposited on a lab-made Super P/H-PSS substrate via the chronoamperometry method, while the cPEDOT:PSS was blended with Super P and coated on a Al foil via the slurry coating method.

It should be mentioned that other cathode materials having higher cycling potential windows, e.g. 3–4.2 V for lithium cobalt/manganese oxide and 2–4.2 V for lithium iron phosphate, PEDOT would be more heavily doped during the cell operation. In this regard, it is expected that PEDOT would contribute more to improving the conductivity of the cathode when it is used for these high voltage batteries. On the other hand, the doping/dedoping windows of different CPs vary. The cathode conductivity and performance of Li–S batteries may be further improved if an appropriate monomer is selected to make a CP that has lower oxidation and reduction potentials compared to the sulfur cathode. The dependence of the conductivity of ePEDOT on the cell potential was further studied by combined CV and EIS measurements. To eliminate the interference of carbon materials (Super P and carbon paper) with the EIS results, a bare ITO-coated glass substrate was used to grow ePEDOT by the CA method at 4.10 V vs. Li⁺/Li for 800 s. After in-cell e-polymerization, the cell was scanned using CV for 20 cycles to obtain a stabilized CV diagram (Figure 4.14a) and then subjected immediately to the EIS measurement at 1.7 or 3.36 V for four consecutive CV cycles (Figure 4.14b and c). The obtained EIS spectra were fitted using the equivalent circuit shown in Figure 4.2c to obtain the R_{ct} values, which are plotted in Figure 4.14d. The average R_{ct} at 3.36 V vs. Li⁺/Li (ePEDOT in the doped state) is $2.22 \times 10^3 \Omega$, which is much smaller than the value of $4.92 \times 10^3 \Omega$ at 1.7 V vs. Li⁺/Li (ePEDOT in the dedoped state). Similar R_{ct} values are maintained at 1.7 and 3.36 V, respectively, for different cycles, demonstrating the reversible switching between the doped and the dedoped states of ePEDOT during the cell cycling process. More data points were collected during one CV cycle at additional potential points which are critical for Li–S batteries (Figure 4.15). The results show a more detailed resistance-potential dependence of ePEDOT, where the R_{ct} decreases with increasing cell potential during the oxidation (doping) process and increases with decreasing cell potential during the reverse reduction (dedoping) process.

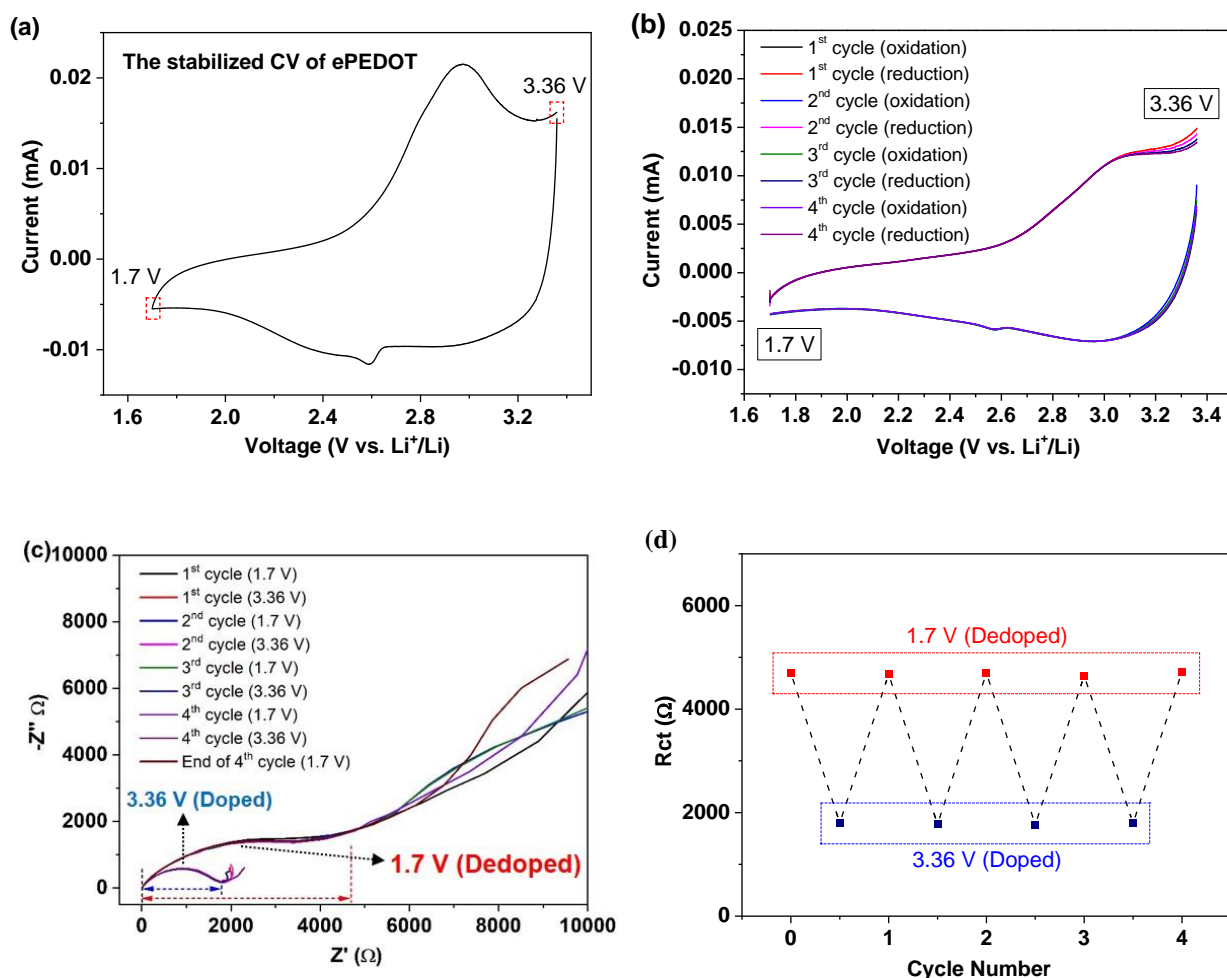


Figure 4.14 Investigation of the conductivity difference of ePEDOT in the doped state (3.36 V) and dedoped state (1.7 V). (a) The stabilized CV curve of a cell having ePEDOT grown on an ITO-coated glass substrate. The ePEDOT-containing cell was prepared by e-polymerization of EDOT using the CA method at 4.10 V vs. Li/Li^+ for 800 s in a two-electrode coin cell with ITO and Li as electrodes. The 60 mM EDOT-containing electrolyte was used. (b) Combined CV (or LSV) segments (oxidation and reduction processes) for four consecutive cycles using the same cell in (a). The cell was switched between CV testing and EIS testing automatically using a VMP3 Bio-Logic potentiostat at both 1.7 and 3.36 V. (c) EIS spectra of the cell measured at 1.7 or 3.36 V vs. Li/Li^+ for four consecutive CV cycles. (d) R_{ct} values for ePEDOT deposited on an ITO-coated glass substrate at high (3.36 V vs. Li^+/Li) and low (1.7 V vs. Li^+/Li) potentials.

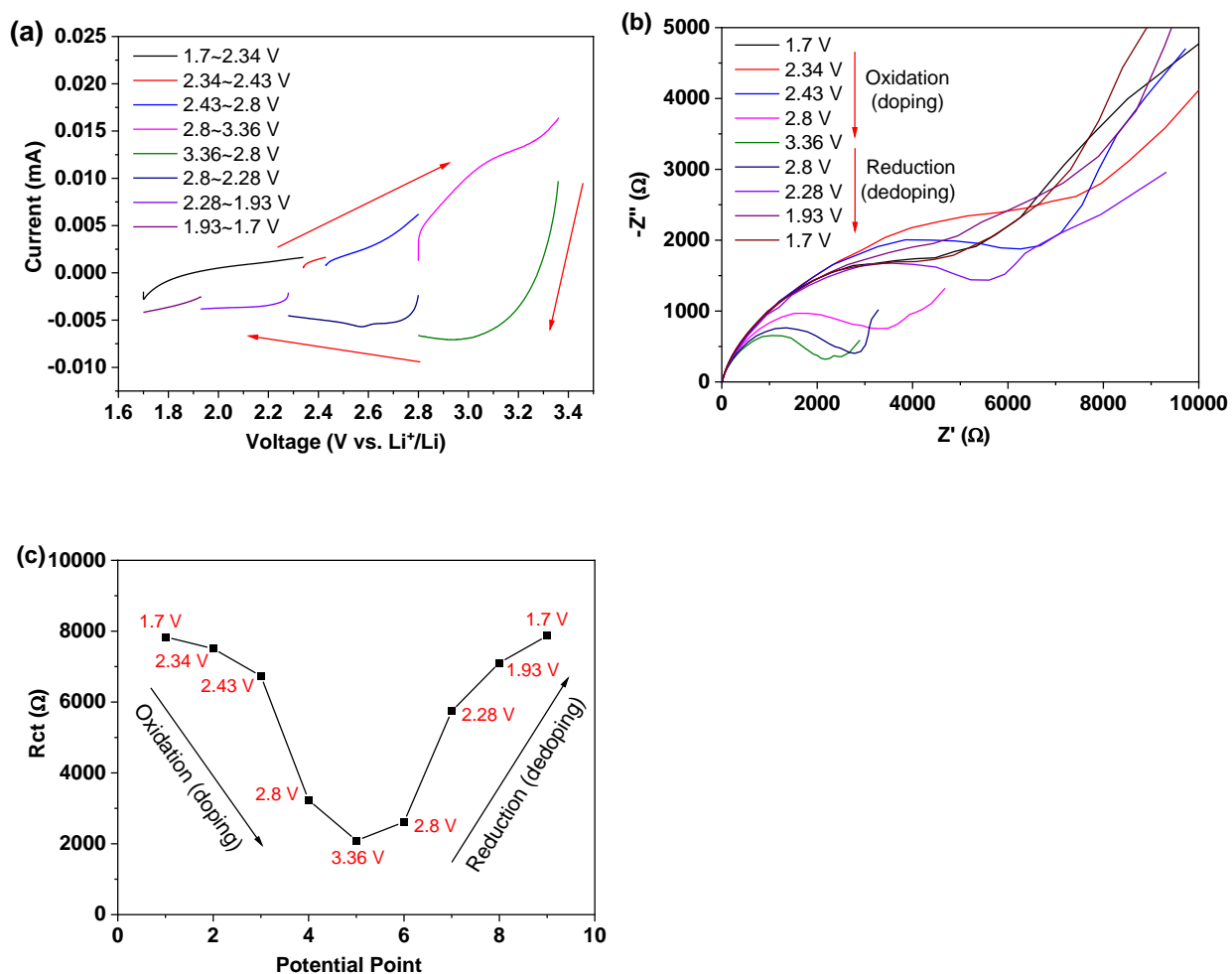


Figure 4.15 Investigation of the conductivity difference of ePEDOT at different potentials during the oxidation (doping) and reduction (dedoping) processes. (a) Combined CV segments during one CV cycle. The cell was switched between CV testing and EIS testing sequentially at 1.7, 2.34, 2.43, 2.8, and 3.36 V for the oxidation process, and 2.8, 2.28, 1.93, and 1.7 V for the following reduction process. (b) EIS spectra of the cell collected at the potential points shown in (a) during one CV cycle of oxidation (doping) and reduction (dedoping) processes. (c) R_{ct} values at different potential points derived from the EIS spectra in (b).

4.3.6 Electropolymerized PEDOT for lithium iron phosphate (LFP) cathode

The electrolyte used for the e-polymerization was changed from ether-based electrolyte (1 M LiTFSI in DOL/DME) to carbonate-based electrolyte (1 M LiPF₆ in ethylene carbonate

(EC)/ethyl methyl carbonate (EMC)/dimethyl carbonate (DMC) electrolyte as the latter electrolyte can withstand higher potentials and is the standard electrolyte for the LFP cathode. To verify whether e-polymerization can still occur with this electrolyte, the afore-mentioned CV method was employed. As shown in Figure 4.16a, the CV curve for the 1st cycle is similar to that obtained using the LiTFSI in DOL/DME electrolyte (Figure 4.2a), indicating e-polymerization occurs in the LiPF₆ electrolyte. Subsequent CV cycles show a gradual intensification of the oxidation peak at 3.25 V and two reduction peaks at 2.04 V and 3.13 V (Figure 4.16b), indicating the growth of ePEDOT.¹⁶⁴

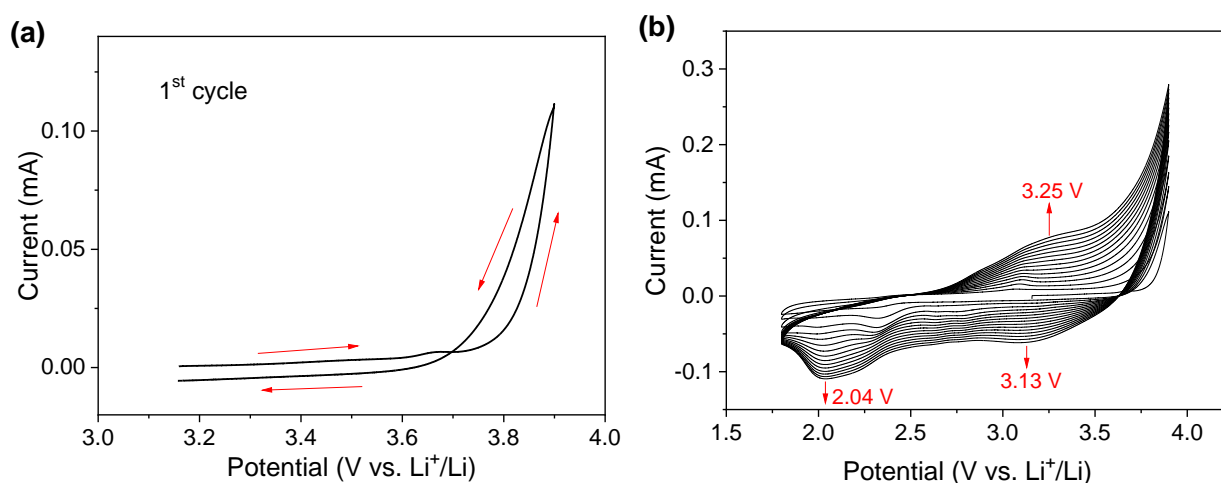


Figure 4.16 Cyclic voltammograms for a cell loaded with a 60 mM EDOT in 1:1:1 EC/EMC/DMC based electrolyte. (a) First cycle in the potential range from 3.16 V (open circuit voltage) to 3.9 V. (b) 15 consecutive cycles in the potential range of 1.8~3.9 V. The scan rate was 5 mV s⁻¹.

The CA method was chosen to better control the charge injected into the cell during the e-polymerization. The polymerization conditions were optimized using different concentrations of EDOT in the electrolyte. As shown in Figure 4.17a-c, the general characteristics of these chronoamperograms are similar to those obtained using the LiTFSI in DOL/DME electrolyte. As the potential increases from 3.70 to 4.20 V, the main peak becomes sharper and appears earlier. Assuming a doping level of 0.4 for the as-prepared e-PEDOT, the calculated charges for monomer oxidation and polymer doping in the electrolytes with 10, 20, and 60 mM EDOT are 0.093, 0.19, and 0.56 C, respectively. The experimentally obtained charges are close to the calculated values in the potential range of 4.00~4.05, 4.05~4.10, and 4.10~4.20 V for the electrolytes containing 10, 20, and 60 mM EDOT, respectively (circles in Figure 4.17d).

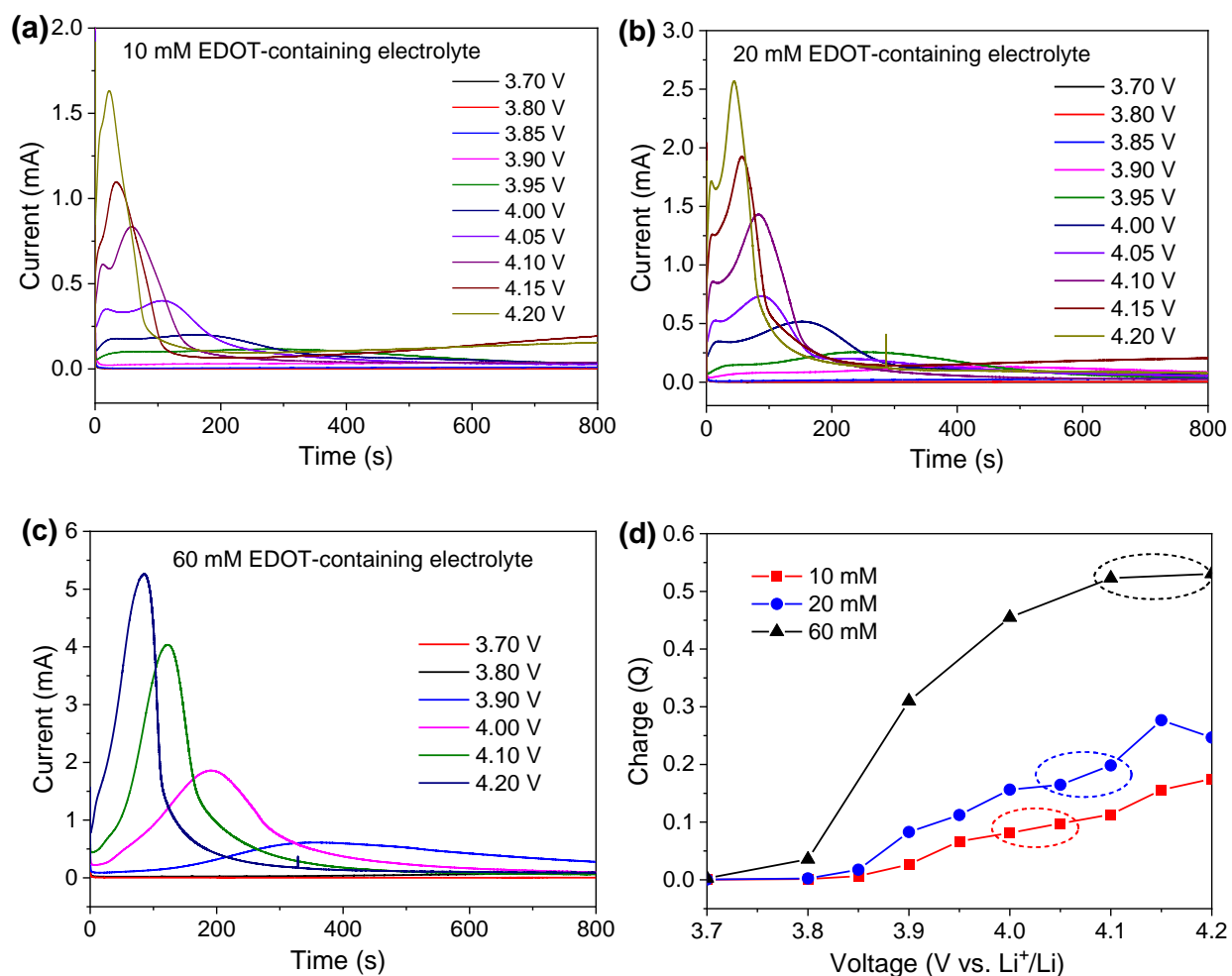


Figure 4.17 Optimization for the e-polymerization of EDOT on the carbon paper substrate by the CA method. Chronoamperograms at different potentials using the EDOT-containing electrolytes of different concentrations, (a) 10 mM, (b) 20 mM, and (c) 60 mM. (d) The charge injected into the coin cell at different potentials using the EDOT-containing electrolytes of different concentrations. The circles in each curve indicate the potentials at which the experimental charges are close to the calculated ones.

Figure 4.18 shows the carbon paper substrates modified with ePEDOT prepared using the electrolytes with different EDOT concentrations. The colors of the carbon paper substrates with ePEDOT obtained using the 10 and 20 mM EDOT electrolytes are much lighter than those obtained using the 60 mM EDOT electrolyte at the potentials of >3.90 V, indicating that the ePEDOT films in the former samples are much thinner than the latter ones.

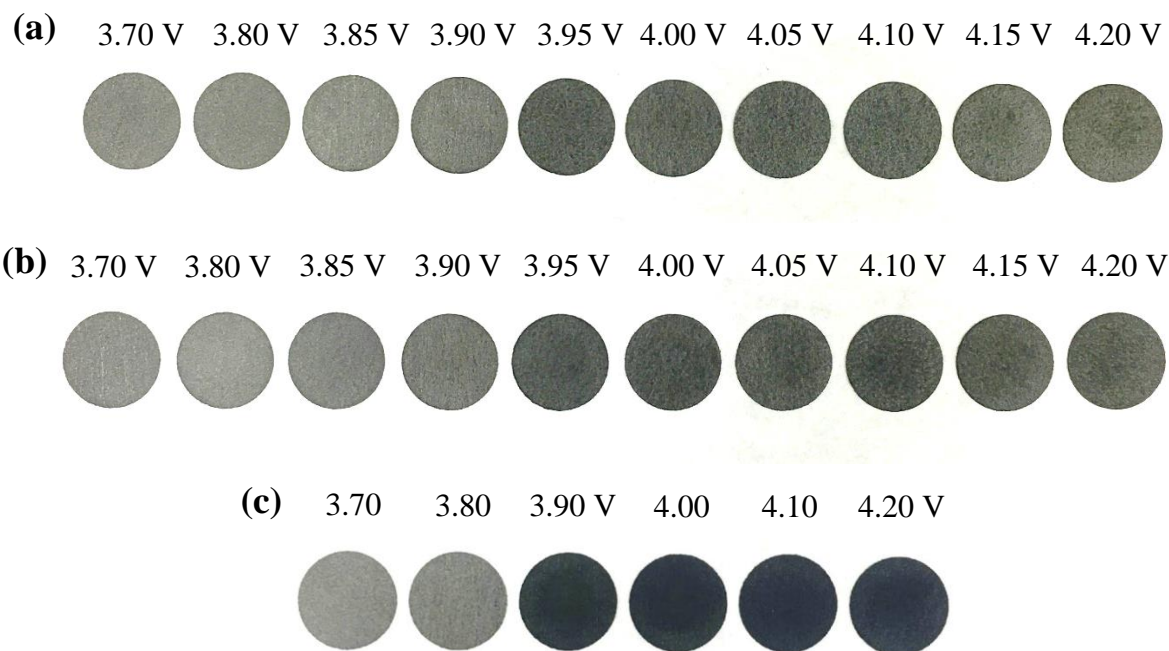


Figure 4.18 Photos of ePEDOT on carbon paper obtained by the CA method using the EDOT-containing electrolytes of different concentrations. (a) 10 mM, (b) 20 mM, and (c) 60 mM.

To ensure the formation of a thin ePEDOT film on the LFP cathode, the concentration of 20 mM was chosen. Figure 4.19a shows the chronoamperogram for the e-polymerization of EDOT on the LFP cathode by the CA method at 4.10 V for 800 s. The CA curve shows a similar feature to that obtained using a carbon paper substrate. The cycling performance of unmodified and ePEDOT modified LFP cathodes were then evaluated by galvanostatic cycling (Figure 4.19c). Compared with the unmodified LFP cathode, the ePEDOT modified one shows smaller polarizations at both 0.1 and 1 C (Table 4.2). The potential difference (ΔE) at 70 mA h g⁻¹ and 1 C was calculated to be 81 mV for the modified cathode, which is much smaller than that of the unmodified one (141 mV), indicating ePEDOT can effectively reduce the polarization. The specific capacities at 0.1 C (1st cycle in Figure 4.19c) for the modified and unmodified cathodes are close (160.4 vs. 160.2 mA h g⁻¹), but at the capacity 1 C (4th cycle in Figure 4.19c) for the modified (141.2 mA h g⁻¹) is much higher than that of the unmodified (132.4 mA h g⁻¹). The smaller polarization and the improved capacity at 1 C for the ePEDOT modified cathode can be attributed to the increased conductivity of the cathode by ePEDOT. As discussed earlier in this chapter, the potential range of 2–4.2 V can keep ePEDOT doped and conductive during

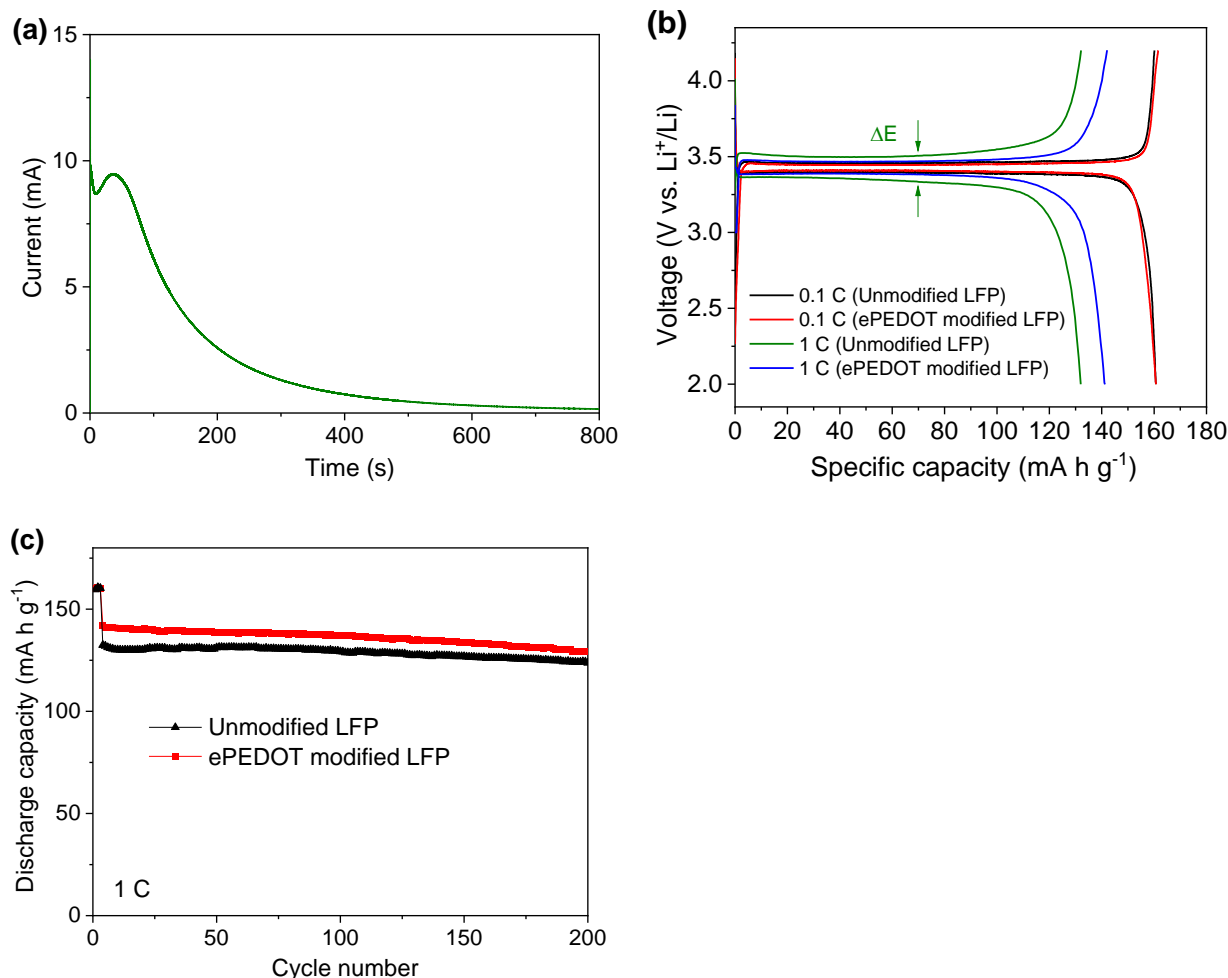


Figure 4.19 Application of ePEDOT in the LFP cathode. (a) Chronoamperogram for the e-polymerization of EDOT on the LFP cathode by the CA method at 4.10 V for 800 s. (b) Charge/discharge curves at different rates for unmodified and ePEDOT modified LFP cathodes. The voltage range is 2~4.2 V. (c) Cycling performances of unmodified and ePEDOT modified LFP cathodes at 1 C. The first three cycles were conducted at 0.1 C as an activation process.

electrochemical cycling, thereby enhancing conductivity of the LFP cathode. Furthermore, the in-situ synthesis method ensures good contact among ePEDOT, Super P particles and LFP particles, which also contributes to the improved electronic conduction. After 200 cycles, the unmodified cathode had a capacity of 123.7 mA h g⁻¹, corresponding to capacity retention of 93.4% (with respect to the 4th cycle), while the modified cathode maintained a capacity of 129.4 mA h g⁻¹,

corresponding to a capacity retention of 91.6%. The specific capacity of the modified cathode is still higher than the unmodified one, indicating that the positive effects of ePEDOT remained after long cycling. On the other hand, the ePEDOT modification did not improve the cycling stability of the LFP cathode, since the causes for the capacity fading of these LFP cathodes may be related to mechanisms that cannot be addressed by ePEDOT,^{165,166} such as side reactions between the electrolyte and electrode,^{167,168} detrimental impurities such as traces of water,¹⁶⁹ and dendrite formation in the Li anode.¹⁷⁰

Table 4.2 Features of unmodified and ePEDOT modified LFP cathodes.

	ΔE at 0.1 C	ΔE at 1 C	Capacity at the 1 st cycle (0.1 C)	Capacity at the 4 th cycle (1 C)	Capacity at the 200 th cycle (1 C)	Capacity retention in the 200 th cycle relative to the 4 th cycle
Unmodified LFP cathode	43 mV	141 mV	160.2	132.4	123.7	93.4%
ePEDOT modified LFP cathode	38 mV	81 mV	160.4	141.2	129.4	91.6%

4.4 Conclusions

In-cell e-polymerization of EDOT to produce a conductive polymer ePEDOT as a binder in the cathode of a Li-S battery is explored as a simple approach to improve the battery performance. It was found that the e-polymerization of an EDOT-containing electrolyte at a potential of 4.10 V vs. Li⁺/Li for 800 s using chronoamperometry could form an ePEDOT:H-PSS or ePEDOT:Li-PSS binder in the sulfur cathode in the presence of an H-PSS or Li-PSS pre-binder. The Li-S batteries with the ePEDOT:H-PSS or ePEDOT:Li-PSS binder prepared by in-cell e-polymerization showed notably improved specific capacity, cycling stability, and rate performance compared to the cell prepared using the analogous commercial cPEDOT:PSS binder. The enhanced performance is attributed to the tightly integrated interfaces between the ePEDOT and

other components including Super P in the cathode, where the trapped lithium polysulfides by ePEDOT might be in close proximity to Super P for efficient charge transfer.

Through a comparison of the redox profiles of the sulfur cathode and ePEDOT:H-PSS under identical conditions, it was found that ePEDOT might be dedoped within the typical Li-S battery cycling potential window of 1.7–2.8 V vs. Li^+/Li . The EIS measurements of ePEDOT further confirmed that the conductivity decreases with decreasing potential in the range of 1.7–2.8 V vs. Li^+/Li . These results indicate that PEDOT (ePEDOT or cPEDOT) and most other CPs may not contribute as much to the enhancement of the electrical conductivity of the cathode as previously expected in Li-S batteries. However, this issue may be alleviated in batteries with higher charge/discharge potentials or a conductive polymer with relatively low oxidation (doping) and reduction (dedoping) potentials. Nonetheless, this study offered a novel, facile, and low-cost in-cell e-polymerization method to produce a conductive polymer binder to boost the performance of Li-S batteries and potentially other types of rechargeable batteries.

Finally, the in-situ e-polymerization method has been applied in the LFP cathode. Smaller polarization and improved capacity at high rate are achieved with the ePEDOT modification. The ePEDOT can be electrochemically doped and become conductive during the cycling of the LFP cathode, which facilitates the electron transport.

Chapter 5. A Stable 2,5-Dihydroxy-1,4-benzoquinone (DHBQ) Based Organic Cathode Enabled by Coordination Polymer Formation and Binder Optimization

5.1 Introduction

With the merits of low cost, sustainability, environmental benignity, structural designability, and versatility in metal-ion batteries (Li-ion, Na-ion, K-ion, Zn-ion, Mg-ion), organic cathode materials have stimulated considerable research interest for the past few decades.^{54,171} Among the various electroactive functional groups, quinone group has been studied intensively due to its excellent electrochemical reversibility, high specific capacity, and high working potential.¹⁷² The biggest challenge to hinder the application of quinone cathodes is their high solubility in liquid electrolytes which results in low utilization of the quinone groups and fast capacity decay. A variety of strategies have been proposed to solve this challenge, including polymerization,^{57,65} formation of macrostructures,^{85,173} formation of metal complexes (coordination polymers),^{174,175} formation of covalent organic frameworks (COFs),^{68,153} salification (formation of organic salts),^{74,171} nanocomposite formation with mesoporous carbons,^{78,79} the use of solid electrolytes,⁸⁵ and binder/electrolyte optimization.^{55,176,177}

Recently, coordination polymers (CPs) and metal organic frameworks (MOFs) have emerged as new promising candidates for electrochemical energy storage.^{178,179} Among various CPs and MOFs, those containing the 2,5-dihydroxy-1,4-benzoquinone (DHBQ) ligand show interesting electrical and magnetic properties in addition to the electrochemical properties for energy storage.^{180,181} The formation of one-dimensional (linear) coordination polymers using divalent metal ions and the DHBQ ligand was reported as early as the 1950s,^{182,183} while their crystal structures were identified much later in 2009.^{184,185} Surprisingly, the electrochemical properties of these compounds have not been systematically studied yet. On the other hand, a coordination polymer can also be formed between the monovalent ion (Li^+) and the DHBQ ligand, but the specific capacity of this compound is low and decays rapidly (163 mA h g^{-1} in the initial cycle and 137 mA h g^{-1} in the 10th cycle).¹⁸⁶

In this paper, a series of one-dimensional coordination polymers were prepared using the first row of the transition metals (Ni, Co, Mn, Zn, and Cu) and the DHBQ ligand. The

electrochemical properties of these compounds were systematically investigated. We demonstrate that the formation of coordination polymer is a highly effective strategy to reduce the solubilities of small organic molecules in the electrolyte. Moreover, it has been found that the coordination polymers M-DHBQ·2H₂O (M=Ni, Co, Mn, and Zn) exhibit the redox activities of both metal and ligand in the potential range around 0.5~3 V, while the coordination polymer Cu-DHBQ exhibits the redox activity of the ligand only in the same potential range. In the potential range around 1.3~3 V where only the ligand is redox active, Cu-DHBQ exhibits the highest capacity among the as-synthesized coordination polymers. Furthermore, the UV-Vis results show that the capacity decay of Cu-DHBQ cathode is caused by the dissolution of discharged product or intermediate in the electrolyte. By using alginate binder (with the content of 25 wt% in the cathode) which can strongly bond the electrode film and effectively trap the soluble species, Cu-DHBQ cathode exhibits a high initial capacity of 212 mA h g⁻¹ (80% of the theoretical capacity) at the current rate of 100 mA g⁻¹, and can maintain a capacity of 194 mA h g⁻¹ after 200 cycles at 100 mA g⁻¹ with a capacity retention of 91.5%. Finally, our approach for coordination polymer synthesis is very versatile and can be extended to the synthesis of other structurally similar coordination polymers by varying the organic ligand, such as DHBQ-Cl which has a higher discharge voltage than that of DHBQ. Our results show the promise of coordination polymers as emerging organic electrode materials for energy storage.

5.2 Experimental section

5.2.1 Preparation of coordination polymers

2,5-dihydroxy-1,4-benzoquinone (DHBQ), nickel acetate tetrahydrate (Ni(OAc)₂·4H₂O), cobalt acetate tetrahydrate (Co(OAc)₂·4H₂O), manganese acetate tetrahydrate (Mn(OAc)₂·4H₂O), zinc acetate tetrahydrate (Zn(OAc)₂·4H₂O), anhydrous copper chloride (CuCl₂), sodium alginate from brown algae (Product No. A2033, medium viscosity), and sodium carboxymethyl cellulose (CMC, Mw ~700,000) were all purchased from Sigma Aldrich and used as received. Polyvinylidene fluoride (PVDF, Kynar HSV 900, Mw ~1 million) was purchased from Arkema.

Preparation of M-DHBQ·2H₂O (M=Ni, Co, Mn, and Zn) and Cu-DHBQ: DHBQ (1 g, 7.14 mmol) was added to 400 mL of DI H₂O in an open Erlenmeyer flask, and heated with vigorous stirring at 90 °C for half an hour. Then another pre-warmed (at 50 °C) solution containing the metal salt (Ni(OAc)₂·4H₂O (4 g, 16.08 mmol), Co(OAc)₂·4H₂O (4 g, 16.06 mmol),

Mn(OAc)₂·4H₂O (4 g, 16.32 mmol), Zn(OAc)₂·2H₂O (4 g, 18.22 mmol), and anhydrous CuCl₂ (4 g, 29.74 mmol) in 50 mL DI H₂O was added slowly into the DHBQ solution. After that the mixture continued to be heated at 90 °C for 1 h with strong stirring. Then the mixture was cooled to room temperature naturally. The solid was recovered by centrifugation, washed with DI water and ethanol, then dried at 60 °C. Yield: Ni-DHBQ·2H₂O (90%), Co-DHBQ·2H₂O (93%), Mn-DHBQ·2H₂O (78%), Zn-DHBQ·2H₂O (80%), Cu-DHBQ (88%).

5.2.2 Material characterizations and electrochemical measurements

X-ray diffraction (XRD) measurement was conducted on a Bruker D8 Discover X-ray diffractometer. Thermogravimetric analysis (TGA) was performed using a TA Instruments Q500 analyzer under N₂ atmosphere with a heating rate of 10 °C min⁻¹. Fourier-transform infrared spectrum (FTIR) was collected with a PerkinElmer Spectrum 100 FTIR spectrometer. UV-Vis spectrum was obtained with a Cary 7000 Universal Measurement Spectrophotometer (UMS). Peel test was performed using a Universal Macro-Tribometer (UNMT-2MT, Centre for Tribology Inc.) equipped with a 1 kg load cell.

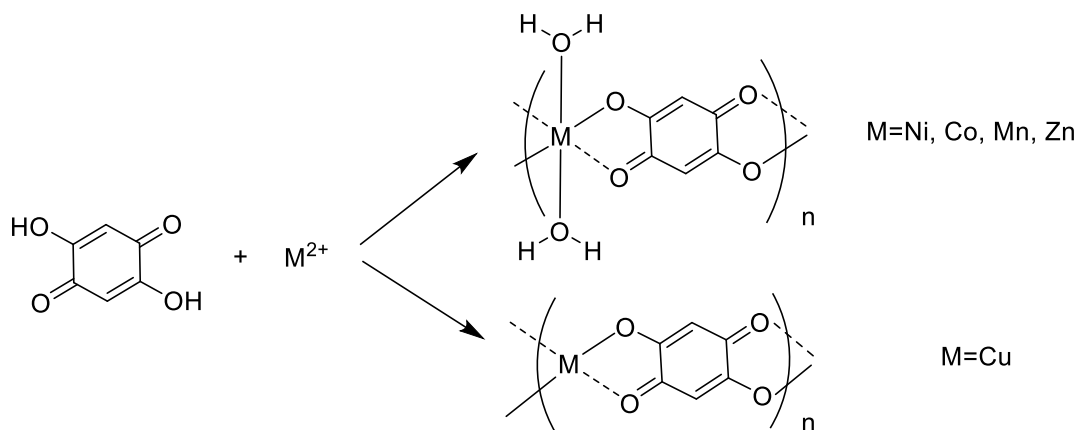
The electrode films were prepared by the doctor blading method. For the preparation of electrode films with 10 wt%, 15 wt%, 20 wt%, 25 wt%, 40 wt% binder, the weight ratios of active material : Super P : binder = 6 : 3 : 1, 5.5 : 3 : 1.5, 5 : 3 : 2, 4.5 : 3 : 2.5, 3 : 3 : 4 were used, respectively. For the preparation of slurries, 1-Methyl-2-Pyrrolidone (NMP) was used as the dispersing solvent for PVDF binder, and water was used for alginate and CMC binders. The slurry was ground in a mortar with a pestle manually. The areal loading of the active material in the cathode film is 0.9~1.1 mg cm⁻². The assembly of CR2032 coin cells was conducted in an Ar-filled glovebox with O₂ and H₂O levels below 0.1 ppm. 25 μL of the electrolyte, 1 M LiTFSI in 1:1 (v:v) 1,3-dioxolane (DOL)/1,2-dimethoxyethane (DME), was added to each cell. The CV and EIS measurements were recorded on a VMP3 Bio-Logic potentiostat. Galvanostatic cycling of the cells was performed with LAND CT2001A battery testers at room temperature.

UV-Vis measurement on a cycled cell: after cycling, the cell was disassembled in a glovebox, all the cell components including cell cases, cathode film, Li anode film and separator were soaked in 3 mL of stabilizer-free DME, gently shook, and then the supernatant was taken out for UV-Vis measurement.

5.3 Results and discussion

5.3.1 Synthetic route and material characterizations

The M-DHBQ·2H₂O (M=Ni, Co, Mn, and Zn) or M-DHBQ (M=Cu) coordination polymers were synthesized according to Bottei and Fangman's method,¹⁸³ as shown Scheme 5.1.



Scheme 5.1 Schematic for the synthesis of M-DHBQ (M=Ni, Co, Mn, Zn, and Zn) coordination polymers.

The FTIR spectra of DHBQ and the as-synthesized coordination polymers are shown in Figure 5.1a, which are similar to those reported by other groups.^{183,187} The detailed assignment of the peaks is shown in Table 5.1. In brief, DHBQ shows O-H stretching from hydroxyl group at 3296 cm^{-1} , C=O stretching at 1709 cm^{-1} , C=C stretching at 1608 cm^{-1} , O-H in plane bending at 1375 cm^{-1} , C-O stretching from 1101 to 1303 cm^{-1} , O-H out-of-plane bending from 650 to 771 cm^{-1} . By contrast, the M-DHBQ·2H₂O (M=Ni, Co, Mn, and Zn) coordination polymers show O-H stretching from coordinated water molecules at $\sim 3300\text{ cm}^{-1}$, C=O stretching at 1650 cm^{-1} , C=C stretching at $\sim 1520\text{ cm}^{-1}$, O-H in plane bending at $\sim 1380\text{ cm}^{-1}$, C-O stretching at $\sim 1260\text{ cm}^{-1}$, O-H out-of-plane bending at $\sim 770\text{ cm}^{-1}$. The coordination polymers show additional peaks from 450 to 520 cm^{-1} , which are ascribed to the M-O (M=Ni, Co, Mn, Zn) stretching and bending vibrations.^{188,189} Compared with other coordination polymers (Ni, Co, Mn, Zn), the Cu coordination polymer (Cu-DHBQ) shows C=O stretching, C=C stretching, O-H in plane bending, C-O stretching, O-H out-of-plane bending, and M-O stretching and bending vibrations at similar

positions. However, the Cu coordination polymer does not show O-H stretching at $\sim 3300\text{ cm}^{-1}$, indicating it does not contain any coordinated water molecules.

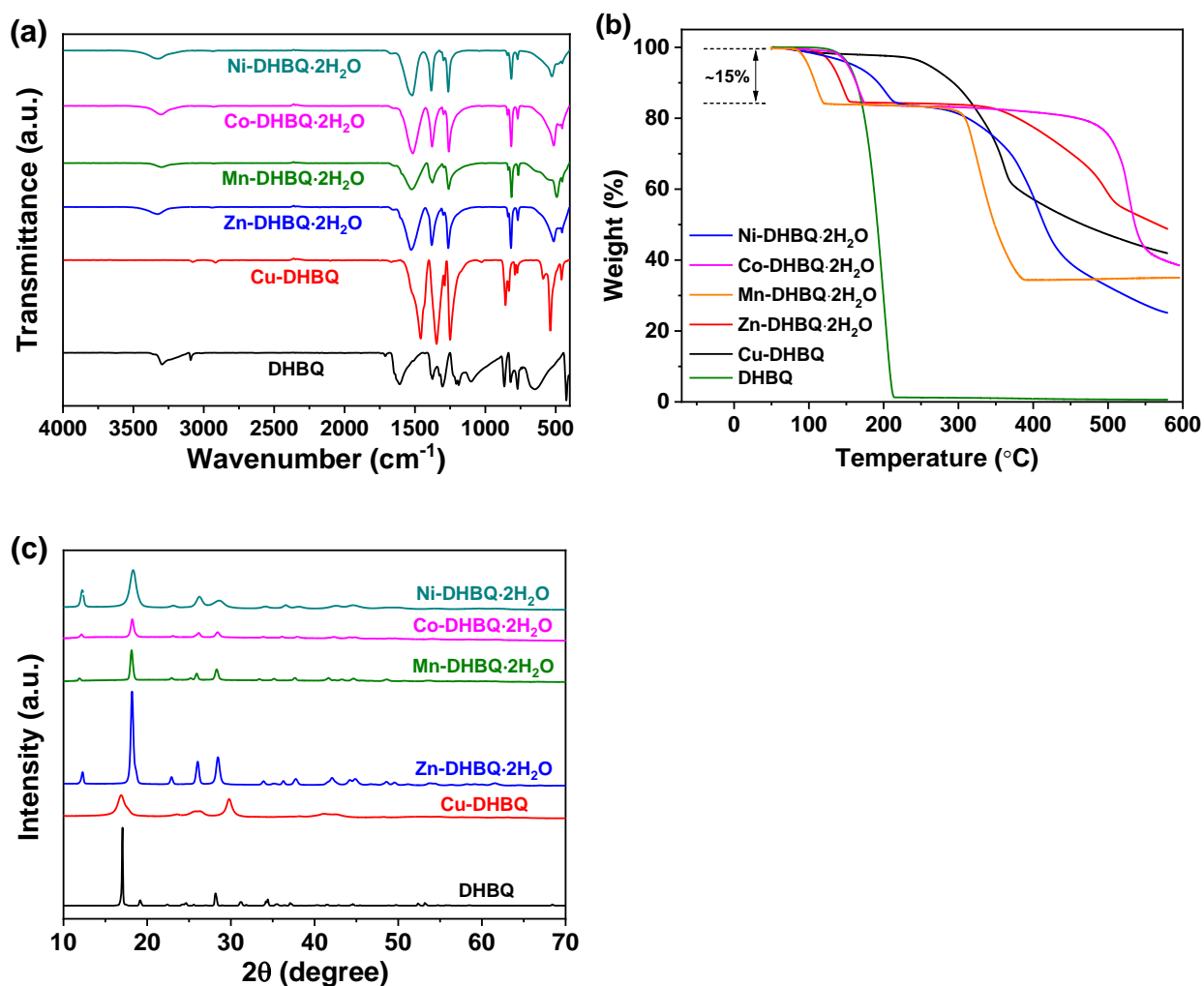


Figure 5.1 FTIR, TGA, and XRD data of as-prepared coordination polymers. (a) FTIR spectra, (b) TGA data with N_2 atmosphere and a heating rate of $10\text{ }^{\circ}\text{C min}^{-1}$, and (c) XRD data.

In the TGA data (Figure 5.1b), the 1st stage weight losses, due to the removal of coordinated water molecules, for the coordination polymers (Ni, Co, Mn, Zn) are 15.64%, 15.70%, 15.45%, 15.34%, respectively, which agrees well with the theoretical water contents of these compounds (Table 5.2). By contrast, the 1st stage weight loss for the Cu coordination polymer is only 2.02%, which may be caused the removal of moisture contained in the compound. This implies that the Cu-coordination polymer does not contain any coordinated water molecule, which is consistent with the FTIR data. DHBQ starts to decompose at $110\text{ }^{\circ}\text{C}$, while the anhydrous

coordination polymers (after the removal of coordinated water), Ni, Co, Mn, Zn, and Cu, start to decompose at 218, 300, 235, 318, and 210 °C, respectively, suggesting the formation of coordination polymers dramatically enhances the thermal stability of DHBQ.

The XRD data (Figure 5.1c) of Ni, Co, Mn, Zn coordination polymers are similar to those reported by other groups,^{184,185,190} confirming the formation of one-dimensional coordination polymers.

Table 5.1 The assignment of the peaks in the FTIR spectra of as-synthesized coordination polymers.

	O-H stretching / cm ⁻¹	=C-H stretching / cm ⁻¹	C=O stretching / cm ⁻¹	O-H bending (in-plane) / cm ⁻¹	C-O stretching / cm ⁻¹	=C-H bending / cm ⁻¹	O-H bending (out-of-plane) / cm ⁻¹	M-O stretching & bending (M=Ni, Co, Mn, Zn, and Cu) / cm ⁻¹
Ni-DHBQ·2H ₂ O	3325 (from water)	2937	1663, 1519	1382	1263	815	771	526, 453
Co-DHBQ·2H ₂ O	3304 (from water)	2928	1648, 1516	1379	1259	815	769	514, 453
Mn-DHBQ·2H ₂ O	3298 (from water)	2928	1639, 1525	1375	1259	813	765	493, 453
Zn-DHBQ·2H ₂ O	3327 (from water)	2942	1648, 1527	1381	1263	817	769	514, 455
Cu-DHBQ	absence	3079, 2919	1667, 1458	1346	1249	856, 833	788, 773	538, 459
DHBQ	3296 (from hydroxyl)	3093	1709, 1608	1375	1303, 1190, 1101	866, 821	771, 650	absent

Table 5.2 Molecular formula, molecular weight, theoretical and experimental water content, and the features about the TGA data of as-prepared coordination polymers.

	Molecular formula	Molecular weight (g mol ⁻¹)	Theoretical water content (%)	Temperature range for the 1 st stage weight loss (°C)	Water content corresponding to the 1 st stage weight loss (%)	Onset decomposition temperature after the removal of coordinated water (°C)
Ni-DHBQ·2H ₂ O	NiC ₆ H ₆ O ₆	232.8	15.5	60~218	15.64	218
Co-DHBQ·2H ₂ O	CoC ₆ H ₆ O ₆	233.0	15.5	80~178	15.70	300
Mn-DHBQ·2H ₂ O	MnC ₆ H ₆ O ₆	229.1	15.7	80~122	15.45	235
Zn-DHBQ·2H ₂ O	ZnC ₆ H ₆ O ₆	239.5	15.0	70~158	15.34	318
Cu-DHBQ	CuC ₆ H ₂ O ₄	201.6	0	58~170	2.02	210
DHBQ	C ₆ H ₄ O ₄	140.1	0			110

5.3.2 Electrochemical performance of as-synthesized coordination polymers

CV is used to investigate the electrochemical properties of the as-synthesized coordination polymers first. Alginate is used as the binder to prepare the cathode films as it has been reported to enhance the electrochemical performance of organic cathodes.¹⁷⁷ A wide potential range of 0.5~3.5 V is chosen for the CV testing to probe any possible electrochemical reactions. The spikes (noises) in Figure 5.2a is caused by experimental error. As shown in Figure 5.2, the electrochemical activity of these compounds in the potential range around 0.5~1.4 V can be attributed to the redox reactions of the metals, while the activity in the range around 1.4~3.5 V can be attributed to the redox reactions of the DHBQ ligand.^{186,191-194} Interestingly, it can be seen that Cu-DHBQ shows the activity of only the ligand while the other coordination polymers show the activities of both the ligand and the metal. This might be attributed to the different crystal structures between Cu-DHBQ and other coordination polymers (M-DHBQ·2H₂O, M=Ni, Co, Mn, Zn) (Figure 5.1c). The absence of coordinated water molecules in Cu-DHBQ may influence the packing of polymer chains and consequently the electronic structure of Cu-DHBQ, making it difficult/impossible for Cu^{II} to gain electrons to be reduced to Cu⁰ in the potential range of 0.5~1.4 V.

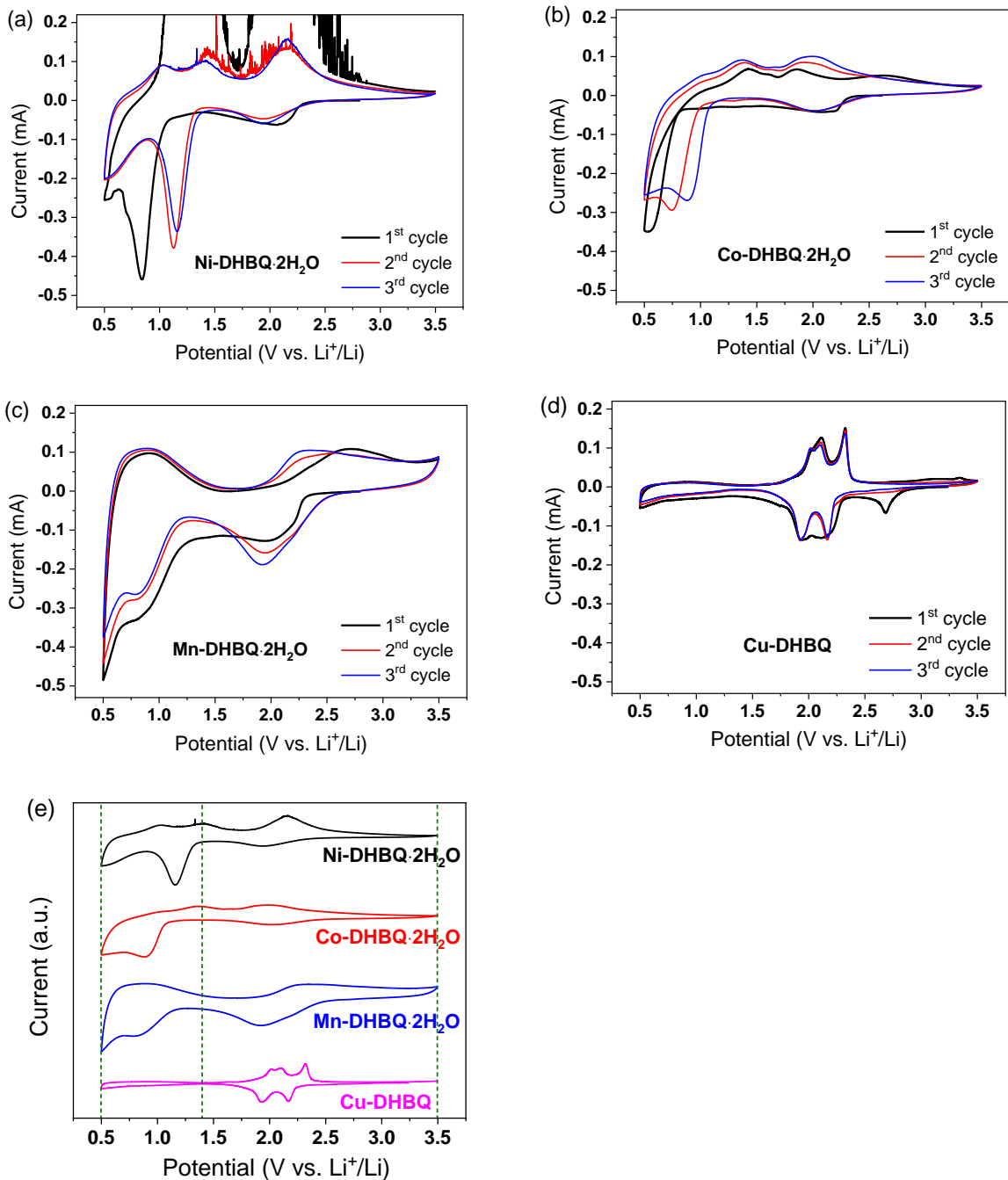


Figure 5.2 CV testing of as-prepared coordination polymers. CV curves of as-synthesized coordination polymers in the potential range of 0.5~3.5 V with a scan rate of 0.05 mV s⁻¹: (a) Ni-DHBQ·2H₂O, (b) Co-DHBQ·2H₂O, (c) Mn-DHBQ·2H₂O, and (d) Cu-DHBQ. (e) The 3rd cycle of the CV curve. The dashed lines separate the potential range into two regions, 0.5~1.4 V and 1.4~3.5 V. The cathode compositions for the CV testing are active material : Super P : alginate binder=6:3:1.

The theoretical capacities of as-synthesized coordination polymers are shown in Table 5.3. Firstly, the galvanostatic cycling performances of these compounds are evaluated in the potential range where the redox activities of both metal and ligand are involved. While the upper potential limit is fixed at 3 V, the lower potential limit is varied to avoid undesired side reactions. Specifically, the potential ranges for Ni-DHBQ·2H₂O, Co-DHBQ·2H₂O, and Mn-DHBQ·2H₂O are 0.88~3, 0.68~3, and 0.68~3 V, respectively. Cu-DHBQ is also cycled in a similar potential range (0.8~3 V) for comparison, although the metal Cu does not participate in the electrochemical reactions, as indicated by the CV testing. In the voltage profiles of Ni-DHBQ·2H₂O, Co-DHBQ·2H₂O, and Mn-DHBQ·2H₂O (Figures 5.3a-c), the plateaus at 0.68 (or 0.88)~1.4 V and 1.4~3 V are assigned to the redox reactions of metal and DHBQ ligand, respectively, which agrees well with the respective CV curves. In the voltage profile of Cu-DHBQ (Figure 5.3d), two plateaus are observed, one at 1.4~2 V, and the other at 2~3 V, which is consistent with the CV curve of Cu-DHBQ. However, these two plateaus are assigned to the stepwise redox reactions of DHBQ ligand (one DHBQ molecule contains two carbonyl groups). The experimentally obtained 1st discharge capacities and theoretical capacities of as-synthesized coordination polymers are shown in Table 5.3. Except for Mn-DHBQ·2H₂O, the 1st discharge capacities of the other three compounds are all much larger than the theoretical values. This phenomenon is common for organic cathodes, which can be explained by the formation of solid electrolyte interface (SEI),^{69,192,195} large volume expansion during the first lithiation.⁶⁹ All the electrodes show drastic capacity decays in the first few cycles, partly due to the change in the current rate from 20 mA g⁻¹ to 100 mA g⁻¹ in the 3rd cycle, and the other due to the intrinsic properties of the materials. Starting from the 4th cycle for Ni-DHBQ·2H₂O, the 6th cycle for Co-DHBQ·2H₂O, the 4th cycle for Mn-DHBQ·2H₂O, and the 2nd cycle for Cu-DHBQ, the capacity change after each cycle is much smaller and nearly constant. And the capacities at these cycle numbers are 414.2 mA h g⁻¹ for Ni-DHBQ·2H₂O, 424.7 mA h g⁻¹ for Co-DHBQ·2H₂O, 68.8 mA h g⁻¹ for Mn-DHBQ·2H₂O, and 280.3 mA h g⁻¹ for Cu-DHBQ. The capacities at these cycle numbers are more reversible than those at previous cycles and can be considered as the true capacities of these materials. The higher capacities of Ni-DHBQ·2H₂O and Co-DHBQ·2H₂O than that of Cu-DHBQ is consistent with their respective charge storage mechanisms, four electrons transferred for the former while two electrons transferred for the latter. After 60 cycles, the capacities for Ni-DHBQ·2H₂O, Co-DHBQ·2H₂O, Mn-DHBQ·2H₂O, and Cu-DHBQ are 268.3, 264.4, 81.2, and 135.2 mA h g⁻¹, respectively. Somehow the Mn-DHBQ·2H₂O

electrode shows a slow but steady increase in the capacity after the 4th cycle, indicating a slow activation process, which is similar to the phthalocyanine-based covalent organic framework electrode¹⁹⁶ and might be caused by the slow diffusion of Li⁺ ions into the pores of the material to reach the active sites of the material.

Table 5.3 Molecular formula, molecular weight, and theoretical capacities of as-prepared coordination polymers.

	Molecular formula	Molecular weight (g mol⁻¹)	Theoretical capacity for the redox reaction of metal (mA h g⁻¹)^a	Theoretical capacity for the redox reaction of ligand (mA h g⁻¹)	Total theoretical capacity (mA h g⁻¹)	1st discharge capacity (mA h g⁻¹)
Ni-DHBQ·2H₂O	NiC ₆ H ₆ O ₆	232.8	230.2	230.2	460.4	751.0
Co-DHBQ·2H₂O	CoC ₆ H ₆ O ₆	233.0	230.1	230.1	460.2	1085.5
Mn-DHBQ·2H₂O	MnC ₆ H ₆ O ₆	229.1	234.0	234.0	468	207.7
Zn-DHBQ·2H₂O	ZnC ₆ H ₆ O ₆	239.5	223.8	223.8	447.6	—
Cu-DHBQ	CuC ₆ H ₂ O ₄	201.6	0	265.9	265.9	547.8

^a The valence of metal in the as-prepared coordination polymers is assumed to be +2, and the redox reaction of metal is metal^(II) ⇌ metal⁽⁰⁾.

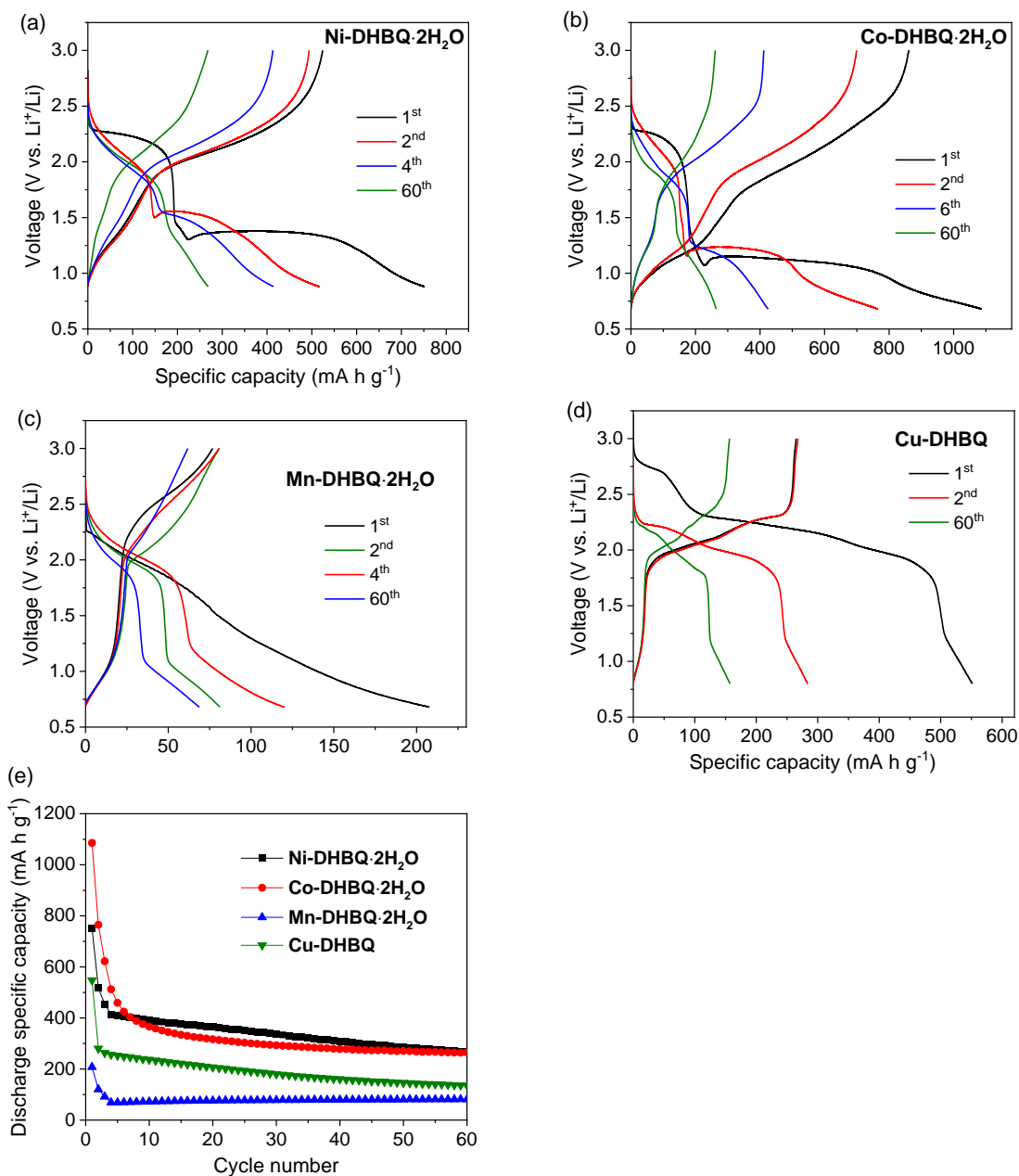


Figure 5.3 Battery performance of as-synthesized coordination polymers involving the redox reactions of both metal and ligand. Charge/discharge curves of (a) Ni-DHBQ·2H₂O, (b) Co-DHBQ·2H₂O, (c) Mn-DHBQ·2H₂O, and (d) Cu-DHBQ. The first two cycles were tested at 20 mA g⁻¹, and the rest at 100 mA g⁻¹. (e) Cycling performances of as-synthesized coordination polymers at 100 mA g⁻¹. The electrodes were activated at 20 mA g⁻¹ for two cycles and cycled at 100 mA g⁻¹ afterwards. The potential ranges for Ni-DHBQ·2H₂O, Co-DHBQ·2H₂O, Mn-DHBQ·2H₂O, and Cu-DHBQ are 0.88~3 V, 0.68~3 V, 0.68~3 V, and 0.8~3 V, respectively. The cathode compositions are active material : Super P : alginate binder=6:3:1.

Secondly, the galvanostatic cycling performances of as-synthesized coordination polymers are compared in the potential range where the redox activity of the ligand only is involved (Figure 5.4). Starting from the 4th cycle for all the compounds, the capacity change after each cycle is much smaller compared with the first three cycles. And the capacities at these cycle numbers are 55.7 mA h g⁻¹ for Ni-DHBQ·2H₂O, 58.5 mA h g⁻¹ for Co-DHBQ·2H₂O, 29.9 mA h g⁻¹ for Mn-DHBQ·2H₂O, and 221.8 mA h g⁻¹ for Cu-DHBQ. These reversible capacities are used to obtain the initial utilizations of the carbonyl groups, which is calculated by dividing the reversible capacity with the theoretical capacity. The utilizations follow the order of Cu-DHBQ (83.4%) > Co-DHBQ·2H₂O (25.4%) ≈ Ni-DHBQ·2H₂O (24.2%) > Mn-DHBQ·2H₂O (12.8%), indicating Cu-DHBQ has the highest utilization. With the average discharge voltage of ~2 V vs. Li⁺/Li and the experimental capacity of 221.8 mA h g⁻¹, Cu-DHBQ has the potential to be used as a high energy cathode material. After 35 cycles, the capacities for Ni-DHBQ·2H₂O, Co-DHBQ·2H₂O, Mn-DHBQ·2H₂O, and Cu-DHBQ are 52.1, 72.7, 38.2, and 170.2 mA h g⁻¹, respectively. The Ni-DHBQ·2H₂O, Co-DHBQ·2H₂O, and Mn-DHBQ·2H₂O electrodes show a slow increasing in the capacity after the 4th cycle, indicating a slow activation process for these electrodes. By contrast, the Cu-DHBQ electrode shows a gradual capacity decay after the 4th cycle, with a capacity retention of 76.7% after 35 cycles.

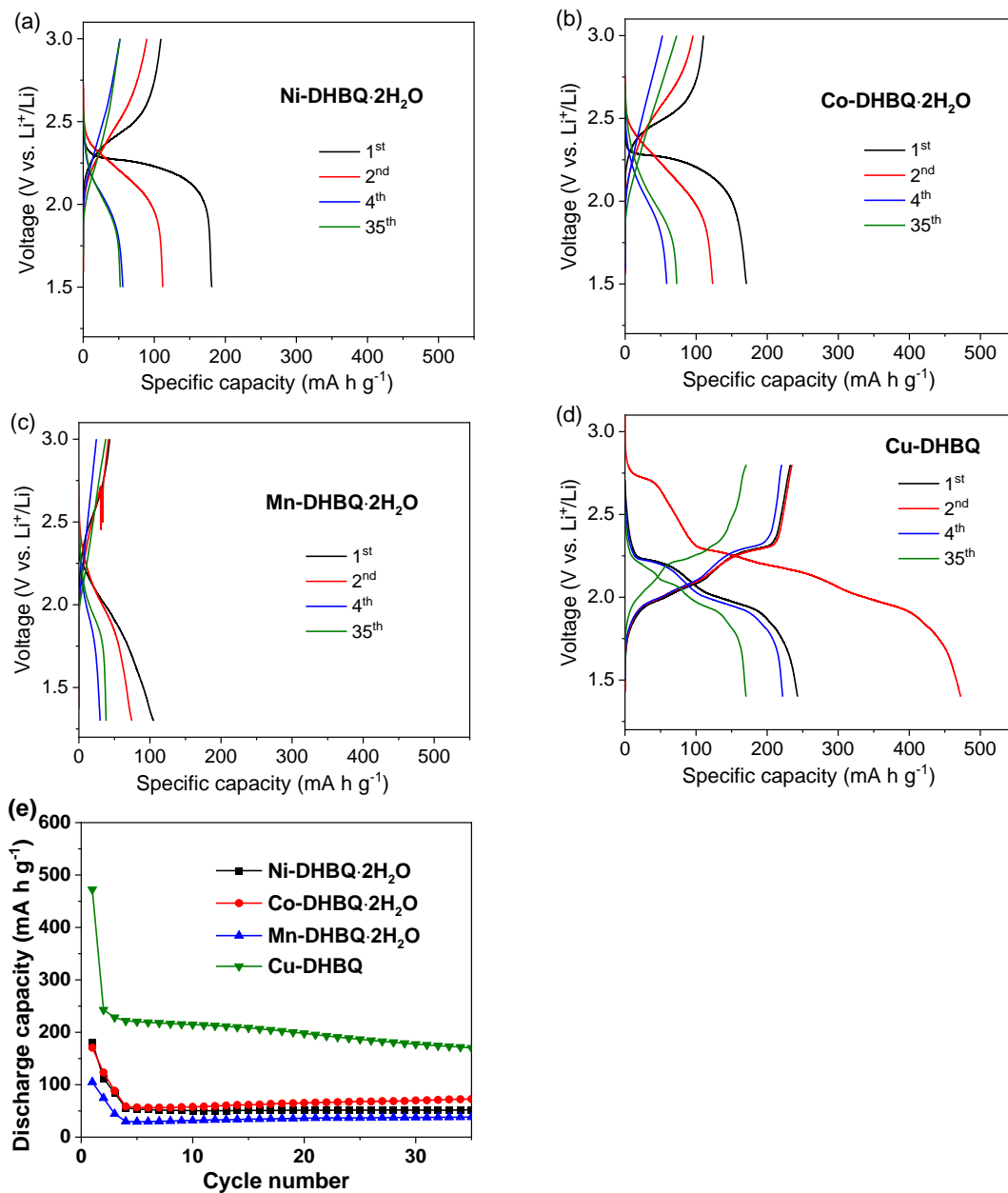


Figure 5.4 Battery performance of as-synthesized coordination polymers involving the redox reaction of the ligand only. Charge/discharge curves (a) Ni-DHBQ·2H₂O, (b) Co-DHBQ·2H₂O, (c) Mn-DHBQ·2H₂O, and (d) Cu-DHBQ. The first two cycles were tested at 20 mA g⁻¹, and the rest at 100 mA g⁻¹. (e) Cycling performances of as-synthesized coordination polymers at 100 mA g⁻¹. The electrodes were activated at 20 mA g⁻¹ for two cycles and cycled at 100 mA g⁻¹ afterwards. The potential ranges for the cycling test of Ni-DHBQ·2H₂O, Co-DHBQ·2H₂O, Mn-DHBQ·2H₂O, and Cu-DHBQ are 1.5~3 V, 1.5~3 V, 1.3~3 V, and 1.4~2.8 V, respectively. The cathode compositions are active material : Super P : alginate binder=6:3:1.

5.3.3 Optimization on the electrochemical performance of Cu-DHBQ cathode

The most common cause for the capacity decay of organic electrodes is the dissolution of the electrode materials, including the starting material and the discharged intermediates or products, in the electrolyte.^{54,64} To verify this, the solubilities of DHBQ and the as-prepared coordination polymers were measured by UV-Vis spectroscopy first. The DHBQ saturated solution was prepared by dissolving DHBQ in the electrolyte, 1 M LiTFSI in 1:1 (v:v) DOL/DME. Then the saturated solution was diluted by inhibitor-free DME for different times to prepare a set of standard solutions. The saturated solutions of as-synthesized coordination polymers were prepared by dissolving the compounds in the electrolyte. To investigate how different solvents (electrolyte, DOL/DME (v:v=1:1), or DME) influence the solubilities of the coordination polymers, DOL/DME and DME were also used to prepare the saturated solutions for Ni-DHBQ·2H₂O and Cu-DHBQ. All the solutions were prepared at room temperature. As shown in Figure 5.5a, DHBQ shows shoulder peaks at 280 and 286 nm, which is attributed to the $\pi \rightarrow \pi^*$ transition of the -C=C- bond in the benzene ring.¹⁹⁷ The molar absorptivity (ϵ) for the peak at 280 nm for DHBQ determined from the fitting is 19539 L·mol⁻¹·cm⁻¹ (Figure 5.5b), and the solubility of DHBQ in the electrolyte is 9.6 g L⁻¹. By contrast, the coordination polymers show a strong single peak at 240 nm, and a broad weak peak at 285-343 nm (Figure 5.5c), which might be attributed to the absorption of the DHBQ ligand in the middle and at the edges of the polymer chain, respectively.^{197,198} By assuming the molar absorptivity for the peak at 240 nm for the coordination polymers is the same as that for the peak at 280 nm for DHBQ, the solubilities of the coordination polymers in the electrolyte are: Ni-DHBQ·2H₂O (0.0064 g L⁻¹), Co-DHBQ·2H₂O (0.0067 g L⁻¹), Mn-DHBQ·2H₂O (0.0108 g L⁻¹), Zn-DHBQ·2H₂O (0.0078 g L⁻¹), and Cu-DHBQ (0.0063 g L⁻¹). Therefore, the solubilities of the coordination polymers are more than ~1000 times lower than that of DHBQ. By comparison, 2,5-diamino-1,4-benzoquinone (DABQ) shows a solubility of 0.084 g L⁻¹ in the same electrolyte,¹⁹⁹ indicating the strategy of coordination polymer formation is more effective than hydrogen-bond stabilization in reducing the solubilities of small organic molecules in the electrolyte. It should be noted that the intensity of the peak at 240 nm for Ni-DHBQ·2H₂O or Cu-DHBQ using the electrolyte as the solvent is slightly higher than using DOL/DME or DME as the solvent, suggesting the coordination polymers have slightly higher solubilities in the electrolyte than DOL/DME or DME (Figure 5.5d and e).

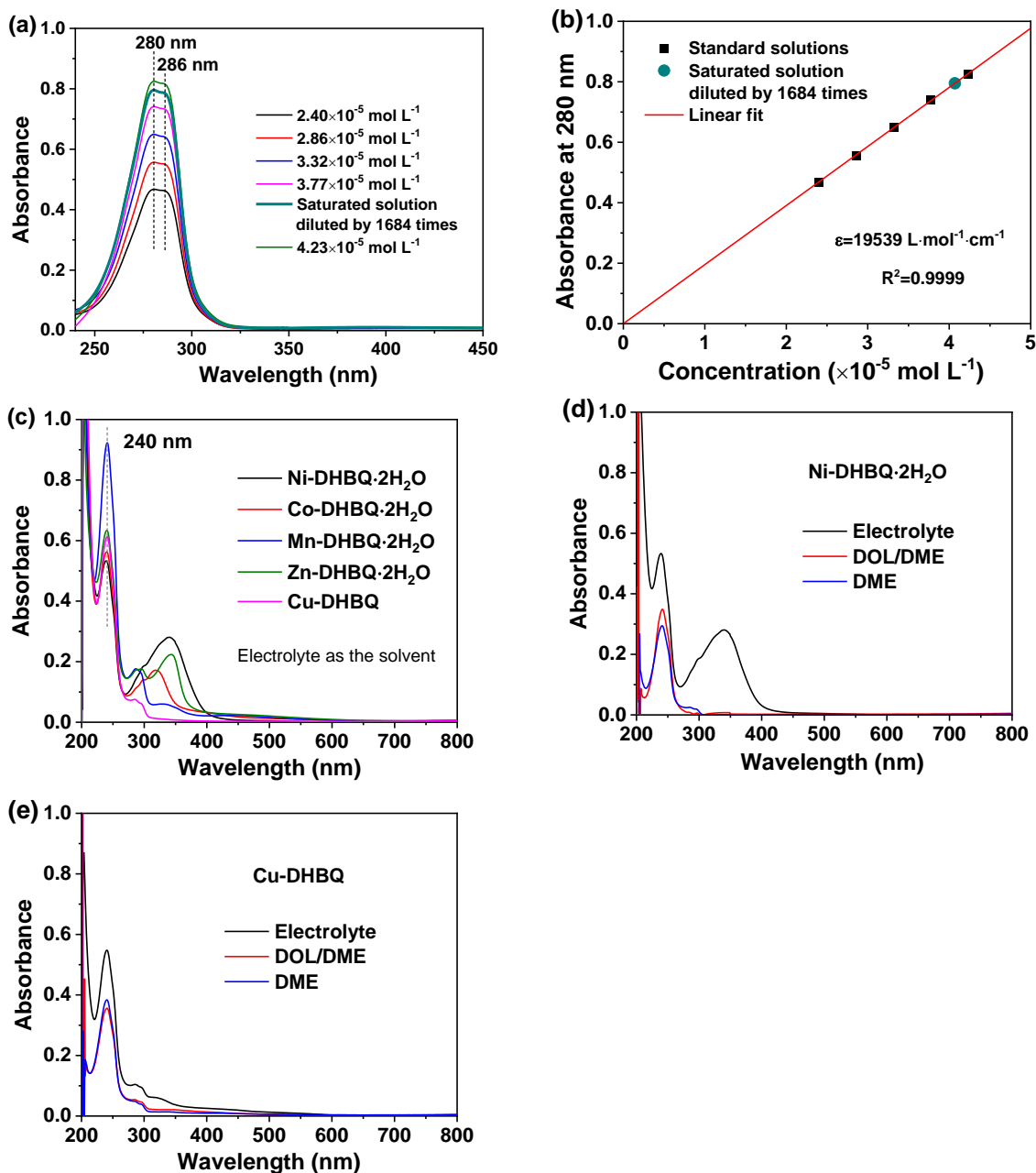


Figure 5.5 Determination of the solubilities of DHBQ and Ni-, Co-, Mn-, Zn-, and Cu-coordination polymers in the electrolyte by UV-Vis spectroscopy. (a) UV-Vis spectra of a set of lab-prepared DHBQ standard solutions and a saturated DHBQ solution diluted by 1684 times. The solvent is inhibitor-free DME. (b) Calibration curve for the as-prepared DHBQ standard solutions. The data point of a saturated DHBQ solution diluted by 1684 times is also shown. (c) UV-Vis spectra of a saturated Cu-DHBQ solution.

The calculation for the solubility of DHBQ using the Beer-Lambert Law is shown below:

The saturated DHBQ solution was prepared first, then it was diluted by $\left(\frac{3073}{73}\right) \times \left(\frac{1000}{25}\right) = 1684$ times for measuring the UV-Vis.

Concentration of the saturated DHBQ solution diluted by 1684 times:

$$c = \frac{A}{\varepsilon \cdot l} = \frac{0.795}{(19539 \text{ L} \cdot \text{mol}^{-1} \cdot \text{cm}^{-1}) \cdot (1 \text{ cm})} = 4.07 \times 10^{-5} \text{ mol L}^{-1}$$

Concentration of the as-prepared (undiluted) saturated DHBQ solution:

$$(4.07 \times 10^{-5} \text{ mol L}^{-1}) \times 1684 = 0.0685 \text{ mol L}^{-1}$$

Solubility of DHBQ (molecular weight of DHBQ is 140.1 g mol^{-1}):

$$(0.0685 \text{ mol L}^{-1}) \times (140.1 \text{ g mol}^{-1}) = 9.6 \text{ g L}^{-1}$$

The calculation of the solubility of Ni-DHBQ·2H₂O is shown below:

Concentration of the saturated Ni-DHBQ·2H₂O solution:

$$c = \frac{A}{\varepsilon \cdot l} = \frac{0.5325}{(19539 \text{ L} \cdot \text{mol}^{-1} \cdot \text{cm}^{-1}) \cdot (1 \text{ cm})} = 2.73 \times 10^{-5} \text{ mol L}^{-1}$$

Solubility of Ni-DHBQ·2H₂O (molecular weight of Ni-DHBQ·2H₂O is 232.8 g mol^{-1}):

$$(2.73 \times 10^{-5} \text{ mol L}^{-1}) \times (232.8 \text{ g mol}^{-1}) = 0.0064 \text{ g L}^{-1}$$

Since the solubility of the starting material Cu-DHBQ in the electrolyte is extremely low, the capacity fading may be caused by two reasons, one is the dissolution of its discharged intermediate or product in the electrolyte, and the other is the damage of the Cu-DHBQ particles after cycling leading to cracked particles which can fall off the cathode film due to loosened contact with the polymer binder. It was reported that the alginate binder can strongly interact with the carbonyl groups via hydrogen-bonding thereby preserving the structural integrity of the active material particle and enhancing the cycling performance.¹⁷⁷ The carboxymethylcellulose sodium

salt (CMC) binder also possesses abundant hydroxyl groups and should have similar hydrogen-bonding effect as alginate binder, while the PVDF binder is not expected to have such an effect. Next, the effect of these binders on the electrochemical performance of the Cu-DHBQ cathode is investigated.

The CV curves of Cu-DHBQ cathodes with different binders at the binder content of 10 wt% are compared (Figure 5.6). Regardless of the binder being used, the Cu-DHBQ cathode shows a reduction peak at 2.67 V in the 1st reduction process, which disappears after the 1st cycle. This irreversible peak may be attributed to the reduction of moisture trapped in the material.²⁰⁰ The comparison of the 3rd CV cycle is shown in Figure 5.6d. Compared with the cathode using PVDF binder, the peaks are much sharper and the areas under the curves (which represent capacities) are larger for the cathodes with alginate and CMC binders. For the 2nd redox process, the PVDF binder shows single peaks (C_2 and A_2), whereas the alginate and CMC binders show split peaks ($C_{2,a}$, $C_{2,b}$, $A_{2,a}$, $A_{2,b}$). The peak position of C_1 for different binders follows the order of alginate (2.19 V) \approx CMC (2.18 V) > PVDF (2.10 V), indicating the cathodes with alginate and CMC binders can be more easily reduced than that with the PVDF binder (Figure 5.6e). By contrast, the peak position of A_1 for the cathodes with different binders are close, alginate (2.32 V), CMC (2.33 V), and PVDF (2.30 V), indicating that the energy barriers of the oxidation process for the cathodes with different binders are similar (Figure 5.6e). The peak separations between C_1 and A_1 (Figure 5.6f), namely polarizations, for the cathodes with different binders follows the order of alginate (129 mV) < CMC (144 mV) < PVDF (202 mV), suggesting the cathodes with alginate and CMC binders have better kinetics than that with PVDF binder.

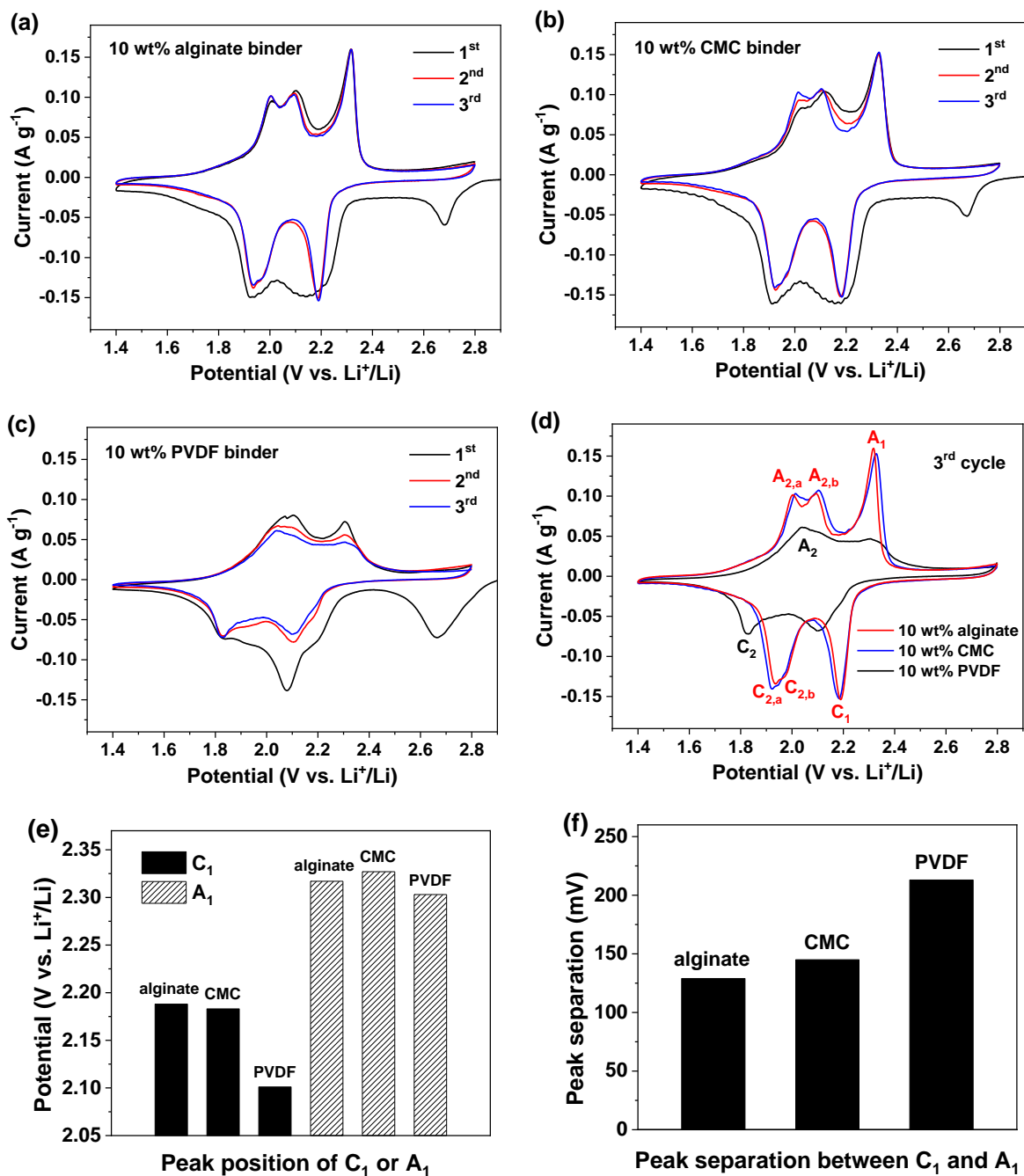


Figure 5.6 CV curves of Cu-DHBQ cathodes with different binders at the binder content of 10 wt%. (a) alginate, (b) CMC, and (c) PVDF. The potential range is 1.4~2.8 V and the scan rate is 0.05 mV s⁻¹. (d) Comparison of the CV curves in the 3rd cycle for different binders. (e) Peak positions of C₁ and A₁, and (f) peak separations between C₁ and A₁ in Figure (d).

Next, the galvanostatic cycling performances of Cu-DHBQ cathodes with different binders at the binder content of 10 wt% were tested. The EIS spectra of fresh and cycled (after 200 cycles at 100 mA g^{-1} in the charged state) cells were measured and simulated using the respective equivalent circuits (Figure 5.7a and b). R_s , R_{ct} , R_{surf} , W_o , and CPE represent electrolyte resistance, charge transfer resistance, surface/interfacial resistance due to the solid electrolyte interphase (SEI) formation, Warburg diffusion impedance, and constant phase element to replace capacitor, respectively. For fresh cells, R_{ct} follows the order of alginate ($74 \text{ } \Omega$) < CMC ($90 \text{ } \Omega$) < PVDF ($120 \text{ } \Omega$). For cycled cells, R_{ct} follows the order of CMC ($10 \text{ } \Omega$) < alginate ($13 \text{ } \Omega$) < PVDF ($70 \text{ } \Omega$) while R_{surf} follows the order of alginate ($8 \text{ } \Omega$) < CMC ($10 \text{ } \Omega$) < PVDF ($17 \text{ } \Omega$). The results indicate that the resistance in the cathode with the alginate or CMC binder is smaller than that with the PVDF binder.

The charge/discharge curves of Cu-DHBQ cathodes with different binders (at the binder content of 10 wt%) are shown in Figure 5.7c-e, and the cycling performance is shown in Figure 5.7f. The discharge capacities of Cu-DHBQ cathodes using different binders in the 4th cycle (at the current rate of 100 mA g^{-1}) follow the order of alginate ($236.6 \text{ mA h g}^{-1}$) > CMC ($222.5 \text{ mA h g}^{-1}$) > PVDF ($123.1 \text{ mA h g}^{-1}$), indicating alginate and CMC binders result in a higher utilization of the carbonyl groups compared with PVDF binder. After 200 cycles at 100 mA g^{-1} , the cathodes using alginate, CMC, and PVDF binders retain the capacities of 81, 60, and 52 mA h g^{-1} , respectively. The larger capacities with alginate and CMC binders than that with PVDF binder is attributed to the better bonding and trapping capabilities of alginate and CMC binders than those of PVDF binder, which will be discussed below.

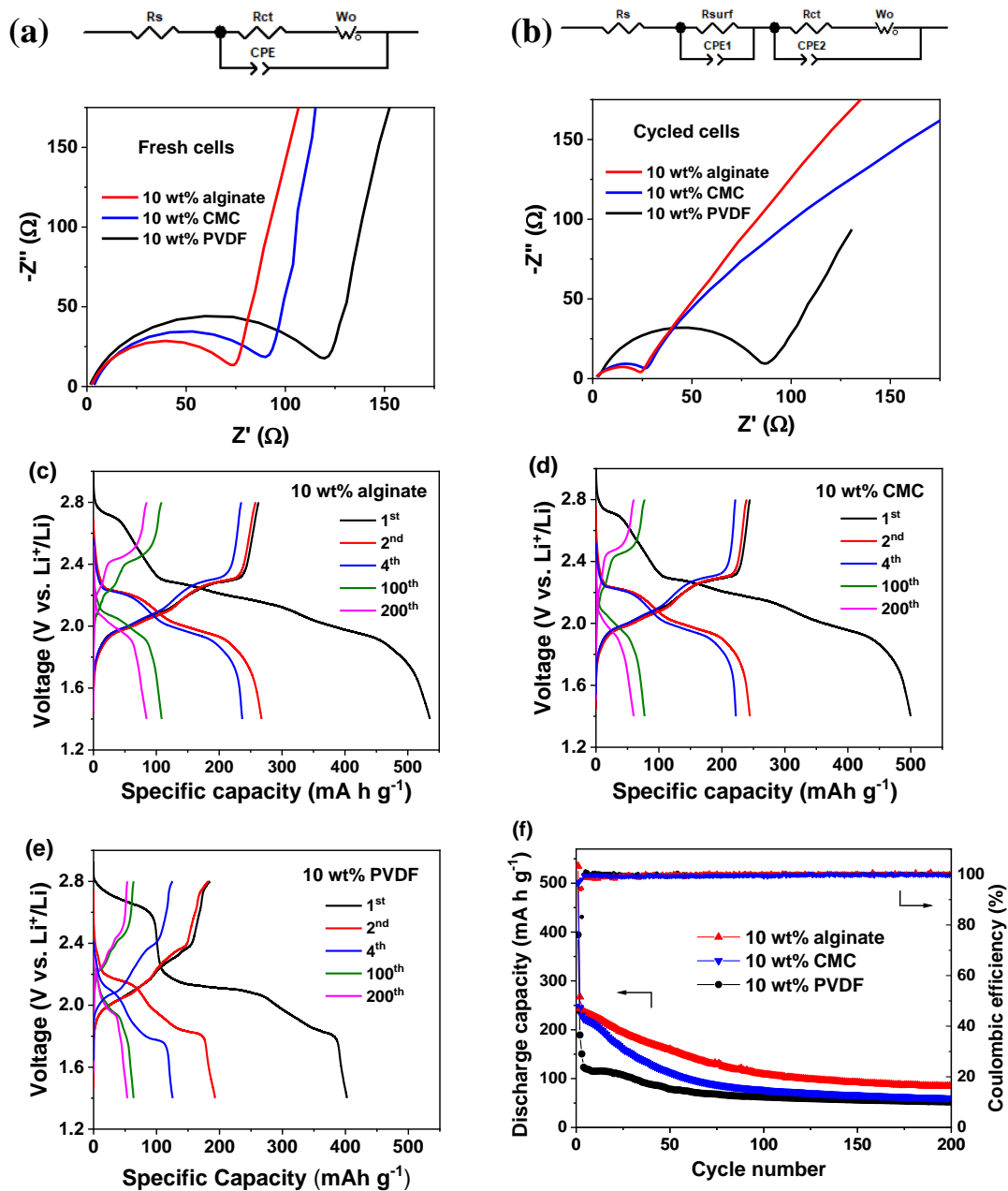


Figure 5.7 EIS data, charge/discharge curves, and cycling performance of Cu-DHBQ cathodes with different types of binders at the binder content of 10 wt%. All the cathode compositions are Cu-DHBQ : Super P : binder=6:3:1 (weight ratio). EIS data of (a) fresh and (b) cycled (after 200 cycles at $100 mA g^{-1}$ in the charged state) Cu-DHBQ cathodes. The respective equivalent circuits are also shown. Charge/discharge curves of Cu-DHBQ cathodes: (c) alginate, (d) CMC, (e) PVDF. The first two cycles were tested at $20 mA g^{-1}$ and the rest at $100 mA g^{-1}$. (f) Cycling performance of Cu-DHBQ cathodes at $100 mA g^{-1}$ in the potential range of 1.4~2.8 V. The cells were activated at $20 mA g^{-1}$ for two cycles and cycled at $100 mA g^{-1}$ afterwards.

To investigate the bonding or adhesive properties of different binders, peel test was performed, as shown in Figure 5.8. The peel strengths for different binders follow the order of CMC ($0.142 \pm 0.009 \text{ N mm}^{-1}$) > alginate ($0.131 \pm 0.012 \text{ N mm}^{-1}$) > PVDF ($0.032 \pm 0.003 \text{ N mm}^{-1}$). The better adhesive properties of CMC and alginate binders than that of PVDF binder contribute to the improved contact among active material particles, Super P particles and current collector, leading to facilitated electron transport and higher capacity.

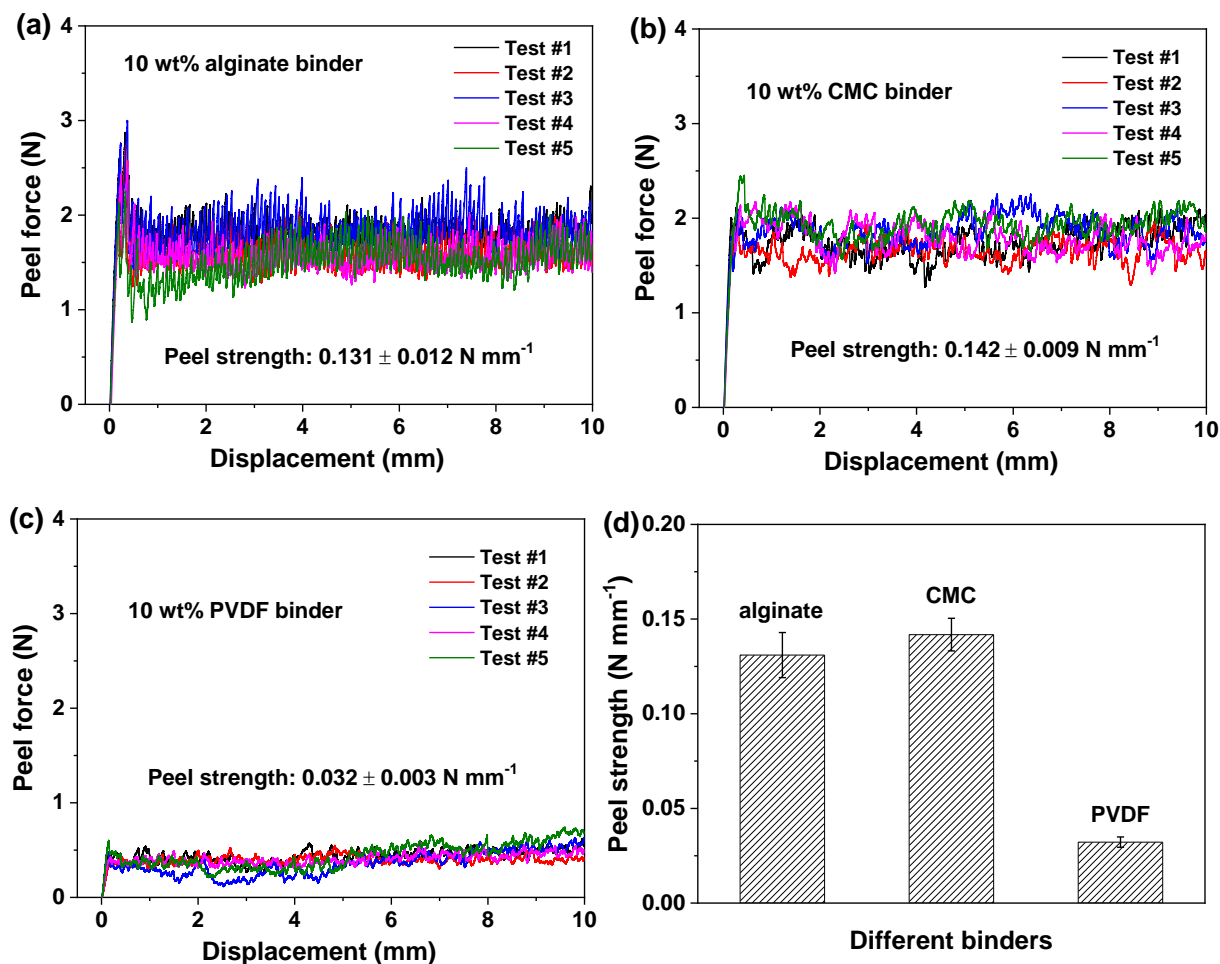


Figure 5.8 Peel test on Cu-DHBQ cathode films with different types of binders. Peel force versus displacement curves for (a) 10 wt% alginate binder, (b) 10 wt% CMC binder, and (c) 10 wt% PVDF binder. Five tests were performed for each binder. (d) Comparison of the peel strength for different binders. The compositions of the cathode films are Cu-DHBQ : Super P : binder=6:3:1.

To investigate the solubilities of discharged intermediate or product in the electrolyte, UV-Vis on cycled cells (after 200 cycles in the charged state) using different types of binders was performed, as shown in Figure 5.9. Cycled Cu-DHBQ cathodes with different binders show a strong peak at 230 nm which is assigned to the absorption of charged Cu-DHBQ, and shoulder peaks at 311 and 318 nm which are assigned to the absorption of discharged intermediate or product. For charged Cu-DHBQ, the shift from 240 nm in the fresh state to 230 nm in the cycled state may be caused by the change in the crystallinity of Cu-DHBQ before and after cycling (Li^+ ion insertion/desertion). Cu-DHBQ in the fresh state (before cycling) is more crystalline than that after cycling. The intensities of the shoulder peaks at 311 and 318 nm for cycled cathodes follow the order of PVDF > CMC > alginate, indicating alginate and CMC binders can better preserve the structural integrity of Cu-DHBQ preventing it from dissolving into the electrolyte.

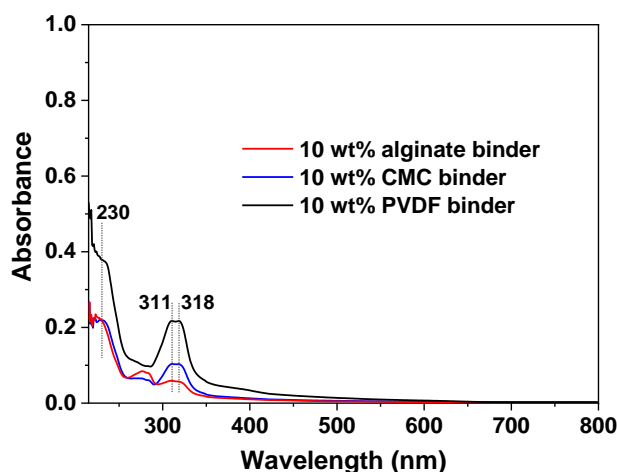


Figure 5.9 UV-Vis spectra of cycled Cu-DHBQ cathodes in the charged state after 200 cycles at 100 mA g^{-1} . The compositions of the cathodes are Cu-DHBQ : Super P : binder=6:3:1.

Since alginate binder can strongly interact with Cu-DHBQ via hydrogen bonding, increasing its content in the cathode film may strengthen such an effect and lead to a stable cycling performance. Next, an optimization on the content of alginate binder from 10 to 40 wt% is performed, as shown in Figure 5.10a. The cycling stability of Cu-DHBQ cathode increases on increasing the binder content from 10 to 25 wt%, with the capacity retentions after 200 cycles at 100 mA g^{-1} (calculated by dividing the discharge capacity at the 200th cycle with that at the 4th cycle) increase from 35.4 to 91.5%. The charge/discharge curves of Cu-DHBQ cathode with 25 wt%

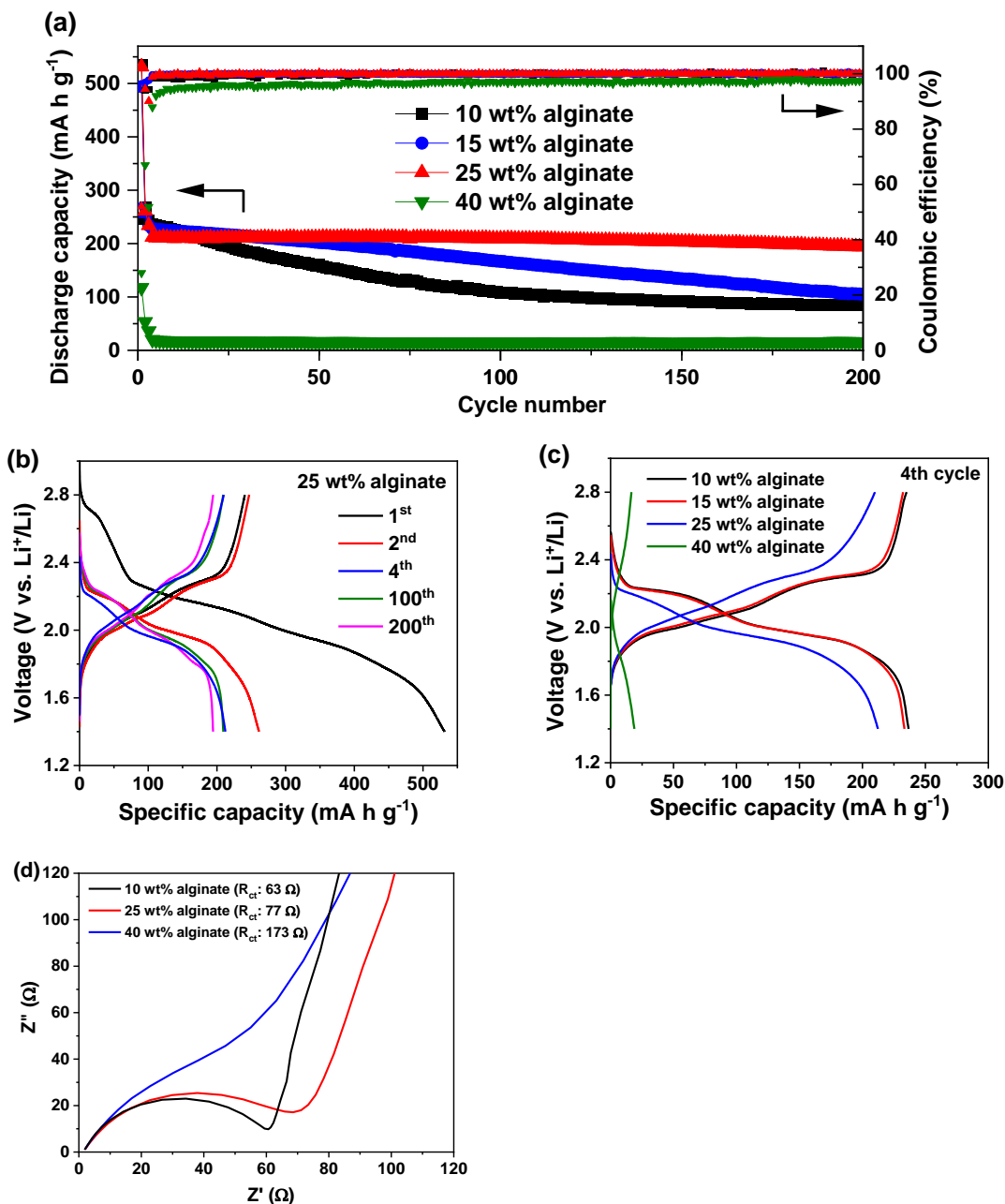


Figure 5.10 Electrochemical performance of Cu-DHBQ cathode with different contents of alginate binder. (a) cycling performance, (b) charge/discharge curves at the binder content of 25 wt%, (c) a comparison of the charge/discharge curves for different binder contents, and (d) EIS data of fresh Cu-DHBQ cathodes with different binder contents. The compositions for the cathodes with 10 wt%, 15 wt%, 25 wt%, and 40 wt% alginate binder are Cu-DHBQ : Super P : alginate binder (weight ratio)=6:3:1, 5.5:3:1.5, 4.5:3:2.5, and 3:3:4, respectively. The cells were tested at 20 mA g⁻¹ for two cycles as an activation process and then cycled at 100 mA g⁻¹.

binder at different cycles are shown in Figure 5.10b. The curves at the 100th cycle almost overlap those at the 200th cycle, implying the superior reversibility of the cathode. For the Cu-DHBQ cathode with 25 wt% binder, the capacity retention of 91.5% and the capacity of 194 mA h g⁻¹ after 200 cycles at 100 mA g⁻¹ render it a promising candidate for future energy storage. It must be pointed out that the capacity at the 4th cycle (before the capacity degradation begins) decreases with increasing the binder content. Figure 5.10c shows that the polarization of Cu-DHBQ cathode with different binder contents follows the order of 10 wt% \approx 15 wt% < 25 wt% < 40 wt%. As shown in Figure 5.10d, the R_{ct} values of fresh cathodes, obtained by simulating the EIS data with the afore-mentioned equivalent circuits, increase from 63 to 173 Ω on increasing the binder content from 10 to 40 wt%, implying the reduction in the electrical conductivity. This is expected as alginate binder is nonconductive. The Cu-DHBQ cathode with 40 wt% alginate binder exhibits a much-lowered capacity (20 mA h g⁻¹) in the 4th cycle and a decreased coulombic efficiency of 97%, compared with those (a capacity of 212.3 mA h g⁻¹ in the 4th cycle and a coulombic efficiency of \sim 100%) of the cathode with 25 wt% binder.

To further verify the dissolution of the cathode materials during the electrochemical cycling, the cells after 200 cycles at 100 mA g⁻¹ were disassembled, and the photos of the separator and the Li anode chip were taken. As shown in Figure 5.11, when 10 wt% PVDF binder is used, a lot of the soluble species are adsorbed in the pores of the separator, and almost the entire surface of the Li anode chip is covered with coloured materials which are produced by the corrosion reaction between the soluble species and the Li metal. Also, a rough surface with lots of concave spots for the Li anode is observed. In contrast, the coloured materials adsorbed in the separator and deposited on the Li anode surface are less when 10 wt% CMC binder or 10 wt% alginate binder is used, which is attributed to the trapping effect of these binders. When 25 wt% alginate binder is used, the amount of coloured materials adsorbed in the separator is the smallest, and the Li anode surface is smooth with no observable concave spots. These results demonstrate that the trapping of soluble species is the most effective when 25 wt% alginate binder is used. It should be noted that some coloured materials are also present in the middle of Li anode when 25 wt% alginate binder is used, which is similar to those in the other three cases. This may be explained by that the as-prepared Cu-DHBQ sample contains some short-chain coordination polymers which are dissolved in the electrolyte, diffuse to the Li anode side and react with Li metal during the 1st discharge process. Apart from the SEI formation mentioned in the literature,^{69,192,195} the loss of

these active materials may also cause the capacity loss during the 1st discharge process of the cycling performance test.

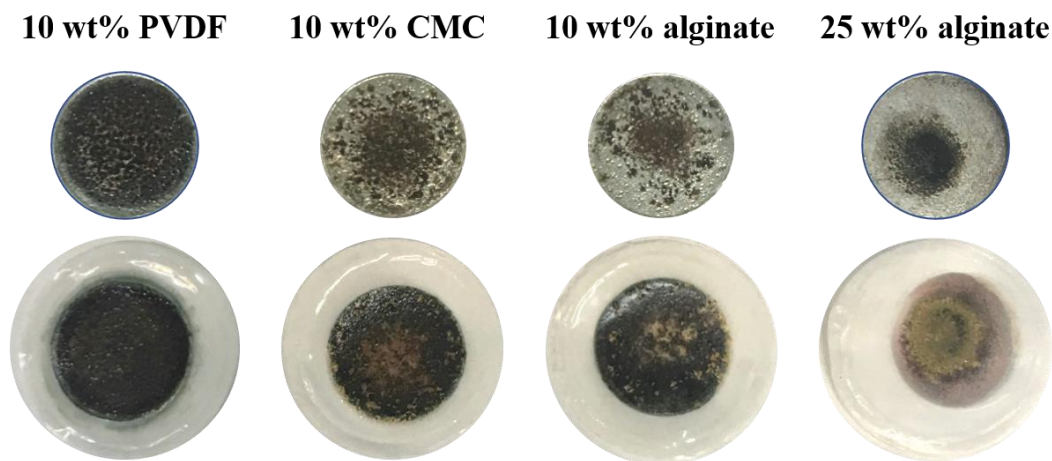


Figure 5.11 Photos showing the Li anode (top) and the separator (bottom) from disassembled cycled cells (after 200 cycles at 100 mA g⁻¹ in the charged state).

The rate performance testing of the Cu-DHBQ cathode with 25 wt% alginate binder is shown in Figure 5.12, and the charge/discharge curves at different rates are shown in Figure 5.12a. The Cu-DHBQ cathode exhibits a reversible capacity of 235.4 mA h g⁻¹ at the current rate of 20 mA g⁻¹ (~0.075 C), and can maintain a capacity of 191.7 mA h g⁻¹ at 400 mA g⁻¹ (~1.5 C).

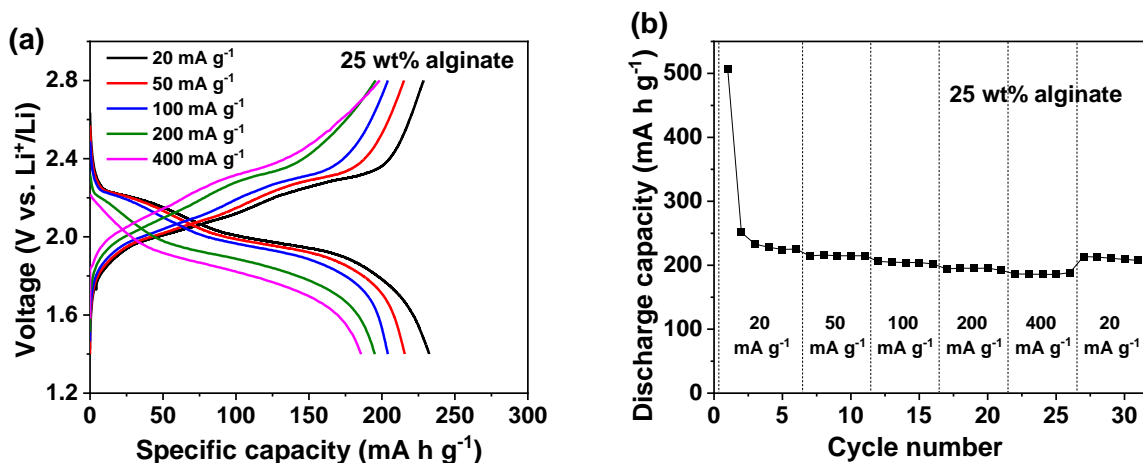


Figure 5.12 Rate performance testing of Cu-DHBQ cathode with 25 wt% alginate binder. (a) Voltage profiles and (b) discharge capacities at different current rates.

5.3.4 Study of the electrochemical reaction kinetics

For an electrode material, the charge storage mechanism can be classified into three types, namely electrical double-layer charge storage, the pseudocapacitive charge storage, and the battery-type charge storage.²⁰¹ The electrical double-layer charge storage is a non-faradaic process arising from the electrical double-layer effect. The pseudocapacitive charge storage is a faradaic process arising from the charge transfer with surface/subsurface atoms. The battery-type charge storage is a faradaic and diffusion-controlled process arising from Li⁺ ion insertion, conversion and alloying reactions.^{202,203} In the CV data, the current response (i) and the scan rate (ν) obey a power law relationship:

$$i = a \cdot \nu^b \quad (\text{Equation 5.1})$$

$$\text{or } \log(i) = \log(a) + b \cdot \log(\nu) \quad (\text{Equation 5.2})$$

where a and b are adjustable parameters.

When $b=0.5$, i.e. current (i) is proportional to $\nu^{1/2}$, the above equation can be written in a more detailed way:²⁰⁴

$$i = nFAC^*D^{\frac{1}{2}}\nu^{\frac{1}{2}}\left(\frac{\alpha nF}{RT}\right)^{\frac{1}{2}}\pi^{\frac{1}{2}}\chi(bt) \quad (\text{Equation 5.3})$$

where n is the number of electrons transferred, F is the Faraday constant, A is the surface area of the electrode material, C^* is the surface concentration of the electrode material, D is the diffusion coefficient of Li⁺ ion, ν is the scan rate, α is the transfer coefficient, R is the molar gas constant, T is the temperature, and $\chi(bt)$ is the normalized current for a totally irreversible system as indicated by the CV curve. Equation (5.3) indicates that the current response is diffusion controlled.

When $b=1$, i.e. current (i) is proportional to ν , Equation (5.1) can be written in a more detailed way:²⁰⁴

$$i = \nu C_d A \quad (\text{Equation 5.4})$$

where C_d is the capacitance.

The CV curves at different scan rates are shown in Figure 5.13a. The b values for the C₁, A₁, C₂, A_{2,a}, and A_{2,b} peaks are determined from the log (|current|) vs. log (scan rate) plot (Figure 5.13b). The b values can be categorized into two groups, C₁ and A₁ are one group with a b value

of 0.76, C₂, A_{2,a}, and A_{2,b} are another group with a *b* value of 0.87~0.91. As all the *b* values are between 0.5 and 1, both capacitive ($k_1\nu$) and diffusion-controlled ($k_2\nu^{\frac{1}{2}}$) processes are involved. The contribution of each component to the current can be quantified using the Dunn's method.²⁰⁴ The current at a fixed potential can be written as:

$$i(V)_{total} = i_{capacitive} + i_{diffusion} = k_1\nu + k_2\nu^{\frac{1}{2}} \quad (\text{Equation 5.5})$$

$$\text{or} \quad \frac{i(V)_{total}}{\nu^{\frac{1}{2}}} = k_1\nu^{\frac{1}{2}} + k_2 \quad (\text{Equation 5.6})$$

The contribution ratio of $i_{capacitive}$ is calculated below:

$$\frac{i_{capacitive}}{i_{total}} = \frac{k_1\nu}{k_1\nu + k_2\nu^{\frac{1}{2}}} = \frac{1}{1 + \frac{k_2}{k_1}\nu^{-\frac{1}{2}}} \quad (\text{Equation 5.7})$$

According to Equation 5.6, by making a plot of $i/\nu^{1/2}$ vs. $\nu^{1/2}$, k_1 and k_2 can be determined from the slope and the intercept, respectively. Then the contributions of $i_{capacitive}$ and $i_{diffusion}$ to the current at a specific potential can be calculated. Some examples for the plots of $i/\nu^{1/2}$ vs. $\nu^{1/2}$ in the potential range of 2~2.4 V for the anodic data are shown in Figure 5.13c, and the k_1 and k_2 values determined from these plots are shown in Table 5.4. At the scan rate of 0.05 mV s⁻¹, the charge stored due to the capacitive effect is shown in Figure 5.13d. It must be pointed out that k_2 values at some potentials (e.g. 2.2 and 2.4 V, Table 5.4) are negative, meaning the currents due to the diffusion-controlled process ($i_{diffusion}, k_2\nu^{\frac{1}{2}}$) at those potentials are negative while the currents due to the capacitive effect ($i_{capacitive}, k_1\nu$) are larger than the actual measured currents (i_{total}), as shown in Figure 5.13d. Such a phenomenon is also seen in other reports,²⁰⁵⁻²⁰⁷ which might be explained by the imperfection of the theoretical model. The contribution ratios of the charge due to the capacitive effect to the total stored charge at different scan rates are all very high (Figure 5.13e), 84.9%~93%, indicating the major charge storage process for Cu-DHBQ cathode is pseudocapacitive, which is beneficial for fast reaction kinetics.²⁰⁸ On increasing the scan rate, the contribution ratio of the charge due to the capacitive effect increases, which is expected as

$i_{capacitive}/i_{total}$ follows the relationship shown in Equation 5.7.

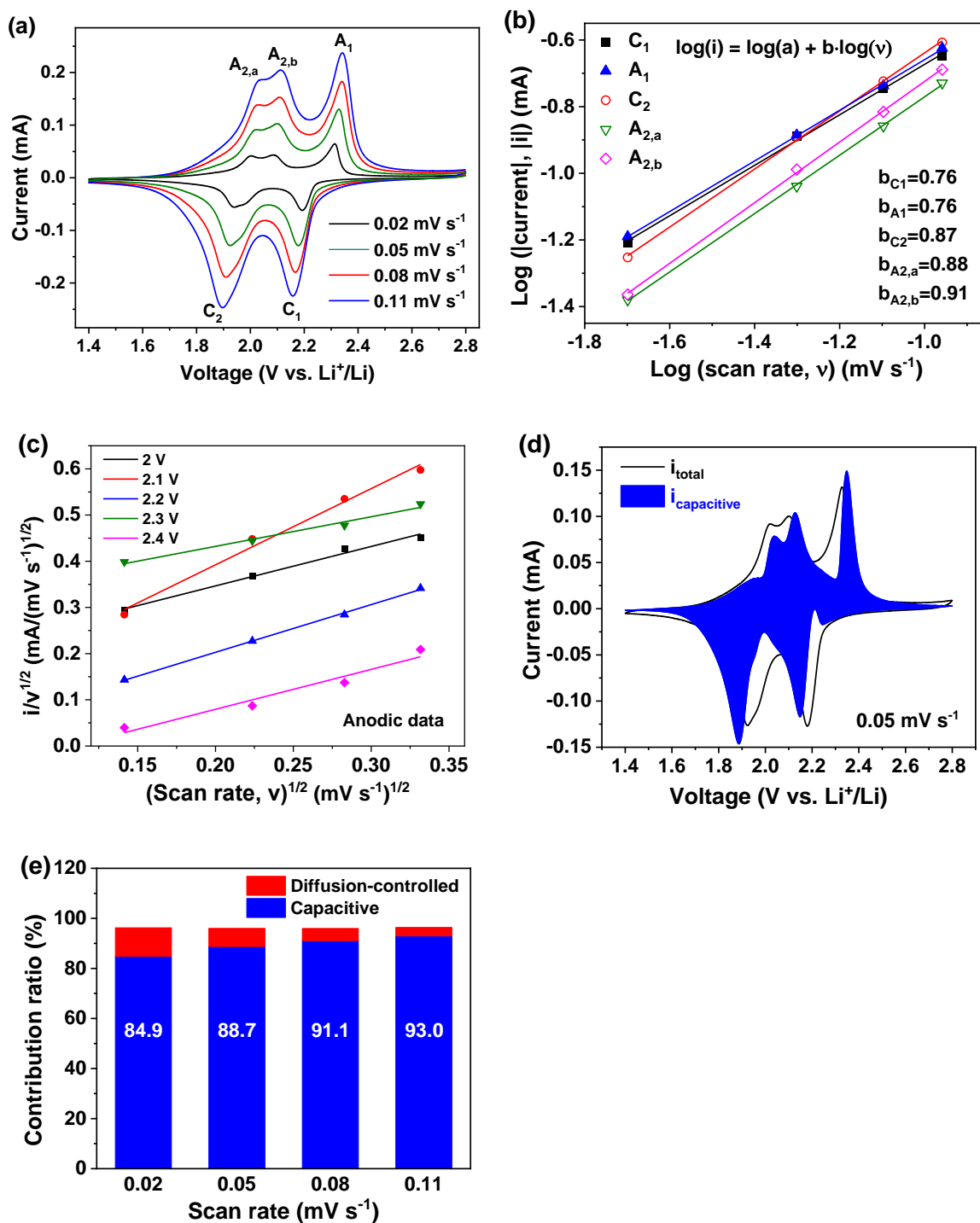


Figure 5.13 Study of the electrochemical reaction kinetics by CV for the Cu-DHBQ cathode with 25 wt% alginate binder. (a) CV curves with varied scan rates from 0.02 to 0.11 mV s^{-1} . (b) Log (|current|) vs. log (scan rate) plot. (c) $i/V^{1/2}$ vs. $\nu^{1/2}$ plot. (d) CV curve at the scan rate of 0.05 mV s^{-1} (black curve) and the charge being stored due to the capacitive process (blue region). (e) Contribution ratio of capacitive process at different scan rates.

Table 5.4 k_1 and k_2 values for the anodic current in the potential range of 2~2.4 V.

	2 V	2.1 V	2.2 V	2.3 V	2.4 V
k_1	0.854	1.649	1.033	0.640	0.864
k_2	0.176	0.062	-0.004	0.304	-0.093

5.3.5 Preparation of other structurally similar coordination polymers using different ligands

The above sections demonstrate that a number of coordination polymers can be prepared by varying the divalent metal ions (Ni, Co, Mn, Zn, and Cu) while using the same DHBQ ligand. Next, we demonstrate that other structurally similar coordination polymers can be prepared by varying the ligand. It is of particular interest to prepare a cathode material with a higher output voltage as the specific energy of a material is proportional to its output voltage, and it has been reported that electron-withdrawing groups is beneficial for increasing the output voltage.^{54,64} As shown in Figure 5.14, density functional theory (DFT) calculation shows that the LUMO level of 2,5-dichloro-3,6-dihydroxy-1,4-benzoquinone (denoted as DHBQ-Cl) is -3.79 eV, which is 0.53 eV lower than that of DHBQ (-3.26 eV) due to the influence of the electron withdrawing groups (two chlorine atoms). A lower LUMO level can result in a higher discharge voltage.⁶³ Thus DHBQ-Cl is expected to have a higher discharge voltage compared with DHBQ. Next, the DHBQ ligand is replaced with the DHBQ-Cl ligand while still using copper salt as the metal centre, and the resulted coordination polymer is denoted as Cu-DHBQ-Cl. The characterizations (FTIR, TGA and XRD data) of Cu-DHBQ-Cl are shown in Figure 5.15. In the FTIR spectrum, the absence of -OH stretching at $\sim 3300\text{ cm}^{-1}$ implies Cu-DHBQ-Cl does not contain any coordinated water molecules. The TGA data shows no noticeable weight loss before 322 °C, which also indicates the as-synthesized compound does not contain coordinated water, consistent with the FTIR data.

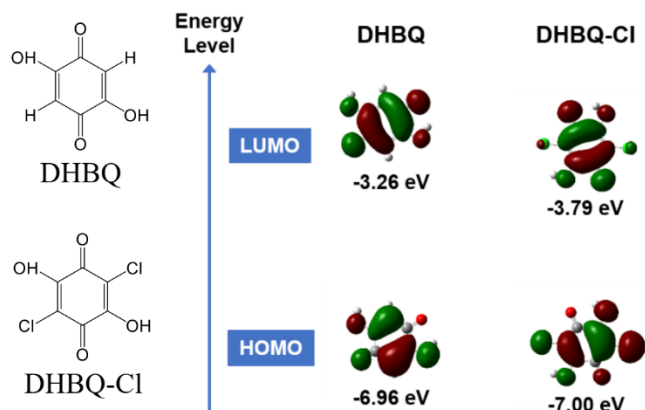


Figure 5.14 Structures and energy levels of DHBQ and DHBQ-Cl.

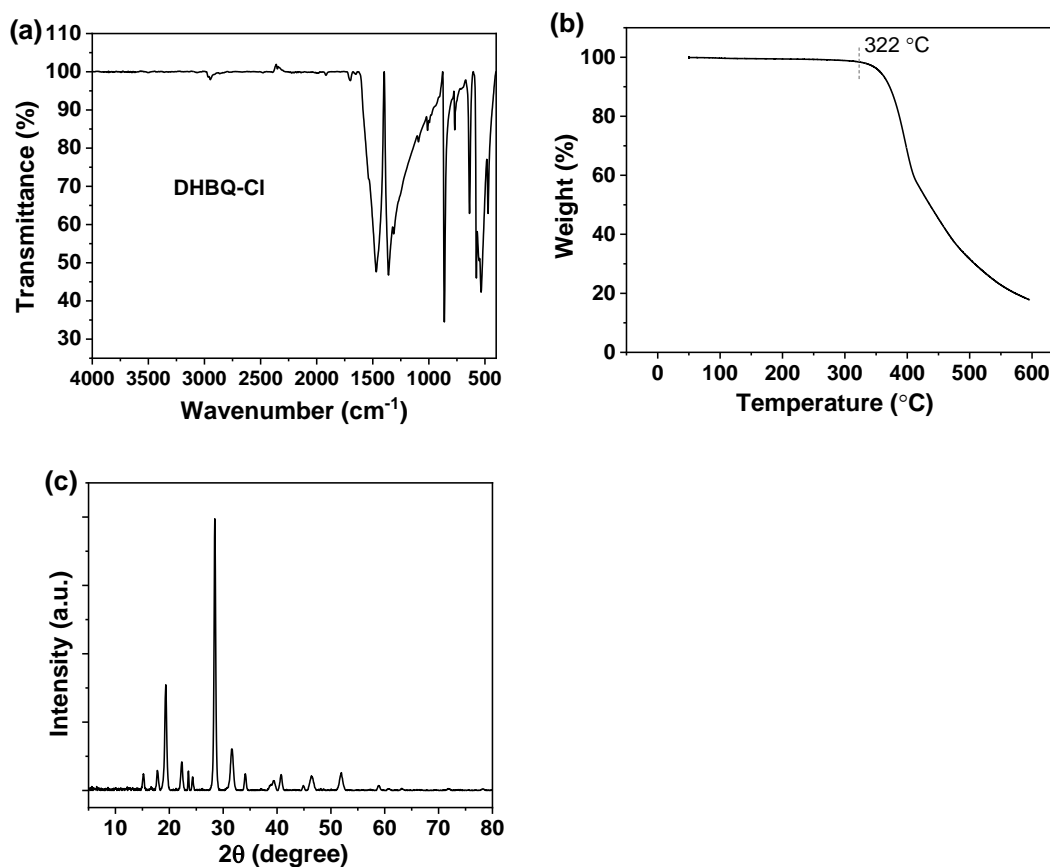


Figure 5.15 Characterizations of the Cu-DHBQ-Cl coordination polymer. (a) FTIR, (b) TGA, and (c) XRD.

The electrochemical performance of Cu-DHBQ-Cl is shown in Figure 5.16. An abrupt capacity fading is observed with the Cu-DHBQ-Cl cathode. Under the same testing condition, the Cu-DHBQ-Cl cathode maintains a capacity of only 18 mA h g⁻¹ (9.1% of its theoretical capacity) at the 3rd cycle, while the Cu-DHBQ cathode shows a capacity of 233 mA h g⁻¹ (87.6% of its theoretical capacity) at the 3rd cycle. To reveal the cause of the drastic capacity decay for the Cu-DHBQ-Cl cathode, the Cu-DHBQ-Cl cell and the Cu-DHBQ cell after the 1st discharge process were disassembled, all the cell components were soaked in 3 mL of DME, then the supernatant was subjected to UV-Vis measurement. In the UV-Vis spectra, shown in Figure 5.17, the discharged Cu-DHBQ-Cl shows shoulder peaks at 318 and 328 nm with the absorbance of 2.73 and 2.88, respectively, while the discharged Cu-DHBQ shows a single peak at 324 nm with an absorbance of 0.02. This implies that the concentration of soluble species in the electrolyte for the discharged Cu-DHBQ-Cl cathode is considerably higher than that for the discharged Cu-DHBQ cathode, which accounts for the poor cycling performance of Cu-DHBQ-Cl cathode. The much higher concentration of soluble species in the electrolyte for the discharged Cu-DHBQ-Cl may be caused by that the crystal structure of Cu-DHBQ-Cl collapses after the insertion of Li⁺ ions, which has been reported for some MOF-based electrode materials.¹⁷⁹

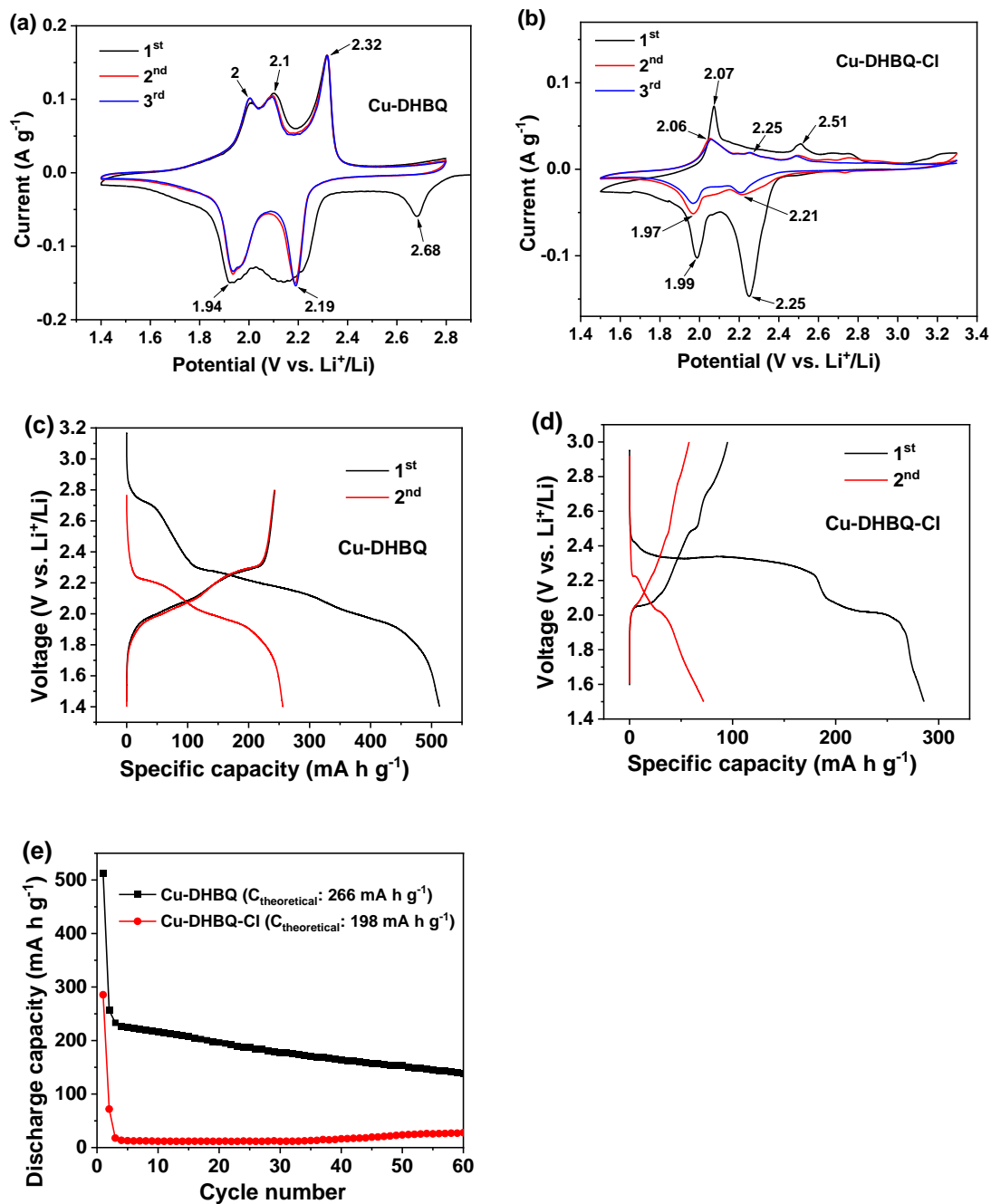


Figure 5.16 Comparison for the electrochemical performance of Cu-DHBQ and Cu-DHBQ-Cl. CV curves of (a) Cu-DHBQ cathode, and (b) Cu-DHBQ-Cl cathode. The scan rate was 0.05 mV s^{-1} . Voltage profiles of (c) Cu-DHBQ cathode, and (d) Cu-DHBQ-Cl cathode for the first two cycles at 20 mA g^{-1} . (e) Cycling performance of Cu-DHBQ and Cu-DHBQ-Cl cathodes. The first two cycles were tested at 20 mA g^{-1} and the rest of cycling at 100 mA g^{-1} . The cathode compositions are active material (Cu-DHBQ or Cu-DHBQ-Cl) : Super P : alginate binder=6:3:1.

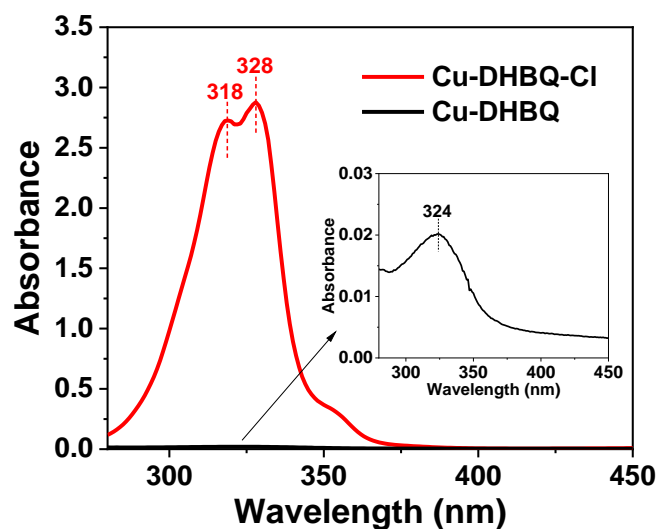


Figure 5.17 UV-Vis spectra of Cu-DHBQ-Cl and Cu-DHBQ cells after the 1st discharge process. The inset is the enlarged UV-Vis spectrum of the Cu-DHBQ cell after the 1st discharge.

5.3.6 Stabilization of organic cathode by acid-base interaction with polymer binder

The structures of 1,5-diaminoanthraquinone and 2,6-diaminoanthraquinone which contain basic amine groups are shown in Figure 5.18a and b. From the respective CV curves (Figure 5.18), the peak separations (ΔP), potential difference between the cathodic and anodic peaks, of 1,5-diaminoanthraquinone and 2,6-diaminoanthraquinone at the 2nd cycle are 41.6 and 51.2 mV, respectively, implying 1,5-diaminoanthraquinone has better redox kinetics. Therefore, 1,5-diaminoanthraquinone was chosen as an example to explore the effect of acid-base attraction on the cycling stability.

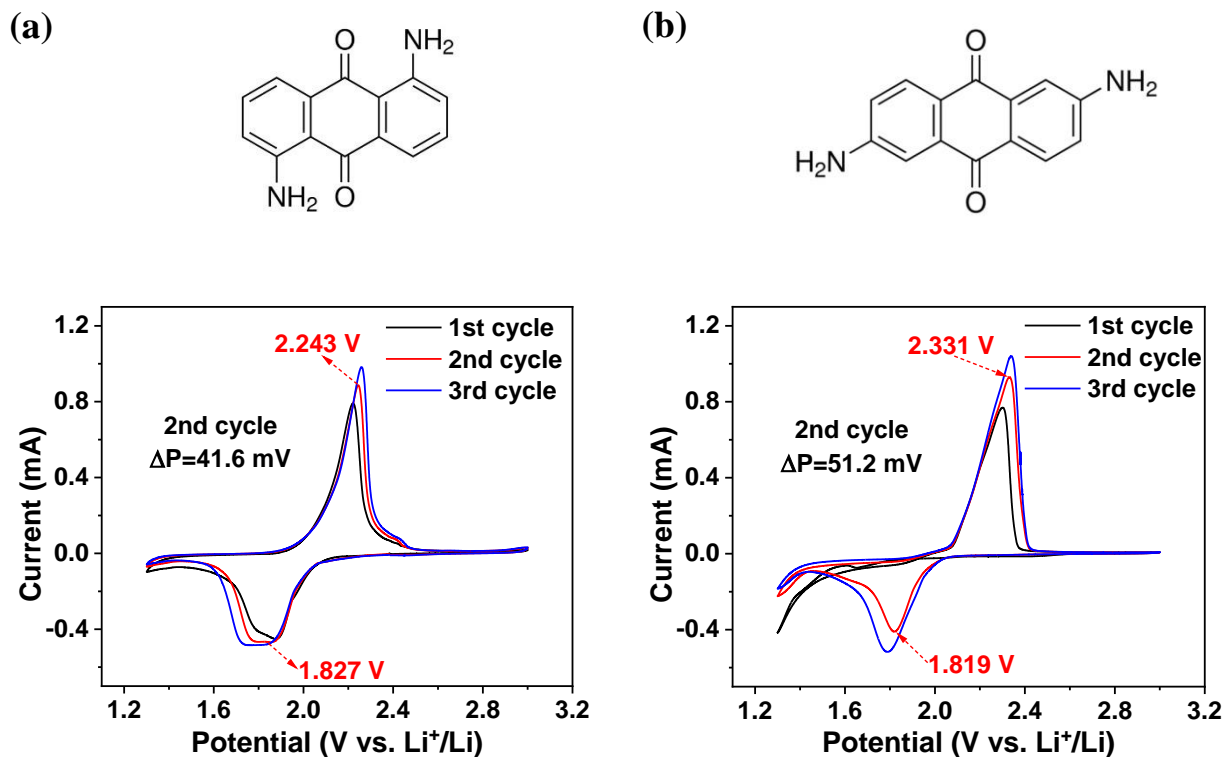


Figure 5.18 CV curves of (a) 1,5-diaminoanthraquinone, and (b) 2,6-diaminoanthraquinone with a scan rate of 0.2 mV s⁻¹. Peak separations (ΔP) for the 2nd cycle are labeled on the graphs. The cathode composition is active material : Super P : poly(acrylic acid) (PAA) binder=6:3:1.

The cycling performance of 1,5-diaminoanthraquinone cathode with different types of binders, including alginic acid (H-alginate), sodium alginate (Na-alginate), poly(4-styrenesulfonic acid) (H-PSS) and poly(styrene sulfonic acid) sodium salt (Na-PSS), was compared. As shown in Figure 5.19, for either alginate or PSS based binder, the acid-type binder (H-alginate or H-PSS) results in slower capacity decay than the respective salt-type one (Na-alginate or Na-PSS), which can be attributed to that the acid-base interaction (attraction) between the acid group (-H) in the acid-type binder and the amino group (-NH₂) in 1,5-diaminoanthraquinone helps to adsorb the active material in the electrode. The cycling performance of 1,5-diaminoanthraquinone cathode with the PVDF binder, which does not have such acid-base attraction, was also obtained for comparison. It can be seen that the improvement in the capacity retention resulted from such acid-base attraction is rather limited. The capacity retention after 60 cycles for the H-alginate binder which shows the best cycling stability is 19.3%. This is only slightly higher than that (15.5%) for the PVDF binder. The limited improvement in the cycling stability by the binder approach is

attributed to the insufficient amount of binder. Considering a 1:1 molar ratio between the amino group in 1,5-diaminoanthraquinone and the acid group in the H-alginate binder, the weight ratio of 1,5-diaminoanthraquinone/H-alginate would be 1.35 : 1. However, if such a large amount of binder is added to the electrode, the energy density of the electrode would be greatly compromised. Therefore, the binder approach for improving the cycling stability is only an auxiliary approach, while the polymerization approach including the formation of polymers, macrostructures, COFs and MOFs should be considered as the primary approach.

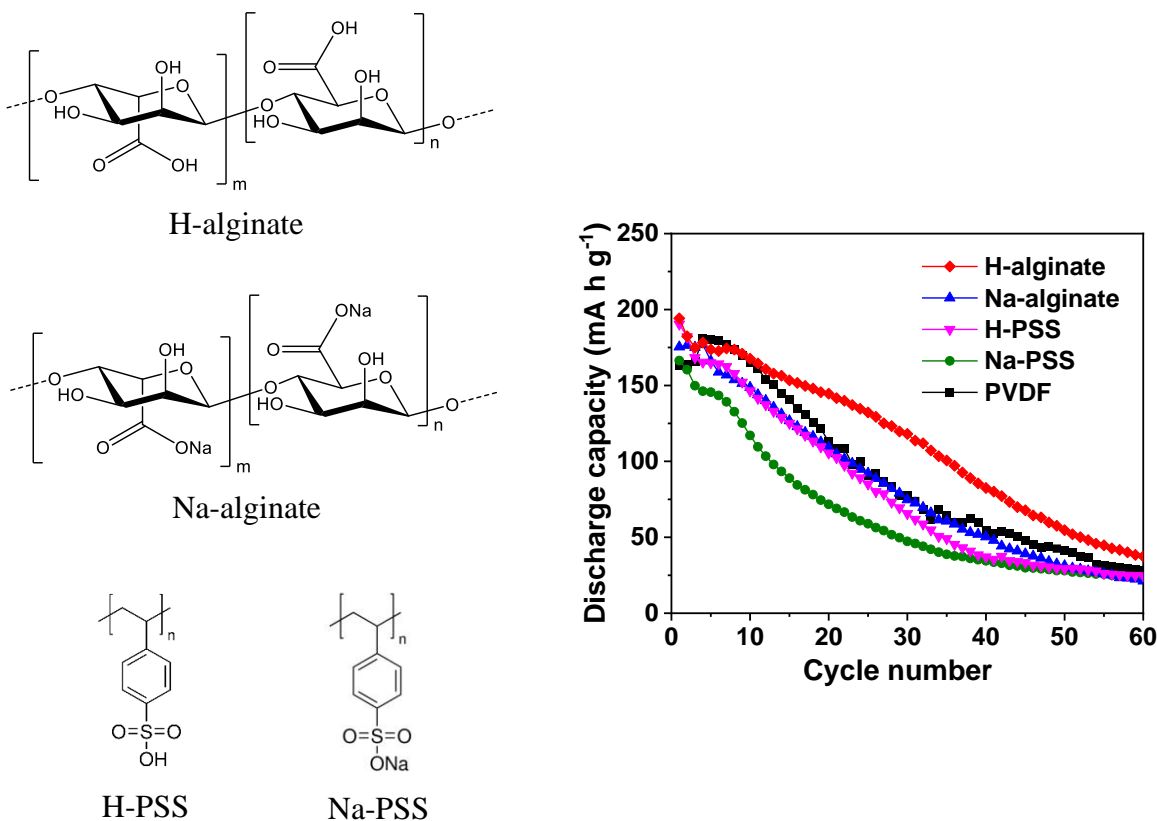


Figure 5.19 Chemical structures of binders containing acidic and neutral groups and the influence of these binders on the cycling performance of 1,5-diaminoanthraquinone cathode. Left: Structures of H-alginate, Na-alginate, H-PSS and Na-PSS binders. Right: Cycling performance of 1,5-diaminoanthraquinone cathode with different types of binders at the current rate of 20 mA g⁻¹. The cathode composition is 1,5-diaminoanthraquinone : Super P : binder=6:3:1.

5.4 Conclusions

A series of one-dimensional coordination polymers using DHBQ and divalent metal ions (Ni, Co, Mn, Zn, and Cu) have been synthesized and their electrochemical properties have been investigated. We have demonstrated that the formation of coordination polymers is a highly effective strategy to reduce the solubilities of small organic molecules in the electrolyte. Moreover, it has been found that the coordination polymers M-DHBQ·2H₂O (M=Ni, Co, and Mn) exhibit the redox activities of both metal and ligand in the potential range around 0.5~3 V, while the coordination polymer Cu-DHBQ exhibits the redox activity of the ligand only in the same potential range. In the potential range around 1.3~3 V where only the ligand is redox active, Cu-DHBQ exhibits the highest capacity among the as-synthesized coordination polymers. Furthermore, the UV-Vis results show that the capacity decay of Cu-DHBQ cathode is caused by the dissolution of discharged product or intermediate in the electrolyte. By using alginate binder (with the content of 25 wt% in the cathode) which can strongly bond the electrode film and effectively trap the soluble species, Cu-DHBQ cathode exhibits a high initial capacity of 212 mA h g⁻¹ (80% of the theoretical capacity) at the current rate of 100 mA g⁻¹, and can maintain a capacity of 194 mA h g⁻¹ after 200 cycles at 100 mA g⁻¹ with a capacity retention of 91.5%. Finally, our approach for coordination polymer synthesis is very versatile and can be extended to the synthesis of other structurally similar coordination polymers by varying the organic ligand, such as DHBQ-Cl which has a higher discharge voltage than that of DHBQ. Our results show the promise of coordination polymers as emerging organic electrode materials for energy storage.

Furthermore, the stabilization of organic cathode through the acid-base interaction with polymer binder has also been explored. It was found that the binder optimization strategy for improving the cycling stability of organic cathode is only an auxiliary approach, whereas the polymerization strategy, which includes the formation of polymers, macrostructures, COFs and MOFs, should be considered as the primary approach.

Chapter 6. Conjugated Diketopyrrolopyrrole (DPP) Polymer Based P-type and Bipolar-type Organic Cathodes

6.1 Introduction

Organic cathodes possess the advantages of high capacity, structural diversity and designability, sustainability, low cost, and environmental friendliness, and thus have been studied intensively in recent years.⁵⁴ Organic cathodes based on small molecules are plagued with drastic capacity fading due to their high solubilities in the electrolyte. To solve this problem, a variety of polymers from the polymerization of small molecules have been reported. These polymers can be categorized into three types according to the position of the redox active group and the conjugation of the polymer. The first type is that the redox active group is located in the side position while the backbone is either conjugated or non-conjugated, e.g. TEMPO radical attached polymethacrylate (PTMA),^{209–211} thianthrene-substituted polynorbornene,²¹² and poly(3-vinyl-N-methylphenothiazine) (PVMPT).²¹³ The second type is that the redox active group is located in the non-conjugated backbone, e.g. poly(benzoquinonyl sulfide) (PBQS),⁵⁶ poly(1,4-anthraquinone) (P14AQ),⁶⁵ and polyquinoneimine (PQI).²¹⁴ The third type is that the redox active group is located in the π -conjugated backbone, e.g. n-type naphthalenediimide (NDI)-bithiophene copolymer P(NDI2ODT2),²¹⁵ p-type phenothiazine-bithiophene copolymer,²¹⁶ and n-type diketopyrrolopyrrole (DPP) based polymer (2DPP-OD-HEX).²¹⁷

The third type polymers (conjugated polymers) have found applications in organic thin film transistors (OTFTs), organic photovoltaics (OPVs) and organic solar cells (OSCs),^{218–220} while their application in the energy storage area have just started.²²¹ Their solution processability, excellent film-forming and mechanical properties have enabled the fabrication of flexible electrode films, and their intrinsic conducting/semiconducting properties have resulted in significantly enhanced rate capability.^{215–217} The charge storage mechanism of conjugated polymers can be categorized as n-doping, p-doping, and bipolar (both n- and p-) doping. The doping levels of p-type conjugated polymers (polypyrrole and polythiophene) are generally between 0.25 and 0.4, with an optimum value of 0.33, representing every third heterocycle is charged. It is challenging to achieve a p-doping level higher than 0.4 due to the strong coulombic repulsion between the charged heterocycles. On the other hand, the ambipolar properties of conjugated polymers with the transport of both holes and electrons have been reported in OTFTs,²²² but their application in

rechargeable batteries has rarely been reported. The bipolar charge storage can enhance the specific capacity and ultimately the energy density of conjugated polymers when they are used as electrode materials in rechargeable batteries.

Diketopyrrolopyrrole (DPP)-containing conjugated polymers have been reported to exhibit both high electron and hole mobilities in OTFTs, which can result in high electrical conductivities when they are used as electrode materials in rechargeable batteries. High electrical conductivity is crucial for electrode materials as it can reduce the amount of additional conductive carbon, leading to enhanced energy density. This is particularly important for organic materials which generally have low electrical conductivities compared with conventional electrode materials based on intercalation compounds. A DPP-containing conjugated polymer, 2DPP-OD-HEX, was reported to show a reversible one-electron n-doping in the DPP unit, with the potential range of 1.6~2.8 V vs. Li⁺/Li and the average discharge voltage of ~2.15 V vs. Li⁺/Li. In this chapter, two DPP based polymers, namely diketopyrrolopyrrole (DPP)-quaterthiophene copolymer (PDQT) and diketopyrrolopyrrole-bithiophene polymer (PDBT), have been explored as p-type and bipolar-type cathode materials, respectively. The PDQT electrode shows a high doping level of ~0.5, which is rare among p-type conjugated polymers. And the p-doping reaction is relatively reversible, potentially due to the stabilization effect of the DPP unit. Another advantage of the PDQT cathode is its high discharge voltage of ~3.8 V, one of the highest among the conjugated polymer cathodes. In contrast, the PDBT cathode shows a bipolar charge storage mechanism, resulting in a doubled theoretical capacity compared with the PDQT cathode. The experimentally obtained capacity for the PDBT cathode is low, probably due to its large particle size leading to ineffective electron and ion transports. ⁷¹

6.2 Experimental section

6.2.1 Material synthesis

PDQT²²³ and PDBT²²² were synthesized according to the methods reported previously.

6.2.2 Electrochemical measurements

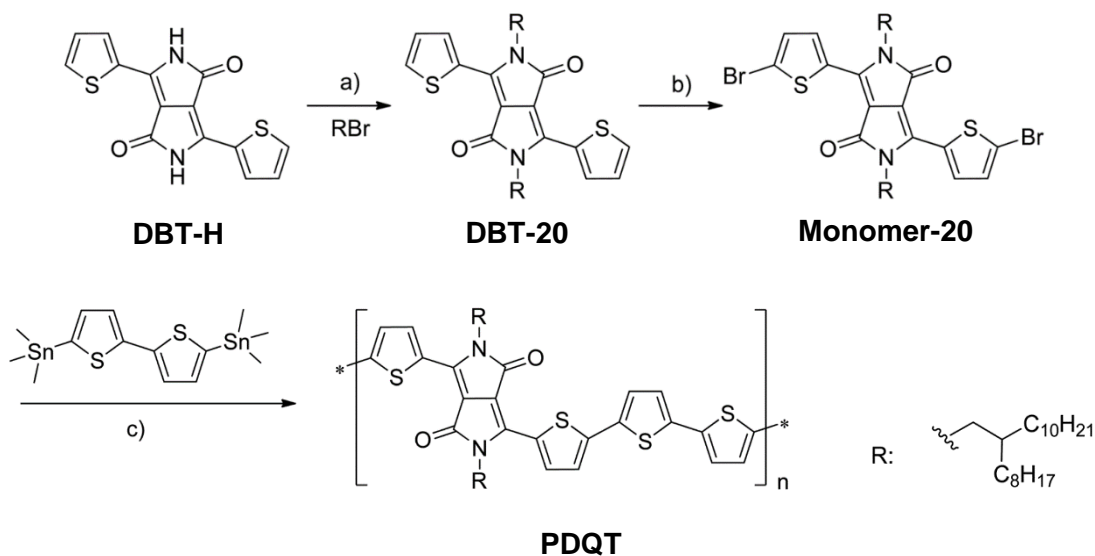
PDQT or PDBT was dissolved in chloroform with the aid of heating at 40 °C. The concentrations of PDQT and PDBT in chloroform were controlled at 30 and 15 mg mL⁻¹, respectively, as PDBT is less soluble than PDQT. A carbon paper disk (Toray TGP-H060) with a diameter of 12 mm was immersed into the as-prepared solution for dip coating (no additional

binder was used). After coating, the electrode was dried at 60 °C. The areal loadings of PDQT and PDBT in the electrode films were 1.2 and 0.6 mg cm⁻², respectively. The assembly of CR2032 coin cells was conducted in an Ar-filled glovebox with O₂ and H₂O levels below 0.1 ppm. 35 μL of the electrolyte, 1 M LiPF₆ in ethylene carbonate (EC)/ethyl methyl carbonate (EMC)/dimethyl carbonate (DMC) (1:1:1 volume ratios), was added to each cell. The CV testing was conducted on a VMP3 Bio-Logic potentiostat. The galvanostatic cycling of the cells was performed with LAND CT2001A battery testers at room temperature.

6.3 Results and discussion

6.3.1 Electrochemical performance of PDQT

PDQT was synthesized according to Scheme 6.1, following a previous paper from our group.²²³



Scheme 6.1 Synthetic route to PDQT.^a

^a The synthesis of PDQT was conducted by a previous group member (Dr. Wei Hong).

A non-porous ITO or a porous carbon paper substrate was used for the CV testing of PDQT. The peak positions and peak shapes for the CV curves of PDQT on different substrates are similar with the potential range of 3~4.6 V and the scan rate of 10 mV s⁻¹ (Figure 6.1a and b). However, when the scan rate is reduced to 0.1 mV s⁻¹, the current at the potential of 4.5 V for the carbon paper substrate is much higher (~11 times higher) than that for the ITO substrate, which is attributed to the decomposition of the LiPF₆ electrolyte, 1 M LiPF₆ in 1:1:1 (volume ratio) EC/EMC/DMC, as the electrolyte is known to be unstable and subject to oxidation under high voltage condition.²²⁴ The difference in the current at the potential of 4.5 V for different substrates can be explained by two reasons. One reason is that the carbon paper substrate is porous and can contain the electrolyte in the pores, leading to a larger amount of electrolyte between the cathode and anode compared to the non-porous ITO substrate. Consequently, the larger amount of electrolyte results in larger current. Another reason is that the porosity of the carbon paper substrate affords a larger surface area. Since the decomposition reaction of the electrolyte occurs on the conductive surfaces, the larger surface area leads to higher current. To experimentally determine the electrolyte stability, a linear sweep voltammetry (LSV) testing was conducted, as shown in Figure 6.1e. The notable decomposition of the electrolyte occurs at the potential of ~5.3 V. However, when zoomed in, it can be seen that the minor decomposition of the electrolyte starts at a potential as low as 4.5 V. The current response at the potential of 4.5~5 V due to the electrolyte decomposition is comparable to that caused by the redox reaction of the polymer. Therefore, the CV testing of the polymer should be kept below 4.5 V. The observation of the upper potential limit (4.5 V) for the EC/EMC/DMC electrolyte solvent is consistent with that (2~4.5 V for EC/DMC) reported in the literature.²²⁴

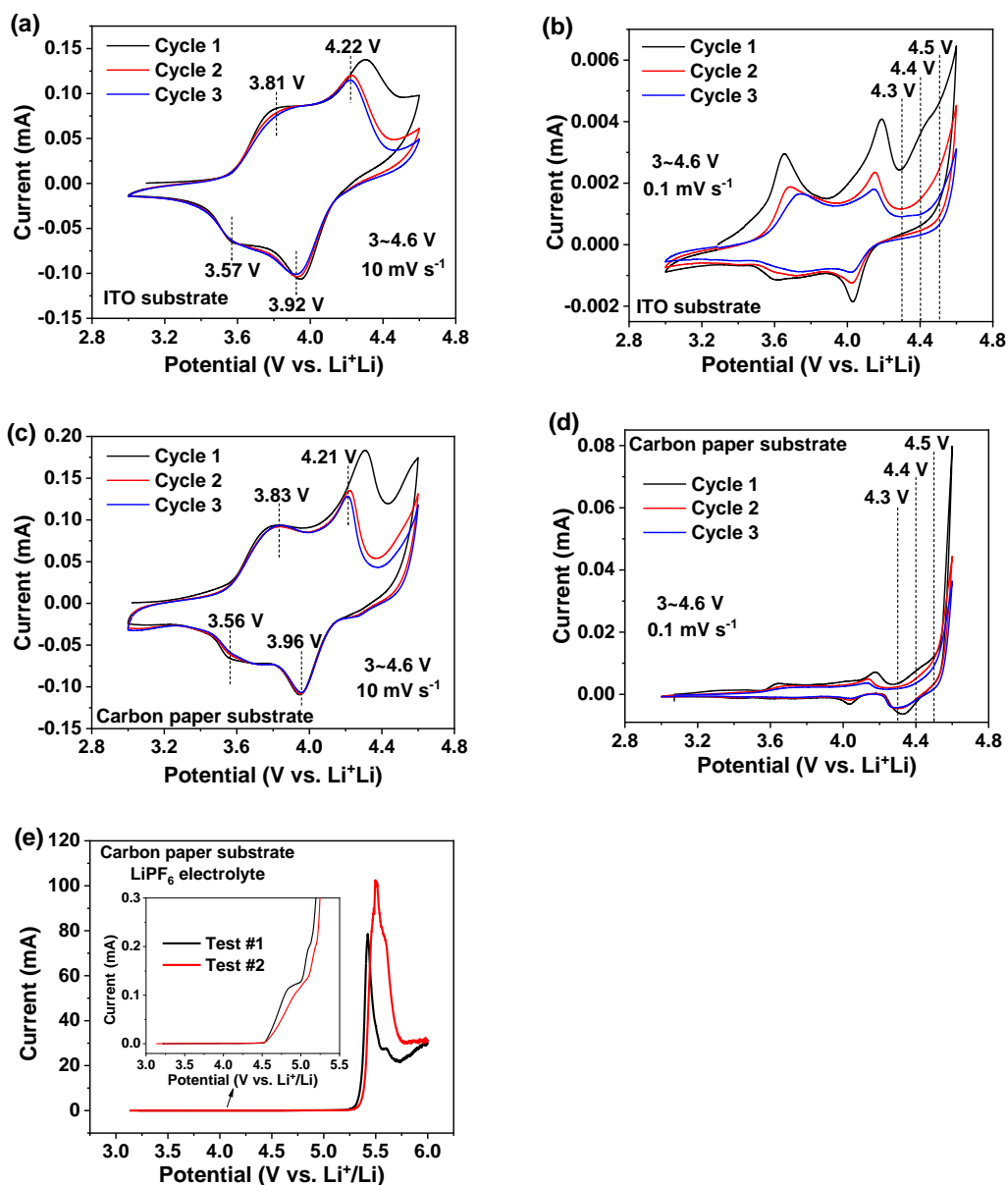


Figure 6.1 Optimization of the experimental condition for the CV testing of PDQT in 1 M LiPF₆ in 1:1:1 EC/EMC/DMC (volume ratio) electrolyte. ITO substrate in the potential range of 3~4.6 V with a scan rate of (a) 10 mV s⁻¹ and (b) 0.1 mV s⁻¹. Carbon paper substrate in the potential range of 3~4.6 V with a scan rate of (c) 10 mV s⁻¹ and (d) 0.1 mV s⁻¹. (e) LSV curve of the LiPF₆ electrolyte with a scan rate of 0.1 mV s⁻¹ in the potential range from 3.14 V (open circuit potential for the cell after fabrication) to 6 V, measured using a carbon paper substrate. The inset is the magnified data.

The CV curves of PDQT using the carbon paper substrate with the scan rate of 0.1 mV s^{-1} and the potential ranges of 3~4.2 V, 3~4.3 V, 3~4.4 V, and 3~4.5 V are shown in Figure 6.2. The CV curves at the 2nd and 3rd cycles overlap each other for the potential range of 3~4.3 V to 3~4.5 V, indicating the electrochemical reaction is reversible under these potential ranges.

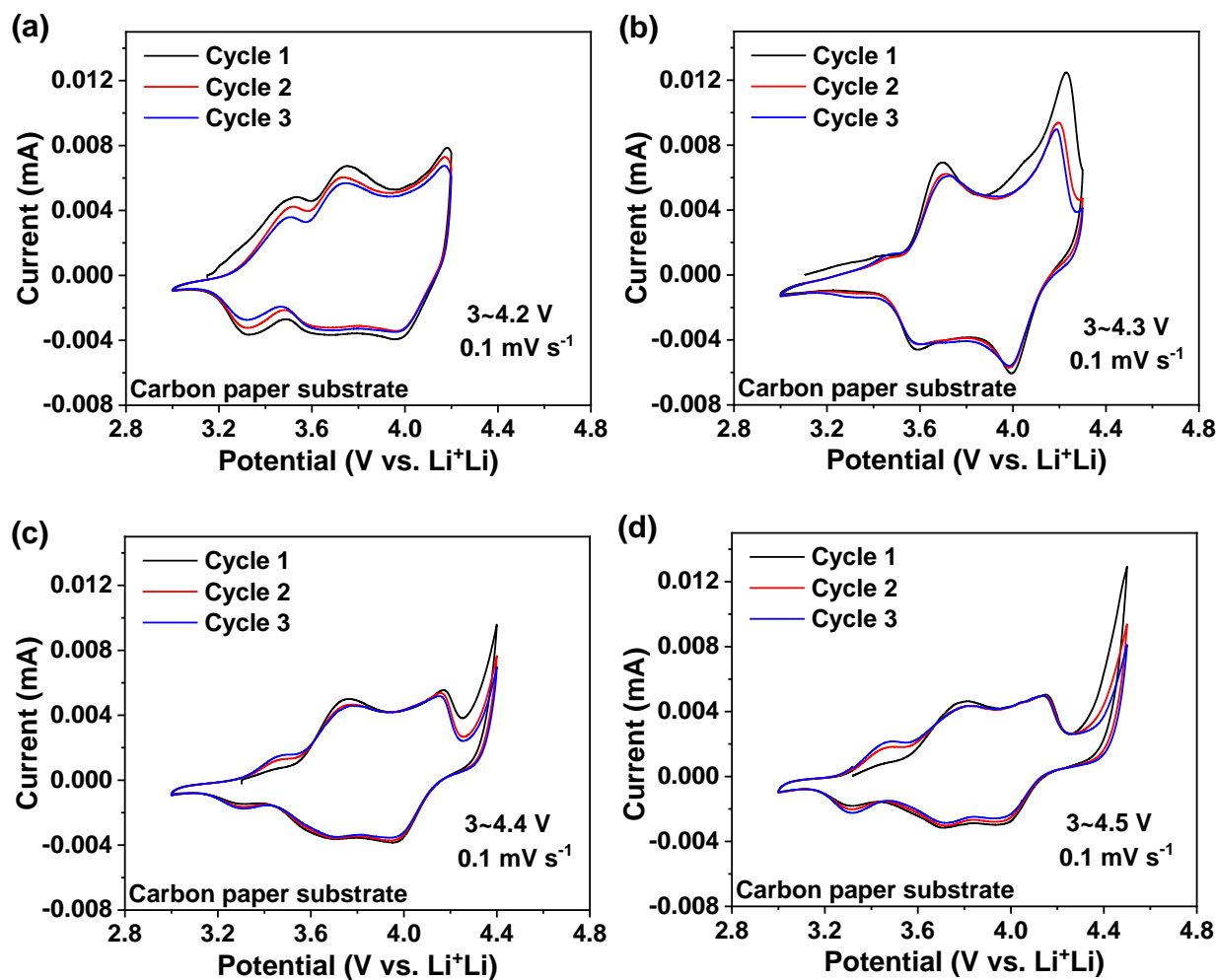


Figure 6.2 CV curves of PDQT using the carbon paper substrate with different potential ranges. (a) 3~4.2 V, (b) 3~4.3 V, (c) 3~4.4 V, and (d) 3~4.5 V. The scan rate is 0.1 mV s^{-1} .

Similar to the p-doping reaction of polythiophene,¹³⁴ PDQT can undergo the electrochemical p-doping reaction shown in Scheme 6.2. x is the doping level of the polymer and

is dependant on the nature of the polymer and the experimental conditions. For example, poly(thiophene) has been reported to have a doping level of 20% when LiClO₄ was used as the electrolyte salt at an applied potential of 4.05 V vs. Li⁺/Li. For battery materials, the actual doping level can be calculated from the measured charge (capacity) divided by the capacity at the 100% doping level.

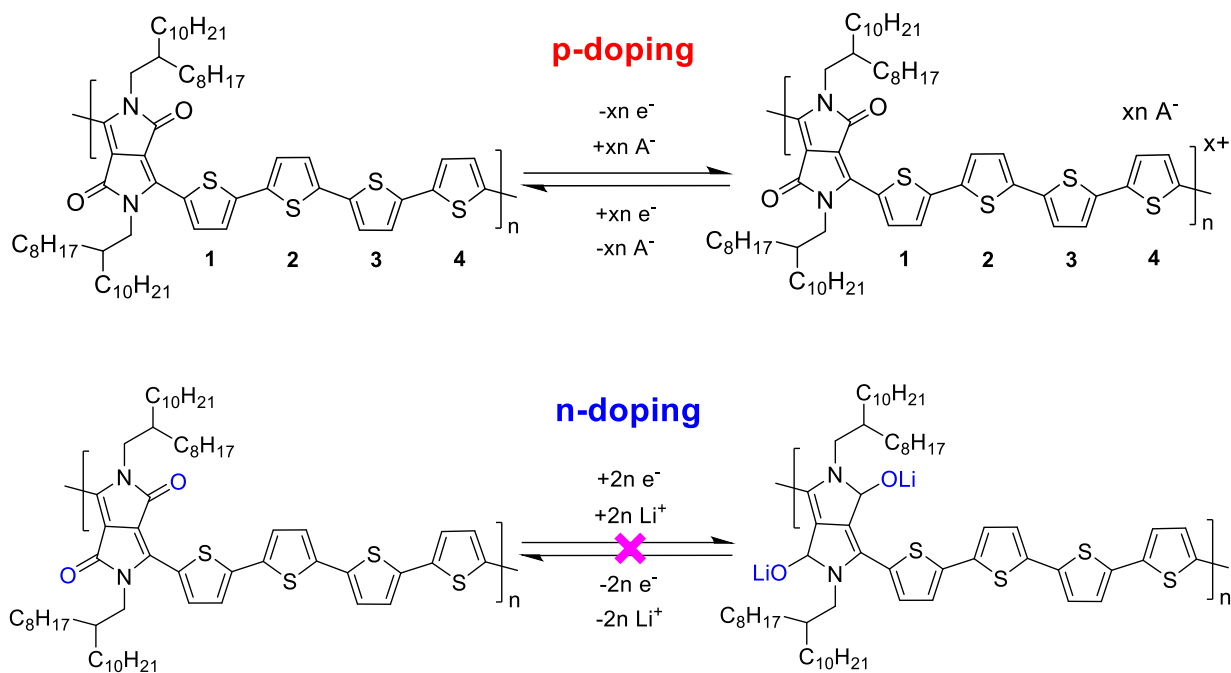
The capacity of the p-doping reaction, at a doping level of 100%, for the PDQT cathode is:

$$C_{theoretical (p-doping)} = \frac{n \times 26801}{M} = \frac{4 \times 26801 (mA h mol^{-1})}{1023.7 (g mol^{-1})} = 104.8 mA h g^{-1},$$

where n is the number of electrons transferred (one at each thiophene unit) and M is the molecular weight of the repeat unit of PDQT.

The electrochemical performance of PDQT cathode is shown in Figure 6.3. The average discharge voltage of PDQT (~3.8 V) is much higher than that of the quinones (~2 V) which belong to the n-type cathode material. As mentioned in Chapter One, one of the advantages of the p-type cathode material is their high discharge voltage. The discharge voltage can be calculated by the energy gap (ΔE , unit: eV) between the energy level of the cathode material and the energy of the Li⁺/Li electrode divided by the number of electrons transferred. The ΔE for a p-type cathode material is the energy difference between the HOMO level of the cathode material and the energy of the Li⁺/Li electrode, while the ΔE for a n-type cathode material is the energy difference between the LUMO level of the cathode material and the energy of the Li⁺/Li electrode. The lower energy of the HOMO level than the LUMO level indicates a larger ΔE for the p-type cathode material and therefore a higher discharge voltage. The PDQT cathode shows a high capacity of 46.9 mA h g⁻¹ at the current rate of 10 mA g⁻¹ and a capacity of 44.4 mA h g⁻¹ at the current rate of 50 mA g⁻¹, corresponding to the p-doping levels of $x=46.9/104.8=45\%$ and $x=44.4/104.8=42\%$, respectively. The doping level of 42%~45% for the PDQT cathode is higher than that (20%, LiClO₄ as the electrolyte salt at the potential of 4.05 V vs. Li⁺/Li) for the electrochemical doping of poly(thiophene), and that (20%, I₂ as the dopant) for the chemical doping of poly(thiophene-2,5-diyl) and poly(3-alkylthiophene-2,5-diyl). The much higher doping level of the PDQT cathode may suggest that the presence of DPP unit in a Donor-Acceptor (D-A) polymer is beneficial for achieving a high doping level. The reason is still unclear, but it may be related to the smaller

bandgap of PDQT, which may generate more stable mid-gaps to accommodate polaron or bipolarons. The PDQT cathode can maintain a capacity of 35 mA h g^{-1} after 250 cycles at 50 mA g^{-1} corresponding to a capacity retention of 79.5%.



Scheme 6.2 Electrochemical reaction schemes for the PDQT cathode. Top: schematic of the p-doping reaction for the PDQT cathode. x represents the doping level. Bottom: restricted n-doping reaction for the PDQT cathode. The only place where the n-doping can occur is highlighted in blue.

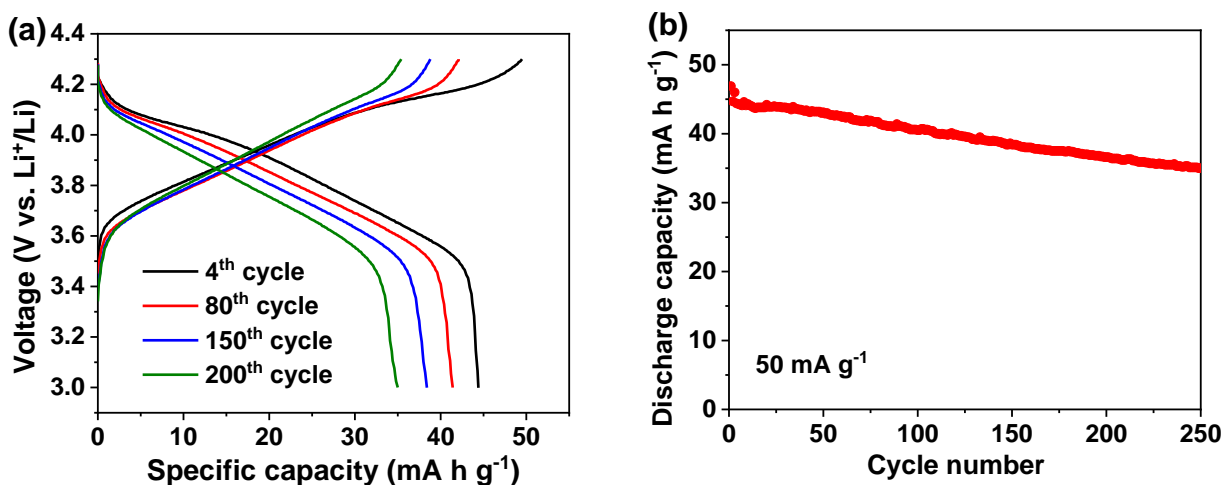


Figure 6.3 Galvanostatic cycling performance of PDQT cathode in the potential range of 3~4.3 V. (a) Voltage profiles, and (b) cycling performance. The cell was activated at 10 mA g⁻¹ for 3 cycles and cycled at 50 mA g⁻¹ afterwards. The PDQT electrode was prepared by dip coating using a carbon paper substrate. The areal loading of PDQT in the electrode is 1.2 mg cm⁻².

It was reported that another structure-similar conductive polymer, 2DPP-OD-TEG, which backbone (-T-DPP-T-) has a DPP unit linked by a thiophene unit (T) on each side, can undergo the n-doping reaction in the potential range of 1~2.8 V vs. Li⁺/Li.²²⁵ The PDQT cathode may also undergo such a n-doping reaction. To verify this, the CV data of PDQT cathode was measured in both the potential ranges of 1~3 V and 1~4.3 V (Figure 6.4). The areas under the curve for the n-doping region and the p-doping region are 0.0074 and 0.03629, respectively, corresponding to a ratio of n-doping/p-doping=0.2. This implies that the n-doping process for PDQT is largely restricted (Scheme 6.2).¹³⁴

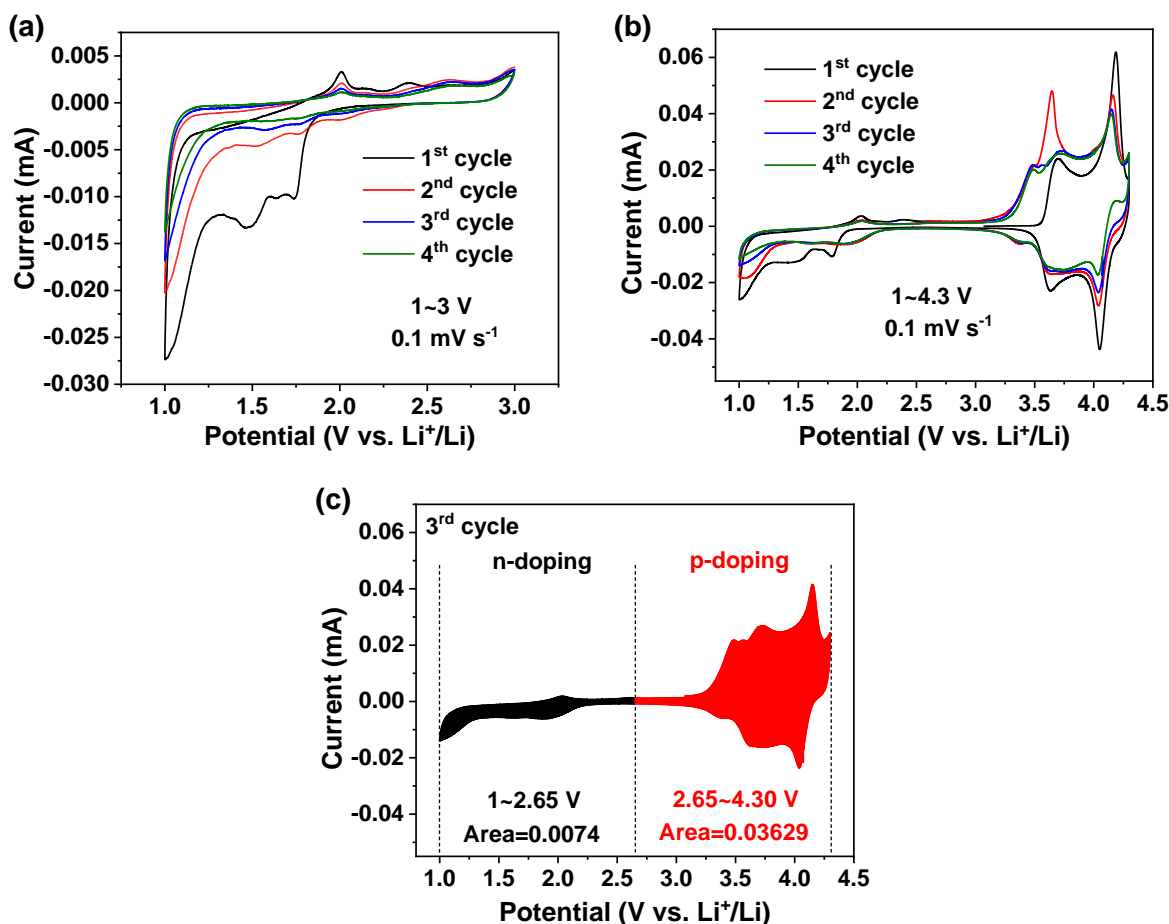
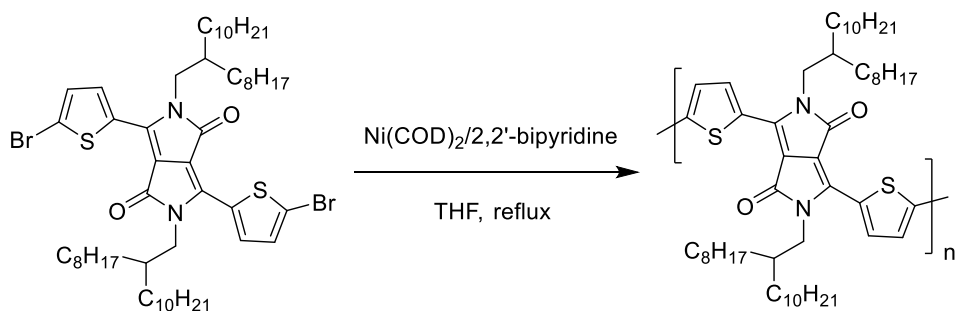


Figure 6.4 CV curves of PDQT cathode in both the n-doping and p-doping potential ranges. (a) 1~3 V, (b) 1~4.3 V, and (c) the 3rd CV cycle in (b). The areas under the curve for the n-doping and the p-doping regions are labeled. The scan rate is 0.1 mV s⁻¹.

6.3.2 Electrochemical performance of PDBT

To enable the possible bipolar charge storage mechanism so that the specific energy of the material is maximized, an ambipolar polymer with the -T-DPP-T- repeat unit, namely diketopyrrolopyrrole-bithiophene polymer (PDBT), was prepared according to Scheme 6.3, following a previous paper from our group.²²² The CV testing of PDBT was conducted first, and the results are shown in Figure 6.5. Unlike PDQT, PDBT shows notable redox activities in both the n-doping region (1~3 V) and the p-doping region (3~4.3 V). The areas under the curve for the n-doping region and the p-doping region are 0.01207 and 0.01305, respectively, corresponding to a ratio of n-doping/p-doping=0.92, which is 4.6 times of that of PDQT cathode (0.2).



Scheme 6.3 Synthetic route to PDBT.^b

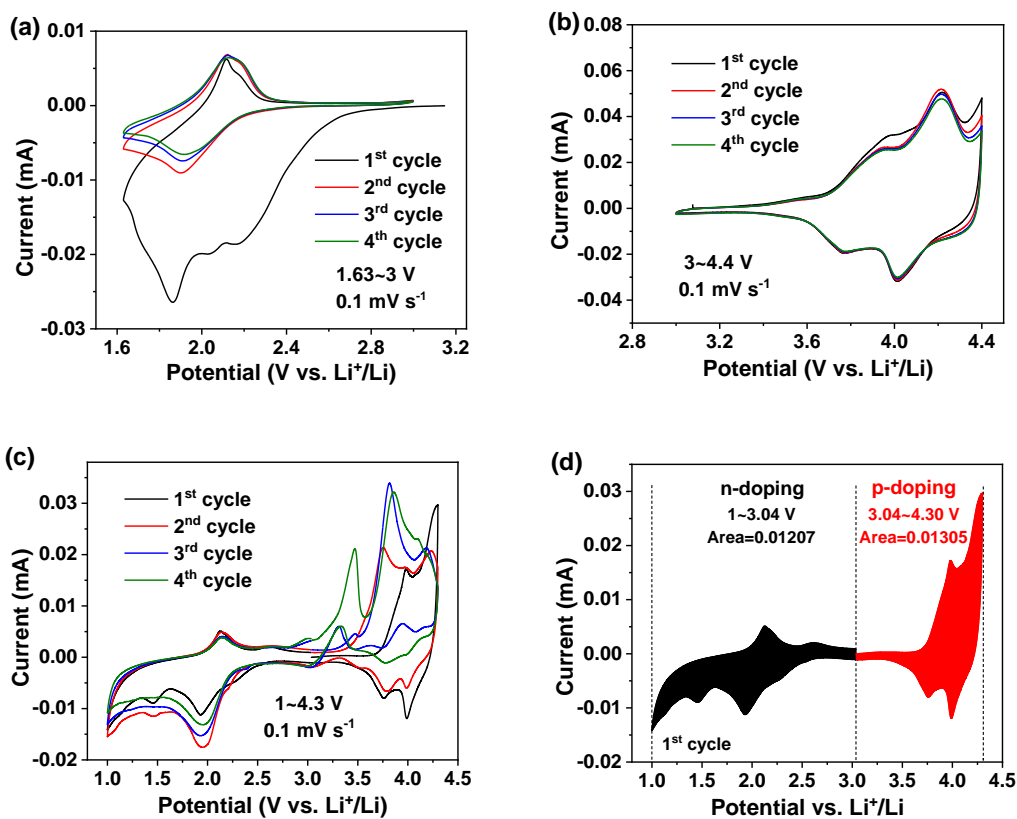
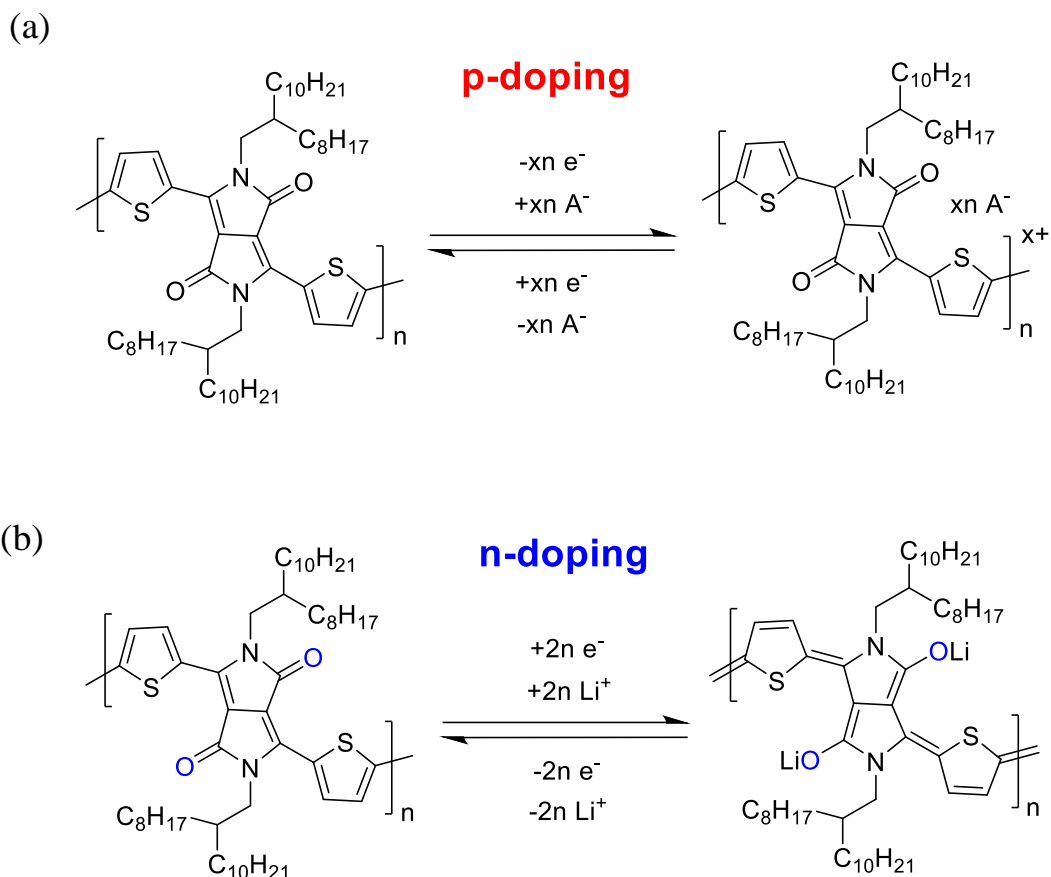


Figure 6.5 CV curves of PDBT cathode in both the n-doping and p-doping potential ranges. (a) 1.63~3 V, (b) 3~4.4 V, (c) 1~4.3 V, and (d) the 1st CV cycle in (c). The areas under the curve for the n-doping and the p-doping regions are labeled. The scan rate is 0.1 mV s⁻¹.

^b The synthesis of PDBT was conducted by a previous group member (Dr. Jenner H. L. Ngai).



Scheme 6.4 Electrochemical reaction schemes for the PDBT cathode. (a) p-doping, and (b) n-doping.

The theoretical capacity of the p-doping reaction for the PDBT cathode, at a doping level of 100%, is:

$$C_{\text{theoretical (p-doping)}} = \frac{n \times 26801}{M} = \frac{2 \times 26801 \text{ (mA h mol}^{-1}\text{)}}{859.4 \text{ (g mol}^{-1}\text{)}} = 62.4 \text{ mA h g}^{-1}$$

The theoretical capacity of the n-doping reaction:

$$C_{\text{theoretical (n-doping)}} = \frac{n \times 26801}{M} = \frac{2 \times 26801 \text{ (mA h mol}^{-1}\text{)}}{859.4 \text{ (g mol}^{-1}\text{)}} = 62.4 \text{ mA h g}^{-1}$$

Therefore, the total theoretical capacity for PDBT is: $62.4 + 62.4 = 124.8 \text{ mA h g}^{-1}$.

The galvanostatic cycling performances of the PDBT cathode in the p-doping and the n-doping regions were measured separately, as shown in Figure 6.6. In the p-doping region with the current rate of 50 mA g^{-1} , the PDBT cathode delivers an initial capacity of 17.1 mA h g^{-1} (corresponding to the p-doping level of $x=17.1/62.4=27\%$), then gradually decreases to 6.8 mA h g^{-1} after 250 cycles. The lower doping level of PDBT than PDQT (27.4% vs. 42~45%) may be caused by the ineffective electron and ion transfers as a result of the large size of the PDBT particles. The aforementioned PDQT can be well dispersed in chloroform, thus it can form thin films which are uniformly coated on the surface of carbon paper after the dip coating process, facilitating the electron transport from the carbon paper to the PDQT solid and the ion transport from the electrolyte to PDQT. By contrast, PDBT can hardly be dispersed in chloroform or 1,1,2,2-tetrachloroethane even after heating. As a result, it remains large particles on the surface of carbon paper after dip coating, making it rather difficult for electrons and ions to be transported to the cores of particles. In the n-doping region with the current rate of 50 mA g^{-1} , the capacity of the PDBT cathode is even lower than expected, with an initial capacity of 3.6 mA h g^{-1} and a capacity of 2.7 mA h g^{-1} after 250 cycles. Such low capacities in the n-doping region may also be caused by the large particle size issue.

Apart from the solubility issue of PDBT, the much higher areal loading of the active material in my experiment ($0.7\sim 1 \text{ mg cm}^{-2}$) than those ($0.1\sim 0.4 \text{ mg cm}^{-2}$) reported for the conjugated polymer electrodes^{216,217,226} may also result in the unsatisfactory performance in my case, indicating further optimization on the experimental condition is needed.

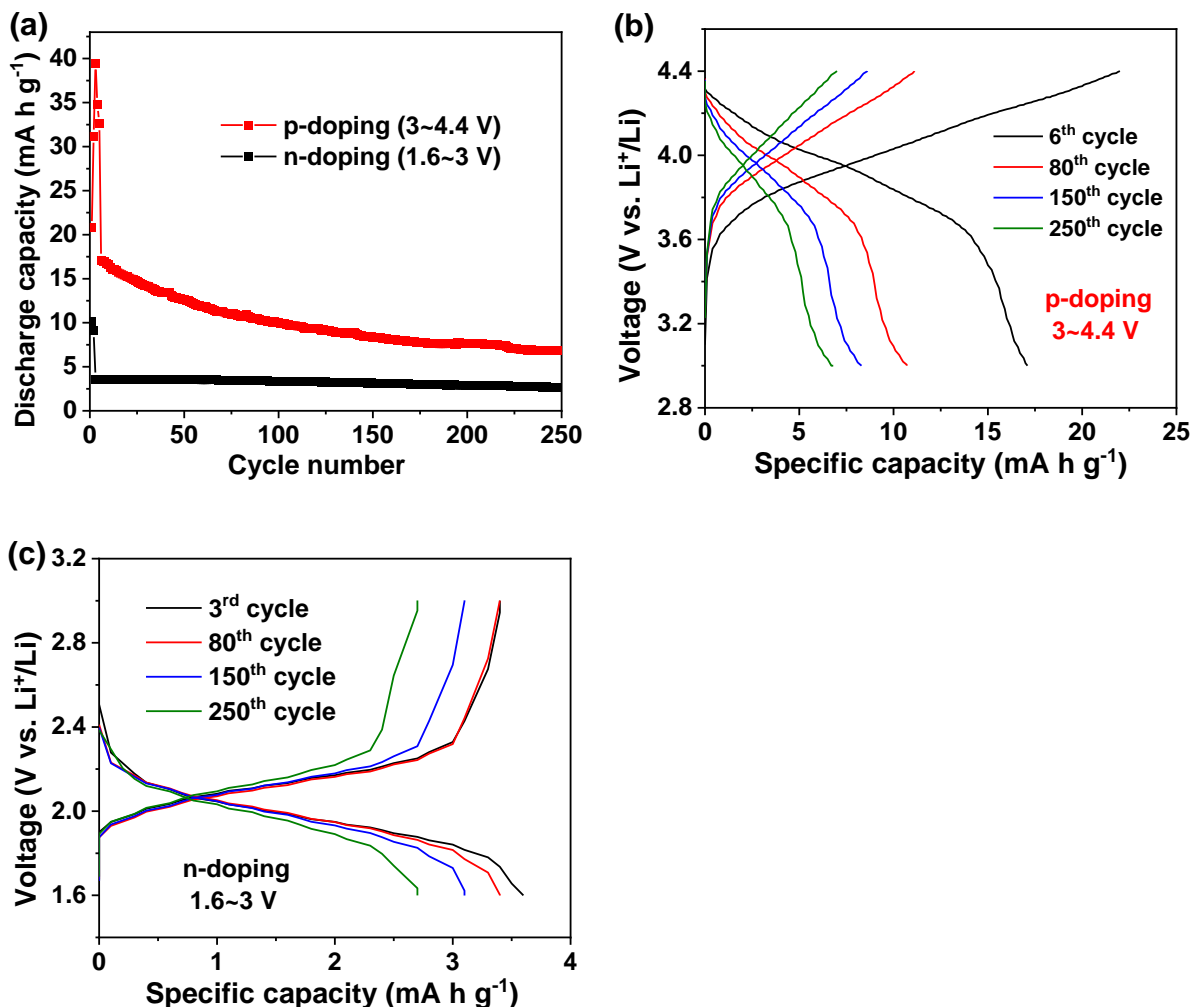
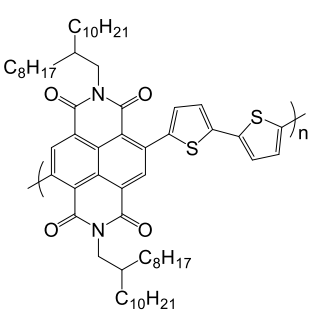
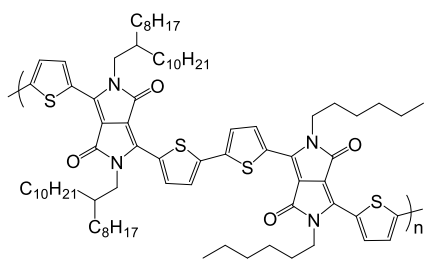
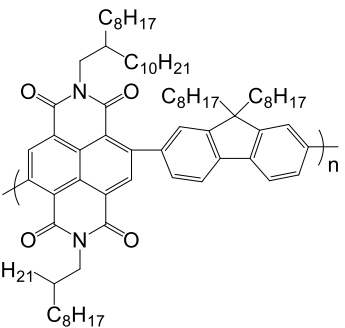


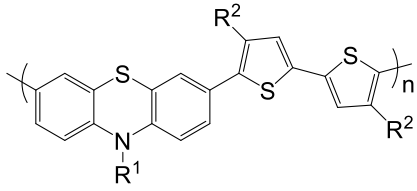
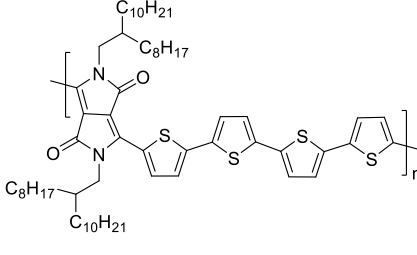
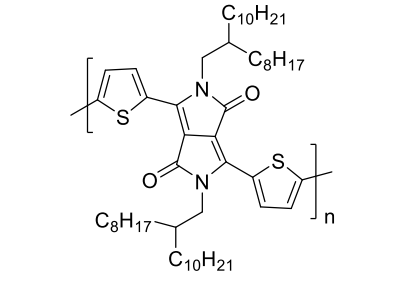
Figure 6.6 Galvanostatic cycling performance of the PDBT cathode in the p-doping or n-doping region. (a) Cycling performance in the p-doping (3~4.4 V) or n-doping (1.6~3 V) region. In the p-doping region, the cell was activated at 10 mA g⁻¹ for 5 cycles and cycled at 50 mA g⁻¹ afterwards. In the n-doping region, the cell was activated at 10 mA g⁻¹ for 2 cycles and cycled at 50 mA g⁻¹ afterwards. Voltage profiles with the current rate of 50 mA g⁻¹ at different cycle numbers for (b) the p-doping region, and (c) the n-doping region.

A comparison of the electrochemical performances of PDQT and PDBT cathodes with other solution processable conjugated polymer-based cathodes reported in the literature is shown in Table 6.1. It can be seen that the average discharge voltages of PDQT and PDBT are much higher than others. The experimentally obtained capacity of 44.4 mA h g⁻¹ for the PDQT cathode

is comparable to the best one in the table (P(NDI2OD-T2), 54.2 mA h g⁻¹). The PDBT cathode has the highest theoretical capacity among the cathodes listed in the table due to its unique bipolar-type charge storage mechanism. The experimentally obtained capacity for the PDBT cathode is only 17.1 mA h g⁻¹, which may be caused by the large particle size issue.

Table 6.1 Comparison of our work with other solution-processable conjugated polymer based cathodes.

	Charge storage mechanism	Theoretical capacity (mA h g ⁻¹)	Experimental reversible capacity (mA h g ⁻¹)	Average discharge voltage (V vs. Li ⁺ /Li)	References
	n	54.2	54.2	~2.4	215
	n	40.1	40	~2.15	217
	n	48.6	39.8	~2.45	226

	p	36.4	34	~3.55	216
	p	104.8	44.4	~3.8	Our work
	bipolar	124.8	17.1	~2.95	Our work

6.3.3 Theoretical calculations

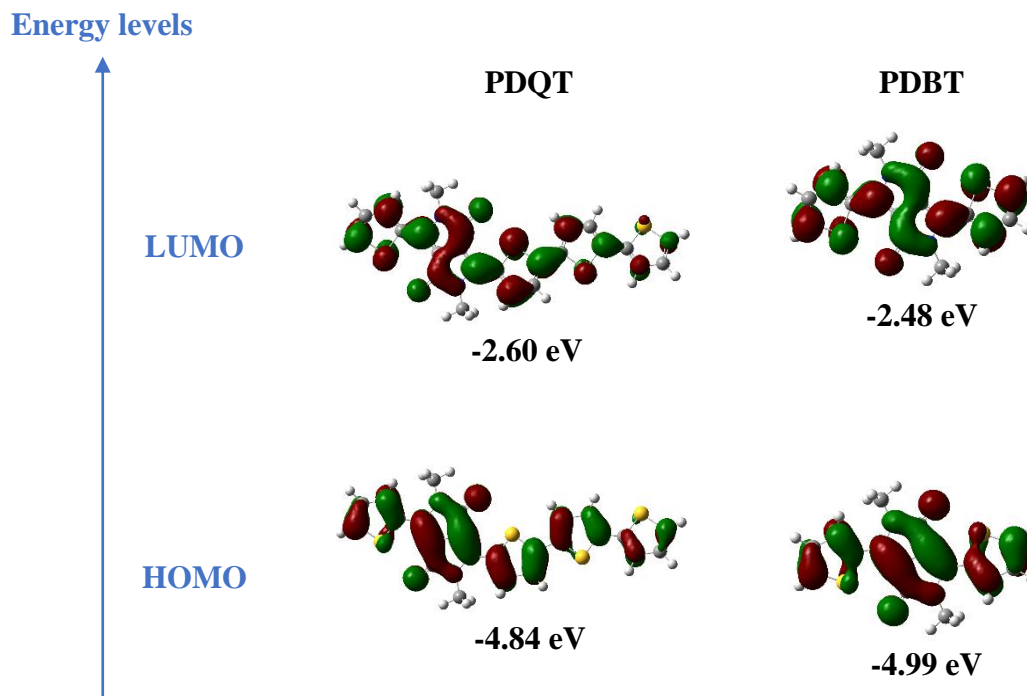


Figure 6.7 Energy levels of PDQT and PDBT.

The energy levels of PDQT and PDBT are obtained by density functional theory (DFT) calculations. As shown in Figure 6.7, the HOMO and LUMO levels of PDQT are -4.84 and -2.60 eV, respectively, which corresponds to a band gap (E_g) of 2.24 eV, whereas they are -4.99 and -2.48 eV, respectively, for PDBT, which corresponds to a band gap of 2.51 eV. The smaller band gap of PDQT is indicative of a higher conductivity.

6.4 Conclusions

Two DPP-based conjugated polymers, PDQT and PDBT have been developed as the cathode materials for Li-ion storage. The PDQT cathode shows a p-type charge storage mechanism with a theoretical capacity of $124.8 \text{ mA h g}^{-1}$ and an experimental capacity of 44.4 mA h g^{-1} (corresponding to a doping level of 42%) while the PDBT cathode shows a bipolar charge storage mechanism with a theoretical capacity of $124.8 \text{ mA h g}^{-1}$ and an experimental capacity of 17.1 mA h g^{-1} . The experimental average discharge voltages for the PDQT and PDBT cathodes are ~ 3.8 and ~ 2.95 V, respectively, which are much higher than other conjugated polymer cathodes. Further

optimization of the testing condition (e.g. nanocomposite formation between the organic material and porous carbon) is needed to increase the experimental capacity of the PDBT cathode.

Chapter 7. Conclusions and Future Outlook

7.1 Conclusions

In this thesis, different strategies, including the use of PEDOT adsorber for polysulfides (chapter 3 and Chapter 4), in-cell polymerization (Chapter 4), coordination polymer formation and binder optimization (Chapter 5) and conventional polymerization (chapter 6), have been designed to improve the specific capacity and cycling stability of sulfur and organic cathodes. These strategies are designed with the aims of maximizing the energy densities and cycling stabilities of the electrodes. By using various characterization techniques, the conductivity change of conductive polymers during battery cycling, the relationship between molecular structure and battery performance, the capacity fading mechanism, and the charge storage mechanism have been revealed.

In Chapter 3, a multi-functional PEDOT:PSS-Mg²⁺ binder formed by cross-linking PEDOT:PSS with Mg²⁺ was developed for the sulfur cathode in Li-S batteries. This new binder has high electrical conductivity, a robust 3-D network structure achieved by the cross-linking of PSS with Mg²⁺ ions, and a strong binding ability toward lithium polysulfides due to the strong interaction between the oxygen atoms in PEDOT and lithium polysulfides. These functionalities can increase the conduction and charge transfer reactions, cushion the drastic volume change during discharge/charge cycling, and trap the soluble lithium polysulfides in the cathode. The Li-S battery with a cathode using this new binder exhibited an initial capacity of 1097 mA h g⁻¹ and capacity retention of 74% over 250 cycles at 0.5C, which are significant improvements compared with the Li-S battery using a conventional PVDF binder. Moreover, the preparation of the cathode slurry and the subsequent cathode fabrication using the PEDOT:PSS-Mg²⁺ binder uses water present in the PEDOT:PSS dispersion as the only dispersing solvent, which eliminates the use of any organic solvent, making the fabrication of Li-S batteries more environmentally friendly. Therefore, this study demonstrated that the cross-linked PEDOT:PSS-Mg²⁺ is a very promising new binder for high-performance Li-S batteries.

In Chapter 4, a facile and innovative in-cell e-polymerization approach has been developed to incorporate a conductive polymer (PEDOT) into the sulfur cathode. Such an approach affords intimate contact between PEDOT and other components in the cathode, which leads to enhanced electron transport and effective trapping of soluble polysulfides. As a result, the sulfur cathode

with the in-cell formed PEDOT shows substantially improved capacity, cycling stability, and rate performance compared with that using commercial PEDOT. Additionally, it has been found that the conductivities of conductive polymers change upon electrochemical doping and dedoping during the battery cycling process, and PEDOT would be more conductive for the cathode with a higher upper potential limit than sulfur cathode. Finally, the in-situ synthesis of PEDOT has been applied in LiFO₄ cathode, and a notable improvement in the specific capacity has been observed, which is in line with our expectation.

In Chapter 5, a series of one-dimensional coordination polymers using DHBQ and divalent metal ions (Ni²⁺, Co²⁺, Mn²⁺, Zn²⁺, and Cu²⁺) have been synthesized and their electrochemical properties have been compared. It has been found that the coordination polymers using Ni, Co, Mn, and Zn (M-DHBQ·2H₂O) exhibit the redox activities of both the metal and the DHBQ ligand in the potential range of 0.5~3 V, while the coordination polymer using Cu (Cu-DHBQ) exhibits the redox activity of only the DHBQ ligand in the same potential range. In the potential range of 1.3~3 V where only the DHBQ ligand is redox active, Cu-DHBQ exhibits the highest utilization of the quinone groups among all the as-synthesized coordination polymers. Moreover, the capacity fading mechanism of the Cu-DHBQ cathode is identified as the dissolution of the discharged product in the electrolyte, which is corroborated by UV-Vis analysis. By using the alginate binder (25 wt% in the cathode), which can strongly bond the electrode film and effectively trap the soluble species, the Cu-DHBQ cathode exhibits a high initial capacity of 261 mA h g⁻¹ at 20 mA g⁻¹ corresponding to a high utilization of 98.1% for the quinone groups, and can maintain a capacity of 194 mA h g⁻¹ after 200 cycles at 100 mA g⁻¹ with a capacity retention of 91.5%. Furthermore, our coordination approach is very versatile and can be extended to other ligand such as DHBQ-Cl which has a higher discharge voltage than that of DHBQ. Although no promising results have been obtained up to now for Cu-DHBQ-Cl, our approach opens up a new avenue for the applications of coordination polymers in energy storage. Additionally, the stabilization of organic cathode through acid-base interaction with the polymer binder has also been explored. It has been found that the binder optimization approach for improving the cycling stability of organic cathodes is only an auxiliary approach, whereas the polymerization approach, which includes the formation of polymers, macrostructures, COFs and MOFs, should be considered as the primary approach.

In Chapter 6, two DPP-based conjugated polymers, PDQT and PDBT have been developed as the cathode materials for Li-ion storage. The PDQT cathode shows a p-type charge storage mechanism with a theoretical capacity of $104.8 \text{ mA h g}^{-1}$ and an experimental value of 44.4 mA h g^{-1} , while the PDBT cathode shows a bipolar charge storage mechanism with a theoretical capacity of $124.8 \text{ mA h g}^{-1}$ and an experimental value of 17.1 mA h g^{-1} . The experimental average discharge voltages of the PDQT and PDBT cathodes are ~ 3.8 and ~ 2.95 V, respectively, which are much higher than other conjugated polymer cathodes. Further optimization of the testing condition (e.g. nanocomposite formation between the organic material and the porous carbon) is needed to increase the experimental capacity of PDBT. The bipolar charge storage substantially increases the theoretical capacity of conjugated polymer cathodes, and may also find applications in symmetric Li-ion cells.

7.2 Future outlook

Surface modification of conventional intercalation cathodes including LiCoO_2 (LCO) and $\text{LiNi}_x\text{Co}_y\text{Mn}_{1-x-y}\text{O}_2$ (NCM) to enhance the specific capacity, rate performance, and cycling stability of these materials under high voltage condition (> 4.2 V) is of paramount importance.^{227–230} Conductive polymers, with intrinsic conductivities upon doping, excellent stabilities under high voltage condition, are promising candidates to modify the intercalation cathodes.^{231–234} However, it is challenging to form a thin and uniform layer of conductive polymer on the cathode particles. Atomic layer deposition (ALD)²³⁵ and oxidative chemical vapor deposition (oCVD)²³¹ have been reported to do so, but these methods are quite expensive and inconvenient. The in-situ electro-polymerization method developed in Chapter 4 is low-cost and facile. Future aspects lie in utilizing this method to modify the intercalation cathodes with a variety of conductive polymers and investigating their influences on the battery performance.

Coordination polymers (CPs) and metal organic frameworks (MOFs) are a well-established research area where a plethora of related compounds have been reported.^{236,237} The coordination polymer approach demonstrated in Chapter 4 is an effective approach to suppress the dissolution issue of organic cathode materials. It is undesirable that the Cu metal in the Cu-DHBQ cathode be electrochemically inactive, resulting in a relatively low capacity. Future aspects lie in exploring other CPs and MOFs in which both metal and ligand are electroactive. It is also important to search for CPs and MOFs with intrinsic electrical conductivities^{181,238–240} as the electronic conduction is

a limiting factor for organic cathodes. Moreover, with so many metals and ligands to choose from, it is crucial to design electroactive CPs and MOFs with high discharge voltage (> 3.5 V) so that their energy densities are comparable to those of commercial intercalation compounds.

Conjugated polymer cathodes are a unique type of organic cathodes which enables mechanically flexible electrode films, superior cycling and rate performance for energy storage. The side chains in these materials render them solution processable, but greatly decrease their specific capacities for energy storage as the side chains are non-electroactive and they take up $\sim 55\%$ of the molecular weight of the repeat unit. The specific capacities of conjugated polymers would be doubled if the side chains can be removed. Future aspects lie in using thermally cleavable side chains during the syntheses of conjugated polymers and removing the side chains by thermal treatment after the electrode preparation.

References

- 1 B. Dunn, H. Kamath and J.-M. Tarascon, *Science*, 2011, **334**, 928–935.
- 2 N. Nitta, F. Wu, J. T. Lee and G. Yushin, *Mater. Today*, 2015, **18**, 252–264.
- 3 H. S. Majdi, Z. A. Latipov, V. Borisov, N. O. Yuryevna, M. M. Kadhim, W. Suksatan, I. H. Khlewee and E. Kianfar, *Nanoscale Res. Lett.*, 2021, **16**, 177.
- 4 J. W. Morgan and E. Anders, *Proc. Natl. Acad. Sci. U.S.A.*, 1980, **77**, 6973–6977.
- 5 Sulfur recovery, <https://www.tkinet.com/en/markets/tessengerlo-kerley-leader-world-marketplace-sulfur-recovery-and-processing>.
- 6 Annual sulfur production, <http://www.essentialchemicalindustry.org/chemicals/sulfur.html>.
- 7 N. S. Choi, Z. Chen, S. A. Freunberger, X. Ji, Y. K. Sun, K. Amine, G. Yushin, L. F. Nazar, J. Cho and P. G. Bruce, *Angew. Chem. Int. Ed.*, 2012, **51**, 9994–10024.
- 8 D. Herbert and J. Ulam, *US Patent*, 1962, 3043896.
- 9 A. Manthiram, Y. Fu, S. H. Chung, C. Zu and Y. S. Su, *Chem. Rev.*, 2014, **114**, 11751–11787.
- 10 R. Fang, S. Zhao, Z. Sun, D. W. Wang, H. M. Cheng and F. Li, *Adv. Mater.*, 2017, 1606823.
- 11 A. Kawase, S. Shirai, Y. Yamoto, R. Arakawa and T. Takata, *Phys. Chem. Chem. Phys.*, 2014, **16**, 9344–9350.
- 12 C. Barchasz, F. Molton, C. Duboc, J. C. Leprêtre, S. Patoux and F. Alloin, *Anal. Chem.*, 2012, **84**, 3973–3980.
- 13 Y. Diao, K. Xie, S. Xiong and X. Hong, *J. Electrochem. Soc.*, 2012, **159**, A421–A425.
- 14 M. Cuisinier, P. E. Cabelguen, S. Evers, G. He, M. Kolbeck, A. Garsuch, T. Bolin, M. Balasubramanian and L. F. Nazar, *J. Phys. Chem. Lett.*, 2013, **4**, 3227–3232.
- 15 J. Xiao, J. Z. Hu, H. Chen, M. Vijayakumar, J. Zheng, H. Pan, E. D. Walter, M. Hu, X. Deng, J. Feng, B. Y. Liaw, M. Gu, Z. D. Deng, D. Lu, S. Xu, C. Wang and J. Liu, *Nano Lett.*, 2015, **15**, 3309–3316.

- 16 M. U. M. Patel, R. Demir-Cakan, M. Morcrette, J. M. Tarascon, M. Gaberscek and R. Dominko, *ChemSusChem*, 2013, **6**, 1177–1181.
- 17 Q. Zou and Y. C. Lu, *J. Phys. Chem. Lett.*, 2016, **7**, 1518–1525.
- 18 W. Chen, T. Qian, J. Xiong, N. Xu, X. Liu, J. Liu, J. Zhou, X. Shen, T. Yang, Y. Chen and C. Yan, *Adv. Mater.*, 2017, **29**, 1605160.
- 19 Y. S. Su, Y. Fu, T. Cochell and A. Manthiram, *Nat. Commun.*, 2013, **4**, 2985.
- 20 X. Liang, C. Hart, Q. Pang, A. Garsuch, T. Weiss and L. F. Nazar, *Nat. Commun.*, 2015, **6**, 5682.
- 21 X. Ji, K. T. Lee and L. F. Nazar, *Nat. Mater.*, 2009, **8**, 500–506.
- 22 H. Chen, C. Wang, W. Dong, W. Lu, Z. Du and L. Chen, *Nano Lett.*, 2015, **15**, 798–802.
- 23 Y. S. Su, Y. Fu and A. Manthiram, *Phys. Chem. Chem. Phys.*, 2012, **14**, 14495–14499.
- 24 H. Wang, Y. Yang, Y. Liang, J. T. Robinson, Y. Li, A. Jackson, Y. Cui and H. Dai, *Nano Lett.*, 2011, **11**, 2644–2647.
- 25 W. Zhou, Y. Yu, H. Chen, F. J. Disalvo and H. D. Abruña, *J. Am. Chem. Soc.*, 2013, **135**, 16736–16743.
- 26 Z. W. Seh, W. Li, J. J. Cha, G. Zheng, Y. Yang, M. T. McDowell, P. C. Hsu and Y. Cui, *Nat. Commun.*, 2013, **4**, 1331.
- 27 R. Cao, W. Xu, D. Lv, J. Xiao and J. G. Zhang, *Adv. Energy Mater.*, 2015, **5**, 1402273.
- 28 D. Aurbach, E. Pollak, R. Elazari, G. Salitra, C. S. Kelley and J. Affinito, *J. Electrochem. Soc.*, 2009, **156**, A694.
- 29 S. Liu, G. R. Li and X. P. Gao, *ACS Appl. Mater. Interfaces*, 2016, **8**, 7783–7789.
- 30 Y. Lu, Z. Tu and L. A. Archer, *Nat. Mater.*, 2014, **13**, 961–969.
- 31 G. Ma, Z. Wen, M. Wu, C. Shen, Q. Wang, J. Jin and X. Wu, *Chem. Commun.*, 2014, **50**, 14209–14212.

- 32 Z. Peng, S. Wang, J. Zhou, Y. Jin, Y. Liu, Y. Qin, C. Shen, W. Han and D. Wang, *J. Mater. Chem. A*, 2016, **4**, 2427–2432.
- 33 G. Zheng, S. W. Lee, Z. Liang, H. W. Lee, K. Yan, H. Yao, H. Wang, W. Li, S. Chu and Y. Cui, *Nat. Nanotechnol.*, 2014, **9**, 618–623.
- 34 D. Lin, Y. Liu, Z. Liang, H. W. Lee, J. Sun, H. Wang, K. Yan, J. Xie and Y. Cui, *Nat. Nanotechnol.*, 2016, **11**, 626–632.
- 35 J. Schuster, G. He, B. Mandlmeier, T. Yim, K. T. Lee, T. Bein and L. F. Nazar, *Angew. Chem. Int. Ed.*, 2012, **51**, 3591–3595.
- 36 X. Li, Y. Cao, W. Qi, L. v. Saraf, J. Xiao, Z. Nie, J. Mietek, J. G. Zhang, B. Schwenzer and J. Liu, *J. Mater. Chem.*, 2011, **21**, 16603–16610.
- 37 Y. S. Su, Y. Fu and A. Manthiram, *Phys. Chem. Chem. Phys.*, 2012, **14**, 14495–14499.
- 38 D. Marmorstein, T. H. Yu, K. A. Striebel, F. R. McLarnon, J. Hou and E. J. Cairns, *J. Power Sources*, 2000, **89**, 219–226.
- 39 J. Hassoun and B. Scrosati, *Adv. Mater.*, 2010, **22**, 5198–5201.
- 40 K. Fu, Y. Gong, G. T. Hitz, D. W. McOwen, Y. Li, S. Xu, Y. Wen, L. Zhang, C. Wang, G. Pastel, J. Dai, B. Liu, H. Xie, Y. Yao, E. D. Wachsman and L. Hu, *Energy Environ. Sci.*, 2017, **10**, 1568–1575.
- 41 X. Yao, N. Huang, F. Han, Q. Zhang, H. Wan, J. P. Mwizerwa, C. Wang and X. Xu, *Adv. Energy Mater.*, 2017, **7**, 1602923.
- 42 W. Li, Q. Zhang, G. Zheng, Z. W. Seh, H. Yao and Y. Cui, *Nano Lett.*, 2013, **13**, 5534–5540.
- 43 Y. Yang, G. Yu, J. J. Cha, H. Wu, M. Vosgueritchian, Y. Yao, Z. Bao and Y. Cui, *ACS Nano*, 2011, **5**, 9187–9193.
- 44 Z. W. Seh, Q. Zhang, W. Li, G. Zheng, H. Yao and Y. Cui, *Chem. Sci.*, 2013, **4**, 3673–3677.
- 45 G. Li, M. Ling, Y. Ye, Z. Li, J. Guo, Y. Yao, J. Zhu, Z. Lin and S. Zhang, *Adv. Energy Mater.*, 2015, **5**, 1500878.

- 46 P. Bhattacharya, M. I. Nandasiri, D. Lv, A. M. Schwarz, J. T. Darsell, W. A. Henderson, D. A. Tomalia, J. Liu, J. G. Zhang and J. Xiao, *Nano Energy*, 2016, **19**, 176–186.
- 47 Q. Pang, D. Kundu, M. Cuisinier and L. F. Nazar, *Nat. Commun.*, 2014, **5**, 4759.
- 48 G. Zhou, H. Tian, Y. Jin, X. Tao, B. Liu, R. Zhang, Z. W. Seh, D. Zhuo, Y. Liu, J. Sun, J. Zhao, C. Zu, D. S. Wu, Q. Zhang and Y. Cui, *Proc. Natl. Acad. Sci. U.S.A.*, 2017, **114**, 840–845.
- 49 Z. Yuan, H. J. Peng, T. Z. Hou, J. Q. Huang, C. M. Chen, D. W. Wang, X. B. Cheng, F. Wei and Q. Zhang, *Nano Lett.*, 2016, **16**, 519–527.
- 50 X. Tao, J. Wan, C. Liu, H. Wang, H. Yao, G. Zheng, Z. W. Seh, Q. Cai, W. Li, G. Zhou, C. Zu and Y. Cui, *Nat. Commun.*, 2016, **7**, 11203.
- 51 R. Ponraj, A. G. Kannan, J. H. Ahn and D. W. Kim, *ACS Appl. Mater. Interfaces*, 2016, **8**, 4000–4006.
- 52 Y. Lu, X. Hou, L. Miao, L. Li, R. Shi, L. Liu and J. Chen, *Angew. Chem. Int. Ed.*, 2019, **131**, 7094–7098.
- 53 X. Liu and Z. Ye, *Adv. Energy Mater.*, 2021, **11**, 2003281.
- 54 Y. Lu and J. Chen, *Nat. Rev. Chem.*, 2020, **4**, 127–142.
- 55 T. Ma, Q. Zhao, J. Wang, Z. Pan and J. Chen, *Angew. Chem. Int. Ed.*, 2016, **128**, 6538–6542.
- 56 Z. Song, Y. Qian, T. Zhang, M. Otani and H. Zhou, *Adv. Sci.*, 2015, **2**, 1500124.
- 57 Z. Song, Y. Qian, X. Liu, T. Zhang, Y. Zhu, H. Yu, M. Otani and H. Zhou, *Energy Environ. Sci.*, 2014, **7**, 4077–4086.
- 58 Z. Song, H. Zhan and Y. Zhou, *Chem. Commun.*, 2009, 448–450.
- 59 M. Yao, H. Senoh, S. I. Yamazaki, Z. Siroma, T. Sakai and K. Yasuda, *J. Power Sources*, 2010, **195**, 8336–8340.
- 60 T. Yokoji, H. Matsubara and M. Satoh, *J. Mater. Chem. A*, 2014, **2**, 19347–19354.

- 61 H. Kim, J. E. Kwon, B. Lee, J. Hong, M. Lee, S. Y. Park and K. Kang, *Chem. Mater.*, 2015, **27**, 7258–7264.
- 62 Y. Liang, P. Zhang and J. Chen, *Chem. Sci.*, 2013, **4**, 1330–1337.
- 63 Y. Liang, P. Zhang, S. Yang, Z. Tao and J. Chen, *Adv. Energy Mater.*, 2013, **3**, 600–605.
- 64 Y. Lu, Q. Zhang, L. Li, Z. Niu and J. Chen, *Chem*, 2018, **4**, 2786–2813.
- 65 Z. Song, Y. Qian, M. L. Gordin, D. Tang, T. Xu, M. Otani, H. Zhan, H. Zhou and D. Wang, *Angew. Chem. Int. Ed.*, 2015, **127**, 14153–14157.
- 66 Z. Zhu, M. Hong, D. Guo, J. Shi, Z. Tao and J. Chen, *J. Am. Chem. Soc.*, 2014, **136**, 16461–16464.
- 67 W. Ai, W. Zhou, Z. Du, C. Sun, J. Yang, Y. Chen, Z. Sun, S. Feng, J. Zhao, X. Dong, W. Huang and T. Yu, *Adv. Funct. Mater.*, 2017, **27**, 1603603.
- 68 R. Shi, L. Liu, Y. Lu, C. Wang, Y. Li, L. Li, Z. Yan and J. Chen, *Nat. Commun.*, 2020, **11**, 178.
- 69 Z. Zhu, H. Li, J. Liang, Z. Tao and J. Chen, *Chem. Commun.*, 2015, **51**, 1446–1448.
- 70 H. Chen, M. Armand, G. Demailly, F. Dolhem, P. Poizot and J. M. Tarascon, *ChemSusChem*, 2008, **1**, 348–355.
- 71 H. Chen, M. Armand, M. Courty, M. Jiang, C. P. Grey, F. Dolhem, J. M. Tarascon and P. Poizot, *J. Am. Chem. Soc.*, 2009, **131**, 8984–8988.
- 72 R. H. Zeng, X. P. Li, Y. C. Qiu, W. S. Li, J. Yi, D. S. Lu, C. L. Tan and M. Q. Xu, *Electrochem. commun.*, 2010, **12**, 1253–1256.
- 73 J. Xiang, C. Chang, M. Li, S. Wu, L. Yuan and J. Sun, *Cryst. Growth Des.*, 2008, **8**, 280–282.
- 74 C. Luo, G.-L. Xu, X. Ji, S. Hou, L. Chen, F. Wang, J. Jiang, Z. Chen, Y. Ren, K. Amine and C. Wang, *Angew. Chem. Int. Ed.*, 2018, **130**, 2929–2933.
- 75 C. Luo, O. Borodin, X. Ji, S. Hou, K. J. Gaskell, X. Fan, J. Chen, T. Deng, R. Wang, J. Jiang and C. Wang, *Proc. Natl. Acad. Sci. U.S.A.*, 2018, **115**, 2004–2009.

- 76 M. Yao, K. Kuratani, T. Kojima, N. Takeichi, H. Senoh and T. Kiyobayashi, *Sci. Rep.*, 2014, **4**, 3650.
- 77 M. Yao, M. Araki, H. Senoh, S. I. Yamazaki, T. Sakai and K. Yasuda, *Chem. Lett.*, 2010, **39**, 950–952.
- 78 W. Xiong, W. Huang, M. Zhang, P. Hu, H. Cui and Q. Zhang, *Chem. Mater.*, 2019, **31**, 8069–8075.
- 79 H. Li, W. Duan, Q. Zhao, F. Cheng, J. Liang and J. Chen, *Inorg. Chem. Front.*, 2014, **1**, 193–199.
- 80 J. K. Kim, *J. Power Sources*, 2020, **477**, 228670.
- 81 Z. Luo, L. Liu, J. Ning, K. Lei, Y. Lu, F. Li and J. Chen, *Angew. Chem. Int. Ed.*, 2018, **130**, 9587–9590.
- 82 J. Lee, H. Kim and M. J. Park, *Chem. Mater.*, 2016, **28**, 2408–2416.
- 83 A. Yang, X. Wang, Y. Lu, L. Miao, W. Xie and J. Chen, *J. Energy Chem.*, 2018, **27**, 1644–1650.
- 84 W. Huang, Z. Zhu, L. Wang, S. Wang, H. Li, Z. Tao, J. Shi, L. Guan and J. Chen, *Angew. Chem. Int. Ed.*, 2013, **52**, 9162–9166.
- 85 Z. Zhu, M. Hong, D. Guo, J. Shi, Z. Tao and J. Chen, *J. Am. Chem. Soc.*, 2014, **136**, 16461–16464.
- 86 M. Gumustas, C. T. Sengel-Turk, A. Gumustas, S. A. Ozkan and B. Uslu, in *Multifunctional Systems for Combined Delivery, Biosensing and Diagnostics*, Elsevier, 2017, pp. 67–108.
- 87 R. Bottom, in *Principles and applications of thermal analysis*, ed. P. Gabbott, Blackwell, 2008, p. 88.
- 88 R. B. Prime, H. E. Bair, S. Vyazovkin, P. K. Gallagher and A. Riga, in *Thermal Analysis of Polymers - Fundamentals and Applications*, eds. J. D. Menczel and R. B. Prime, John Wiley & Sons, Inc., 2009, p. 241.

- 89 N. Saadatkah, A. Carillo Garcia, S. Ackermann, P. Leclerc, M. Latifi, S. Samih, G. S. Patience and J. Chaouki, *Can. J. Chem. Eng.*, 2020, **98**, 34–43.
- 90 J. Liu, C. Wang, J. Cui, J. Li, Q. Li, M. Liu and Y. Xi, *RSC Adv.*, 2019, **9**, 12331–12338.
- 91 D. K. Chattopadhyay and D. C. Webster, *Prog. Polym. Sci.*, 2009, **34**, 1068–1133.
- 92 J. Cai, D. Xu, Z. Dong, X. Yu, Y. Yang, S. W. Banks and A. v. Bridgwater, *Renewable and Sustainable Energy Rev.*, 2018, **82**, 2705–2715.
- 93 F. C. Jentoft, *Adv. Catal.*, 2009, **52**, 129–211.
- 94 D. A. Skoog, F. J. Holler and S. R. Crouch, in *Principles of Instrumental Analysis*, Cengage Learning, 2018, p. 318.
- 95 J. He, Y. Chen and A. Manthiram, *iScience*, 2018, **4**, 36–43.
- 96 Introduction to Fourier Transform Infrared Spectroscopy by ThermoFisher, <http://assets.thermofisher.com/TFS-Assets/MSD/brochures/introduction-fourier-transform-infraredspectroscopy-br50555.pdf>.
- 97 S.-Y. Yang, Y.-J. Chen, G. Zhou and Z.-W. Fu, *J. Electrochem. Soc.*, 2018, **165**, A1422–A1429.
- 98 K. L. Devries and A. Adams, in *Adhesion Science and Engineering*, 2002, **1**, 193–234.
- 99 B. A. Morris, in *The Science and Technology of Flexible Packaging*, Elsevier, 2017, pp. 351–400.
- 100 H. Jeon, J. Choi, M. H. Ryou and Y. M. Lee, *ACS Omega*, 2017, **2**, 2159–2164.
- 101 L. Wei, C. Chen, Z. Hou and H. Wei, *Sci. Rep.*, 2016, **6**, 19583.
- 102 L. Wei and Z. Hou, *J. Mater. Chem. A*, 2017, **5**, 22156–22162.
- 103 A. M. Gaikwad and A. C. Arias, *ACS Appl. Mater. Interfaces*, 2017, **9**, 6390–6400.
- 104 E. Talaie, P. Bonnick, X. Sun, Q. Pang, X. Liang and L. F. Nazar, *Chem. Mater.*, 2017, **29**, 90–105.

- 105 N. Elgrishi, K. J. Rountree, B. D. McCarthy, E. S. Rountree, T. T. Eisenhart and J. L. Dempsey, *J. Chem. Educ.*, 2018, **95**, 197–206.
- 106 G. Zhou, H. Tian, Y. Jin, X. Tao, B. Liu, R. Zhang, Z. W. Seh, D. Zhuo, Y. Liu, J. Sun, J. Zhao, C. Zu, D. S. Wu, Q. Zhang and Y. Cui, *Proc. Natl. Acad. Sci. U.S.A.*, 2017, **114**, 840–845.
- 107 L. Yan, X. Gao, J. P. Thomas, J. Ngai, H. Altounian, K. T. Leung, Y. Meng and Y. Li, *Sustain. Energy Fuels*, 2018, **2**, 1574–1581.
- 108 Y. Yang, G. Zheng and Y. Cui, *Chem. Soc. Rev.*, 2013, **42**, 3018–3032.
- 109 P. G. Bruce, S. A. Freunberger, L. J. Hardwick and J. M. Tarascon, *Nat. Mater.*, 2012, **11**, 19–29.
- 110 A. Rosenman, E. Markevich, G. Salitra, D. Aurbach, A. Garsuch and F. F. Chesneau, *Adv. Energy Mater.*, 2015, **5**, 1500212.
- 111 W. Kang, N. Deng, J. Ju, Q. Li, D. Wu, X. Ma, L. Li, M. Naebe and B. Cheng, *Nanoscale*, 2016, **8**, 16541–16588.
- 112 B. D. McCloskey, *J. Phys. Chem. Lett.*, 2015, **6**, 4581–4588.
- 113 J. Gao and H. D. Abruña, *J. Phys. Chem. Lett.*, 2014, **5**, 882–885.
- 114 G. Xu, Q. bo Yan, A. Kushima, X. Zhang, J. Pan and J. Li, *Nano Energy*, 2017, **31**, 568–574.
- 115 Z. Wang, Y. Chen, V. Battaglia and G. Liu, *J. Mater. Res.*, 2014, **29**, 1027–1033.
- 116 J. Pan, G. Xu, B. Ding, Z. Chang, A. Wang, H. Dou and X. Zhang, *RSC Adv.*, 2016, **6**, 40650–40655.
- 117 G. Ai, Y. Dai, Y. Ye, W. Mao, Z. Wang, H. Zhao, Y. Chen, J. Zhu, Y. Fu, V. Battaglia, J. Guo, V. Srinivasan and G. Liu, *Nano Energy*, 2015, **16**, 28–37.
- 118 L. ^{bert} Groenendaal, F. Jonas, D. Freitag, H. Pielartzik and J. R. Reynolds, *Adv. Mater.*, 2000, **12**, 481–494.

- 119 B. J. Worfolk, S. C. Andrews, S. Park, J. Reinspach, N. Liu, M. F. Toney, S. C. B. Mannsfeld and Z. Bao, *Proc. Natl. Acad. Sci. U.S.A.*, 2015, **112**, 14138–14143.
- 120 J. Rivnay, S. Inal, B. A. Collins, M. Sessolo, E. Stavrinidou, X. Strakosas, C. Tassone, D. M. Delongchamp and G. G. Malliaras, *Nat. Commun.*, 2016, **7**, 11287.
- 121 Z. Sun, J. Zhang, L. Yin, G. Hu, R. Fang, H. M. Cheng and F. Li, *Nat. Commun.*, 2017, **8**, 14627.
- 122 M. Barghamadi, A. Kapoor and C. Wen, *J. Electrochem. Soc.*, 2013, **160**, A1256–A1263.
- 123 Z. Lin and C. Liang, *J. Mater. Chem. A*, 2015, **3**, 936–958.
- 124 D. Zheng, D. Liu, J. B. Harris, T. Ding, J. Si, S. Andrew, D. Qu, X. Q. Yang and D. Qu, *ACS Appl. Mater. Interfaces*, 2017, **9**, 4326–4332.
- 125 A. Kawase, S. Shirai, Y. Yamoto, R. Arakawa and T. Takata, *Phys. Chem. Chem. Phys.*, 2014, **16**, 9344–9350.
- 126 W. Hua, Z. Yang, H. Nie, Z. Li, J. Yang, Z. Guo, C. Ruan, X. Chen and S. Huang, *ACS Nano*, 2017, **11**, 2209–2218.
- 127 Z. Zhang, L. L. Kong, S. Liu, G. R. Li and X. P. Gao, *Adv. Energy Mater.*, 2017, **7**, 1602543.
- 128 F. Y. Fan, W. H. Woodford, Z. Li, N. Baram, K. C. Smith, A. Helal, G. H. McKinley, W. C. Carter and Y. M. Chiang, *Nano Lett.*, 2014, **14**, 2210–2218.
- 129 Z. Deng, Z. Zhang, Y. Lai, J. Liu, J. Li and Y. Liu, *J. Electrochem. Soc.*, 2013, **160**, A553–A558.
- 130 H. Chen, Q. Zou, Z. Liang, H. Liu, Q. Li and Y. C. Lu, *Nat. Commun.*, 2015, **6**, 5877.
- 131 L. Ji, M. Rao, H. Zheng, L. Zhang, Y. Li, W. Duan, J. Guo, E. J. Cairns and Y. Zhang, *J. Am. Chem. Soc.*, 2011, **133**, 18522–18525.
- 132 X. Liang, A. Garsuch and L. F. Nazar, *Angew. Chem. Int. Ed.*, 2015, **127**, 3979–3983.
- 133 Z. Yu, Y. Xia, D. Du and J. Ouyang, *ACS Appl. Mater. Interfaces*, 2016, **8**, 11629–11638.
- 134 T. H. Le, Y. Kim and H. Yoon, *Polymers*, 2017, **9**, 150.

- 135 W. Li, Q. Zhang, G. Zheng, Z. W. Seh, H. Yao and Y. Cui, *Nano Lett.*, 2013, **13**, 5534–5540.
- 136 L. Yan, X. Gao, J. P. Thomas, J. Ngai, H. Altounian, K. T. Leung, Y. Meng and Y. Li, *Sustain. Energy Fuels*, 2018, **2**, 1574–1581.
- 137 Z. Wang, Y. Chen, V. Battaglia and G. Liu, *J. Mater. Res.*, 2014, **29**, 1027–1033.
- 138 Y. Fu and A. Manthiram, *J. Phys. Chem. C*, 2012, **116**, 8910–8915.
- 139 Y. Yang, G. Yu, J. J. Cha, H. Wu, M. Vosgueritchian, Y. Yao, Z. Bao and Y. Cui, *ACS Nano*, 2011, **5**, 9187–9193.
- 140 G. C. Li, G. R. Li, S. H. Ye and X. P. Gao, *Adv. Energy Mater.*, 2012, **2**, 1238–1245.
- 141 N. Nakamura, T. Yokoshima, H. Nara, T. Momma and T. Osaka, *J. Power Sources*, 2015, **274**, 1263–1266.
- 142 N. Nakamura, Y. Wu, T. Yokoshima, H. Nara, T. Momma and T. Osaka, *J. Electrochem. Soc.*, 2016, **163**, A683–A689.
- 143 F. Li, M. R. Kaiser, J. Ma, Z. Guo, H. Liu and J. Wang, *Energy Storage Mater.*, 2018, **13**, 312–322.
- 144 Y. Li, W. Wang, X. Liu, E. Mao, M. Wang, G. Li, L. Fu, Z. Li, A. Y. S. Eng, Z. W. Seh and Y. Sun, *Energy Storage Mater.*, 2019, **23**, 261–268.
- 145 H. Zhou, H. Liu, Y. Li, X. Yue, X. Wang, M. Gonzalez, Y. S. Meng and P. Liu, *J. Mater. Chem. A*, 2019, **7**, 16984–16991.
- 146 Q. Zhao, X. Liu, S. Stalin, K. Khan and L. A. Archer, *Nat. Energy.*, 2019, **4**, 365–373.
- 147 C. Z. Zhao, Q. Zhao, X. Liu, J. Zheng, S. Stalin, Q. Zhang and L. A. Archer, *Adv. Mater.*, 2020, **32**, 1905629.
- 148 Q. Liu, B. Cai, S. Li, Q. Yu, F. Lv, F. Kang, Q. Wang and B. Li, *J. Mater. Chem. A*, 2020, **8**, 7197–7204.
- 149 J. G. Ibanez, M. E. Rincón, S. Gutierrez-Granados, M. Chahma, O. A. Jaramillo-Quintero and B. A. Frontana-Uribe, *Chem. Rev.*, 2018, **118**, 4731–4816.

- 150 C. Li, H. Bai and G. Shi, *Chem. Soc. Rev.*, 2009, **38**, 2397–2409.
- 151 W. J. Albery, F. Li and A. R. Mount, *J. Electroanal. Chem.*, 1991, **310**, 239–253.
- 152 A. J. Downard and D. Pletcher, *J. Electroanal. Chem.*, 1986, **206**, 147–152.
- 153 S. Wang, Q. Wang, P. Shao, Y. Han, X. Gao, L. Ma, S. Yuan, X. Ma, J. Zhou, X. Feng and B. Wang, *J. Am. Chem. Soc.*, 2017, **139**, 4258–4261.
- 154 J. F. Rubinson and Y. P. Kayinamura, *Chem. Soc. Rev.*, 2009, **38**, 3339–3347.
- 155 D. Wei, P. Espindola, T. Lindfors, C. Kvarnström, J. Heinze and A. Ivaska, *J. Electroanal. Chem.*, 2007, **602**, 203–209.
- 156 T. A. Yemata, Y. Zheng, A. K. K. Kyaw, X. Wang, J. Song, W. S. Chin and J. Xu, *RSC Adv.*, 2020, **10**, 1786–1792.
- 157 M. Wieland, C. Malacrida, Q. Yu, C. Schlewitz, L. Scapinello, A. Penoni and S. Ludwigs, *Flex. Print. Electron.*, 2020, **5**, 014016.
- 158 C. Li and T. Imae, *Macromolecules*, 2004, **37**, 2411–2416.
- 159 T. Liu, K. C. Kim, B. Lee, S. Jin, M. J. Lee, M. Li, S. Noda, S. S. Jang and S. W. Lee, *ACS Appl. Energy Mater.*, 2020, **3**, 3728–3735.
- 160 J. Heinze, B. A. Frontana-Uribe and S. Ludwigs, *Chem. Rev.*, 2010, **110**, 4724–4771.
- 161 L. Hu, C. Dai, J. M. Lim, Y. Chen, X. Lian, M. Wang, Y. Li, P. Xiao, G. Henkelman and M. Xu, *Chem. Sci.*, 2018, **9**, 666–675.
- 162 V. S. Bryantsev, J. Uddin, V. Giordani, W. Walker, G. v. Chase and D. Addison, *J. Am. Chem. Soc.*, 2014, **136**, 3087–3096.
- 163 W. Walker, V. Giordani, J. Uddin, V. S. Bryantsev, G. v. Chase and D. Addison, *J. Am. Chem. Soc.*, 2013, **135**, 2076–2079.
- 164 C. Li and T. Imae, *Macromolecules*, 2004, **37**, 2411–2416.
- 165 J. P. Pender, G. Jha, D. H. Youn, J. M. Ziegler, I. Andoni, E. J. Choi, A. Heller, B. S. Dunn, P. S. Weiss, R. M. Penner and C. B. Mullins, *ACS Nano*, 2020, **14**, 1243–1295.

- 166 L. Wang, J. Qiu, X. Wang, L. Chen, G. Cao, J. Wang, H. Zhang and X. He, *eScience*, 2022, **2**, 125–137.
- 167 J. Jiang, W. Shi, J. Zheng, P. Zuo, J. Xiao, X. Chen, W. Xu and J.-G. Zhang, *J. Electrochem. Soc.*, 2014, **161**, A336–A341.
- 168 M. Klett, R. Eriksson, J. Groot, P. Svens, K. Ciosek Högström, R. W. Lindström, H. Berg, T. Gustafson, G. Lindbergh and K. Edström, *J. Power Sources*, 2014, **257**, 126–137.
- 169 E. R. Logan, H. Hebecker, A. Eldesoky, A. Luscombe, M. B. Johnson and J. R. Dahn, *J. Electrochem. Soc.*, 2020, **167**, 130543.
- 170 G. García, S. Dieckhöfer, W. Schuhmann and E. Ventosa, *J. Mater. Chem. A*, 2018, **6**, 4746–4751.
- 171 M. Armand, S. Grugéon, H. Vezin, S. Laruelle, P. Ribière, P. Poizot and J. M. Tarascon, *Nat. Mater.*, 2009, **8**, 120–125.
- 172 L. Zhu, G. Ding, L. Xie, X. Cao, J. Liu, X. Lei and J. Ma, *Chem. Mater.*, 2019, **31**, 8582–8612.
- 173 Z. Luo, L. Liu, Q. Zhao, F. Li and J. Chen, *Angew. Chem. Int. Ed.*, 2017, **129**, 12735–12739.
- 174 G. Li, H. Yang, F. Li, F. Cheng, W. Shi, J. Chen and P. Cheng, *Inorg. Chem.*, 2016, **55**, 4935–4940.
- 175 J. Du, Y. Li, H. Liu, W. Shi, L. v. Moskaleva and P. Cheng, *ACS Appl. Mater. Interfaces*, 2019, **11**, 25863–25869.
- 176 M. Lee, J. Hong, J. Lopez, Y. Sun, D. Feng, K. Lim, W. C. Chueh, M. F. Toney, Y. Cui and Z. Bao, *Nat. Energy*, 2017, **2**, 861–868.
- 177 C. Luo, X. Fan, Z. Ma, T. Gao and C. Wang, *Chem*, 2017, **3**, 1050–1062.
- 178 J. Liu, D. Xie, W. Shi and P. Cheng, *Chem. Soc. Rev.*, 2020, **49**, 1624–1642.
- 179 A. E. Baumann, D. A. Burns, B. Liu and V. S. Thoi, *Commun. Chem.*, 2019, **2**, 86.
- 180 L. E. Darago, M. L. Aubrey, C. J. Yu, M. I. Gonzalez and J. R. Long, *J. Am. Chem. Soc.*, 2015, **137**, 15703–15711.

- 181 M. E. Ziebel, L. E. Darago and J. R. Long, *J. Am. Chem. Soc.*, 2018, **140**, 3040–3051.
- 182 Robert Frank, G. R. Clark and J. N. Coker, *J. Am. Chem. Soc.*, 1950, **72**, 1827–1829.
- 183 R. S. Bottei and J. T. Fangmant, *J. Inorg. Nucl. Chem.*, 1966, **28**, 1259–1264.
- 184 S. Morikawa, T. Yamada and H. Kitagawa, *Chem. Lett.*, 2009, **38**, 654–655.
- 185 T. Yamada, S. Morikawa and H. Kitagawa, *Bull. Chem. Soc. Jpn.*, 2010, **83**, 42–48.
- 186 J. Xiang, C. Chang, M. Li, S. Wu, L. Yuan and J. Sun, *Cryst. Growth Des.*, 2008, **8**, 280–282.
- 187 K. Kon, K. Uchida, K. Fuku, S. Yamanaka, B. Wu, D. Yamazui, H. Iguchi, H. Kobayashi, Y. Gambe, I. Honma and S. Takaishi, *ACS Appl. Mater. Interfaces*, 2021, **13**, 38188–38193.
- 188 W. Phoohinkong, T. Foophow and W. Pecharapa, *Adv. Nat. Sci.: Nanosci. Nanotechnol.*, 2017, **8**, 035003.
- 189 Z. Luo, W. Cheng, H. Chen, X. Fu, X. Peng, F. Luo and L. Nie, *J. Agric. Food Chem.*, 2013, **61**, 4631–4638.
- 190 K. v. Nielson, L. Zhang, Q. Zhang and T. L. Liu, *Inorg. Chem.*, 2019, **58**, 10756–10760.
- 191 H. Liu, H. Li, F. Cheng, W. Shi, J. Chen and P. Cheng, *Inorg. Chem.*, 2018, **57**, 10640–10648.
- 192 L. Zhang, F. Cheng, W. Shi, J. Chen and P. Cheng, *ACS Appl. Mater. Interfaces*, 2018, **10**, 6398–6406.
- 193 H. H. Lee, J. bin Lee, Y. Park, K. H. Park, M. S. Okyay, D. S. Shin, S. Kim, J. Park, N. Park, B. K. An, Y. S. Jung, H. W. Lee, K. T. Lee and S. Y. Hong, *ACS Appl. Mater. Interfaces*, 2018, **10**, 22110–22118.
- 194 H. Senoh, M. Yao, H. Sakaebe, K. Yasuda and Z. Siroma, *Electrochim. Acta*, 2011, **56**, 10145–10150.
- 195 S. Goriparti, M. N. K. Harish and S. Sampath, *Chem. Commun.*, 2013, **49**, 7234–7236.

- 196 J. Zhao, M. Zhou, J. Chen, L. Tao, Q. Zhang, Z. Li, S. Zhong, H. Fu, H. Wang and L. Wu, *Chem. Eng. J.*, 2021, **425**, 131630.
- 197 C. Hu, P. Li, W. Zhang, Y. Che, Y. Sun, F. Chi, S. Ran, X. Liu and Y. Lv, *Mater. Res.*, 2017, **20**, 407–412.
- 198 S. Zhu and L. Lu, *Molecules*, 2020, **25**, 612.
- 199 L. Sieuw, A. Jouhara, É. Quarez, C. Auger, J. F. Gohy, P. Poizot and A. Vlad, *Chem. Sci.*, 2019, **10**, 418–426.
- 200 L. Suo, O. Borodin, T. Gao, M. Olguin, J. Ho, X. Fan, C. Luo, C. Wang and K. Xu, *Science*, 2015, **350**, 938–943.
- 201 T. S. Mathis, N. Kurra, X. Wang, D. Pinto, P. Simon and Y. Gogotsi, *Adv. Energy Mater.*, 2019, **9**, 1902007.
- 202 D. Chao, C. Zhu, P. Yang, X. Xia, J. Liu, J. Wang, X. Fan, S. v. Savilov, J. Lin, H. J. Fan and Z. X. Shen, *Nat. Commun.*, 2016, **7**, 12122.
- 203 T. Brezesinski, J. Wang, S. H. Tolbert and B. Dunn, *Nat. Mater.*, 2010, **9**, 146–151.
- 204 J. Wang, J. Polleux, J. Lim and B. Dunn, *J. Phys. Chem. C*, 2007, **111**, 14925–14931.
- 205 Z. Sun, H. Liu, M. Shu, Z. Lin, B. Liu, Y. Li, J. Li, T. Yu, H. Yao, S. Zhu and S. Guan, *ACS Appl. Mater. Interfaces*, 2022, **14**, 36700–36710.
- 206 P. Zheng, C. Han, L. W. Luo, P. Dong, W. Ma, C. Zhang, Y. Chen and J. X. Jiang, *Chem. Commun.*, 2022, **58**, 4763–4766.
- 207 Z. Song, L. Miao, H. Duan, L. Ruhlmann, Y. Lv, D. Zhu, L. Li, L. Gan and M. Liu, *Angew. Chem. Int. Ed.*, 2022, **61**, e202208821.
- 208 J. Wang, H. Liu, C. Du, X. Zhang, Y. Liu, H. Yao, Z. Sun and S. Guan, *Chem. Eng. J.*, 2022, **444**, 136598.
- 209 K. Nakahara, S. Iwasa, M. Satoh, Y. Morioka, J. Iriyama, M. Suguro and E. Hasegawa, *Chem. Phys. Lett.*, 2002, **359**, 351–354.

- 210 H. Nishide, S. Iwasa, Y. J. Pu, T. Suga, K. Nakahara and M. Satoh, *Electrochim. Acta*, 2004, **50**, 827–831.
- 211 K. Nakahara, K. Oyaizu and H. Nishide, *Chem. Lett.*, 2011, **40**, 222–227.
- 212 M. E. Speer, M. Kolek, J. J. Jassoy, J. Heine, M. Winter, P. M. Bieker and B. Esser, *Chem. Commun.*, 2015, **51**, 15261–15264.
- 213 M. Kolek, F. Otteny, P. Schmidt, C. Mück-Lichtenfeld, C. Einholz, J. Becking, E. Schleicher, M. Winter, P. Bieker and B. Esser, *Energy Environ. Sci.*, 2017, **10**, 2334–2341.
- 214 B. Tian, G. H. Ning, W. Tang, C. Peng, D. Yu, Z. Chen, Y. Xiao, C. Su and K. P. Loh, *Mater. Horiz.*, 2016, **3**, 429–433.
- 215 Y. Liang, Z. Chen, Y. Jing, Y. Rong, A. Facchetti and Y. Yao, *J. Am. Chem. Soc.*, 2015, **137**, 4956–4959.
- 216 P. Acker, L. Rzesny, C. F. N. Marchiori, C. M. Araujo and B. Esser, *Adv. Funct. Mater.*, 2019, **29**, 1906436.
- 217 J. J. Samuel, V. K. Karrothu, R. K. Canjeevaram Balasubramanyam, A. A. Mohapatra, C. Gangadharappa, V. R. Kankanallu, S. Patil and N. P. B. Aetukuri, *J. Phys. Chem. C*, 2021, **125**, 4449–4457.
- 218 T. M. Swager, *Macromolecules*, 2017, **50**, 4867–4886.
- 219 S. Griggs, A. Marks, H. Bristow and I. McCulloch, *J. Mater. Chem. C*, 2021, **9**, 8099–8128.
- 220 C. B. Nielsen, M. Turbiez and I. McCulloch, *Adv. Mater.*, 2013, **25**, 1859–1880.
- 221 T. B. Schon, B. T. McAllister, P. F. Li and D. S. Seferos, *Chem. Soc. Rev.*, 2016, **45**, 6345–6404.
- 222 Y. Li, B. Sun, P. Sonar and S. P. Singh, *Org. Electron.*, 2012, **13**, 1606–1613.
- 223 S. Chen, B. Sun, W. Hong, H. Aziz, Y. Meng and Y. Li, *J. Mater. Chem. C*, 2014, **2**, 2183–2190.
- 224 K. Xu, S. P. Ding and T. R. Jow, *J. Electrochem. Soc.*, 1999, **146**, 4172–4178.

- 225 J. J. Samuel, V. K. Karrothu, R. K. Canjeevaram Balasubramanyam, A. A. Mohapatra, C. Gangadharappa, V. R. Kankanallu, S. Patil and N. P. B. Aetukuri, *J. Phys. Chem. C*, 2021, **125**, 4449–4457.
- 226 K. T. Sarang, A. Miranda, H. An, E. S. Oh, R. Verduzco and J. L. Lutkenhaus, *ACS Appl. Polym. Mater.*, 2019, **1**, 1155–1164.
- 227 Z. Chen, Y. Qin, K. Amine and Y. K. Sun, *J. Mater. Chem.*, 2010, **20**, 7606–7612.
- 228 W. Li, B. Song and A. Manthiram, *Chem. Soc. Rev.*, 2017, **46**, 3006–3059.
- 229 S. Kalluri, M. Yoon, M. Jo, S. Park, S. Myeong, J. Kim, S. X. Dou, Z. Guo and J. Cho, *Adv. Energy Mater.*, 2017, **7**, 1601507.
- 230 P. K. Nayak, E. M. Erickson, F. Schipper, T. R. Penki, N. Munichandraiah, P. Adelhelm, H. Sclar, F. Amalraj, B. Markovsky and D. Aurbach, *Adv. Energy Mater.*, 2018, **8**, 1702397.
- 231 G. L. Xu, Q. Liu, K. K. S. Lau, Y. Liu, X. Liu, H. Gao, X. Zhou, M. Zhuang, Y. Ren, J. Li, M. Shao, M. Ouyang, F. Pan, Z. Chen, K. Amine and G. Chen, *Nat. Energy*, 2019, **4**, 484–494.
- 232 S. Chen, T. He, Y. Su, Y. Lu, L. Bao, L. Chen, Q. Zhang, J. Wang, R. Chen and F. Wu, *ACS Appl. Mater. Interfaces*, 2017, **9**, 29732–29743.
- 233 Y. Cao, X. Qi, K. Hu, Y. Wang, Z. Gan, Y. Li, G. Hu, Z. Peng and K. Du, *ACS Appl. Mater. Interfaces*, 2018, **10**, 18270–18280.
- 234 C. H. Lai, D. S. Ashby, T. C. Lin, J. Lau, A. Dawson, S. H. Tolbert and B. S. Dunn, *Chem. Mater.*, 2018, **30**, 2589–2599.
- 235 X. Meng, X. Q. Yang and X. Sun, *Adv. Mater.*, 2012, **24**, 3589–3615.
- 236 M. Safaei, M. M. Foroughi, N. Ebrahimpoor, S. Jahani, A. Omidi and M. Khatami, *Trends Anal. Chem.*, 2019, **118**, 401–425.
- 237 H. Furukawa, K. E. Cordova, M. O’Keeffe and O. M. Yaghi, *Science*, 2013, **341**, 1230444.
- 238 J. Park, M. Lee, D. Feng, Z. Huang, A. C. Hinckley, A. Yakovenko, X. Zou, Y. Cui and Z. Bao, *J. Am. Chem. Soc.*, 2018, **140**, 10315–10323.

- 239 M. E. Ziebel, C. A. Gaggioli, A. B. Turkiewicz, W. Ryu, L. Gagliardi and J. R. Long, *J. Am. Chem. Soc.*, 2020, **142**, 2653–2664.
- 240 J. Park, A. C. Hinckley, Z. Huang, D. Feng, A. A. Yakovenko, M. Lee, S. Chen, X. Zou and Z. Bao, *J. Am. Chem. Soc.*, 2018, **140**, 14533–14537.